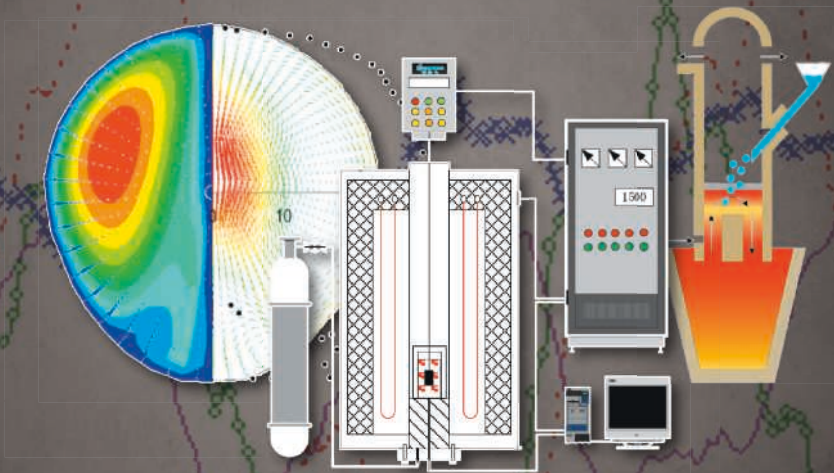


MATERIALS PROCESSING FUNDAMENTALS 2021



EDITED BY

Jonghyun Lee

Samuel Wagstaff

Alexandra Anderson

Fiseha Tesfaye

Guillaume Lambotte

Antoine Allanore

TMS

 Springer

The Minerals, Metals & Materials Series

Jonghyun Lee · Samuel Wagstaff ·
Alexandra Anderson · Fiseha Tesfaye ·
Guillaume Lambotte · Antoine Allanore
Editors

Materials Processing Fundamentals 2021

TMS

 Springer

Editors

Jonghyun Lee
Iowa State University
Ames, IA, USA

Samuel Wagstaff
Oculatus
Marietta, GA, USA

Alexandra Anderson
Gopher Resource
Tampa, FL, USA

Fiseha Tesfaye
Åbo Akademi University
Turku, Finland

Guillaume Lambotte
Boston Metal
Woburn, MA, USA

Antoine Allanore
Massachusetts Institute of Technology
Cambridge, MA, USA

ISSN 2367-1181

ISSN 2367-1696 (electronic)

The Minerals, Metals & Materials Series

ISBN 978-3-030-65252-4

ISBN 978-3-030-65253-1 (eBook)

<https://doi.org/10.1007/978-3-030-65253-1>

© The Minerals, Metals & Materials Society 2021

This work is subject to copyright. All rights are solely and exclusively licensed by the Publisher, whether the whole or part of the material is concerned, specifically the rights of translation, reprinting, reuse of illustrations, recitation, broadcasting, reproduction on microfilms or in any other physical way, and transmission or information storage and retrieval, electronic adaptation, computer software, or by similar or dissimilar methodology now known or hereafter developed.

The use of general descriptive names, registered names, trademarks, service marks, etc. in this publication does not imply, even in the absence of a specific statement, that such names are exempt from the relevant protective laws and regulations and therefore free for general use.

The publisher, the authors and the editors are safe to assume that the advice and information in this book are believed to be true and accurate at the date of publication. Neither the publisher nor the authors or the editors give a warranty, expressed or implied, with respect to the material contained herein or for any errors or omissions that may have been made. The publisher remains neutral with regard to jurisdictional claims in published maps and institutional affiliations.

Cover Illustration: Left: From Chapter “Containerless Materials Processing for Materials Science on Earth and in Space”, Jonghyun Lee et al., Figure 3: Left [33]: Convection velocity field in an EM-levitated Co–Cu droplet. Black dots indicate surface convection velocity along the meridian. Convection velocity near the equator is predicted as $\sim 30 \text{ cm}\cdot\text{s}^{-1}$; middle [37]: numerically predicted maximum convection velocity as a function of heater current in a Fe–Co droplet processed using the ISS-EML; right [31]: predicted accessible range of convection (gray parallelogram) in a Fe–Co sample during ISS-EML processing. https://doi.org/10.1007/978-3-030-65253-1_16. Middle: From Chapter “Influence of Cr_2O_3 Content on Phase of Chromium-Containing High-Titanium Blast Furnace Slag”, Ding Yang et al., Figure 1: Experimental apparatus for the slag viscosity measurements. https://doi.org/10.1007/978-3-030-65253-1_19. Right: From Chapter “Study on Evolution of Inclusions in Tinplate Production During RH Refining—Continuous Casting Process”, Xiaobao Li et al., Figure 1: Illustration of sampling during RH refining process. https://doi.org/10.1007/978-3-030-65253-1_5.

This Springer imprint is published by the registered company Springer Nature Switzerland AG
The registered company address is: Gewerbestrasse 11, 6330 Cham, Switzerland

Preface

The symposium Materials Processing Fundamentals is hosted at the Annual Meeting of The Minerals, Metals & Materials Society (TMS) as the flagship symposium of the Process Technology and Modeling Committee. It is a unique opportunity for interdisciplinary presentations and discussions about, among others, processing, sensing, modeling, multi-physics, computational fluid dynamics, and thermodynamics.

The materials covered include ferrous and non-ferrous elements, and the processes range from mining unit operations to jointing and surface finishing of materials. Acknowledging that modern processes involve multi-physics, the symposium and its proceedings allow the reader to learn the methods and outcome of other fields' modeling practices, often enabling the development of practical solutions to common problems. Modeling of basic thermodynamic and physical properties plays a key role, along with computational fluid dynamics and multi-phase transport and interface modeling.

Contributions to the proceedings include applications such as steel processing, modeling of steel and non-ferrous alloys treatments for properties control, multi-physics and computational fluid dynamics modeling for molten metal processes and properties measurement. Extractive, recovery, and recycling process modeling is also presented, completing a broad view of the field and practices of modeling in materials processing.

The engagement of TMS and committee members to chair sessions and review manuscripts makes this symposium and its proceedings possible. The editor and co-editors acknowledge the invaluable support and contribution of these volunteers as well as TMS staff members, in particular, Patricia Warren, Trudi Dunlap, and Matt Baker.

Jonghyun Lee
Samuel Wagstaff
Alexandra Anderson
Fiseha Tesfaye
Guillaume Lambotte
Antoine Allanore

Contents

Part I Molten Metal Processing and Modeling

Effect of Turbulence Suppressor on Molten Steel Flow in Tundish	3
Jie Luo, Si-kun Peng, Ai-ping Zhang, and Yong Zhong	
X-Ray and Neutron Radiographic Experiments on Particle-Laden Molten Metal Flows	13
Tobias Lappan, Mărtinș Sarma, Sascha Heitkam, David Mannes, Pavel Trtik, Natalia Shevchenko, Kerstin Eckert, and Sven Eckert	
Study on the Effect of Long Shroud Structure on Molten Steel Flow in Single Strand Tundish by Numerical Simulation	31
Ai-ping Zhang, Ming-mei Zhu, and Jie Luo	
Numerical Simulation of the Influence of Particle Physical Properties on Flow Field During the Aeration Leaching Process	43
Mingzhao Zheng, Qiuyue Zhao, Zimu Zhang, Lei Zhou, and Tingan Zhang	

Part II Steel Casting

Study on Evolution of Inclusions in Tinplate Production During RH Refining—Continuous Casting Process	55
Xiaoao Li, Nan Wang, and Min Chen	
Flotation of Molybdenite in the Presence of Sheared Polyacrylamide Flocculants	69
Luver Echeverry, Darwin Estrada, and Leopoldo Gutierrez	

Part III Thermodynamics on Metals and Slags Processing

Modelling of Metal Loss in Ferromanganese Furnace Tapping Operations	83
Quinn Gareth Reynolds and Jan Erik Olsen	

Carbothermic Reduction of Brazilian Linz–Donawitz (LD) Steel Sludges	93
Mery C. Gómez-Marroquín, José Carlos D’Abreu, Enrique R. Dionisio-Calderón, Nilton Cárdenas-Falcón, Abraham J. Terrones-Ramirez, Jhony F. Huarcaya-Nina, Kim J. Phatti-Satto, and Fernando Huamán-Pérez	
Liquid–Liquid Extraction Thermodynamic Parameter Estimator (LLEPE) for Multicomponent Separation Systems	107
Titus Quah and Chukwunwike O. Iloeje	
Thermodynamic Modeling of Iron-Copper-Sulfuric Acid Solutions During Solvent Extraction and Electrowinning for Copper Production	121
Jiahao Xu and Guikuan Yue	
Part IV Metal Processing and Manufacturing	
An Experimental Study on the Melting Temperature of Mould Flux Under Electromagnetic Field	133
Yijia Wang, Mingxing Wang, Li Zhao, and Yu Wang	
Effect of Dissolution of Titanium Ions on Ti Alloys Electrodeposition from EMIC-AlCl₃ Ionic Liquid at Low Temperature	141
Pravin S. Shinde and Ramana G. Reddy	
Effect of ZrO₂ Filters on Inclusions in Steel	155
Ming Li, Biao Tao, Huajie Wu, and Yanhui Sun	
Part V Poster Session	
A Hybrid Model for Predicting the End-Point Phosphorus Content of Electric Arc Furnace	167
Chao Chen, Nan Wang, and Min Chen	
Considerations of Removing Arsenic from Molten Steel by Adding Rare Earth Elements	177
Yu Peng, Hongpo Wang, and Silu Jiang	
Containerless Materials Processing for Materials Science on Earth and in Space	187
Jonghyun Lee, Sai Katamreddy, Yong Chan Cho, Sooheyong Lee, and Geun Woo Lee	
Effect of Nitrogen on Weldability and the Microstructure in Laser Beam Welding of Duplex Stainless Steel	201
Yunxing Xia, Kenshiro Amatsu, Fumikazu Miyasaka, and Hiroaki Mori	

Experimental Measurements and Optimized Iida Model Estimations of Viscosity in Vanadium Slag with Different FeO Content 211
 Lingxi Zhang and Min Chen

Influence of Cr₂O₃ Content on Phase of Chromium-Containing High-Titanium Blast Furnace Slag 221
 Ding Yang, Hanghang Zhou, Jian Wang, and Guibao Qiu

Influence of Natural Convection Caused by Slag Density Difference on Temperature and Solidification of Molten Slag 227
 Chunming Zhang, Nan Wang, and Min Chen

Influence of Rotation Speed and Temperature on Dissolution Rate of Cr₂O₃ in Ti-Bearing Blast-Furnace Slag 239
 Guibao Qiu, Ding Yang, Feng Zhang, and Jian Wang

Numerical Simulation of Microscale Metallic Particle Impact Using Eulerian Approach 249
 Cal Vin Wong and Jonghyun Lee

Optimal Design of the Submerged Entry Nozzle Structure and Modification of Technology for ASP Continuous Casting 261
 Mingtao Xuan, Min Chen, Xiaojie Hua, and Kaizhu Zhang

Thermodynamic Examination of Quaternary Compounds in the Ag–Fe–(Ge, Sn)–Se Systems by the Solid-State EMF Method 271
 Mykola Moroz, Fiseha Tesfaye, Pavlo Demchenko, Myroslava Prokhorenko, Bohdan Rudyk, Lyudmyla Soliak, Daniel Lindberg, Oleksandr Reshetnyak, and Leena Hupa

Author Index 285

Subject Index 287

About the Editors



Jonghyun Lee is an assistant professor in the Department of Mechanical Engineering at Iowa State University. He has been conducting multiple industry and government-funded projects in the field of materials processing as PI and Co-PI. He is the recipient of the Young Leaders Professional Development Award in 2013 from The Minerals, Metals & Materials Society where he has been serving as a co-organizer and co-editor of the Materials Processing Fundamentals Symposium since 2014 and as chair of the Process Technology and Modeling Committee since 2019. Prior to joining his current institution, he was a research assistant professor at the University of Massachusetts, Amherst. He also had nearly 5 years of industry experience and worked as a postdoctoral associate for Tufts University, Medford, Massachusetts. He earned his M.S. and Ph.D. in Mechanical Engineering from the University of Massachusetts Amherst and his B.S. in the same discipline from Inha University in Incheon, South Korea.



Samuel Wagstaff is currently a partner at Oculatus Consulting, specializing in aluminum processing and product development. He earned his B.Sc. degree from Cornell University in Mechanical and Aerospace Engineering in 2013. He earned a M.Sc. degree at the Massachusetts Institute of Technology focusing on characterizing macrosegregation patterns in large format rolling slabs. He then earned a Sc.D. in 2016 also from MIT for his work on engineering convective flows to minimize the appearance of macrosegregation. Following his graduate studies, he worked at Novelis in their rolling facility in Sierre, Switzerland in their automotive development department, focusing on process refinement and product troubleshooting. In 2018 he moved to the Novelis R&D center in Kennesaw, Georgia where he became a lead scientist for product and process development. At Oculatus, he works on next-generation technologies for the aluminum sector and improvements in current processes. His current focus is on improving the profitability of existing centers via casting process improvement and recycle-based product development. Dr. Wagstaff is the author of 16 peer-reviewed articles, and inventor of over 25 patent applications.



Alexandra Anderson is a senior research and development engineer at Gopher Resource, a lead battery recycler, in Tampa, Florida. She received her Bachelor of Science degree in Mechanical Engineering from Gonzaga University in 2013, continuing her education at the Colorado School of Mines where she earned both a Master of Science and a Doctor of Philosophy in Metallurgical and Materials Engineering. Her doctoral research focused on computational fluid-dynamic modeling of reverberatory furnaces use for secondary lead production. At Gopher Resource, Alexandra directs the reverberatory furnace productivity program, encompassing all optimization and expansion projects related to the furnace as well as burner technology implementation and computational modeling initiatives. Dr. Anderson is an active TMS volunteer, serving as

secretary of both the Process Technology and Modeling Committee and the Recycling and Environmental Technologies Committee.



Fiseha Tesfaye is a senior researcher with the title of Docent in metallurgical thermodynamics in the Johan Gadolin Process Chemistry Centre of Åbo Akademi University, Finland. He received his M.Sc. degree in materials processing technology and Ph.D. degree in metallurgy from Aalto University, Finland. His research activities are focused mainly on the thermodynamic investigation of inorganic materials as well as rigorous theoretical and experimental investigations for promoting improved valuable metals and renewable energy production. In 2018, Dr. Tesfaye was also appointed as a visiting research scientist in Seoul National University, South Korea.

Dr. Tesfaye is a regular contributor and active member of The Minerals, Metals & Materials Society (TMS), and is a winner of the 2018 TMS Young Leaders Professional Development Award. He serves as a subject editor for *JOM*, the member journal of TMS, and has edited several scientific research books. His personal research achievements include remarkable improvement of experimental research applying the solid-state EMF technique for thermodynamic investigations of inorganic materials, as well as noticeable contribution for promoting the move toward the circular economy. In his research areas, Dr. Tesfaye has published over 55 peer-reviewed publications.



Guillaume Lambotte is the VP of Research and Development at Boston Metal, a Massachusetts Institute of Technology (MIT) spin-off startup focusing on the development of an environmentally friendly and energetically efficient primary metal extraction process. Dr. Lambotte primarily focuses on computational thermodynamic modeling, electrochemistry, and high-temperature equilibrium. Prior to joining Boston Metal, he conducted research as a post-doctoral associate at the University of Massachusetts Amherst and MIT. Before his graduate studies, Dr. Lambotte worked as a production assistant manager at Alcan Extruded Products (Crailsheim, Germany).

Dr. Lambotte obtained his bachelor's degree from the European Engineer School for Materials Science (Nancy, France). He received a M.Sc. and a Ph.D. in metallurgical engineering from Ecole Polytechnique of Montreal (Montreal, Canada).

Dr. Lambotte was the recipient of the 2015 TMS EPD Young Leaders Professional Development Award. The same year he was one of the TMS representatives at the Emerging Leaders Alliance Conference.



Antoine Allanore is an associate professor of metallurgy in the Department of Materials Science and Engineering at MIT. He received his higher education in Nancy (France) where he earned a chemical process engineer diploma from Ecole Nationale Supérieure des Industries Chimiques and a M.Sc. and Ph.D. from Lorraine University. Dr. Allanore joined MIT in 2012 as a faculty member, leading a research group that develops sustainable materials extraction and manufacturing processes. He has developed numerous alternative approaches for metals and minerals extraction and processing. With an emphasis on electrochemical methods for both analytical and processing purposes, his group combines experimental and modeling approaches to promptly investigate the ultimate state of condensed matter, the molten state. He teaches thermodynamics and sustainable chemical metallurgy at both the undergraduate and graduate levels. He received the Vittorio de Nora Award from TMS in 2012, and the TMS Early Career Faculty Fellow Award in 2015.

Part I
Molten Metal Processing and Modeling

Effect of Turbulence Suppressor on Molten Steel Flow in Tundish



Jie Luo, Si-kun Peng, Ai-ping Zhang, and Yong Zhong

Abstract In this paper, the influence of the structure of turbulence inhibitor on the flow of molten steel in tundish is studied. By means of numerical simulation, by changing the shape of turbulence inhibitor and adding eaves on the top, the different influences on the flow field, temperature field, inclusion removal rate, molten steel quality, and residence time distribution curve of the whole tundish and the injection zone are obtained. By comparing the effects of four different shapes of turbulence inhibitors, this paper provides guidance for the design of flow control device in tundish.

Keywords Turbulence suppressor · Numerical simulation · Flow field · Temperature field

Introduction

As a fluid reactor, tundish plays an important role in the continuous casting process. The molten steel from the ladle flows to the tundish through the long nozzle and flows to the mold through the tundish to achieve the purpose of continuous casting. The flow mode and residence time of molten steel in tundish will affect the flow mode of molten steel and the floating of inclusions, which are closely related to the quality of continuous casting billet [1–4]. Therefore, setting reasonable flow control device in tundish is an important way to optimize the flow mode and mixing uniformity of molten steel in tundish. In recent years, turbulence inhibitors have been widely used. Turbulence inhibitors have different shapes. Their outer wall size and structure are of great significance to the flow pattern of molten steel in tundish.

He et al. [5] pointed out that the effect of circular turbulence inhibitor on the flow characteristics of molten steel in the impact zone is very obvious. It can improve the mixing ability of molten steel, promote the collision, growth, and removal of non-metallic inclusions, promote the homogenization of temperature and composition

J. Luo (✉) · S. Peng · A. Zhang · Y. Zhong
College of Materials Science and Engineering, Chongqing University, Chongqing 400044, China
e-mail: 201909131200@cqu.edu.cn

of molten steel, and prevent the erosion of tundish lining in impact zone by high-speed molten steel. Yang et al. [6] found that in asymmetric double-flow tundish, the temperature difference between two outlets can be effectively reduced by using asymmetric turbulence inhibitor and wall with guide hole. Merder [7] found that turbulence inhibitors have a favorable effect on the durability of refractory lining near the inlet zone; compared with tundish without turbulence inhibitors, the application of turbulence inhibitors makes the mixing of molten steel better. This improvement is based on increasing the dynamics of molten steel mixing, so that the centralized mixing zone of molten steel is also larger. This situation is conducive to floating non-metallic inclusions into the slag.

To sum up, in order to obtain the ideal flow mode and mixing degree of molten steel in tundish and improve the impurity removal rate, this paper takes the rectangular large capacity tundish as the research object, carries on the numerical simulation for several different turbulence inhibitors in the injection area, compares with the original tundish, and concludes that the influence of turbulence inhibitors with different shapes and structures on the molten steel flow is in the injection zone. Finally, it provides guidance for designing reasonable turbulence inhibitor in large capacity tundish.

Numerical Simulation Research Method

Model Hypothesis

The flow of molten steel in the actual tundish is very complicated, and the high-temperature working environment makes experimentation and measurement extremely difficult. In order to facilitate the study of the flow phenomenon in the tundish, this study has the following assumptions:

- (1) The flow of molten steel in the tundish is a steady-state incompressible viscous fluid.
- (2) The inclusions are spherical particles, and the movements are independent of each other.
- (3) The effect of temperature on flow, density, and viscosity is negligible.
- (4) In order to make the flow of molten steel in tundish close to the real situation, the movement of molten steel is turbulent motion.

Model Formulation

The flow of molten steel in the continuous casting tundish is a three-dimensional turbulent flow, and the mass equation, momentum equation, energy equation, and turbulent kinetic energy equation used in the calculation are as follows.

Continuity equation:

$$\frac{\partial P}{\partial t} + \frac{\partial(\rho\mu_i)}{\partial x_i} = 0 \quad (1)$$

Momentum equation:

$$\frac{\partial(\rho\mu_i\mu_j)}{\partial x_j} = -\frac{\partial P}{\partial x_j} + \frac{\partial}{\partial x_j} \left(\mu_{\text{eff}} \frac{\partial \mu_i}{\partial x_j} \right) + \frac{\partial}{\partial x_i} \left(\mu_{\text{eff}} \frac{\partial \mu_j}{\partial x_i} \right) + \rho g_i \quad (2)$$

Standard k - ε equation describing the turbulent viscosity coefficient (the model can be used to calculate the complicated turbulent flow):

$$\frac{\partial(\rho\mu_i)}{\partial x_i} = \frac{\partial}{\partial x_i} \left[\left(\mu_{\text{eff}} + \frac{\mu_t}{\sigma_k} \right) \frac{\partial k}{\partial x_i} \right] + G - \rho \varepsilon \quad (3)$$

$$\frac{\partial(\rho\mu_i\varepsilon)}{\partial x_i} = \frac{\partial}{\partial x_i} \left[\left(\mu_{\text{eff}} + \frac{\mu_t}{\sigma_\varepsilon} \right) \frac{\partial \varepsilon}{\partial x_i} \right] + c_1 \frac{\varepsilon}{k} G - c_2 \frac{\varepsilon^2}{k} \rho \quad (4)$$

among them: $G = \mu_t \frac{\partial \mu_j}{\partial x_i} \left(\frac{\partial \mu_j}{\partial x_j} + \frac{\partial \mu_i}{\partial x_j} \right)$; $\mu_{\text{eff}} = \mu + \mu_t = \mu + c_\mu \rho \frac{k^2}{\varepsilon}$.

Energy equation related to temperature field calculation:

$$\rho \left(\frac{\partial T}{\partial t} + C_p \frac{\partial T}{\partial x_i} \right) = \frac{\partial}{\partial x_i} \left(k_{\text{eff}} \frac{\partial T}{\partial x_i} \right) \quad (5)$$

Equation of transport behavior of inclusions in tundish:

$$\frac{du_{pi}}{dt} = \frac{18u}{\rho_p d_p^2} \cdot \frac{C_D \text{Re}}{24} (u_i - u_{pi}) + \frac{(\rho_p - \rho)}{\rho_p} g_p + F_i \quad (6)$$

Mass transfer equation of tracer in tundish:

$$\left(\frac{\partial C}{\partial t} + \nabla \times U_c \right) = \nabla \times \left(\rho D_c + \frac{\mu_t}{S_{c_t}} \right) \nabla \times \left(\frac{C}{\rho} \right) + S_c \quad (7)$$

where ρ is the density, kg m^{-3} ; u_i and u_j are the velocity of molten steel in the i and j directions, m s^{-1} ; p is the pressure, Pa; μ_{eff} is the effective viscosity, $\text{kg m}^{-1} \text{S}^{-1}$; C_1 , C_2 , C_μ , C_k , and C_ε are empirical constants; their values are 1.44, 1.93, 0.99, 1.0, and 1.3, respectively; k_{eff} is the effective thermal conductivity, $\text{W m}^{-1} \text{K}^{-1}$; ρ_p is the particle density, kg m^{-3} ; d_p is the particle diameter, m; u_{pi} is the particle velocity, m s^{-1} ; C_D is the drag coefficient; Re is the relative Reynolds coefficient; F_i is the force, N; S_c is the volume source phase, is the residual mass per unit volume of the tracer unit time, $\text{kg}/(\text{m}^3 \text{s})$; and D_c is the tracer diffusion coefficient; this paper takes

$1.1 \times 10^{-8} \text{ m}^2/\text{s}$; μ_t is the turbulent viscosity of molten steel, $\text{kg}/(\text{m s})$; SC_t is the turbulent Schmidt number of the tracer, taken 0.9.

Boundary Conditions

This study defines the ladle shroud as the velocity inlet and assumes that the velocity profile on the inlet section is the same; the outlet is the pressure outlet; the liquid–solid interface is considered to have no slip boundary, the velocity value on the solid wall is 0; the free surface is zero shear stress. The heat radiation loss of the wall and the free surface is neglected; the inclusion particles are adsorbed and removed by the molten steel surface slag layer; the inclusions in contact with the wall surface of the intermediate tundish are considered to be completely rebounded. The simulation parameters involved in the numerical simulation calculation are shown in Table 1.

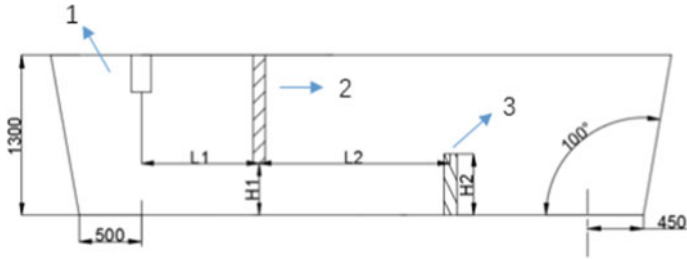
Simulation Scheme

The tundish studied in this paper has retaining wall and dam. In the simulation process, the immersion depth of the long nozzle is 300 mm, the working liquid level is 1300 mm, the distance between the long nozzle and the wall is 500 mm, the distance from the outlet to the wall is 450 mm, the distance between the two nozzles is 3990 mm, the distance from the center of the retaining wall to the center of the long nozzle is 1300 mm, the distance from the bottom of the tundish is 500 mm, the distance from the center of the retaining wall to the center of the retaining wall is 700 mm, the height of the dam is 650 mm, and the thickness of the retaining wall is 100 mm. The original tundish and its flow control device are shown in Fig. 1.

In this paper, four kinds of turbulence inhibitors with different geometries are considered, as shown in Fig. 2. The adjustment of flow control device in tundish

Table 1 Important physical parameters for simulation of fluid flow in tundish

Parameters	Values	Parameters	Values
Viscosity	$0.0067 \text{ kg m}^{-1} \text{ s}^{-1}$	Thermal conductivity	$41 \text{ W m}^{-2} \text{ K}^{-1}$
Specific heat	$750 \text{ J kg}^{-1} \text{ K}^{-1}$	Free surface heat flow	15 kW m^{-2}
Density	7020 kg m^{-3}	Bottom wall heat loss	1.4 kW m^{-2}
Turbulent kinetic energy at the inlet	$0.01 V_{in}^2 \text{ m}^2/\text{s}^2$	Long wall heat loss	3.8 kW m^{-2}
Dissipation rate at the inlet	$33.33 K_{in}^{1.5} \text{ m}^2/\text{s}^3$	Short wall heat loss	3.2 kW m^{-2}
Inlet temperature	1823 K	Inlet diameter	160 mm
Inlet velocity	0.744 m/s	Tracer diffusion coefficient	$1.1 \times 10^{-8} \text{ m}^2/\text{s}$



1-Long nozzle:2-Retaining wall:3-Retaining dam

Fig. 1 Diagram of original tundish. (Color figure online)

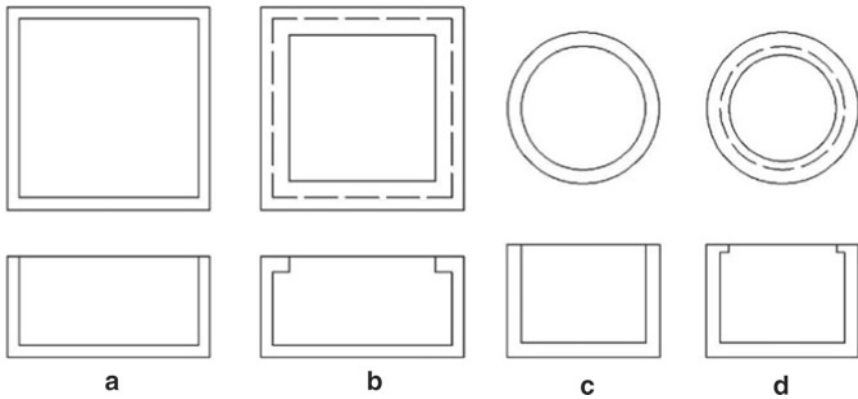


Fig. 2 Four kinds of turbulence inhibitors

should help to form obvious dense mixing area, can increase the average residence time of molten steel in tundish, control the renewal rate of molten steel, and provide time for inclusion floating. In addition, it will affect the improvement of ingot structure and the reduction of impurities in the produced steel.

Results and Discussion

Through the simulation of the original tundish (case 0) and the tundish with four different turbulence inhibitors added, the predicted values of flow field, temperature field and inclusion trajectory in the tundish under each scheme were obtained.

Comparison of Flow Fields

Figure 3 shows the velocity vector characteristic diagram of molten steel on the symmetry plane in the tundish under each scheme.

In the tundish with turbulence inhibitors, the first thing to pay attention to is the injection area at the inlet. In the original tundish shown in Fig. 3a, the fluid flows at high speed all the way down to the bottom of the tundish, forming a high negative velocity gradient upward. In the upper left of these high-speed vectors, a large recirculation flow with a smaller velocity is found. The molten steel flows into the tundish from the nozzle, collides with the bottom of the tundish, and then hits the retaining wall and dam to the right. A part of the molten steel flows along the bottom of the tundish to the dam, forming a small backflow near the dam. It can be seen from Fig. 3b–e that the number of reflux in the injection zone is significantly increased, which is conducive to the full mixing of molten steel in the injection zone, improving the mixing degree of molten steel, and playing an important role in improving the quality of molten steel and improving the removal rate of inclusions. The stirring degree of B and C is similar to that of A. D has a small reflux near the liquid surface in the upper right part of the injection zone, and the velocity vector density decreases.

Figure 4 shows the velocity nephogram of liquid level under each scheme. It can be seen that except case A, the areas with higher velocity are in the injection zone.

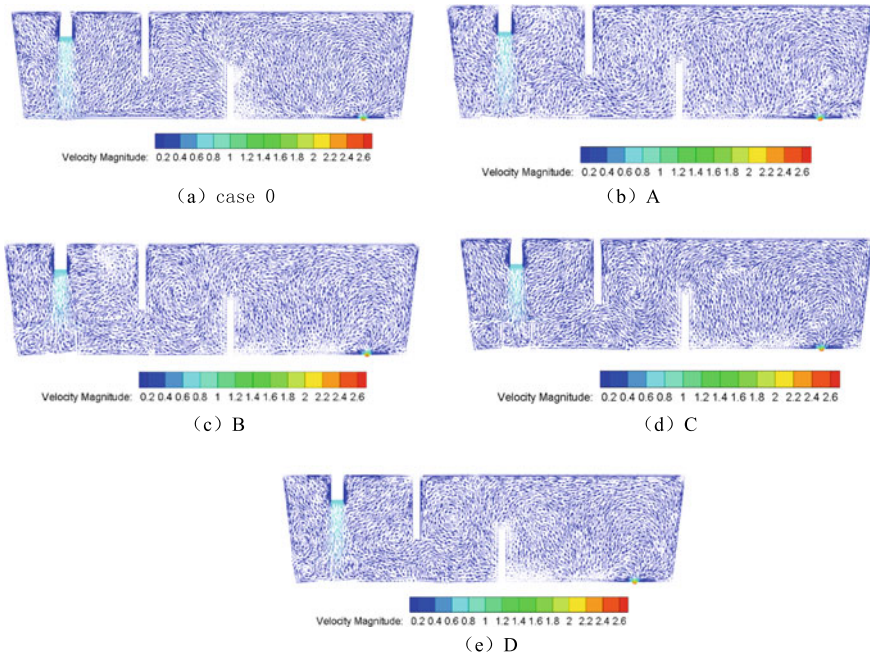


Fig. 3 Velocity vector diagram of symmetry plane. (Color figure online)

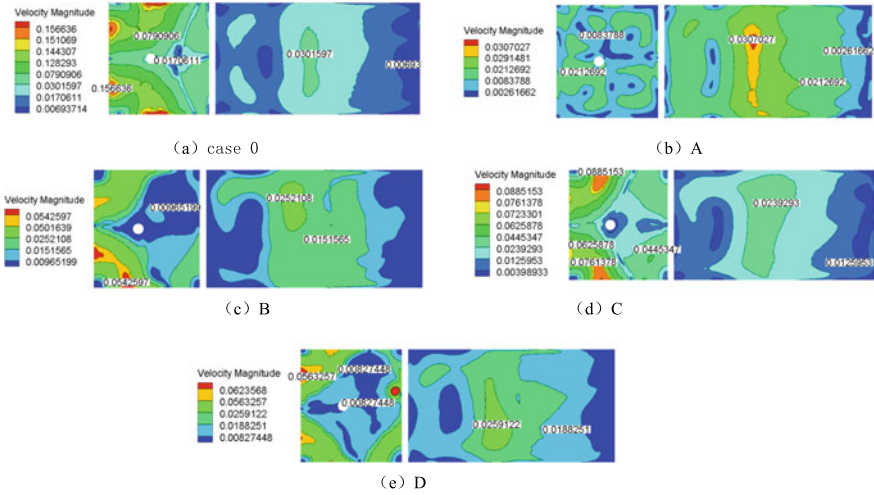


Fig. 4 Nephogram of velocity distribution of free surface. (Color figure online)

Table 2 Scheme A-D: free surface velocity

Scheme	Average velocity of free surface (m/s)
A	0.013082756
B	0.015983118
C	0.022407318
D	0.017380551

The free surface velocity of the original tundish without turbulence inhibitor is much higher than that of the schemes with turbulence inhibitor. The overall free surface velocity of scheme A is the lowest, the difference between scheme B and scheme D is not much, and the free surface velocity of scheme C is larger than that of other schemes. Table 2 shows the average free surface velocity values of A-D scheme.

Comparison of Temperature Fields

The temperature field distribution of symmetrical surface of tundish under each scheme is shown in Fig. 5. It can be seen that the temperature distribution of the symmetry surface of the original tundish and the tundish under various schemes can be seen. Combined with Table 3, it can be found that the minimum temperature in the tundish mostly occurs in the dead zone at the upper right corner. It can be seen that the addition of turbulence suppressor is beneficial to the uniform temperature distribution in the left injection zone. On the whole, the effect of turbulence inhibitor on the temperature difference between left and right sides is not obvious.

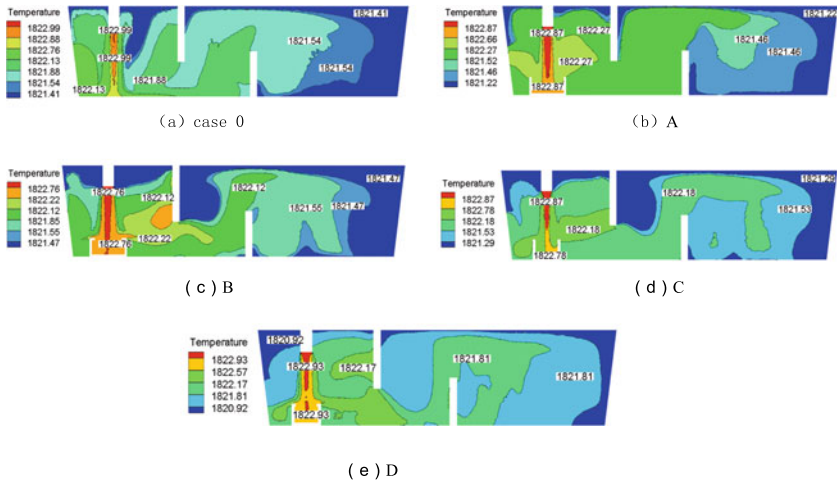


Fig. 5 Temperature distribution nephogram of symmetry plane. (Color figure online)

Table 3 Temperature in tundish

Scheme	Maximum temperature in tundish (°C)	Minimum temperature in tundish (°C)
Case 0	1823.52	1794.55
A	1823.03	1774.06
B	1823.13	1787.10
C	1824.10	1792.20
D	1823.07	1789.99

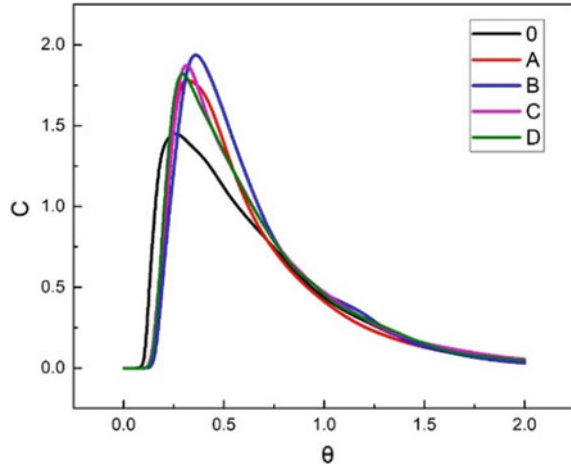
Comparison of Inclusion Removal Effects

After the calculation by Fluent, the DPM model was used to simulate the inclusion with certain particle size and density added from the long nozzle, and the free surface boundary condition was set as tarp. The inclusion removal rate can be calculated by dividing the captured particles by the total number, as shown in Table 4. It can be seen that the removal rate of inclusions in scheme B and scheme D is relatively high.

Table 4 Inclusion removal rate

Scheme	Inclusion removal rate (%)
Case 0	67.5
A	75.5
B	78.3
C	77.8
D	79.4

Fig. 6 RTD curve. (Color figure online)



RTD Curve

The concentration of tracer in tundish with time was calculated by component transfer equation, and the RTD curves under different schemes were obtained. It can be seen from Fig. 6 that the peak value of the original tundish curve is on the left and the peak value is low, and the smoothness degree of other curves is similar. The peak value of curve corresponding to scheme B is right, which indicates that the residence time of molten steel in tundish is increased.

Conclusions

Through the above analysis of the simulation results, compared with the original tundish, the following conclusions can be drawn for other schemes:

- (1) The addition of turbulence inhibitor can make the molten steel fully agitated after entering into the injection zone, make the molten steel well mixed, and increase the probability of inclusion floating.
- (2) The maximum velocity of free surface in scheme a is the smallest, followed by BD, and scheme C is larger, but both are smaller and more uniform than the original tundish.
- (3) The temperature distribution in the injection region has been improved obviously, but the turbulence suppressor has little effect on the temperature difference between the inlet and outlet regions.
- (4) The removal rate of inclusions has been improved obviously, and B and D schemes are the best.

- (5) The RTD curve has obvious changes, which indirectly reflects the residence time of molten steel in tundish. The peak value is generally increased and right, and the peak value of scheme B is the most right.

References

1. Sun H-b, Zhang J-q (2014) Effect of actual cooling rate of ladle stream on persistent metallurgical performance of a given tundish. *J Iron Steel Res (Int)* 21(10):915–922
2. Chen D, Xie X, Long M (2014) Hydraulics and mathematics simulation on the weir and gas curtain in tundish of ultrathick slab continuous casting. *Metall Mater Trans B* 45B(2):392–398
3. Chen C, Cheng G, Zhang J et al (2012) Effects of salt tracer amount, concentration and kind on the fluid flow behavior in a hydrodynamic model of continuous casting tundish. *Steel Res Int* 83(12):1141–1151
4. Ding N, Bao Y-p, Sun Q-s et al (2011) Optimization of flow control devices in a single-strand slab continuous casting tundish. *Int J Miner Metall Mater* 18(3):292–296
5. He F, Zhang L-y, Xu Q-Y (2016) Optimization of flow control devices for a T-type five-strand billet caster tundish: water modeling and numerical simulation. *China Foundry* 03:166–175
6. Yang B, Lei H, Zhao Y et al (2019) Quasi-symmetric transfer behavior in an asymmetric two-strand tundish with different turbulence inhibitor. *Metals* 9(8)
7. Merder T (2013) The influence of the shape of turbulence inhibitors on the hydrodynamic conditions occurring in a tundish. *Arch Metall Mater* 58(4):1111–1117

X-Ray and Neutron Radiographic Experiments on Particle-Laden Molten Metal Flows



Tobias Lappan, Márton Sarma, Sascha Heitkam, David Mannes, Pavel Trtik, Natalia Shevchenko, Kerstin Eckert, and Sven Eckert

Abstract In metallurgical processing, non-metallic inclusions contaminating metallic materials are one highly relevant challenge. Bubble injection into molten metals boosts the inclusion control and removal, thus enhancing metal homogenisation and purification. Although this principle of bubble flotation has been used for a long time, the effects of bubble–inclusion interactions in molten metals are not yet well researched. Imaging measurements of multiphase metal flows are challenging for two main reasons: the metals’ high melting temperatures and their opaqueness for visible light. This work focuses on X-ray and neutron radiographic experiments employing low-melting gallium alloys laden with model particles smaller than 1 mm in diameter. Both, bubbles and particles, are visualised simultaneously with high spatial and temporal resolution in order to analyse their motions by tracking algorithms. We demonstrate the capability of time-resolved X-ray and neutron radiography to image multiphase flows in particle-laden and optically opaque liquid metals, thus contributing to pave the way for systematic investigations on bubble–inclusion interactions in molten metals.

Keywords X-ray radiography · Neutron radiography · Non-metallic inclusions · Liquid metal · Bubble flotation

T. Lappan (✉) · M. Sarma · S. Heitkam · N. Shevchenko · K. Eckert · S. Eckert (✉)
Institute of Fluid Dynamics, Helmholtz-Zentrum Dresden-Rossendorf, Bautzner Landstr. 400,
01328 Dresden, Germany
e-mail: t.lappan@hzdr.de

S. Eckert
e-mail: s.eckert@hzdr.de

S. Heitkam · K. Eckert
Institute of Process Engineering and Environmental Technology, Technische Universität Dresden,
01062 Dresden, Germany

D. Mannes · P. Trtik
Laboratory for Neutron Scattering and Imaging, Paul Scherrer Institut, 5232 Villigen PSI,
Switzerland

Introduction

In aluminium- and steelmaking, the molten metals and alloys get contaminated with inorganic non-metallic inclusions, which typically have inclusion size distributions of the order of 0.01–0.1 mm [1, 2]. Incorporated into the solidified microstructures, such solid inclusions act as three-dimensional defects, affecting the materials' formability and fatigue behaviour.

To control inclusion size distributions and to remove inclusions from molten metals, metallurgical processing employs the principle of bubble flotation [3]. Injecting gas into the molten metal, bubble swarms provide turbulent shear flow, which drives collisions and agglomerations of small inclusions, speeding up the buoyancy-driven removal of larger agglomerates. Additionally, large inclusions are more likely to collide with and attach to bubbles in turbulent flows [4, 5].

For inclusion removal in steel refining, a simple mathematical model predicts an optimum bubble size of 1–5 mm [3]. Flow simulations have quantified collision rates for 0.01 mm aluminium oxide inclusions around a single bubble of 1.4 mm in diameter rising in molten steel [6]. Collision simulations at the inclusion scale show a strong influence of short-distance hydrodynamic effects, particularly when the size ratio of the interacting inclusions is far from unity [7]. Multiscale simulations of an industrial-type gas-stirred steel ladle highlight that steel cleanliness is mainly ruled by agglomeration of the non-metallic inclusions [8], stressing their size ratio as the prevalent parameter [9].

To validate models and simulations, experimental measurement data on bubble–inclusion interactions are lacking. Imaging measurements of multiphase flows in molten metals are challenging for two main reasons: the metals' high melting temperatures and their opaqueness for visible light. Instead, specialised imaging techniques use X-rays or neutrons to gain visual insight into liquid gallium-based alloys at room temperature. In terms of the surface tension and the dynamic viscosity, the eutectic gallium–indium–tin alloy (GaInSn) is comparable to liquid aluminium and liquid iron (Table 1).

Table 1 Material characteristics of water (H₂O) [10] compared to the eutectic gallium–indium–tin alloy (GaInSn) [11], pure gallium (Ga), aluminium (Al), and iron (Fe) [12–14]: melting temperature T_m , mass density ρ_l , surface tension σ_{lg} , and dynamic viscosity η_l

Material	T_m (°C)	ρ_l (g cm ⁻³)	σ_{lg} (mN m ⁻¹)	η_l (mPa s)
H ₂ O	0	1.0	73	1.0
GaInSn	11	6.4	590	2.1
Ga	30	6.2	720	2.0
Al	660	2.4	1050	1.4
Fe	1538	7.0	1880	5.6

The properties of water are given at room temperature ($T = 20$ °C), those of the liquid metals at their respective T_m

X-ray radiography (XR) has been validated for the characterisation of argon bubbles rising in liquid GaInSn alloy [15]. The effects of bubble coalescence [16] and bubble breakup [17] as well as the influence of a horizontal magnetic field [18] have been investigated in bubble chain experiments. Bubble flows injected through a top submerged lance into liquid GaInSn alloy have been visualised in a recent experimental study [19].

Neutron radiography (NR) has provided insight into single-phase [20, 21] and two-phase flows in the liquid eutectic lead–bismuth alloy [22]. In liquid gallium experiments, NR has imaged rising bubbles under the influence of an electromagnetically driven flow [23] and bubble shape dynamics in samples of representative thickness with and without the application of an external horizontal magnetic field [24, 25]. Further, NR has been employed to study particle motions in an intense liquid gallium flow [26–28] and to observe particle trapping during directional solidification of liquid tin [29].

In addition to radiographic measurements in liquid metals, both XR and NR have proven useful for flow visualisation in optically opaque liquid foam and froth [30, 31], especially in combination with custom-tailored tracer particles [32].

This work employs X-ray radiography as well as neutron radiography to visualise and measure multiphase flows of both gas bubbles and solid particles in low-melting gallium-based alloys at room temperature. Two different types of flow experiments are investigated: first, bubbles rising in particle-laden liquid metal, and second, particle-laden liquid metal flow around a fixed cylindrical obstacle, which is motivated by a single rising bubble. In particular, the radiographic measurements focus on suitable particles of smallest possible diameter that can be imaged in liquid metals using either X-ray or neutron radiation. Such model particles of less than 1.0 mm in diameter – preferably even smaller than 0.1 mm – are the basis to further investigate effects on bubble–inclusion interactions in molten metals by means of radiographic model experiments.

Experimental Setup

Bubble Column

The experiments on rising bubbles are performed in a flat cuvette-like container (Fig. 1) filled with the liquid metal and the respective model particles for either X-ray radiography or neutron radiography. Made from acrylic glass, the container is resistant to gallium-based alloys as well as to X-ray and neutron radiation. Because acrylic glass is opaque to neutrons, the front and back window can be replaced by soda lime glass plates. The container's inner cross-section measures 70 mm in width, but only 3 mm in depth, along the X-ray or neutron beam direction. This limited thickness results from the attenuation characteristics of the multiphase system. To generate a reproducible bubble chain, argon gas is injected continuously through a

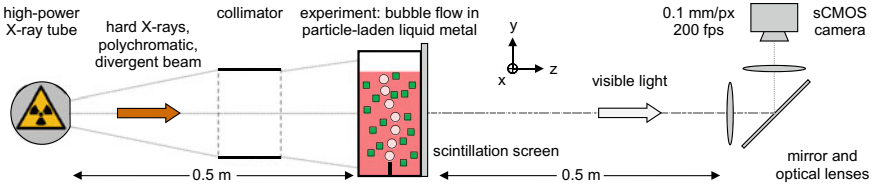


Fig. 1 Experimental arrangement for X-ray radiography of bubble flows in particle-laden liquid metals: the divergent X-ray beam penetrates the liquid metal experiment placed between the high-power X-ray tube and the X-ray image detection system. (Color figure online)

stainless steel hollow needle with 0.4 mm outer diameter, controlled by a digital mass flow controller (type 1179B, MKS Instruments). After detachment from the faceted needle tip, which is centred 10 mm above the container bottom and 105 mm below the filling level, the bubbles ascend to the free surface of the particle-laden liquid metal. In order to concentrate the particles near the needle tip and, hence, to increase the probability of particle interactions with the detaching bubbles, the width of rectangular cross-section tapers in the lower part of the bubble column. Both the bubbles' and particles' trajectories are visualised and measured within the liquid metal volume above the nozzle tip.

For X-ray radiography, the ternary eutectic gallium–indium–tin alloy (GaInSn, mass fractions: $w_{\text{Ga}} = 0.670$, $w_{\text{In}} = 0.205$, $w_{\text{Sn}} = 0.125$) [11] serves as the model liquid metal. For neutron radiography, this work employs liquid gallium alloyed with tin (GaSn: $w_{\text{Ga}} = 0.93$, $w_{\text{Sn}} = 0.07$). The chemical composition is close to the system's eutectic point ($w_{\text{Sn}} = 0.12$) at $T_{\text{m,GaSn}} = 21$ °C [33]. Because the tin content is low, the binary GaSn alloy is assumed to resemble pure gallium rather than the ternary GaInSn alloy in terms of surface tension and dynamic viscosity (cf. Table 1).

Setting the argon gas flow rate to 10 sccm, the bubble chain detaches from the needle with a frequency of approximately 20 bubbles per second, yielding the bubbles' Sauter mean diameter $d_b = 2.5$ mm. For the given bubble diameter and material parameters, Grace's bubble shape diagram [34] predicts the transition between spherical and wobbling shapes in unhindered gravitational motion. However, the 3-mm-thin container confines the comparatively large bubbles: X-ray radiographic experiments reveal effects of flow confinement on bubble shape dynamics [35].

Liquid Metal Loop

The experiments on the particle-laden liquid metal flow around a fixed cylindrical obstacle are performed in a flat channel constructed as a closed circuit. The channel's rectangular cross-section measures 30 mm in width and, in agreement with the bubble column, 3 mm in depth. Motivated by a single rising bubble, a rigid cylinder of 5 mm in diameter is fixed in the centre of the straight channel section. The liquid metal loop is equipped with a disc-type electromagnetic induction pump to drive the flow. Contrary to the bubble column, the liquid metal loop is exclusively used for

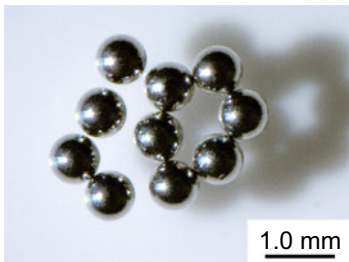
neutron radiographic experiments, employing the liquid GaSn alloy with gadolinium oxide particles. Further details on the experimental setup with the electromagnetic induction pump as well as on the particle dispersion procedure are described in [36].

Model Particles

For X-ray radiography in the liquid GaInSn alloy, model particles based on lead (Pb) or tungsten (W) are employed, because these heavy metals have high X-ray attenuation coefficients. The contrast-to-noise ratio CNR_X is measured for static lead–tin spheres (Pb90Sn10) of 0.1–0.9 mm in diameter and tungsten carbide – cobalt spheres (WC–Co) of 0.6–0.8 mm in diameter. The bubble flow experiments are performed with either Pb90Sn10 spheres of 0.76 mm in diameter (Fig. 2a) or WC–Co granules larger than 0.71 mm (Fig. 2b).

For neutron radiography in the liquid GaSn alloy, model particles based on gadolinium (Gd) are employed, because this rare-earth metal has an outstandingly high neutron attenuation coefficient $\mu_{n,Gd} = 1.5 \times 10^3 \text{ cm}^{-1}$, compared to the liquid metal $\mu_{n,GaSn} = 0.5 \text{ cm}^{-1}$ [36]. The particles made from either gadolinium or gadolinium oxide (Gd_2O_3) have an irregular shape with a minimum Feret diameter between 0.3 and 0.5 mm. Both particle materials are tested in bubble flow experiments, but only Gd_2O_3 particles are used in the liquid metal loop with the electromagnetic induction pump.

The terminal velocity v_t and the Stokes number St_p [37] of different model particles of 0.5 and 0.1 mm in diameter are estimated and listed in Table 2. The terminal velocity characterises the particles' buoyancy-driven motion. The Stokes number expresses how quickly the particles adapt to an accelerated flow field, here induced by a rising argon bubble of 2.5 mm in diameter at 0.28 m s^{-1} terminal rising velocity and bubble Reynolds number $Re_b \approx 2100$. Particles with Stokes numbers $St_p < 1$ have good capabilities to follow the acceleration.



(a) $d_{Pb90Sn10} = 0.76 \text{ mm}$, spherical shape



(b) $d_{WC-Co} > 0.71 \text{ mm}$, irregular shape

Fig. 2 Model particles for X-ray radiographic experiments on particle-laden liquid metal flows: **a** the lead–tin spheres (Pb90Sn10) and **b** the tungsten carbide – cobalt granules (WC–Co) are of a different size and shape; stereo-microscopic images

Table 2 Model particles in buoyancy-driven motion and their following behaviour in bubbly liquid metal flows: mass density ρ_p of various particles, namely lead–tin (Pb90Sn10), tungsten carbide – cobalt (WC–Co), aluminium oxide (Al_2O_3), silicon dioxide (SiO_2), gadolinium (Gd) as well as gadolinium oxide (Gd_2O_3), mass density difference $\Delta\rho = \rho_p - \rho_l$ between those particles and the liquid, terminal velocity v_t of the particles rising ($v_t = v_r > 0$) or settling ($v_t = v_s < 0$) in the gallium-based alloys, and the Stokes number St_p of the respective particles depending on their size d_p

Particle	ρ_p (g cm ⁻³)	$\Delta\rho/\rho_l$	v_t for $d_p = 0.5$ mm (cm s ⁻¹)	St_p for $d_p = 0.5$ mm	St_p for $d_p = 0.1$ mm
<i>X-ray radiography in the liquid gallium–indium–tin alloy ($\rho_{\text{GaInSn}} = 6.4$ g cm⁻³)</i>					
Pb90Sn10	10.9	-0.70	-6.5	16.1	0.6
WC–Co	14.7	-1.29	-9.6	21.7	0.9
Al_2O_3	3.9	0.39	4.3	5.8	0.2
SiO_2	2.7	0.58	5.8	3.9	0.2
<i>Neutron radiography in the liquid gallium–tin alloy ($\rho_{\text{GaSn}} = 6.2$ g cm⁻³)</i>					
Gd	7.7	-0.20	-3.2	11.4	0.5
Gd_2O_3	5.6	0.13	1.5	8.3	0.3

X-Ray and Neutron Radiography

Attenuation Characteristics

The universal Beer–Lambert law describes the attenuation of X-ray or neutron radiation passing through matter (Fig. 3). In a first approximation, the transmittance through a sequence of $i = 1 \dots n$ material layers calculates as

$$I/I_0 = \exp\left[-\sum_i \mu_i d_{z,i}\right] \quad (1)$$

with the intensity I_0 of the incident beam, the intensity I of the transmitted beam, the linear attenuation coefficient μ_i of the irradiated material layer, and its thickness $d_{z,i}$ along the X-ray or neutron beam direction. As Fig. 3 shows schematically, particles with an attenuation coefficient μ_p higher than μ_l of the surrounding liquid appear as dark grey spots in the transmission image. In contrast, bubbles with a low attenuation coefficient $\mu_b < \mu_l$ are imaged as bright grey projections.

Figure 4 compares the X-ray attenuation coefficients μ_X of different model particles, argon bubbles, and the liquid GaInSn alloy, which also depend on the X-ray photon energy E_X . Estimated by Beer–Lambert’s law, Fig. 5 illustrates the X-ray and neutron beam transmittance of those model particles and the gallium-based alloys that are employed in this work. For X-ray radiography at $E_X = 100 \dots 150$ keV, Pb90Sn10 spheres have to be larger than 0.5 mm in diameter to achieve sufficient contrast. The liquid metal container of 3-mm thickness attenuates more than 50% of the incident X-rays. On the one hand, this yields acceptable X-ray transmittance to image the

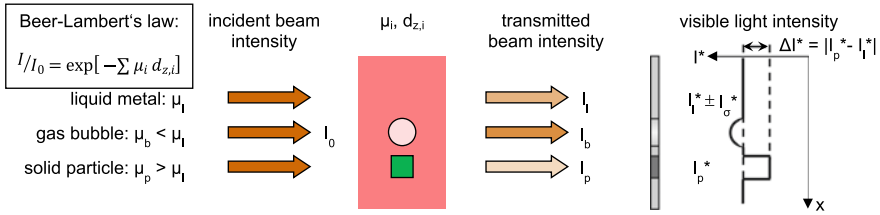


Fig. 3 Measurement principle of transmission imaging: the attenuation of radiation that passes through matter is described by Beer–Lambert’s law. Compared to the intensity I_0 of the incident beam, the intensity I of the transmitted beam is reduced by material-specific absorption interactions, yielding the signal intensity I^* in the projected X-ray or neutron transmission images. (Color figure online)

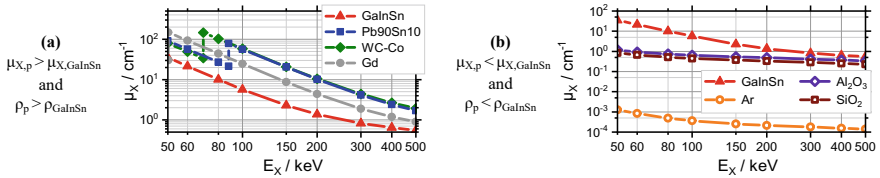


Fig. 4 X-ray attenuation coefficient μ_X of the liquid gallium–indium–tin alloy (GaInSn) compared to different particle materials, namely lead–tin (Pb90Sn10), tungsten carbide – cobalt (WC–Co), gadolinium (Gd), aluminium oxide (Al_2O_3), and silicon dioxide (SiO_2), as well as argon bubbles (Ar), depending on the X-ray photon energy E_X . Both the X-ray attenuation coefficient and the mass density ρ of the respective particle material are either (a) higher or (b) lower than these of the liquid metal. Decreasing E_X from 500 to 50 keV, μ_X increases exponentially. Below $E_X = 100$ keV, the exponential trend is step-like interrupted by the element-specific absorption edges. (Color figure online)

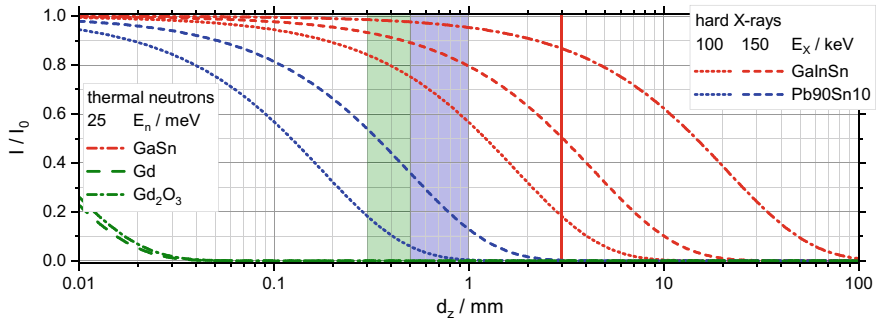


Fig. 5 Beam attenuation characteristics for hard X-rays and thermal neutrons, calculated by means of Beer–Lambert’s law: beam transmittance I/I_0 , depending on the irradiated material and its thickness d_z along the beam direction. In addition, the X-ray beam transmittance depends significantly on the X-ray photon energy E_X . (Color figure online)

Pb90Sn10 spheres. On the other hand, the gradient $\Delta l/\Delta d_z$ is sufficiently large to image bubbles by the corresponding deficit in liquid metal thickness (cf. Fig. 3). For neutron radiography, the liquid metal thickness $d_{\text{GaSn}} = 3$ mm again yields enough neutron transmittance to image Gd or Gd₂O₃ particles down to 0.05 mm in diameter with high contrast.

Radiographic Setup

X-ray radiography on multiphase flows in this work employs the same X-ray radiographic setup (Fig. 1) as previous experiments on bubbles in the liquid GaInSn alloy [15–19]. Polychromatic hard X-rays are generated by a high-power X-ray tube (ISOVOLT 450M1/25-55, GE Sensing & Inspection Technologies), operated between 130 and 200 kV tube voltage in order to optimise the image contrast during the measurements. The divergent X-ray beam is narrowed by means of a collimator and then penetrates the multiphase flow experiment in the flat container. The multiphase system with bubbles and particles in the liquid metal attenuates the incident X-rays. The transmitted X-rays impinge on a scintillation screen (SecureX HB, Applied Scintillation Technologies), which is directly mounted to the container's back window and emits visible light. Using a mirror and optical lenses (custom-made design, TSO Thalheim Spezialoptik), the light pattern from the scintillator is recorded by means of a scientific CMOS camera (pco.edge 5.5, PCO).

Neutron radiography has been performed at the beamlines NEUTRA [38] and ICON [39] of the Swiss Spallation Neutron Source SINQ [40] at the Paul Scherrer Institut. The experimental arrangement and important parameters used for the flow visualisation in particle-laden liquid metal are reported in [36], which highlights the neutron flux φ_n as the crucial parameter. In contrast to the thermal neutron beam ($\varphi_n = 1.3 \times 10^7$ n cm⁻² s⁻¹) at NEUTRA, the ICON beamline has been operated with a maximum cold neutron flux of approximately 2×10^8 n cm⁻² s⁻¹ at the experiment position. Neutron radiographs from ICON provide a sufficient image contrast between the gadolinium-based model particles and the liquid GaSn alloy, although the image noise is rather intense in image sequences captured with short image exposure time.

Both X-ray and neutron radiographs have been acquired with similar spatial and temporal resolution. To visualise individual model particles of the order of 0.5 mm in diameter, the image pixel size equals approximately 0.1 mm in the X-ray and neutron radiographs. To visualise the bubbles' and particles' motions with negligible motion blur, X-ray radiography of bubble flows in the particle-laden liquid metals is conducted with 5 ms image exposure time, which corresponds to a maximum imaging frame rate of 200 fps. The neutron image sequences are captured with a lower imaging frame rate of 100 fps frame, because doubling the image exposure time to 10 ms lowers the image noise level to a certain extent.

Results

Contrast-to-Noise Ratio

High contrast-to-noise ratio (CNR) is required to identify and track bubbles as well as particles in X-ray or neutron radiographs. Neglecting motion blur, the CNR is measured with non-moving particles, depending on their particle diameter d_p and the image exposure time T_e . X-ray radiographs of spherical WC–Co and Pb10Sn90 model particles are exemplarily shown in Fig. 6, and the corresponding CNR_X values are plotted in Fig. 7a. Recently, we have reported the contrast-to-noise ratio CNR_n that was measured and analysed from neutron radiographs of irregular-shaped gadolinium particles, whose minimum Feret diameter ranges between 0.10 and 0.45 mm (Fig. 7b,c [36]).

$$CNR = \frac{\Delta I^*}{I_\sigma^*} = \frac{|I_p^* - I_l^*|}{I_\sigma^*} \tag{2}$$

According to Fig. 3 and Eq. (2), the minimum signal intensity I_p^* in the greyscale transmission images typically corresponds to the spheres’ centre positions. The mean

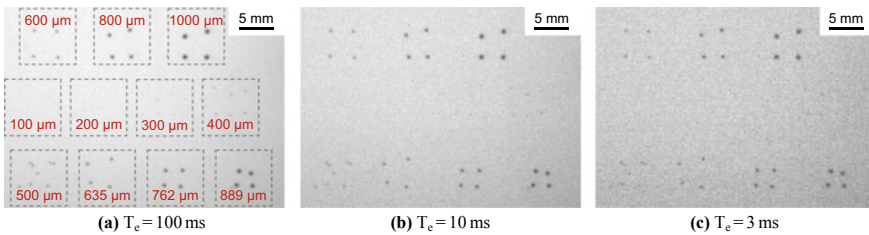


Fig. 6 Preliminary X-ray radiographic measurements to evaluate the contrast-to-noise ratio CNR_X of tungsten carbide – cobalt spheres (top row) and lead–tin spheres (middle and bottom row), depending on their diameter d_p and on the X-ray image exposure time T_e . (Color figure online)

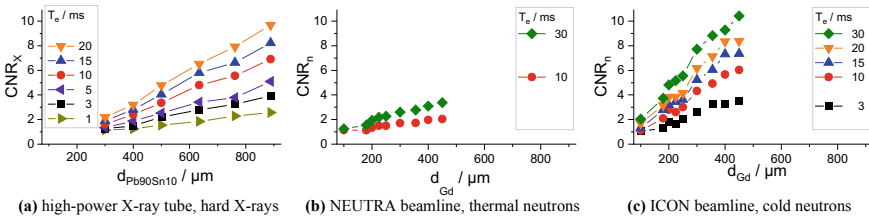


Fig. 7 Contrast-to-noise ratio **a** CNR_X in X-ray radiography of lead–tin spheres (Pb90Sn10) and **b, c** CNR_n in neutron radiography of irregular-shaped gadolinium granules (Gd) [36], depending on their particle diameter d_p and on the image exposure time T_e . (Color figure online)

background signal intensity I_1^* and its standard deviation I_σ^* are measured in the absence of particles.

In both X-ray and neutron radiographs, the particles' CNR declines with decreasing particle diameter, because the thickness of the particle in beam direction decreases and also the geometric unsharpness of the imaging system has an increasing effect. Furthermore, the CNR declines with decreasing image exposure time, because images captured at short exposure time are subjected to high noise. However, a short image exposure time reduces effects of motion blur.

The CNR depends on the transmission image contrast as well as on the image noise level, which differ significantly between both radiographic techniques. Given the same particle diameter and image exposure time, e.g. $d_p = 0.5$ mm and $T_e = 10$ ms, the CNR_n of Gd granules is approximately twice as high as the CNR_x of Pb90Sn10 spheres. In the case of X-ray radiography, the CNR_x is mainly affected by the attenuation characteristics of the irradiated materials and, thus, by the image contrast achievable. Although the X-ray radiographs have a comparatively low image noise, model particles smaller than 0.5 mm in diameter are hardly visible, even in long exposure time images (Fig. 6a). In the case of neutron radiography, the CNR_n is primarily limited by the high image noise level in neutron radiographs captured with low neutron flux at short image exposure times [36]. Additionally, the neutron image noise is not purely stochastic, but shows coherent structures in the size of the three image pixels [31], which is close to the diameter of the Gd_2O_3 particles used in this work.

Bubble Flow in Particle-Laden Liquid Metals

In the X-ray and neutron radiographic experiments, the respective model particles have been imaged together with bubbles. Chain-like rising bubbles drive the liquid metal flow in the thin container. Similar to particle tracking velocimetry (PTV) in an optically transparent multiphase flow [4], both, particles and bubbles, can be tracked simultaneously as individual objects. Generally, particles move towards bubble trajectories and are entrained in each bubble's wake.

For three different model particle materials, Fig. 8 shows X-ray and neutron radiographs captured with short image exposure time in order to visualise the bubbles with negligible motion blur and high image contrast. Compared to X-rays (Fig. 8a,b), neutrons visualise bubbles with lower contrast and higher image noise (Fig. 8c). This experimental observation in the 10-mm-thick container is in line with the theoretical estimation by Beer–Lambert's law illustrated in Fig. 5b: in terms of the neutron intensity, the graph predicts a small intensity gradient $\Delta I/\Delta d_z = 10 \dots 20\%$ between a single bubble and the surrounding liquid metal. Despite the bubbles' low CNR_n , Birjukovs et al. [24, 25] have captured bubble flows in liquid gallium within a 30-mm-thick container and developed a customised image processing pipeline in order to investigate bubble shape dynamics.

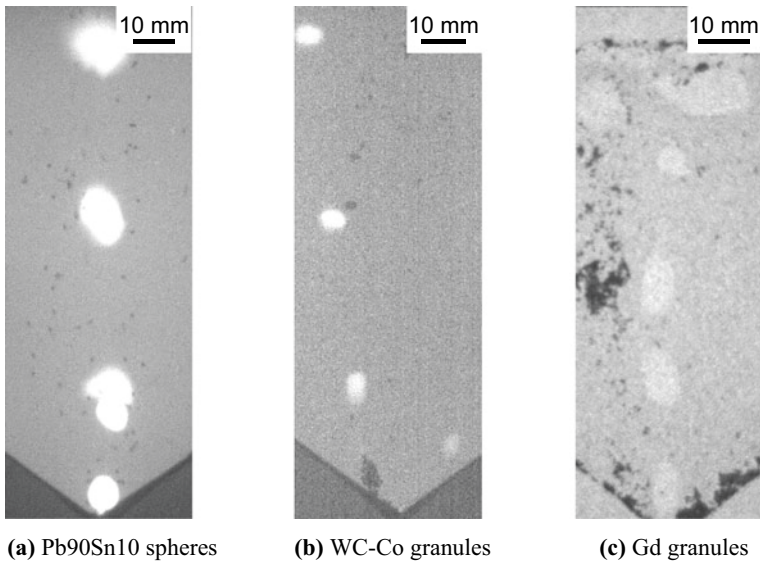


Fig. 8 Bubble flows in particle-laden liquid metals are imaged with **a, b** hard X-rays and **c** cold neutrons. The wetting properties of the respective model particles are the crucial factor for the particle dispersion into the liquid metal in flat containers as well as for bubble–particle attachments. To create an intense flow and disperse the particles, the argon gas flow rate is increased from 10 to 100 sccm in the experiments with **a** the well-wetted Pb90Sn10 spheres and **c** the partly wetted gadolinium granules. **b** The WC–Co granules are hardly wetted by the liquid gallium alloy, mainly stick to the container wall and, hence, are barely affected by the bubble-driven flow

The model particles for X-ray radiography, Pb90Sn10 spheres and WC–Co granules, have to be comparatively large ($d_{\text{Pb90Sn10}} = 0.76 \text{ mm}$, $d_{\text{WC-Co}} > 0.71 \text{ mm}$, cf. Fig. 2) and have to have a high mass density to provide sufficient CNR_X . Thus, they settle at high terminal velocity in the liquid GaInSn alloy (cf. Table 2). Also, these particles are characterised by the highest Stokes number of all model particles considered in this work and are not expected to follow the flow very well, but rather collide with rising bubbles. In consequence, X-ray radiography is suitable to visualise the counterflow of ascending bubbles and descending particles as well as bubble–particle collisions.

The WC–Co granules (Fig. 8b) and the Gd granules used in neutron radiographic experiments (Fig. 8c) are wetted worse than the Pb90Sn10 spheres (Fig. 8a) and, hence, are more likely to stick either to the free surface of the liquid metal or to the wall of the flat container. However, the well-wetted Pb90Sn10 spheres hardly attach to bubble surfaces after bubble–particle collisions, and they dissolve slowly – within a few hours – in the liquid GaInSn alloy.

The X-ray or neutron attenuation characteristics as well as the behaviour in the liquid metal flow depend on the particles' bulk volume, especially the particle material and diameter, but the wetting behaviour depends primarily on the particle surface. Therefore, wetting properties can be modified by an additional surface coating. In this

work, coating with tin in a controlled milling process [41, 42] has been tested. After tin coating, the WC–Co granules show a slightly improved wetting and admixing into the liquid GaInSn alloy. The coating protocol is not applicable to the Gd_2O_3 particles, because the milling process simply grinds the sintered microporous material to its primary particle size of below $0.01\ \mu\text{m}$.

Particle-Laden Liquid Metal Flow around a Cylindrical Obstacle

In the neutron radiographic experiments, Gd_2O_3 model particles have been imaged in the liquid GaSn flow driven by an electromagnetic induction pump. The particle-laden flow around the fixed cylindrical obstacle in the flat channel is motivated by a single bubble rising in the liquid metal. Particle image velocimetry (PIV) algorithms are utilised to analyse the particle motion within the liquid metal flow. If the particles would follow the flow perfectly, the particle motion would represent the velocity field up- and downstream the cylinder. In the cylinder's wake, under turbulent shear flow, the particles collide and presumably agglomerate with each other. However, tracking of individual particles and particle agglomerates in the wake region is challenging, because the particles hardly distinguish from the neutron image noise and the direction of particle motion is changing rapidly.

Operating the disc-type electromagnetic induction pump at constant rotation rate $\omega = 0.57\ \text{s}^{-1}$, the vertical velocity component of the liquid metal flow, averaged within the range $-25\ \text{mm} < y < -15\ \text{mm}$ upstream the cylindrical obstacle, measures $\bar{u}_y = 0.11\ \text{m}\ \text{s}^{-1}$ (Fig. 9c). According to this fluid velocity, the Reynolds number of the cylinder with 5 mm in diameter equals $\text{Re}_{\text{cyl}} \approx 1600$, which is close to the Reynolds number $\text{Re}_b \approx 2100$ of a 2.5 mm rising bubble at $0.28\ \text{m}\ \text{s}^{-1}$ terminal velocity. The bubble diameter and velocity also predefine the image exposure time to

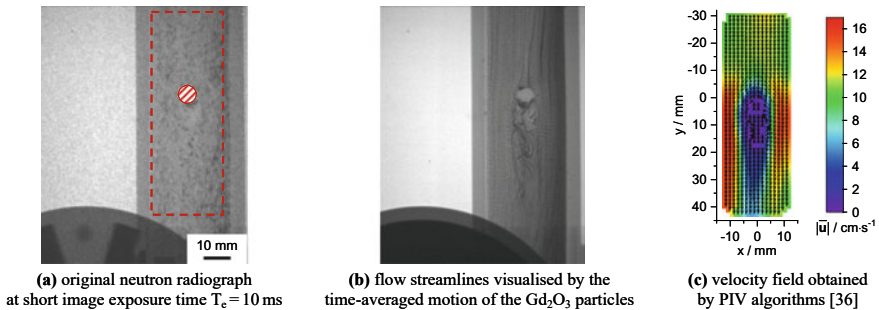


Fig. 9 The particle-laden liquid metal flow around the fixed cylindrical obstacle in the flat channel, equipped with the disc-type electromagnetic induction pump, is imaged with cold neutrons at the ICON beamline. (Color figure online)

capture bubble shape dynamics and particle motions around the bubble with negligible motion blur. As in X-ray radiographic experiments, this would require a short image exposure time of up to 5 ms, diminishing the particles' contrast-to-noise ratio significantly (cf. Fig. 7b). In the case of particle-laden liquid metal flow around the cylindrical obstacle, the flow velocity can be adjusted independently of the cylinder diameter. Reducing the flow velocity by approximately 50%, the image exposure time can be doubled to 10 ms, so that the neutron image sequences provide a sufficient CNR_n . Consequently, on condition of similar Reynolds numbers Re_{cyl} and Re_b , the model particles in the cylinder flow experiment (Fig. 9a) are imaged with a higher CNR_n than in the bubble experiment (Fig. 8c). For upcoming neutron radiographic experiments, the fixed obstacle will be replaced by a single bubble pinned to an orifice, inspired by the experimental flow setup described in [5].

In comparison with the other model particles employed for X-ray or neutron radiographic experiments, Gd_2O_3 particles are most suitable as tracers, whose motion can be analysed by means of PIV algorithms. Two relevant particle characteristics, the terminal velocity and the Stokes number, both depend on the mass density as well as on the diameter of the model particles, and are estimated in Table 2.

The employed Gd_2O_3 particles have a small diameter (0.3–0.5 mm), and their bulk density (5.6 g cm^{-3}) is closest to the mass density of the liquid GaSn alloy (6.2 g cm^{-3}). This yields the slowest terminal velocity (1.5 cm s^{-1}) of all model particles. Although the true density of gadolinium oxide, measured by gas pycnometry, is 8.2 g cm^{-3} , the sintered particle material includes micropores, which reduce the particles' bulk density. To further slow down buoyancy-driven particle motion, customised sintered Gd_2O_3 particles with approximately 30% microporosity would match with the liquid GaSn alloy in terms of the density.

The particle diameter is the free parameter that determines the Stokes number. Among all employed model particles, the Gd_2O_3 particles have also the lowest Stokes number, which equals 8.3 in the vicinity of a bubble with 2.5-mm diameter. Compared to PIV tracer particles in optical measurements with $St \ll 1$ [5], this Stokes number is rather large. Thus, the employed Gd_2O_3 particles are not able to fully follow the liquid metal flow around rising bubbles. They will detach from the flow in case of strong accelerations, which, in turn, enhances the probability of bubble–particle collisions. Particles of 0.1 mm in diameter would be less inertial ($St = 0.4$), thus accumulating at the rim of the bubbles' wakes [43]. To almost completely follow the bubble-driven liquid metal flow, the Gd_2O_3 particles would have to be one order of magnitude smaller ($d_p = 0.05 \text{ mm}$, $St = 0.1$) than in these neutron radiographic experiments.

Discussion and Conclusion

This work compares and highlights the capabilities of X-rays and neutrons for imaging flow measurements in optically opaque liquid metals laden with small solid particles. In model experiments with low-melting gallium-based alloys at room

temperature, both X-ray and neutron radiography have proven appropriate to provide direct visual insights into multiphase flows. Currently, only X-rays can image the motions of bubbles and particles simultaneously with sufficient image contrast and low image noise. In comparison, neutrons offer the prominent advantage to visualise smallest particles in liquid metal flows. The radiographic techniques have been employed for flow visualisation with two different, but comparable experimental setups: bubble-driven flow in particle-laden liquid metal, and externally driven flow around a cylindrical obstacle motivated by a single rising bubble. Such radiographic model experiments are crucial to gain a deeper understanding of bubble–inclusion interactions in molten aluminium alloys and steels during metallurgical processing.

The radiographic model experiments have revealed the importance of the particles' wetting properties. On the one hand, well-wetted particles can be easily dispersed into liquid metals, simplifying the particle handling. On the other hand, non-wetted particles are more likely to form agglomerates and to attach to bubbles. These are two fundamental interaction mechanisms of utmost interest in the radiographic experiments. Wetting relates to the particle surface, which can be functionalised separately from the particles' bulk volume. The material and diameter of the particle bulk volume have the strongest impact on its visualisation by X-rays or neutrons and on the particle behaviour in liquid metal flows. Additional metallic surface coatings such as tin, iron or nickel may enhance the particle wetting by liquid gallium-based alloys.

Radiographic flow measurements in particle-laden liquid metal pose an optimisation problem with several interdependent parameters. These include, among others, the thickness of the liquid gallium alloy that can be penetrated by the X-ray or neutron beam, the particle material with its characteristic X-ray or neutron attenuation coefficient and mass density, the size and velocity of both the model particles and bubbles in the liquid metal flows, and the image exposure time, especially in combination with the beamline-specific neutron flux. The contrast-to-noise (CNR) as a quantitative measure proves useful to evaluate radiographic images of different model particles, depending on their material and size as well as on the image exposure time. In X-ray radiographs, the CNR_X is mainly determined by the achievable contrast between the model particles and the surrounding liquid metal. On the contrary, the CNR_n in neutron radiographs captured with short image exposure time at limited neutron flux is significantly affected by non-stochastic image noise. In terms of the particle material and particle size range, the X-ray and neutron radiographic experiments supplement each other.

Lead-based and tungsten-based model particles have been employed for X-ray radiography because of their high X-ray attenuation coefficients. However, these particles have to be large (0.5–1.0 mm in diameter) compared to the flat liquid metal container of only a few millimetre thickness along the X-ray beam direction. The particle contrast in the liquid gallium–indium–tin alloy increases exponentially with decreasing X-ray photon energy, which, in turn, restricts the container thickness. In further consequence, the thin container confines rising bubbles, thus affecting the bubble shape dynamics. Moreover, the particles that contain heavy lead or tungsten settle in the liquid metal at comparatively high terminal velocity and show a low

ability to follow the bubble-driven flow. Hence, visualising the counterflow of rising bubbles and settling particles under confinement, X-ray radiography enables to track both, bubbles and particles, simultaneously during bubble–particle collisions and attachments in liquid metals.

Neutron radiography has been performed with model particles from gadolinium and gadolinium oxide in the liquid gallium–tin alloy. Although the element gadolinium has a superior neutron attenuation coefficient, the particle size of approximately 0.5 mm in diameter is on average one order of magnitude larger than the typical size of non-metallic inclusions in molten metals. Any further reduction of the particle size to 0.1 mm or even 0.05 mm strongly depends on the experimental arrangement. Particularly, the neutron flux provided by the neutron source at the sample position is of central importance in order to distinguish smaller model particles from the image noise in neutron radiographs. The particles' CNR_n quantifies the pronounced dependency on the neutron flux φ_n : an increase by approximately one order of magnitude, from $1.3 \times 10^7 \text{ n cm}^{-2} \text{ s}^{-1}$ at the NEUTRA beamline to $2 \times 10^8 \text{ n cm}^{-2} \text{ s}^{-1}$ at ICON under otherwise similar imaging conditions, significantly improves the visibility of Gd particles smaller than 0.5 mm in diameter. This promising trend is expected to continue with further increasing neutron flux at future neutron imaging instruments: the ODIN beamline at the European Spallation Source (ESS) will provide $1.2 \times 10^9 \text{ n cm}^{-2} \text{ s}^{-1}$ [44]. However, in addition to the neutron flux, the visualisation of smallest particles and their motion also requires a small image pixel size ($<0.1 \text{ mm}$) and a short image exposure time ($<10 \text{ ms}$), respectively. This higher spatial and temporal resolution has to be achieved by the neutron image acquisition system, including the scintillation screen and the camera. Under upgraded imaging conditions, gadolinium-based model particles will be most suitable as neutron-opaque tracers in liquid metal flows.

In conclusion from the theoretical estimations and experimental findings in this work, neutrons are more promising than X-rays for imaging and investigating bubble–particle interactions in liquid metals. Contrary to the comparatively large and heavy lead- or tungsten-based particles for X-ray radiography, model particles containing gadolinium with a superior neutron attenuation coefficient offer a broader variety to customise the desired profile of properties. These include the particle diameter, the particles' bulk density as well as the metallic or non-metallic character of the particle bulk material, possibly used as substrate for an additional metallic surface coating. To that end, we intend to prepare small and neutrally buoyant tracer particles from sintered gadolinium oxide ($d_p < 0.1 \text{ mm}$, $\text{St}_p < 1$), coating their surface with tin, and employing them for neutron radiography in the liquid gallium–tin alloy. Using such tracer particles for neutron radiographic flow measurements, we aim to reveal the flow field around a pinned single bubble instead of a cylindrical obstacle by means of PIV algorithms, which are well established for optical flow measurements.

Acknowledgements We gratefully acknowledge the financial support provided by the Agence Nationale de la Recherche (ANR) and the Deutsche Forschungsgemeinschaft (DFG) within the collaborative French-German research project FLOTINC under grant number ANR-15-CE08-0040 and EC 217/3-1. The experiments on neutron radiography were performed at the Swiss Spallation

Neutron Source SINQ, Paul Scherrer Institut, Villigen, Switzerland. We thank Sylvain Martin (École des Mines de Saint-Étienne, France) for his valuable support with particle coating tests. Special thanks are due to Michaela Roßner, Peggy Jähnigen, and Michael Knobel for their excellent technical assistance with particle characterisations.

References

1. Simensen CJ, Berg G (1980) A survey of inclusions in aluminum. *Aluminium* 56:335–340
2. Zhang L, Thomas BG (2003) State of the art in evaluation and control of steel cleanliness. *ISIJ Int* 43:271–291
3. Zhang L, Taniguchi S (2000) Fundamentals of inclusion removal from liquid steel by bubble flotation. *Int Mater Rev* 45:59–82
4. Sommer A-E et al (2018) A novel method for measuring flotation recovery by means of 4D particle tracking velocimetry. *Miner Eng* 124:116–122
5. Sommer A-E et al (2020) Application of Positron Emission Particle Tracking (PEPT) to measure the bubble-particle interaction in a turbulent and dense flow. *Miner Eng* 156:106410
6. May R et al (2018) Impact of particle boundary conditions on the collision rates of inclusions around a single bubble rising in liquid metal. *PAMM* 18:1–2
7. Gisselbrecht M et al (2019) Aggregation kernel of globular inclusions in local shear flow: application to aggregation in a gas-stirred ladle. *Metall Res Technol* 116:512
8. Bellot J-P et al (2018) Toward better control of inclusion cleanliness in a gas stirred ladle using multiscale numerical modeling. *Materials* 11:1179
9. Kroll-Rabotin J-S et al (2020) Multiscale simulation of non-metallic inclusion aggregation in a fully resolved bubble swarm in liquid steel. *Metals* 10:517
10. Lide DR, Bruno TJ (2019) *CRC handbook of chemistry and physics*. CRC Press, Boca Raton
11. Plevachuk Y et al (2014) Thermophysical properties of the liquid GaInSn eutectic alloy. *J Chem Eng Data* 59:757–763
12. Brandes EA, Brook GB (1999) *Smithells metals reference book*. Butterworth-Heinemann, Oxford
13. Iida T, Guthrie RIL (2015) *The thermophysical properties of metallic liquids*. Oxford University Press
14. Warlimont H, Martienssen W (eds) (2018) *Springer handbook of materials data*. Springer International Publishing, Cham
15. Keplinger O et al (2017) Validation of X-ray radiography for characterization of gas bubbles in liquid metals. *IOP Conf Ser Mater Sci Eng* 228:012009
16. Keplinger O et al (2018) Visualization of bubble coalescence in bubble chains rising in a liquid metal. *Int J Multiph Flow* 105:159–169
17. Keplinger O et al (2019a) Experimental investigation of bubble breakup in bubble chains rising in a liquid metal. *Int J Multiph Flow* 116:39–50
18. Keplinger O et al (2019b) Experimental investigations of bubble chains in a liquid metal under the influence of a horizontal magnetic field. *Int J Multiph Flow* 121:103111
19. Akashi M et al (2020) X-ray radioscopic visualization of bubbly flows injected through a top submerged lance into a liquid metal. *Metall Mater Trans B* 51:124–139
20. Takenaka N et al (1994) Visualization of streak lines in liquid metal by neutron radiography. *Nondestruct Test Eval* 11:107–113
21. Takenaka N et al (1996) Liquid metal flow measurement by neutron radiography. *Nucl Instrum Methods Phys Res Sect Accel Spectrometers Detect Assoc Equip* 377:156–160
22. Saito Y et al (2004) Velocity field measurement in gas-liquid metal two-phase flow with use of PIV and neutron radiography techniques. *Appl Radiat Isot* 61:683–691

23. Baake E et al (2017) Neutron radiography for visualization of liquid metal processes: bubbly flow for CO₂ free production of hydrogen and solidification processes in EM field. *IOP Conf Ser Mater Sci Eng* 228:012026
24. Birjukovs M et al (2020) Argon bubble flow in liquid gallium in external magnetic field. *Int J Appl Electromagn Mech* 1–7
25. Birjukovs M et al (2020) Phase boundary dynamics of bubble flow in a thick liquid metal layer under an applied magnetic field. *Phys Rev Fluids* 5:061601
26. Scepankis M et al (2015) A report on the first neutron radiography experiment for dynamic visualization of solid particles in an intense liquid metal flow. *Magnetohydrodynamics* 51:257–265
27. Sarma M et al (2015) Neutron radiography visualization of solid particles in stirring liquid metal. *Phys Procedia* 69:457–463
28. Scepankis M et al (2017) Assessment of electromagnetic stirrer agitated liquid metal flows by dynamic neutron radiography. *Metall Mater Trans B* 48:1045–1054
29. Baranovskis R et al (2020) Investigation of particle dynamics and solidification in a two-phase system by neutron radiography. *Magnetohydrodynamics* 56:43–50
30. Heitkam S et al (2018) Neutron imaging of froth structure and particle motion. *Miner Eng* 119:126–129
31. Heitkam S et al (2019) Tracking of particles in froth using neutron imaging. *Chem Ing Technol* 91:1001–1007
32. Lappan T et al (2020a) X-ray particle tracking velocimetry in liquid foam flow. *Soft Matter* 16:2093–2103
33. Anderson TJ, Ansara I (1992) The Ga-Sn (gallium-tin) system. *J Phase Equilibria* 13:181–189
34. Clift R et al (1978) Bubbles, drops, and particles. Academic Press, New York
35. Birjukovs M et al (2021) X-ray imaging of bubble flow in liquid metal: shape dynamics under confinement. Accepted for 25 th international congress of theoretical and applied mechanics, Milano
36. Lappan T et al (2020b) Neutron radiography of particle-laden liquid metal flow driven by an electromagnetic induction pump. *Magnetohydrodynamics* 56:81–90
37. Nguyen AV, Schulze HJ (2004) Colloidal science of flotation. New York
38. Lehmann EH et al (2001) Properties of the radiography facility NEUTRA at SINQ and its potential for use as European reference facility. *Nondestruct Test Eval* 16:191–202
39. Kaestner AP et al (2011) The ICON beamline—a facility for cold neutron imaging at SINQ. *Nucl Instrum Methods Phys Res Sect Accel Spectrometers Detect Assoc Equip* 659:387–393
40. Blau B et al (2009) The Swiss spallation neutron source SINQ at Paul Scherrer Institut. *Neutron News* 20:5–8
41. Auger JM et al (2019a) Preparation of alumina particle suspension in liquid tin using a pre-coating process. *Metall Res Technol* 116:510
42. Auger JM et al (2019b) Wettability-enabling coating on oxide particles through controlled milling. *Powder Technol* 344:302–306
43. Tang L et al (1992) Self-organizing particle dispersion mechanism in a plane wake. *Phys Fluids Fluid Dyn* 4:2244–2251
44. Andersen KH et al (2020) The instrument suite of the European Spallation Source. *Nucl Instrum Methods Phys Res Sect Accel Spectrometers Detect Assoc Equip* 957:163402

Study on the Effect of Long Shroud Structure on Molten Steel Flow in Single Strand Tundish by Numerical Simulation



Ai-ping Zhang, Ming-mei Zhu, and Jie Luo

Abstract In this paper, a single strand tundish is taken as the research object, and a three-dimensional mathematical model is established to analyze the effect of the long shroud structure on the flow field, temperature field, pressure field, and inclusions trajectories of molten steel in the tundish. The fluid flow patterns in the tundish are analyzed by comparing the residence time distribution curves of the four types of long shrouds: traditional long shroud vortex long shroud, dissipative long shroud, and trumpet-shaped long shroud. At the same time, the effects of different long shroud structures on the fluctuation of free surface are compared. The reasonable long shroud structure is conducive to obtaining uniform molten steel and provides theoretical guidance for actual production.

Keywords Long shroud · Tundish · Residence time distribution curve · Numerical simulation · Fluctuation of free surface

Introduction

The molten steel injected into the tundish from the ladle through the shroud has great impingement on the steel in the tundish impact zone. When the fluctuation of the liquid level is too large, the molten steel will be involved in slag inclusion and secondary oxidation, which will reduce the purity of the molten steel and affect the internal quality of the cast slab.

Morales-Higa and Solorio-Diaz et al. [1, 2] proposed a dissipative shroud. Compared with the traditional long shroud and vortex shroud, the dissipative shroud can reduce the turbulent kinetic energy of the molten steel flowing to the tundish, therefore, it allows for obtaining a more stable slag layer and facilitating the contact between the inclusions and the free surface. Rodolfo and Garcia-Hernandez et al. [3, 4] used numerical simulation and water simulation methods to study the slag

A. Zhang · M. Zhu (✉) · J. Luo
College of Materials Science and Engineering, Chongqing University, Chongqing 400044, China
e-mail: zhumingmei@cqu.edu.cn

entrainment and gas entrainment phenomenon of traditional long shroud and dissipative shroud during package change (i.e. the process of molten steel from ladle to tundish). The large turbulent kinetic energy of the fluid flowing out of the traditional long shroud causes unstable three-phase flow, which is more likely to cause slag entrainment; however, the turbulent energy dissipation of the fluid flowing out of the dissipative shroud increases and the velocity of flowing into the tundish decreases. Solorio-Diaz et al. [5] used numerical simulation to calculate the fluid flow conditions and inclusion removal rates of the vortex shroud and different flow control devices at two different mass flow rates. The results show that the use of vortex shroud can replace the role of flow control device. Zhang et al. [6] used large eddy simulation to study the fluid flow process in the traditional long shroud and trumpet shroud, the fluid flowing through the trumpet area can be mixed with the surrounding fluid well, dissipating turbulent kinetic energy and reducing the velocity of the fluid flowing into the tundish. Zhang et al. [7] added two trumpet long shroud on the basis of the traditional long shroud. Three types of shrouds are used in combination with two different turbulence suppressors to study the steady-state and three-dimensional multiphase flow during package change. The results show that the trumpet shroud can reduce the turbulent kinetic energy of the fluid flowing into the tundish; as the inner diameter of the trumpet shroud increases, the area formed by the free surface slag hole decreases.

In summary, obtaining an ideal flow pattern and clean molten steel, and reducing the excessive impact of molten steel in the injection zone of the tundish, can be achieved by designing different shroud structures. This paper mainly investigates the influence of four different shroud structures, including traditional long shroud, vortex shroud, dissipative shroud and trumpet shroud, on the flow field, temperature field and pressure field of molten steel in the tundish. The residence time distribution (RTD) curve is used to analyze the fluid flow pattern in the tundish under different shroud structures and to compare the liquid level fluctuations under four different shroud structures.

Model Hypothesis

In order to facilitate the study of the flow phenomenon in the tundish, this study has the following assumptions: the flow of molten steel in the tundish is a steady-state incompressible viscous fluid; the inclusions are spherical particles and the movements are independent of each other; the effect of temperature on flow is negligible; density and viscosity are constant; the flow of molten steel is turbulent.

Model Formulation

The flow of molten steel in the continuous casting tundish is a three-dimensional turbulent flow, and the mass equation, momentum equation, energy equation and turbulent kinetic energy equation used in the calculation are as follows [8].

Continuity equation:

$$\frac{\partial P}{\partial t} + \frac{\partial(\rho\mu_i)}{\partial x_i} = 0 \quad (1)$$

Momentum equation:

$$\frac{\partial(\rho\mu_i\mu_j)}{\partial x_j} = -\frac{\partial P}{\partial x_j} + \frac{\partial}{\partial x_j} \left(\mu_{\text{eff}} \frac{\partial \mu_i}{\partial x_j} \right) + \frac{\partial}{\partial x_i} \left(\mu_{\text{eff}} \frac{\partial \mu_j}{\partial x_i} \right) + \rho g_i \quad (2)$$

The model assumes that the flow field is turbulent, so standard k - ε equation is used to describe the turbulent viscosity coefficient:

$$\frac{\partial(\rho\mu_i)}{\partial x_i} = \frac{\partial}{\partial x_i} \left[\left(\mu_{\text{eff}} + \frac{\mu_t}{\sigma_k} \right) \frac{\partial k}{\partial x_i} \right] + G - \rho\varepsilon \quad (3)$$

$$\frac{\partial(\rho\mu_i\varepsilon)}{\partial x_i} = \frac{\partial}{\partial x_i} \left[\left(\mu_{\text{eff}} + \frac{\mu_t}{\sigma_\varepsilon} \right) \frac{\partial \varepsilon}{\partial x_i} \right] + c_1 \frac{\varepsilon}{k} G - c_2 \frac{\varepsilon^2}{k} \rho \quad (4)$$

among them

$$G = \mu_t \frac{\partial \mu_j}{\partial x_i} \left(\frac{\partial \mu_j}{\partial x_j} + \frac{\partial \mu_j}{\partial x_j} \right) \quad (5)$$

$$\mu_{\text{eff}} = \mu + \mu_t = \mu + c_\mu \rho \frac{k^2}{\varepsilon} \quad (6)$$

Energy equation related to temperature field calculation:

$$\rho \left(\frac{\partial T}{\partial t} + C_p \frac{\partial T}{\partial x_i} \right) = \frac{\partial}{\partial x_i} \left(k_{\text{eff}} \frac{\partial T}{\partial x_i} \right) \quad (7)$$

Equation of transport behavior of inclusions in tundish:

$$\frac{du_{\text{pi}}}{dt} = \frac{18u}{\rho_p d_p^2} \cdot \frac{C_D \text{Re}}{24} (u_i - u_{\text{pi}}) + \frac{(\rho_p - \rho)}{\rho_p} g_p + F_i \quad (8)$$

Mass transfer equation of tracer in tundish:

$$\left(\frac{\partial C}{\partial t} + \nabla \times U_c\right) = \nabla \times \left(\rho D_c + \frac{\mu_t}{Sc_t}\right) \nabla \times \left(\frac{C}{\rho}\right) + S_c \quad (9)$$

The free liquid surface fluctuation range can be calculated by the following formula:

$$H = \frac{P_{sta} - \overline{P_{sta}}}{\rho|g|} \quad (10)$$

where ρ is the density, kg m^{-3} ; u_i and u_j are the velocity of molten steel in the i and j directions, m s^{-1} ; p is the pressure, Pa; μ_{eff} is the effective viscosity, $\text{kg m}^{-1} \text{S}^{-1}$; $C_1, C_2, C_\mu, C_k, C_\varepsilon$ are empirical constants, and their values are 1.44, 1.93, 0.99, 1.0, 1.3; k_{eff} is the effective thermal conductivity, $\text{W m}^{-1} \text{K}^{-1}$; ρ_p is the particle density, kg m^{-3} ; d_p is the particle diameter, m; u_{pi} is the particle velocity, m s^{-1} ; C_D is the drag coefficient; Re is the relative Reynolds coefficient; F_i is the force, N; S_c is the volume source phase, is the residual mass per unit volume of the tracer unit time, $\text{kg}/(\text{m}^3 \text{s})$; D_c tracer diffusion coefficient, this paper takes $1.1 \times 10^{-8} \text{ m}^2/\text{s}$; μ_t is the turbulent viscosity of molten steel, $\text{kg}/(\text{m s})$; Sc_t is the turbulent Schmidt number of the tracer, taken 0.9. H represents the z -axis coordinate value of the free surface of the molten pool in the coordinate system of (x, y, z) , which is consistent with the direction of gravity, P_{sta} is the static pressure value of the unit calculated by the free surface, and $\overline{P_{sta}}$ is the average static pressure value of the free surface [9].

Boundary Conditions

In this paper, the ladle nozzle is the velocity inlet, the outlet is defined as the pressure outlet, the liquid–solid interface is the non-slip boundary, and the velocity value on the solid wall is 0. The free surface is the zero shear stress surface, and the heat radiation loss of the wall and the free surface is negligible (the schematic diagram is shown in Fig. 1). Inclusion particles are removed by the adsorption of the slag layer on the surface of the molten steel, and the inclusions that touch the wall of the tundish are regarded as rebound.

Calculation Method

The ratio of the tundish model to the actual object is 1:1, and the model grid is divided into uniform unstructured grids (see Fig. 1 for details).

The standard k – ε equation is used to describe the turbulence process, the energy equation is used to calculate the temperature field, the pressure coupling equations are used to solve the semi-implicit method (SIMPLE method), and the convergence residual value is less than 10^{-5} .

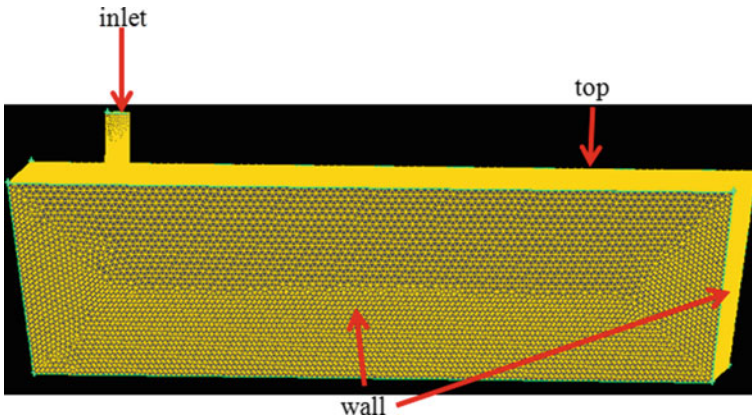


Fig. 1 Tundish meshing diagram. (Color figure online)

Table 1 Important physical parameters for simulation of fluid flow in tundish [10, 11]

Parameters	Values	Parameters	Values
Viscosity	$0.0067 \text{ kg m}^{-1} \text{ s}^{-1}$	Thermal conductivity	$41 \text{ W m}^{-2} \text{ K}^{-1}$
Specific heat	$750 \text{ J kg}^{-1} \text{ K}^{-1}$	Free surface heat flow	15 kW m^{-2}
Density	7020 kg m^{-3}	Bottom wall heat loss	1.4 kW m^{-2}
Turbulent kinetic energy at the inlet	$0.01 V_{in}^2 \text{ m}^2/\text{s}^2$	Long wall heat loss	3.8 kW m^{-2}
Dissipation rate at the inlet	$K_{in}^{1.5}/R_{inlet} \text{ m}^2/\text{s}^3$	Short wall heat loss	3.2 kW m^{-2}
Inlet temperature	1823.00 K	Tracer diffusion coefficient	$1.1 \times 10^{-8} \text{ m}^2/\text{s}$

Regarding the inclusion particles as a discrete phase, the Lagrange particle tracking model and the discrete phase model (DPM) are used to calculate the removal rate of the inclusions in the tundish. The parameters that may be used in the numerical simulation of the tundish are shown in Table 1.

When analyzing the characteristics of the molten pool flow field, the $k-\epsilon$ two-equation model for calculating the flow field and the volume of fluid (VOF) two-phase flow model are coupled to calculate the characteristics of the molten pool liquid level fluctuation.

Simulation Scheme

Figure 2 is a schematic diagram of the continuous casting process. The four different shroud structures are traditional long shroud, vortex shroud, dissipative shroud and trumpet shroud. A simple diagram is shown in Fig. 3.

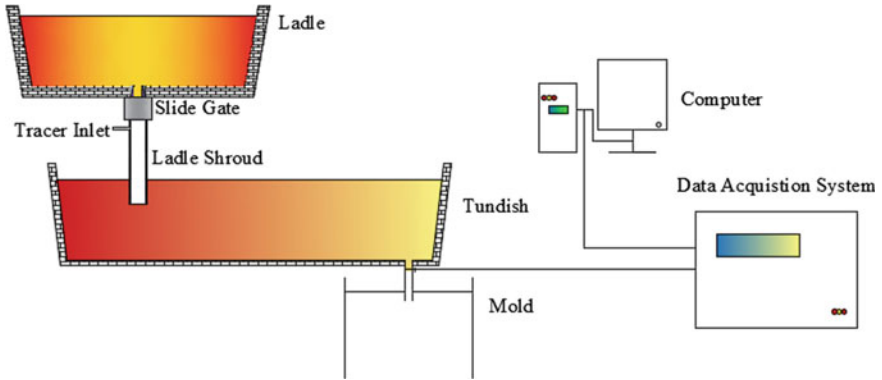


Fig. 2 Simplified diagram of the tundish continuous casting process. (Color figure online)

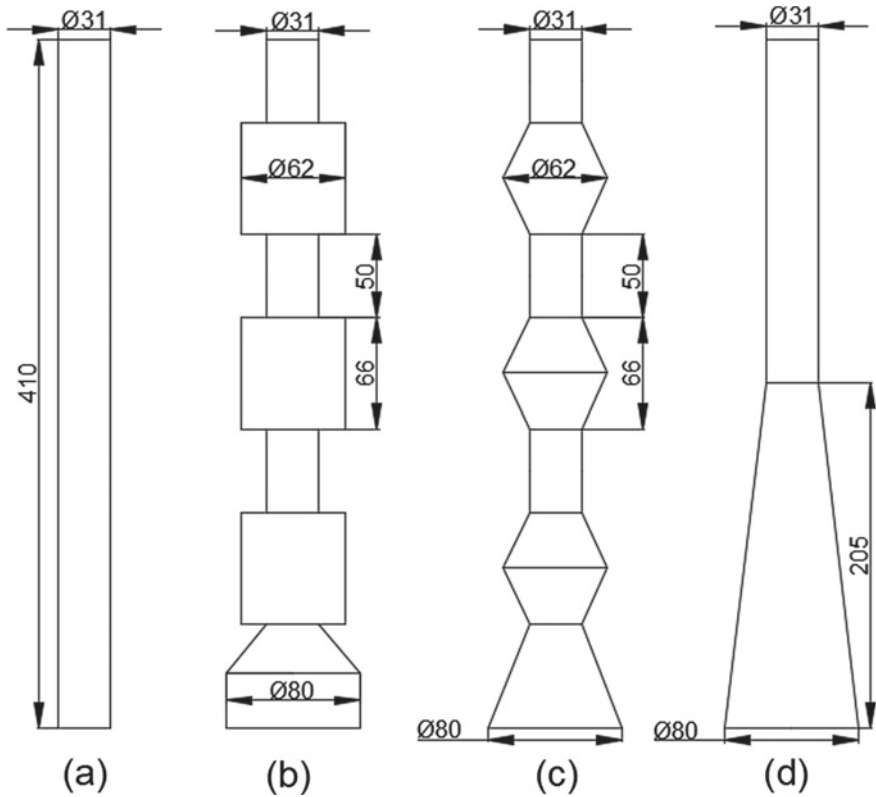


Fig. 3 Schematic diagram of different shrouds structure **a** traditional shroud; **b** vortex shroud; **c** dissipative shroud; **d** trumpet shroud

Results and Analysis

According to the above four different shroud structures, modeling in Gambit software, importing FLUENT calculation, finally after post-processing, the following results are obtained.

Flow Field Comparison

Figure 4 is the velocity cloud diagram of the center surface of the tundish exit and entrance of different shroud structures. It can be seen that the molten steel is injected into the tundish under the action of gravity and directly impacts the bottom of the tundish, and then a part of the molten steel flows upward to form a backflow. However, the impact strength of different shroud structures is different. By comparing the pressure value at the bottom of the tundish, it is found that the maximum impact pressure of the traditional long shroud is about 40,000 Pa, and the rest is about 27,000 Pa. At the same time, the reflux area (the extent of the green area in the picture) formed by the molten steel through the traditional long shroud is wider. The reason may be that the shroud of the other three structures has expansion or contraction parts, so a part of the turbulent strength of the molten steel is dissipated.

Temperature Difference

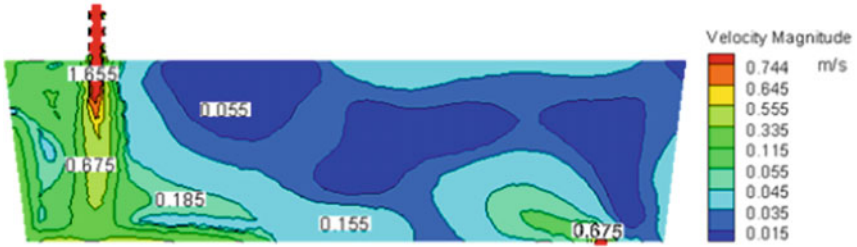
Figure 5 shows the average temperature of top and outlet. Although the former shows an upward trend, but in general, the maximum temperature difference is only 1.35 K. Considering the randomness of temperature distribution, the effect of four shrouds on the temperature of top and outlet cannot be identified.

RTD Curve and Flow Pattern

The concentration of the tracer in the tundish was calculated by the component transmission equation, and the RTD curve(i.e. dimensionless distribution function) was obtained after post-processing. It can be seen from Fig. 6 that the RTD curve of the traditional long shroud has a sharp peak, and the remaining peaks are relatively smooth. The reason may be that the strong turbulence is buffered when the molten steel passes through the abrupt shroud diameter of the latter, and the peak in the former may be caused by the instantaneous molten steel impact. However, the response time and the time to reach the peak concentration of the four different shroud structures



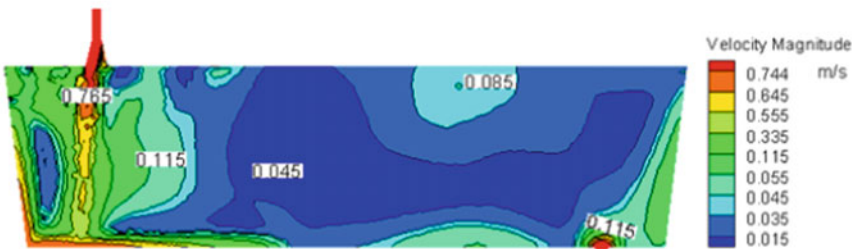
(a) Traditional shroud



(b) Vortex shroud



(c) Dissipative shroud



(d) Trumpet shroud;

Fig. 4 Speed cloud diagram of the center surface of the entrance and exit of the tundish. (Color figure online)

Fig. 5 Temperature difference in the tundish of different structures of the nozzle. (Color figure online)

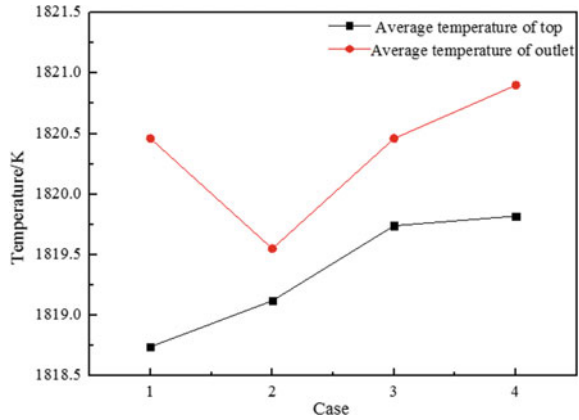
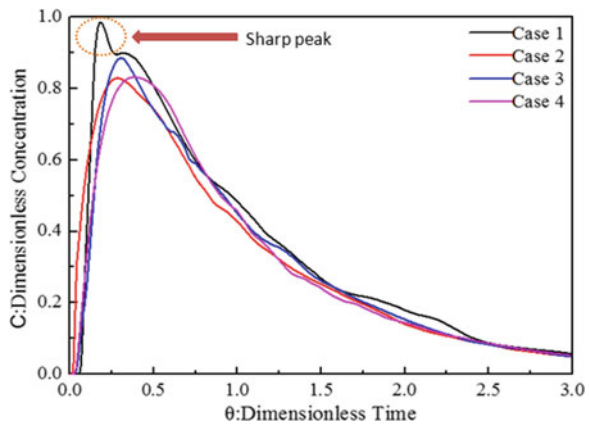


Fig. 6 RTD curve. (Color figure online)

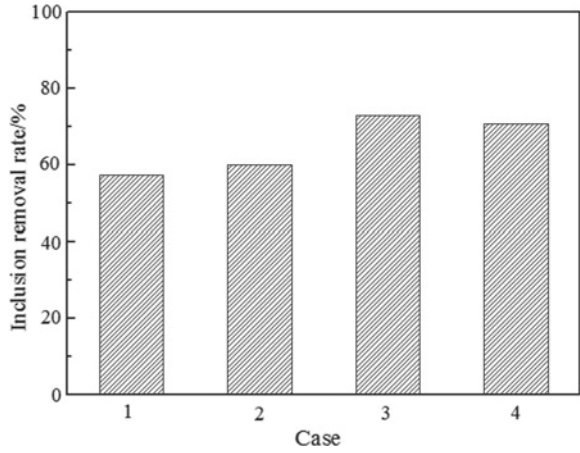


are different. It can be inferred that the shroud structure has little effect on the flow pattern, mainly affecting the turbulence intensity of the inflowing molten steel.

Inclusion Removal Rate

Figure 7 shows the removal rate of inclusions (the amount captured by the top surface accounts for the total injected) in the tundish of the shroud with four different structures. It can be seen that the difference between the first two is small, but the removal rate corresponding to the dissipative shroud is slightly higher. The reason may be that the lower part of the shroud of Case 1 and Case 2 is a straight-through type, while Case 3 and 4 are a trumpet type, and the sudden change area of the trumpet type of Case 3 is greater than that of Case 4.

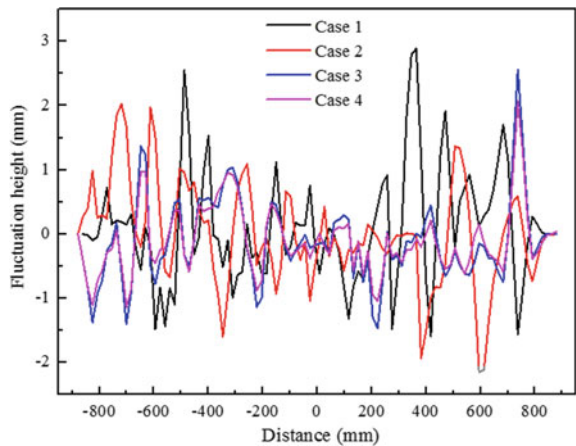
Fig. 7 Inclusion removal rate of different shroud structures



Liquid Level Fluctuation

Combining the $k-\epsilon$ two-equation model and the VOF model, the fluctuation of the tundish level during transient pouring is calculated. Figure 8 shows the center position of the short wall at a distance of 0 mm. It can be seen that the four cases are consistent: the fluctuation in the 350 mm area along the short wall is within 1 mm, while the fluctuation on both sides of the short wall is about 1.5 mm. Some even exceed 2 mm. Comparing the four cases, it can be seen that the traditional long shroud and the vortex shroud have significantly higher liquid level fluctuations than the dissipative shroud and the trumpet shroud; and the fluctuations of the first two are opposite, while the latter two have similar fluctuations. But a more accurate conclusion should be combined with water model experiments to illustrate. Different shroud structures

Fig. 8 Tundish liquid level fluctuations with different shroud structures. (Color figure online)



make the speed of the molten steel reach the impact zone different. The upward reflux increases the liquid steel exchange rate. When the molten steel flows along the bottom of the tundish to the outlet, the impact with the wall causes greater side fluctuations.

Conclusion

This paper compares four different shroud structures of traditional long shroud, vortex shroud, dissipative shroud, and trumpet shroud to analyze the flow in the tundish and the fluctuation of the liquid level. The turbulence intensity and pressure of molten steel passing through the traditional long shroud to the impact area are significantly higher than the other three types; however, the average temperature and inclusion removal rate of the four different shroud structures are similar, the liquid level on both sides of the short wall fluctuates larger than the central area, the liquid level fluctuations of the traditional long shroud and vortex shroud are opposite, and the liquid level fluctuations of the dissipative shroud and trumpet shroud are similar.

References

1. Morales-Higa K, Guthrie RIL, Isac M et al (2013) Ladle shroud as a flow control device for tundish operations. *Metall Mater Trans B*
2. Solorio-Diaz G, Davila-Morales R, Jose BS et al (2014) Numerical modelling of dissipation phenomena in a new ladle shroud for fluidynamic control and its effect on inclusions removal in a slab tundish. *Steel Res Int* 85(5):863–874
3. Morales RD, Calderon-Ramos I et al (2016) Multiphase flow modeling of slag entrainment during ladle change-over operation. *Metall Mater Trans B*
4. Garcia-Hernandez S, Morales RD, de Jesus Barreto J et al (2015) Modeling study of slag emulsification during ladle change-over using a dissipative ladle shroud. *Steel Res Int*
5. Solorio-Diaz G, Ramos-Banderas A, Barreto JDJ et al (2010) Modeling study of turbulent flow effect on inclusion removal in a tundish with swirling ladle shroud. *Steel Res Int* 80(3):223–234
6. Zhang J et al (2016) Comparative study of fluid flow and mass transfer in a trumpet-shaped ladle shroud using large eddy simulation. *Metall Mater Trans B* 47(1):495–507
7. Zhang H, Fang Q, Deng S et al (2019) Multiphase flow in a five-strand tundish using trumpet ladle shroud during steady-state casting and ladle change-over. *Steel Res Int* 90(3)
8. Zhang J, Yang S, Li J et al (2015) Large eddy simulation on flow structure in a dissipative ladle shroud and a tundish. *ISIJ Int* 55(8):1684–1692
9. Morales-Higa K, Guthrie RIL, Isac M et al (2013) Ladle shroud as a flow control device for tundish operations. *Metall Mater Trans B* 44(1):63–79
10. Chatterjee S, Li D, Chattopadhyay K (2018) Modeling of liquid steel/slag/argon gas multiphase flow during tundish open eye formation in a two-strand tundish. *Metall Mater Trans B* 49(2):756
11. Qin X-F, Cheng C-G, Li Y et al (2019) A Simulation study on the flow behavior of liquid steel in tundish with annular argon blowing in the upper nozzle. *Metals* 9(2):225

Numerical Simulation of the Influence of Particle Physical Properties on Flow Field During the Aeration Leaching Process



Mingzhao Zheng, Qiuyue Zhao, Zimu Zhang, Lei Zhou, and Tingan Zhang

Abstract The aeration leaching process is a three-phase reaction of gas, liquid and solid. The solid phase is black opaque particles. It is difficult to observe the flow field and the distribution of each phase. The water model experiment does not involve chemical reactions, and the physical properties of the solid particles remain unchanged. The effect of particle changes on the flow field cannot be explored. This study is based on computational fluid dynamics (CFD) software, using the Euler–Euler three-fluid model. A 60 L stirred reactor was simulated, and the solid–liquid ratio in the tank was 1:4, ventilation rate $Q = 1\text{--}2.5\text{ m}^3/\text{h}$, speed 400–500 rpm. This study simulated the particle changes in the real reaction process and analyzed the phase distribution and flow field.

Keywords Three-phase flow · Aeration leaching reaction · Stirrer · CFD

Introduction

Aeration leaching equipment is widely used in metallurgy, pharmaceutical, wastewater treatment and other industries. Usually, the aeration process is realized by spraying liquid in the gas [1], allowing bubbles to diffuse through the liquid phase [2] or mechanically promoting the renewal of the gas–liquid interface [3]. The core purpose is to increase the contact area between phases. In the aerated leaching process, if solid particles are participating in the reaction, mechanical stirring is usually required to achieve the ideal situation of solid–liquid suspension and gas–liquid dispersion [4].

M. Zheng · Q. Zhao (✉) · Z. Zhang · L. Zhou · T. Zhang
School of Metallurgy, Northeastern University, Shenyang 110004, China
e-mail: zhaoqy@smm.neu.edu.cn

Q. Zhao · Z. Zhang · T. Zhang
Engineering Research Center of Metallurgy of Non-Ferrous Metal Materials Process Technology of Ministry of Education, Shenyang, China

Key Laboratory of Ecological Utilization of Multi-metal Intergrown Ores of Ministry of Education, Shenyang, China

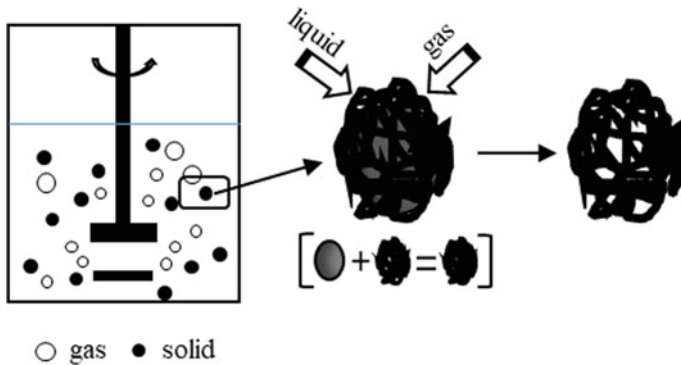


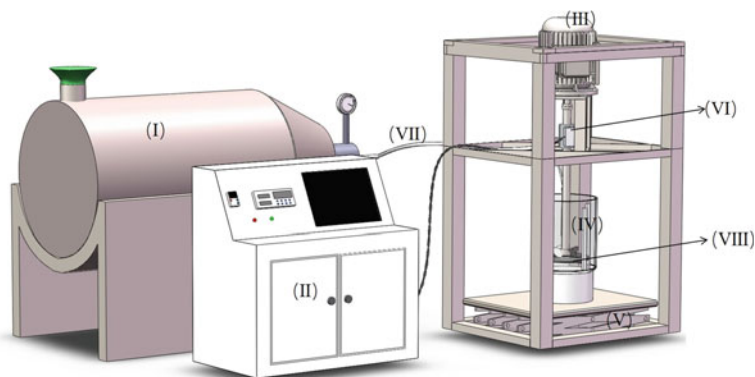
Fig. 1 Schematic diagram of particle change in aeration leaching reaction. (Color figure online)

The solid particles can be divided into floating particles [5, 6] and sinking particles [7, 8] according to the density ratio of the solid particles to the liquid phase. The material properties of the multiphase flow are not constant during the aeration and aeration process. As the reaction progresses, its physical and chemical properties will also change accordingly. For example, in stirred aeration leaching process, due to cyclonic shear and the impact of air bubbles on the particles, the solid particles may be broken and thus the particle diameter becomes smaller, and the change in particle size will affect the morphology of the flow field [9–11], which in turn affects the leaching reaction. Besides, in some reactions, the solid particles are not a single compound, but a mixture of two or more compounds, and have a typical package structure. During aeration and leaching, the gas and liquid phases do not react with the outer solid particle shell, but instead decompose the internal portion of the solids (as shown in Fig. 1). The macroscopic result is that the particle diameter does not change, but the weight of a single particle decreases. It is difficult to consider a chemical reaction and flow field characteristics at the same time in the traditional simulation. This work sets the change of solid particle density to simulate the influence of particle change on the flow field during the aeration leaching reaction.

Model and Experimental Conditions

Geometric Model and Mesh Independence Verification

The numerical simulation process was used as further work for the experiment [12]. The experimental instrument is shown in Fig. 2. The rest of the equipment can be ignored in computational fluid dynamics and only the area where the fluid flows are considered. Therefore, only the modeling of the reactor tank is required for numerical simulation.



(I) air compressor; (II) console; (III) electric motor; (IV) stirring tank ; (V) lifting platform; (VI) torque sensor; (VII) gas transmission device; (VIII) gas distributor.

Fig. 2 Aeration and stirring leaching experimental instrument. (Color figure online)

In this work, MIXSIM and Gambit software are used to establish the geometry and grid model of the flow area of the stirred reactor. The structure of the reactor is shown in Fig. 3.

To eliminate the vortex phenomenon in the tank caused by the central stirring, four baffles are evenly distributed on the inner wall of the stirring tank. The specific dimensions are shown in Table 1.

The processing method of the reactor grid is an unstructured tetrahedral grid. The main body of the reactor is divided into two fluid domains. The flow domain that wraps the blades rotates, and the one domain is static (Fig. 4). When the grid number is 200,000, 550,000 and 1,090,000, the volume fraction of solid phase at different

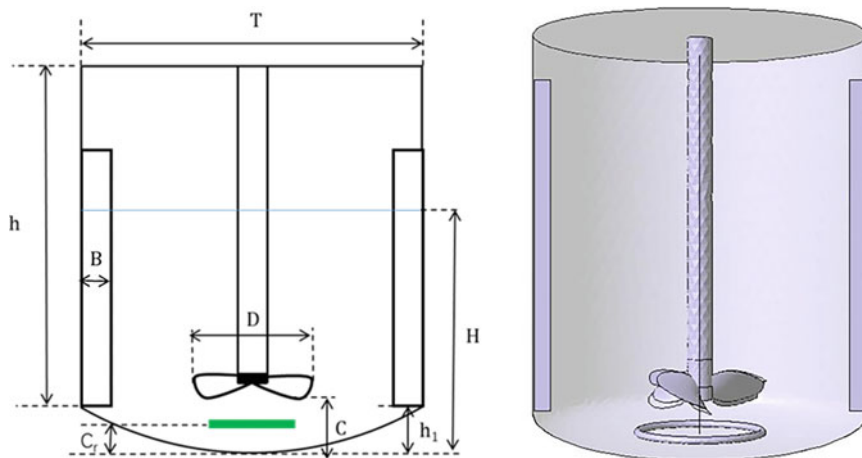
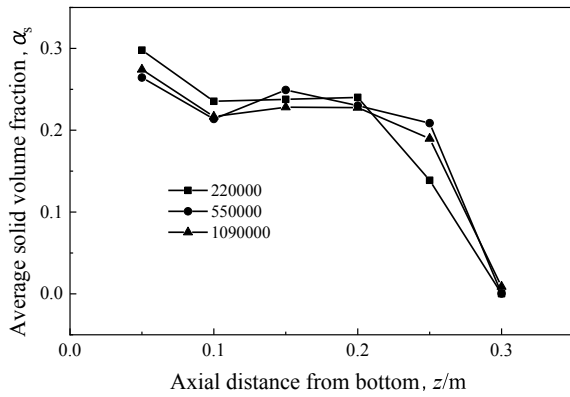


Fig. 3 Schematic diagram of the geometric structure of a stirred reactor. (Color figure online)

Table 1 Stirred reactor geometric parameters

Parameter	Value (mm)
Reactor diameter, T	400
Reactor body height, h	450
Height of reactor bottom, h_1	50
Baffle width, B	40
Mixing blade diameter, D	162
Distance from bottom, C	100
Distance from the bottom of the air inlet, C_r	40
Annular distributor diameter, D_r	120
Liquid level, H	300

Fig. 4 Effect of grid number on solid volume fraction



distance from the bottom is calculated up to 3 s, and it can be found that the volume fraction error is less than 5% after 550,000 grid number, finally 550,000 grid number is chosen, and the grid is shown in Fig. 5.

Physical Parameters

The reactants are gas–liquid–solid three phases, gas phase is air, and liquid phase is water. The parameters of each phase are shown in Table 2.

Boundary Conditions and CFD Model Validation

Due to the high-speed rotation of the blade part of the stirring blade, there is a large speed gradient in this region. Therefore, the multiple reference frame (MRF) [13]

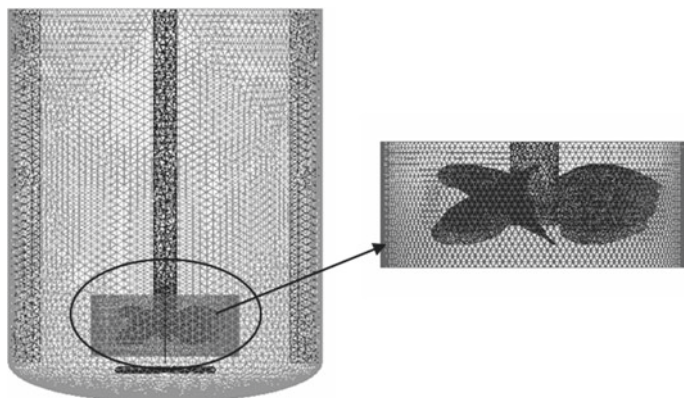


Fig. 5 Grid division diagram of stirred reactor

Table 2 Three-phase physical properties

Parameter	Value
Solid particle density (kg/m^3)	3750, 3000, 2600
Average diameter of solid particles (μm)	180
Liquid density (kg/m^3)	998.2
Liquid viscosity (Pa s)	$1.003\text{e}-03$
Gas density (kg/m^3)	1.225
Gas viscosity (Pa s)	$1.7894\text{e}-05$
Initial solid phase volume fraction (%)	20
Ventilatory capacity (m^3/h)	2

is adopted. By constructing two reference systems, the rotation area is determined according to the speed of the stirring blade. The moving reference system is adopted for the rest of the area, and the speed matching of the two areas is achieved through the exchange of data at the interface. The flow state in the reactor is complex, and a standard k-epsilon model with a wide range of applications is used to describe the turbulence. The Euler–Euler “three-fluid” model is used as the flow characteristics of multiphase flow. The gas–liquid–solid three phases have different characteristics. The Euler–Euler “three-fluid” model is used to describe the flow characteristics of a multiphase flow, in which the gas–liquid–solid phases have different characteristics, with the liquid phase as the primary phase and the solid–liquid phases as secondary phases. The gas phase has a strong upward floating characteristic, while the solid phase has a strong sinking characteristic. The Schiller–Naumann model was used to describe the drag between the phases. Standard wall functions were applied to the wall boundaries of the reactor inner wall, baffles, shafts and blades surfaces. Each parameter is considered convergent when the residuals are less than 10^{-3} . The solution process is transient, and the time step is set to 0.001 s. Since the heat absorption and exotherm during the reaction is not considered, no energy model is involved, for

the flow of each phase in the stirring tank. The two fundamental equations of conservation of mass (continuity equation) and conservation of momentum (Navier–Stokes equation) need to be satisfied.

Continuity equation:

$$\frac{\partial}{\partial t}(\alpha_i \rho_i) + \nabla \cdot (\alpha_i \rho_i u_i) = 0 \quad (1)$$

Navier–Stokes equation:

$$\frac{\partial}{\partial t}(\alpha_i \rho_i u_i) + \nabla \cdot (\alpha_i \rho_i u_i u_i) = -\alpha_i \nabla p + \nabla \cdot \tau_i + \alpha_i \rho_i g + F_i \quad (2)$$

and satisfy

$$\sum \alpha_i = 1 \quad (3)$$

α_i —Phase volume fraction;

ρ_i —Phase density, kg/m³;

u_i —Instantaneous speed, m/s;

P —Pressure, Pa;

τ_i —Stress tensor, N/m²;

F_i —Momentum transfer.

Numerical simulations of the same conditions were performed according to the structural and operational parameters of the model in the literature [12]. For the validation of the simulation of the solid–liquid two-phase flow, the stirring speed is 500 rpm, the volume fraction of solid phase at $r/T = 0.75$ is compared, and several points are selected according to the different distances from the bottom of the radial position for comparison analysis. The maximum error of the Gidaspow model is 11.1%, the average error is 4.952%, and the maximum error of the Gidaspow model is 4.952%. The maximum error of the Schiller–Naumann model is 8.68%, and the average error is 3.2%. The agreement between the numerical simulation and the experimental results is within the error limit, but the Schiller–Naumann model is more suitable for the current simulation condition, and finally the Schiller–Naumann expression of interphase drag is chosen (Fig. 6).

For the simulation validation of gas–liquid two-phase flow, in the literature [12] the ventilation rate is 2 m³/h, the apparent gas velocity in the tank is about 0.0044 m/s, the stirring speed is 200 rpm, and the average diameter of local bubbles in the tank is compared with the simulation values as shown in Fig. 7. According to the comparison, the simulation process better describes the results of the experiment, and the bubbles rise from the bottom of the stirring tank through the process of agitation. The bubbles

Fig. 6 Comparison of experimental value of uniformity axial distribution with CFD value

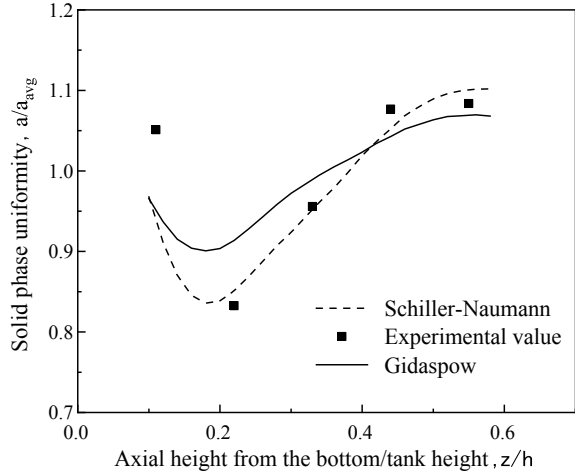
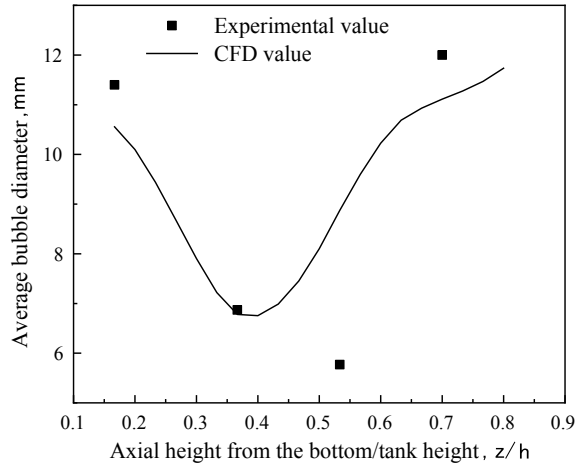


Fig. 7 Comparison of experimental value and CFD value of axial local bubble diameter



break up into small bubbles, which then come together again to form larger diameter bubbles. The simulation process can be judged to accurately reflect the flow behavior of each phase inside the stirring tank.

Results and Discussion

The Effect of Particle Density Changes on Phase Distribution

In order to describe the phase distribution of solid particles in the variable density three-phase stirred aeration reactor, the central plane is cut to obtain the solid volume fraction value in Fig. 8, where the horizontal line represents the liquid level. It can be found that under the same stirring speed, as the solid density decreases during the reaction process, the better the suspension of solid particles in the liquid phase, the more evenly distributed in the flow zone of the reactor. Along the axial direction, 15 sections are selected equidistantly from the bottom of the reactor, and the average value is calculated after selecting several points for each section. The solid volume fraction (SVF) results of different heights are obtained in Fig. 9. It can be found that the density decreases and the maximum difference of the SVF curve decreases.

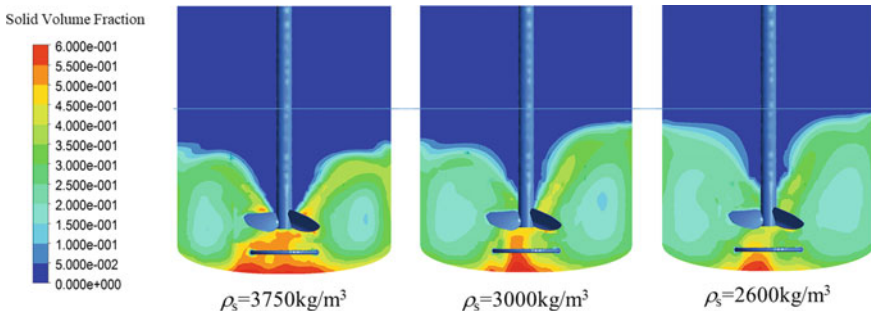
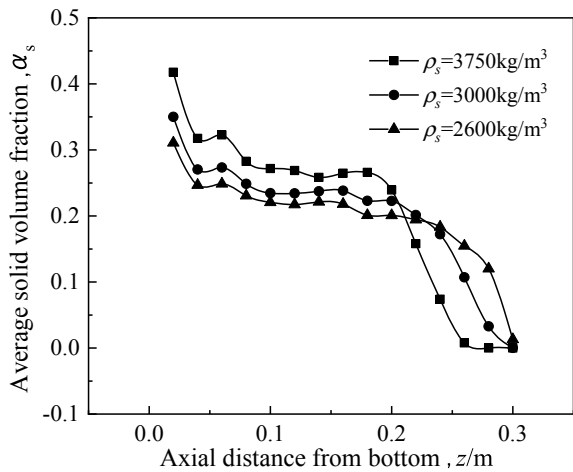


Fig. 8 Solid-phase volume fraction at different solid density. (Color figure online)

Fig. 9 Solid volume fraction at different heights



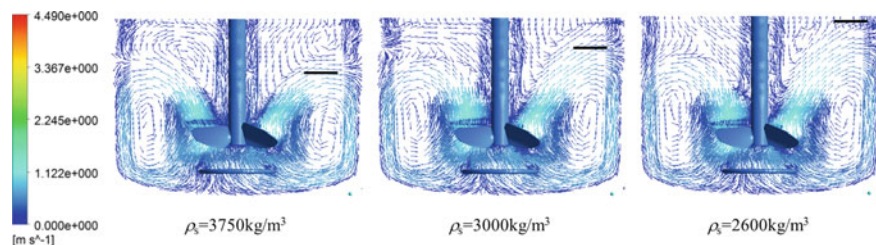


Fig. 10 Flow field at different solid density. (Color figure online)

The Impact of Particle Density Changes on the Flow Field

Because only the flow field in the flow area is considered, the part below the liquid surface is intercepted to observe the flow state, and the result is shown in Fig. 10. From the figure, we can see that as the solid density decreases, the height of the high-speed position of the fluid after the upward lifting action of the stirring paddle blade is gradually increasing (black line in the figure), indicating that the smaller the particle density, the better the flow effect in the reactor under the same paddle type and stirring speed conditions.

Conclusion

Taking the aeration leaching reaction in a gas–liquid–solid three-phase stirred reactor as the research object, the particle distribution and flow field were simulated and analyzed by CFD software, and the following conclusions were drawn:

1. The decrease in the density of solid particles during the aeration leaching reaction will make the solid–liquid suspension effect better, which is conducive to the contact of all phases, thereby promoting the reaction;
2. The decrease in the density of solid particles will increase the high-speed flow area of the fluid in the reactor, which is conducive to mass transfer and can increase the contact frequency of substances in the reactor, which is conducive to the progress of the reaction.

Funding This research was supported by the National Natural Science Foundation of China (NSFC) (Grant No. 51204040); Fundamental Research Funds for the Central Universities (Grant No. N180725023, N2024005-6).

References

1. Fatihah R, Donnelly T (2008) Effect of media volume on mixing of biological aerated filters. *J Environ Eng* 7:229–236. <https://doi.org/10.1139/S07-048>
2. Liu S, Wang QH et al (2009) Effect of micro-bubbles on coagulation flotation process of dyeing wastewater. *Sep Purif Technol* 71(3):337–346
3. Jescovitch LN, Boyd CE, Whitis GN (2017) Effects of mechanical aeration in the waste-treatment cells of split-pond aquaculture systems on water quality. *Aquaculture* 480:32–41
4. Frijlink JJ, Bakker A, Smith JM (1990) Suspension of solid particles with gassed impellers. *Chem Eng Sci* 45(7):1703–1718
5. Cartwright JHE, Magnasco MO et al (2002) Bailout embeddings and neutrally buoyant particles in three-dimensional flows. *Phys Rev Lett* 89(26):264501
6. Guer YL, Reghem P et al (2003) Experimental study of a buoyant particle dispersion in pipe flow. *Chem Eng Res Des* 81(9):1136–1143
7. Kong JY, Wu ZW et al (2014) Numerical simulation for solid-liquid two-phase flow in stirred vanadium leaching tank. *Appl Mech Mater* 2839:314–319
8. Li XM, Niu SL et al (2020) Numerical simulation of solid-liquid flow in stirred tanks based on KTGF model. *Chin J Process Eng* 20(03):265–275
9. Qi NN, Zhang H et al (2013) CFD simulation of particle suspension in a stirred tank. *Particuology* 11(03):317–326
10. Li LC, Xu B (2017) CFD simulation of floating particles suspension in a stirred tank. *Chem Pap* 71(8):1377–1387
11. Gu DY, Cheng C et al (2019) Numerical simulation of solid-liquid mixing characteristics in a stirred tank with fractal impellers. *Adv Powder Technol* 30(10):2126–2138
12. Zhang CY (2019) Study on gas-liquid-solid three-phase stirring performance in corrosion reactor. *Northeastern University*, pp 9–50
13. Bujalski W, Jaworski Z et al (2002) CFD study of homogenization with dual rushton turbines-comparison with experimental results. *Chem Eng Res Des* 80(1):97–104

Part II

Steel Casting

Study on Evolution of Inclusions in Tinsplate Production During RH Refining—Continuous Casting Process



Xiaobao Li, Nan Wang, and Min Chen

Abstract The evolution behaviors of the type, amount, and size of inclusions in tinsplate were studied by industrial experiments and thermodynamic calculations during RH refining process. The results indicated that Al_2O_3 inclusions were generated at first after Al addition. With the slag-steel and refractory-steel reactions, inclusions varied with the route as Al_2O_3 inclusions \rightarrow $\text{CaO-Al}_2\text{O}_3$ system inclusions \rightarrow $\text{CaO-MgO-Al}_2\text{O}_3$ system inclusions and Al_2O_3 inclusions \rightarrow $\text{MgO-Al}_2\text{O}_3$ spinel inclusions \rightarrow $\text{CaO-MgO-Al}_2\text{O}_3$ system inclusions. From Al addition to the end of RH refining, the number density of inclusions increased from 9.32 to 4.09 per mm^2 . The total oxygen content in steel could be decreased from 450 to 37 ppm. The size of inclusions varied mainly less than 10 μm , the proportion of inclusions with size less than 5 μm gradually decreased by 15% and inclusions in the range of 5–10 μm increased by 10%. These inclusions with size less than 10 μm were difficult to be removed from liquid steel through the floatation. The inclusions were Al_2O_3 and $\text{CaO}\cdot\text{Al}_2\text{O}_3$ inclusions with a high melting point at the end of RH refining. In order to obtain inclusions with a low melting point, the reasonable C/A mass ratio of the final RH slag is 1.10 through theoretical calculations.

Keywords Tinsplate steel · Inclusions evolution · Thermodynamic calculations · CaO modification · RH refining

Introduction

Usually, non-metallic inclusions have a great influence on steel performance. In particular, these inclusions with a high melting point are harmful to the quality of product [1–4]. To improve the cleanliness of tinsplate steel, numerous investigations have been carried out to study the evolution and control of inclusions in the past ten years, most of them were focused on the formation and evolution mechanism of inclusions, such as Park et al. [5, 6], Kang et al. [7] and Jiang et al. [8–11]. In

X. Li · N. Wang (✉) · M. Chen
School of Metallurgy, Northeastern University, Shenyang, Liaoning 110819, China
e-mail: wangn@smm.neu.edu.cn

the production of high-quality tinplate steel, the characteristics of inclusions, such as their chemical compositions, number, and size distribution, play a vital role in product quality. As these inclusions can be easily the key influence factor of the surface quality and mechanical property of the substrate, their existence in tinplate must be well controlled.

Non-metallic inclusions have various origins ranging from deoxidation, reoxidation, and slag treatment to chemical reactions during the metallurgical process. Based on the origin, two types of inclusions are distinguished. Exogenous inclusions, on one hand, originate outside the melt, such as rolling slag and refractory material erosion. Endogenous inclusions, on the other hand, are formed in the melt, such as the deoxidation and reoxidation production.

Total oxygen content is the most widely used indirect index when the cleanliness of steel is assessed which includes the dissolved oxygen in steel melts and the fixed oxygen in inclusions [4, 12, 13]. The total oxygen content is generally expressed by TO. However, for high-quality tinplate requiring high surface quality and stable mechanical property, a decrease in TO content is far from enough. In recent years, the formation and evolution of inclusions have become important, and this topic has aroused more attention. During the past few decades, the production of high-quality steel in China has had a rapid development and witnessed an obvious decrease in TO content in steel [2].

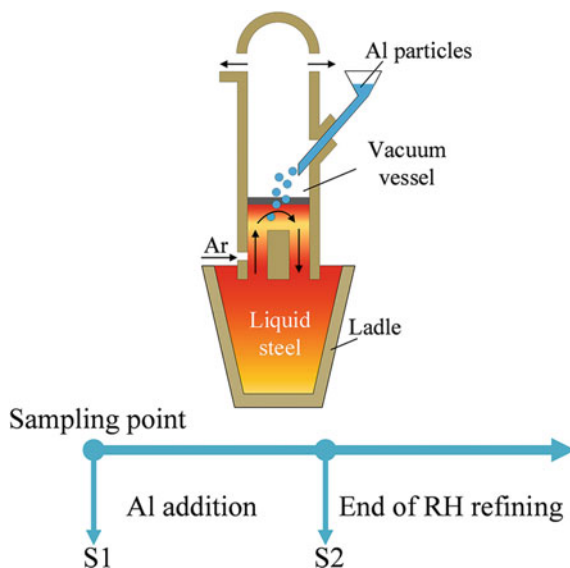
In the present work, with the help of an automatic scanning electron microscope, a large area inspection of inclusions was done. The evolution behaviors of the number, size, and composition of inclusions at different stages were systematically investigated by using industrial tests and sampling analysis. Based on the formation process of dissolved Ca and Mg, the formation of MgO–Al₂O₃ system inclusions and CaO–MgO–Al₂O₃ system inclusions was studied by SEM mapping and phase stability diagram. We focused on the control of inclusions in tinplate steel production during RH refining process. C/A mass ratio of RH refining slag was analyzed and discussed. The research results provided a better and deeper understanding of inclusions for promoting product quality of tinplate.

Experimental

Experiment Procedure and Sampling Scheme

The industrial experiments were carried out in a domestic steel mill. The process route of tinplate is hot metal pre-desulphurization → 180t BOF steelmaking → 80t RH refining → continuous casting. After the hot metal pre-desulphurization, [S] content in the liquid steel was below 0.008%, and at the end of BOF the [C] content was 0.05–0.07% with [O] content was 400–600 ppm. During the tapping process of the BOF, no Al was added into the ladle for deoxidation. A vacuum is first applied for 3 min to reach the specified vacuum degree at the beginning of RH refining. After

Fig. 1 Illustration of sampling during RH refining process. (Color figure online)



that, Al was added to the steel for additional deoxidation. Then, MnFe was added to the steel for composition adjustment after 15 min. No calcium alloy was added to the molten steel to modify solid inclusions during RH refining process. Finally, the refining time lasted for 20 min at a vacuum pressure of less than 133 Pa. After breaking the vacuum, argon bottom blowing time was 5 min.

In the experimental procedure, two liquid steel samples were taken with pie samplers, one after the Al addition during RH refining process (S1) and one at the end of RH refining (S2) as shown in Fig. 1.

Analysis of Inclusions

The metallographic samples for inclusion analysis were cut from pie samples in the experiment. The inclusions on the polished surfaces of specimens were analyzed with a scanning electron microscope of ASPEX PSEM EXPLORER. The size, number, composition, and morphology of each detected non-metallic inclusion was automatically determined in the analyzed area. Then, the number density and average size of inclusions were calculated. In the present investigation, the analyzed area of each specimen was more than 100 mm². The total oxygen content and nitrogen content of steel samples were determined by fusion and the infrared absorption method. The acid-soluble [Al]_s, [Ca], and [Mg] content in tinplate steel samples were analyzed by ICP-AES method.

Table 1 Chemical compositions of steel samples at different stages (mass%)

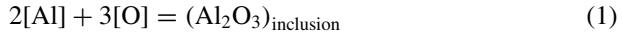
Sample	[C]	[Si]	[Mn]	[P]	[S]	[Al]s	[Ca]	[Mg]	T.O	[N]
S1	0.0420	0.0010	0.1370	0.0170	0.0080	0.0520	0.0013	0.0003	0.0048	0.0018
S2	0.0300	0.0026	0.1600	0.0200	0.0080	0.0360	0.0024	0.0010	0.0037	0.0013

Results and Discussion

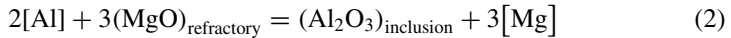
Chemical Compositions of Steel and Slag

The chemical compositions of molten steel samples at different stages are shown in Table 1. The content of oxygen was 450 ppm before Al addition during the RH refining process.

The content of [N] was 0.0013% in S2, indicating that RH has a strong ability to remove nitrogen. Besides, T.O is reduced to 0.0037% after RH refining treatment, and we can conclude that RH also has a strong ability to remove inclusions because TO is mainly in the form of inclusions. The content of [Al]s decreased by 0.016% in this process, and the reaction can be written as Eq. (1), which would generate Al_2O_3 inclusions in steel [3].



At the beginning of RH refining, the oxygen content was so high that the content of dissolved Ca and Mg can be considered as zero. But after Al addition, CaO in the slag and MgO in the refractory could be reduced by Al and generate dissolved Ca and Mg in liquid steel as Eqs. (2) and (3). With the progress of smelting, the content of [Ca] and [Mg] in S2 increased compared with those in S1. The content of [Ca] and [Mg] in S2 is 0.0024% and 0.0010%.



Evolution of Inclusions During RH Refining Process

Morphology of Typical Inclusions

SEM-mappings of typical inclusions morphology and the main chemical composition in S1 are shown in Fig. 2. They were Al_2O_3 in cluster shape with size more

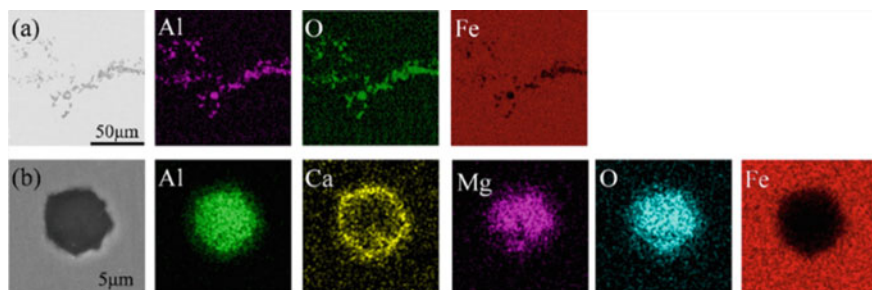


Fig. 2 SEM mapping of typical inclusions in S1. **a** Al_2O_3 inclusion; **b** $\text{CaO-MgO-Al}_2\text{O}_3$ inclusion. (Color figure online)

than $50\ \mu\text{m}$, as shown in Fig. 2a and $\text{CaO-MgO-Al}_2\text{O}_3$ ternary system in spherical morphology, as shown in Fig. 2b.

As can be seen from Fig. 2b, the components of CaO , MgO , and Al_2O_3 were different from the spinel. The components of CaO , MgO , and Al_2O_3 in the inclusion were not uniform. These inclusions had an outside layer that contained higher CaO but less MgO , while the inner part of the inclusion contained high MgO and Al_2O_3 but less CaO content. This indicates that the reduction reaction of $[\text{Ca}]$ with $\text{MgO-Al}_2\text{O}_3$ system inclusions proceeded from outside to inside and finished the transformation of the inclusions from $\text{MgO-Al}_2\text{O}_3$ system to $\text{CaO-MgO-Al}_2\text{O}_3$ ternary system with a relatively lower melting point. Figure 2b shows the elemental mapping of a $5\ \mu\text{m}$ $\text{CaO-MgO-Al}_2\text{O}_3$ inclusion.

SEM-mappings of typical inclusions morphology and the main composition in S2 are shown in Fig. 3. They were Al_2O_3 as shown in Fig. 3a; $\text{CaO-Al}_2\text{O}_3$ system mainly in spherical shape with size larger than $10\ \mu\text{m}$ as shown in Fig. 3b; $\text{MgO-Al}_2\text{O}_3$ system mainly in abnormal shape with size larger than $5\ \mu\text{m}$ as shown in Fig. 3c; $\text{CaO-MgO-Al}_2\text{O}_3$ ternary system in spherical morphology with size larger than $10\ \mu\text{m}$ as shown in Fig. 3d. A comparison of Figs. 2b and 3d shows that the composition of the inclusion gradually homogenized as melting time increased.

Number and Composition Distribution of Inclusions

To better understand the transformation process of inclusions at different stages, the composition distribution of inclusions in S1 and S2 was projected in $\text{CaO-MgO-Al}_2\text{O}_3$ ternary, as shown in Fig. 4a, b. Inclusions with sizes classified into four grades $2\ \mu\text{m} < D \leq 5\ \mu\text{m}$, $5\ \mu\text{m} < D \leq 10\ \mu\text{m}$, $10\ \mu\text{m} < D \leq 15\ \mu\text{m}$, $15\ \mu\text{m} < D$ were analyzed, respectively. The area surrounded by the black line is a lower melting temperature zone ($<1873\ \text{K}$) calculated by FactSage 7.0. In the current work, vacuum treatment lasted for 20 min and the liquid steel was gently stirred for 5 min by argon to promote the inclusions floating upward during RH refining process. The number density of inclusions was defined by Eq. (4).

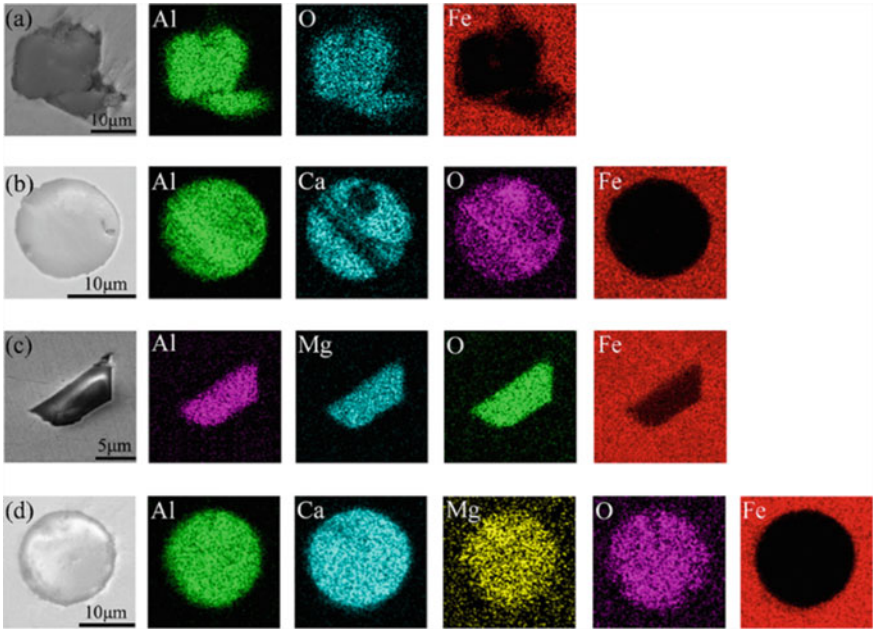


Fig. 3 SEM mapping of typical inclusions in S2 **a** Al₂O₃ inclusion; **b** CaO–Al₂O₃ inclusion; **c** MgO–Al₂O₃ inclusion; **d** CaO–MgO–Al₂O₃ inclusion. (Color figure online)

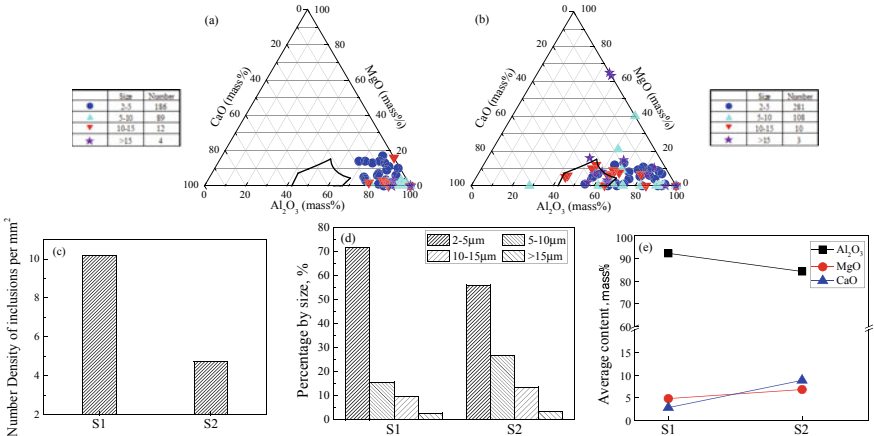


Fig. 4 Composition distribution of the inclusions in S1 and S2. **a** S1; **b** S2; **c** Number density of inclusions; **d** percentage by size; **e** average content of inclusions. (Color figure online)

$$ND = \frac{n}{A_{\text{total}}} \quad (4)$$

where ND is the number density of inclusions, A_{total} is the total area scanned (mm^2), and n is the number of detected inclusions with size $\geq 2 \mu\text{m}$ on A_{total} of steel sample.

It can be seen from Fig. 4c, d, there were 290 inclusions in the scanning area of 125 mm^2 for S1 and 402 inclusions in the scanning area of 130 mm^2 for S2. It can be calculated that ND increased from 9.32 to 4.09 per mm^2 from S1 to S2, indicating that the Al addition generated more oxide inclusions even though RH vacuum treatment has a great potential to remove inclusions.

The average composition of inclusions in S1 and S2 is given in Fig. 4e. It shows that the [Ca] and [Mg] content in the steel slightly decreased from S1 to S2, the contents of CaO and MgO in inclusions increased, while Al_2O_3 content decreased. Some Al_2O_3 inclusions in molten steel were transformed into CaO–MgO– Al_2O_3 system inclusions with a relatively lower melting point in S2. These kind of inclusions were liquid at the temperature of steel-making and easily float upward to be removed through collision and coalescence. However, Al_2O_3 inclusions can be hardly fully modified into CaO– Al_2O_3 inclusions or CaO–MgO– Al_2O_3 system inclusions.

Thermodynamic Calculation for the Formation of Inclusions

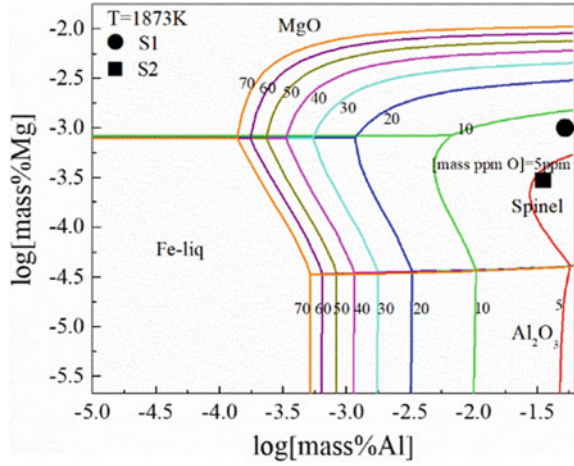
Thermodynamic calculations were carried out to explain the formation of inclusions. In these calculations, the interaction coefficients are listed in Table 2, and the chemical compositions of samples are given in Table 1.

The standard states in this article chosen for activities of the oxides in the inclusions were taken relative to the pure solid using molar fraction units, while the elements activities in liquid steel were taken relative to a dilute solution using mass percent units. The activity of element i can be calculated from Eq. (5). Meanwhile, the activity of dissolved oxygen in liquid steel after Al addition was calculated from Eq. (1). When Al was added to the steel after recycling degassing for 3 min in RH furnace, Al–O deoxidization reaction occurred so fast that the dissolved oxygen content would be very low in the refining process and the dissolved oxygen content was considered as 3 ppm in the following calculations.

Table 2 Interaction coefficients used in thermodynamic calculations at 1873 K [14–17]

J	C	Si	Mn	S	P	Al
i						
Ca	−0.34	−0.097	−0.0156	−336	−0.097	−0.072
Mg	−0.15	−0.09	/	−1.38	/	−0.12
Al	0.091	0.0056	0.035	0.030	0.033	0.045
O	−0.436	−0.131	−0.021	−0.133	0.07	−1.17

Fig. 5 Phase stability diagram of MgO–MgO·Al₂O₃–Al₂O₃. (Color figure online)

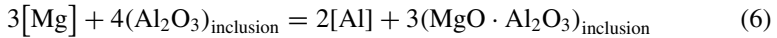


$$\log a_{[i]} = \sum e_i^j [\text{mass}\%j] + \log [\text{mass}\%i] \quad (5)$$

In Eq. (5), e_i^j is the interaction coefficient of element j to i , while $a_{[i]}$ is the activity of constituent $[i]$ in liquid steel.

Formation of MgO·Al₂O₃ Spinel Inclusions

As the dissolved Mg was generated in liquid steel, Al₂O₃ would react with [Mg] to form MgO·Al₂O₃ spinel inclusions, as shown in Eq. (6) [18].



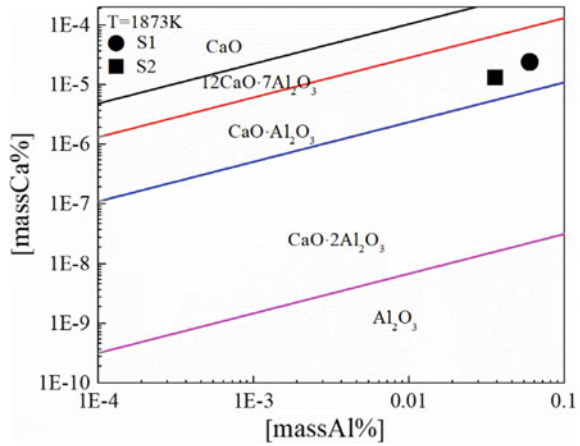
$$\log K_6 = 34.37 - 46950/T \quad (7)$$

Figure 5 shows the phase stability diagram of MgO–MgO·Al₂O₃–Al₂O₃ with different [O] contents. This figure indicates that dissolved Al and Mg contents in S1 and S2 are in the region of MgO·Al₂O₃ formation, which can explain the observation of MgO·Al₂O₃ inclusions in this study as shown in Fig. 3c.

Formation of CaO–MgO–Al₂O₃ Ternary System Inclusions

Inclusions of CaO–MgO–Al₂O₃ ternary system could be easily observed in S1 and S2. CaO in the slag could be reduced by [Al] as shown by Eq. (3) and the reduced products [Ca] diffused from the slag-metal interface to the molten steel. When [Ca]

Fig. 6 Phase stability diagram of $\text{CaO-xCaO}\cdot\text{yAl}_2\text{O}_3\text{-Al}_2\text{O}_3$. (Color figure online)



content increased to a certain level, it would react with $\text{MgO-Al}_2\text{O}_3$ system inclusions. This was mainly due to the reaction between dissolved $[\text{Ca}]$ and $\text{MgO-Al}_2\text{O}_3$ inclusions as expressed by Eq. (8). Finally, $\text{CaO-MgO-Al}_2\text{O}_3$ ternary system inclusions tend to form calcium alumina inclusions. Among all the calcium alumina inclusions, $\text{CaO}\cdot\text{Al}_2\text{O}_3$, $12\text{CaO}\cdot 7\text{Al}_2\text{O}_3$ and $3\text{CaO}\cdot\text{Al}_2\text{O}_3$ are liquid phase at 1873 K. Based on [19], the evolution route of calcium alumina inclusions was described as $\text{CaO}\cdot 2\text{Al}_2\text{O}_3 \rightarrow \text{CaO}\cdot\text{Al}_2\text{O}_3 \rightarrow 12\text{CaO}\cdot 7\text{Al}_2\text{O}_3$. In the calculations, the composition of the molten steel was taken from S2. To analyze the formation and evolution of calcium alumina inclusions, the stability phase diagram of various calcium aluminates was calculated as shown in Fig. 6.

Figure 6 shows the calculated phase stability diagram of $\text{CaO-xCaO}\cdot\text{yAl}_2\text{O}_3\text{-Al}_2\text{O}_3$. This figure indicates that the contents of dissolved Ca and Al in liquid steel are in the region of $\text{CaO}\cdot\text{Al}_2\text{O}_3$ formation. In this study, $\text{CaO}\cdot\text{Al}_2\text{O}_3$ was chosen as the liquid phase for the calculations of phase stability between $\text{MgO}\cdot\text{Al}_2\text{O}_3$ and $\text{CaO}\cdot\text{Al}_2\text{O}_3$. And the boundary between these two phases was calculated by Eq. (8) - (9).

$$[\text{Ca}] + (\text{MgO} \cdot \text{Al}_2\text{O}_3)_{\text{inclusion}} = (\text{CaO} \cdot \text{Al}_2\text{O}_3)_{\text{inclusion}} + [\text{Mg}] \tag{8}$$

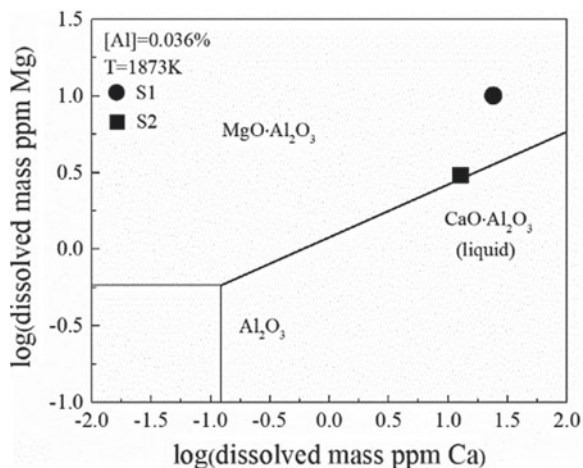
$$\log K_8 = -0.40 + 2476/T \tag{9}$$

The boundary between Al_2O_3 and $\text{CaO}\cdot\text{Al}_2\text{O}_3$ was calculated by (10)–(11).

$$3[\text{Ca}] + 4(\text{Al}_2\text{O}_3)_{\text{inclusion}} = 3(\text{CaO} \cdot \text{Al}_2\text{O}_3)_{\text{inclusion}} + 2[\text{Al}] \tag{10}$$

$$\log K_{10} = 33.17 + 39532/T \tag{11}$$

Fig. 7 Phase stability diagram of $\text{MgO}\cdot\text{Al}_2\text{O}_3$ – $\text{CaO}\cdot\text{Al}_2\text{O}_3$ – Al_2O_3



Besides, according to Eqs. (6) and (7) the boundary between $\text{MgO}\cdot\text{Al}_2\text{O}_3$ and Al_2O_3 could be calculated as above. In the above calculations, the activities of $\text{MgO}\cdot\text{Al}_2\text{O}_3$ and $\text{CaO}\cdot\text{Al}_2\text{O}_3$ in Eq. (8) and Al_2O_3 in Eq. (10) were considered as unity, and the other thermodynamic parameters were calculated from Table 2 and Eq. (5). The phase stability diagram of $\text{MgO}\cdot\text{Al}_2\text{O}_3$ – $\text{CaO}\cdot\text{Al}_2\text{O}_3$ – Al_2O_3 is shown in Fig. 7.

It can be seen that $\text{MgO}\cdot\text{Al}_2\text{O}_3$ phase was stable after Al addition, while low melting point inclusion was more stable at the end of RH refining. Even though the dissolved Ca content in S2 is 18 ppm, calcium alumina inclusion with a low melting point would be generated. Meanwhile, it also implies that the calculation shown in Fig. 6 is reasonable.

From the CaO – MgO – Al_2O_3 ternary phase diagram, it can be concluded that a little amount of MgO could expand the liquid region [20]. So most of CaO – MgO – Al_2O_3 system inclusions may be in the liquid phase before turning into CaO – Al_2O_3 system inclusions. The shapes of CaO – MgO – Al_2O_3 system inclusions would become spherical. As the reaction goes on, the spheroidize degree of inclusions increased, but the composition of all inclusions was not in the liquid region during RH refining process as shown in Fig. 4a, b.

Modification of RH Refining Slag

Because of the complex chemical slag–steel and steel–refractory reactions, the compositions of RH refining slag have a vital influence on inclusions in tinplate steel. The formation and evolution of inclusions in tinplate during RH refining process were studied. CaO in the slag and MgO in the refractory can be reduced by Al in the molten steel, as shown in Eqs. (2) and (3), resulting in the rise of $[\text{Ca}]$ and $[\text{Mg}]$ in molten

steel and the increase of CaO average content in inclusions. The composition of inclusions was controlled by modifying the composition of RH refining slag.

The effect of CaO/Al₂O₃ mass ratio (*C/A*) of RH refining slag was studied by thermodynamic software FactSage 7.0. 12CaO·7Al₂O₃ is the lowest melting point among all kinds of CaO–Al₂O₃ oxides. As a result, it was probable that 12CaO·7Al₂O₃ can be formed after CaO modification addition in the refining slag. From Fig. 6, it can be pointed out that the inclusion of CaO–Al₂O₃ system inclusions was CaO·Al₂O₃ with *C/A* mass ratio 0.55, by contrast, *C/A* mass ratio of 12CaO·7Al₂O₃ was 0.94. According to industrial tests, Al₂O₃ inclusions content of S2 was above 84 mass pct. Most of Al₂O₃ inclusions cannot transform into CaO–Al₂O₃ or CaO–MgO–Al₂O₃ inclusions with a lower melting point. The low *C/A* mass ratio of RH refining slag after Al deoxidation is the key reason. Chemical compositions of RH refining slag with CaO modification in different *C/A* mass ratios are listed in Table 3.

Figure 8 shows the composition distributions of RH refining slag in CaO–Al₂O₃–SiO₂ ternary phase diagram. Before Al deoxidation addition during RH refining process, RH refining slag was located in the region 3CaO·Al₂O₃ with *C/A* mass ratio 1.72. Through theoretical calculations, the dissolved oxygen content in steel was reduced to 0 ppm when Al was added into the steel. All the Al₂O₃ products float up into the refining slag. The composition of RH refining slag was located in the region of CaO·2Al₂O₃ with *C/A* mass ratio 0.39.

CaO modification operation should be added during RH refining process in order to obtain inclusions with low melting point, while considering the melting point and viscosity of the final slag. To optimize the composition of inclusions in tinplate steel, the melting point and viscosity of RH refining slag with CaO modification was studied by FactSage thermodynamic software and reasonable control condition of refining slag was obtained, as shown in Fig. 9. With the rise of *C/A* mass ratio, the melting point and viscosity of RH refining slag decreases at first and then increases. At a *C/A* mass ratio of 1.10, both the melting point and viscosity are the lowest. As a result, with slag-steel reaction, [Ca] in steel would increase, CaO content of inclusions would increase, and more Al₂O₃ inclusions would transform into 12CaO·7Al₂O₃ with a low melting point.

Table 3 Chemical compositional of RH refining slag under different *C/A* ratios (mass%)

Process	<i>C/A</i>	CaO	Al ₂ O ₃	SiO ₂
Before Al deoxidation	1.72	57.33	33.33	9.33
After Al deoxidation	0.39	26.70	68.96	4.35
CaO modification	0.6	36.08	60.13	3.79
	0.8	42.94	53.68	3.38
	1.0	48.47	48.47	3.06
	1.1	50.85	46.23	2.91
	1.2	53.03	44.19	2.79
	1.3	55.01	42.32	2.67

- (1) During the RH refining process, Al_2O_3 inclusions were mainly generated after Al addition. With the slag-steel and refractory-steel reactions, the evolution routes of inclusions were described as Al_2O_3 inclusions \rightarrow $\text{CaO-Al}_2\text{O}_3$ system inclusions \rightarrow $\text{CaO-MgO-Al}_2\text{O}_3$ system inclusions and Al_2O_3 inclusions \rightarrow $\text{MgO-Al}_2\text{O}_3$ spinel inclusions \rightarrow $\text{CaO-MgO-Al}_2\text{O}_3$ system inclusions. From the mapping photos of inclusions, it can be concluded that the formation of $\text{CaO-MgO-Al}_2\text{O}_3$ system inclusions was Ca element substitution for Mg element in $\text{MgO-Al}_2\text{O}_3$ spinel inclusions.
- (2) From Al addition to the end of RH refining, the number density of inclusions increased from 9.32 to 4.09 per mm^2 . T.O could be decreased from 450 to 37 ppm. The size of inclusions varied mainly less than 10 μm , the proportion of inclusions with size less than 5 μm gradually decreased by 15% and inclusions in the range of 5–10 μm increased by 10%. These inclusions with size less than 10 μm were difficult to be removed from liquid steel through the floatation.
- (3) A new strategy for modifying inclusions in tinplate steel was suggested, in which the key reason was low C/A of the final refining slag. In order to obtain the $\text{CaO-Al}_2\text{O}_3$ inclusion with a lower melting point, CaO modification should be added during the RH refining process. The reasonable C/A mass ratio of the final RH refining slag determined through theoretical calculations was 1.10.

Acknowledgements This work was supported by National Key R&D Program of China [Grant numbers 2016YFB0300602, 2017YFB0304201 and 2017YFB0304203] and National Natural Science Foundation of China [Grant numbers 51774072, 51774073 and 51974080].

References

1. Kaushik P, Lowry M, Yin H, Piolet H (2012) Inclusion characterisation for clean steelmaking and quality control. *Ironmaking Steelmaking* 39(4):284–300
2. Deng ZY, Zhu MY (2013) Evolution mechanism of non-metallic inclusions in Al-killed alloyed steel during secondary refining process. *ISIJ Int* 53(3):450–458
3. Yang GW, Wang XH, Huang FX, Wang WJ, Yin YQ, Tang C (2014) Influence of reoxidation in tundish on inclusion for Ca-treated Al-killed steel. *Steel Res Int* 85(5):784–792
4. Li SJ, Cheng GG, Miao ZQ, Dai WX, Chen L, Liu ZQ (2018) Evolution of oxide inclusions in G20CrNi2Mo carburized bearing steel during industrial electroslag remelting. *ISIJ Int* 58(10):1781–1790
5. Park JH, Todoroki H (2010) Control of $\text{MgO-Al}_2\text{O}_3$ spinel inclusions in stainless steels. *ISIJ Int* 50(10):1333–1346
6. Park JH, Lee SB, Gaye HR (2008) Thermodynamics of the formation of $\text{MgO-Al}_2\text{O}_3\text{-TiO}_x$ inclusions in Ti-stabilized 11Cr ferritic stainless steel. *Metall Mater Trans B* 39(6):853–861
7. Kang YJ, Li F, Morita K, Du SC (2006) Mechanism study on the formation of liquid calcium aluminate inclusion from $\text{MgO-Al}_2\text{O}_3$ spinel. *Steel Res Int* 77(11):785–792
8. Jiang M, Wang XH, Chen B, Wang WJ (2008) Formation of $\text{MgO-Al}_2\text{O}_3$ inclusions in high strength alloyed structural steel refined by $\text{CaO-SiO}_2\text{-Al}_2\text{O}_3\text{-MgO}$ slag. *ISIJ Int* 48(7):885–890

9. Jiang M, Wang XH, Chen B, Wang WJ (2010) Laboratory study on evolution mechanisms of non-metallic inclusions in high strength alloyed steel refined by high basicity slag. *ISIJ Int* 50(1):95–104
10. Jiang M, Wang XH, Chen B, Wang WJ (2012) Study on refining slags targeting high cleanliness and lower melting temperature inclusions in Al killed steel. *Ironmaking Steelmaking* 39(1):20–25
11. Jiang M, Wang XH, Wang WJ (2010) Control of non-metallic inclusions by slag-metal reactions for high strength alloying steels. *Steel Res Int* 81(9):759–765
12. Zhang LF, Thomas BG (2003) State of the art in evaluation and control of steel cleanliness. *ISIJ Int* 43(3):271–291
13. Shi CB, Chen XC, Guo HJ, Zhu ZJ, Ren H (2012) Assessment of oxygen control and its effect on inclusion characteristics during electroslag remelting of die steel. *Steel Res Int* 83(5):472–486
14. Suito H, Inoue R (1996) Thermodynamics on control of inclusions composition in ultraclean steels. *ISIJ Int* 36(5):528–536
15. Sigworth GK, Elliott JF (1974) The thermodynamics of liquid dilute iron alloys. *Metal Sci* 8(1):298–310
16. Ohta H, Suito H (1996) Activities in CaO–MgO–Al₂O₃ slags and deoxidation equilibria of Al, Mg, and Ca. *ISIJ Int* 36(8):983–990
17. Itoh H, Hino M, Ban-ya S (1997) Assessment of Al deoxidation equilibrium in liquid iron. *Tetsu-To-Hagané* 83(12):773–778
18. Kishi M, Inoue R, Suito H (1994) Thermodynamics of oxygen and nitrogen in liquid Fe-20mass%Cr alloy equilibrated with titania-based slags. *ISIJ Int* 34(11):859–867
19. Zhao DW, Li HB, Bao CL, Yang J (2015) Inclusion evolution during modification of alumina inclusions by calcium in liquid steel and deformation during hot rolling process. *ISIJ Int* 55(10):2115–2124
20. Ren Y, Zhang LF (2016) Thermodynamic model for prediction of slag-steel-inclusion reactions of 304 stainless steels. *ISIJ Int* 57(1):68–75

Flotation of Molybdenite in the Presence of Sheared Polyacrylamide Flocculants



Luver Echeverry, Darwin Estrada, and Leopoldo Gutierrez

Abstract Flocculants type polyacrylamide (PAM) plays an important role in mineral processing circuits. It is common practice to reuse water from the thickening stages to other unit operations such as grinding and flotation. In the case of molybdenite flotation, an important depressing effect on mineral particles has been demonstrated by the residual flocculant dissolved in the recycled water. The aim of this work was to evaluate the effect of the degradation of a PAM type of flocculant on the flotation recovery of molybdenite. The study considered experiments of microflotation, adsorption isotherms, electrophoretic mobility, and intrinsic viscosity measurements. Molecular dynamic simulations were used to look for mechanisms of interactions between PAM and molybdenite. The results showed that molybdenite recovery was less affected by the flocculant when PAM molecules were subjected to more intense conditions of mechanical shearing. This behavior is related to the adsorption of flocculant on the mineral and the disposition and shape anisotropy of the flocculant chains.

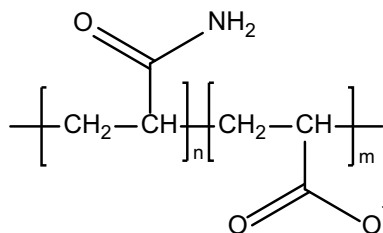
Keywords Flotation · Molybdenite · Polyacrylamides · Shearing

Introduction

The efficiency of mineral separation processes depends on the quality of water. New water suitable for processing is limited, especially in northern Chile, where there are intense mineral exploitation activities [1, 2]. Consequently, wastewater from processing plants must have closed circuits in which the process water is recycled again. As a result of this operational practice, an important part of residual reagents dissolved in water is recirculated to flotation, causing flotation depression of some important minerals such as molybdenite [3].

L. Echeverry (✉) · D. Estrada · L. Gutierrez
Department of Metallurgical Engineering, Universidad de Concepcion, Concepcion, Chile
e-mail: lecheverry@udec.cl

Fig. 1 Chemical structures of anionic polyacrylamide



Most of the flocculants used in mineral processing are high molecular weight polymers based on polyacrylamide. Polyacrylamide (PAM) is substantially a non-ionic uncharged polymer. However, industrial polyacrylamides are hydrolyzed to produce a series of acrylic units along the main chain. These acrylic units containing carboxylic groups make such copolymers weak to moderately anionic [4]. Figure 1 shows the chemical structure of anionic polyacrylamide.

The effectiveness of a flocculant is strongly influenced by the properties of the solution in which the polymer molecules are dissolved. The flocculant adsorption and the bridging process between the particles depend not only on the interactions with the mineral surface, but also on the molecular weight, the degree of anionicity and the conformation that the flocculant molecules take in a particular electrolyte solution [5, 6]. Applying excessive shear to high molecular weight flocculants can lead to chain breakage, substantially reducing bridging ability [7].

The main objective of this study is to investigate the effect of the presence of a polyacrylamide-type flocculant with a low degree of anionicity with three levels of degradation in the flotation of molybdenite in different conditions of concentration and pH.

Materials and Methods

Flocculant Preparation, Characterization, and Degradation

The flocculant used in this work was a polyacrylamide type, provided by SNF CHILE S.A. The sample was received as dry white granules and used without any further treatment or purification. According to the information provided by the manufacturer, this flocculant is anionic, high molecular weight, and low degree of anionicity. Flocculant preparation was done in a daily basis during the experimental program following the procedure described by Arinaitwe [4]. Three levels of mechanical shear degradation were considered: non sheared flocculant (NS-FLOC), moderately sheared flocculant (MS-FLOC)m and strongly sheared flocculant (SS-FLOC). Flocculant shearing was achieved using a 40 mm diameter bladed stirrer which was inserted into 100 mL of a 0.35 g/L flocculant fresh solution. The MS-FLOC was

obtained by shearing for 30 min at 500 rpm, and the SS-FLOC was obtained by shearing for 3 h at 2000 rpm.

Fourier transform infrared (FTIR) spectra of the flocculant was obtained using a PerkinElmer 2000 FTIR spectrophotometer. The sodium and total organic carbon (TOC) concentration in the flocculant was measured using a PerkinElmer Optima 5300 DV ICP-OES and a Shimadzu TOC-L, respectively. The degree of anionicity (DA) of the flocculant under study was determined according to the electroneutrality criterion of polyelectrolyte solutions [4]. The DA of the flocculant can be obtained from the following expression:

$$DA = \left(\frac{\text{Moles } COO^-}{(\text{Moles } TOC)/3} \right) * 100\% \quad (1)$$

Intrinsic viscosity ($[\eta]$) measurements were carried out in order to evaluate the degree of mechanical degradation of the flocculant. The method proposed by Fedors [8] and validated by Rao [9] and Ghimici and Popescu [8] was used to describe the viscosity of PAM. The intrinsic viscosity measurements were done following the procedure described by Klein and Conrad [9], i.e., 0.5 M NaCl and 25 °C, and at natural pH. Solution viscosities (η) were measured using a Cannon-Fenske 200 viscometer at different flocculant concentrations.

Samples and Reagents

The molybdenite sample used in this study was obtained after several collectorless flotation cleaning stages from an industrial molybdenite concentrate. The final sample is obtained after three washing steps with sodium hydrosulfide (NaSH) and acetone to remove residual flotation collectors and other organic reagents. The elimination of organic reagents was verified by analyzing the content of total organic carbon (TOC) of the liquid extracts obtained at different pH values, which did not show the presence of TOC, so it can be said that there was no presence of flotation reagents [10, 11]. Chemical analysis of the molybdenite sample shows a purity of 99.34%, with a chemical composition of 59.6% Mo and 39.8% S. The particle size of the molybdenite sample used in this study was in the range of $-150 + 45 \mu\text{m}$. The oxidation of the molybdenite samples was reduced following the procedure established by Ansari and Pawlik [12, 13] in which the ore samples were stored at 1 °C in sealed plastic bags previously blown with nitrogen. Methyl isobutyl carbinol (MIBC) obtained from Merck was used as frother. Sodium hydroxide (NaOH) obtained from Merck was used as pH modifier. A 0.01 M NaCl solution prepared using Milli-Q water of 18.2 M Ω cm at 25 °C and a chloride salt of sodium (Merck) was used as aqueous medium in the tests.

Microflotation Test

Molybdenite flotation was assessed by microflotation tests in a 150 mL Partridge and Smith glass cell with nitrogen gas at 80 mL/min. The experiments were done using 1 g of molybdenite which was initially conditioned for 2 min in 100 mL of solution containing the PAM reagent (nonsheared and sheared) at varying concentrations (2.5, 5.0, 7.5, and 10.0 ppm) and pH. Then, 25 ppm of MIBC were added along with 50 mL of solution to complete the volume of the microflotation cell and, lastly, mixed for additional 3 min. Then, the process of flotation was performed for 2 min, removing the froth every 10 s. The pulp level in the cell was controlled by adding a solution prepared at the same composition and pH of the original solution. Finally, concentrates and tailings were dried in an oven at 105 °C for 5 h, and molybdenite recovery was calculated as the ratio between the mass of molybdenite in the concentrate, and the mass in the concentrate plus the mass in the tailings. All tests were done in triplicate, and the results presented in the manuscript are average values with the error bars representing a standard deviation.

Adsorption Test

Adsorption of NS-FLOC, MS-FLOC, and SS-FLOC on molybdenite was measured through tests in which 1 g of molybdenite was mixed for 15 min with 150 mL of flocculant solutions of known concentrations. The suspensions were centrifuged, and the filtrate was analyzed for TOC, readings which were translated to flocculant concentrations through a calibration curve. The masses of adsorbed flocculant on molybdenite were calculated as the difference between the initial and final concentrations multiplied by the volume of solution (150 mL). Then, specific adsorption was calculated in mg of flocculant adsorbed per gram of molybdenite (mg/g) and the isotherm was drawn. Temperature was controlled all the time in these experiments by using a thermostatic bath, and the tests were done in duplicates with an average standard error of 4%.

Electrophoretic Mobility and Aggregation Measurements

Molybdenite and flocculant interactions were assessed through electrophoretic mobility measurements using a Zetacompact Z9000 from CAD instrument –20 microns molybdenite particles were tested, and the effects of pH and PAM changes were also studied.

Molecular Dynamics Simulation

PAM solution models were created using the package Materials Studio 2017 (Accelrys Inc., San Diego, CA), The PAM chain was composed of 20 repeating units of acrylamide monomers, of which 8% of the monomers were randomly replaced by sodium carboxylate monomers. The behavior of two PAM chains in aqueous solution was studied using molecular dynamics simulations with the package LAAMPS. (large-scale atomic/molecular massively parallel simulator) [14] at different concentrations of NaOH and at 298 K, employing periodic boundary conditions. For the PAM chain, the force field OPLS-AA was used (all-atom optimized potentials for liquid simulations). The SPC/E water model was used to describe the water. For the ions, 12–6 the Lennard–Jones parameters from Li and Mertz [15] were used. Then, the PAM molecules were embedded in a cube box of $6 \times 6 \times 5$ nm, and then the ions were distributed in random positions, while maintaining a separation distance of 0.3 nm between the atoms. Finally, 5000 water molecules were added to the system. The system initially was simulated in an NVT run for 100 ps at 298 K, and the system was then annealed in an NpT run to accelerate its equilibration avoiding the formation of metastable states; during this stage, the temperature was kept at 298 K. The production step was then performed in an NVT simulation run of 40 ns at 300 K. The data was collected after 6 ns.

Results

Flocculant Characterization

Figure 2 shows the FTIR spectrum of the flocculant under study. This spectrum was obtained using a solid polyacrylamide sample supported on a KBr disk, and it shows the different transmission bands corresponding to the different vibrational modes associated with the functional groups of polyacrylamide (PAM) reported by Sundaraganesan [16]. The analysis will focus on the amino groups (NH_2), carbonyl ($\text{C} = \text{O}$), acrylate (COO^-), and the C-N bond of the amide group (CONH_2). The IR band at 3424 cm^{-1} arises from the asymmetric stretching vibration of the NH_2 group, the band at 3189 cm^{-1} corresponds to the symmetric stretching vibration of the NH_2 group, the band at 1653 cm^{-1} is from the stretching vibration of the bond $\text{C} = \text{O}$ in $-\text{CONH}_2$, the band at 1406 cm^{-1} indicates the stretching vibration of the CN bond, and the band present at 1551 cm^{-1} is attributed to acrylate (COO^-).

The TOC analysis of the flocculant sample indicates that the amount of carbon is close to 720 mg/L, and the ICP-OES analysis reveals that the sodium concentration in the flocculant is 37.5 mg/L; the sodium content in the flocculant sample is high indicating that this flocculant is sodium; therefore, using Eq. 1, the degree of anionicity of the flocculant is equivalent to 8%, value similar to that reported by Deng et al. [17]. Intrinsic viscosities of the NS-FLOC, MS-FLOC, and SS-FLOC were

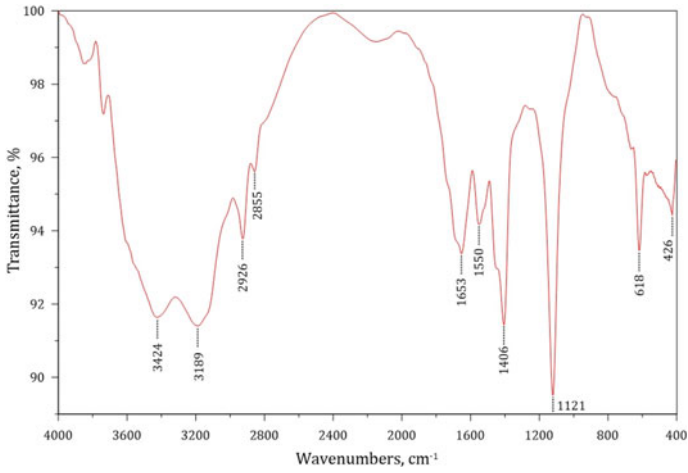
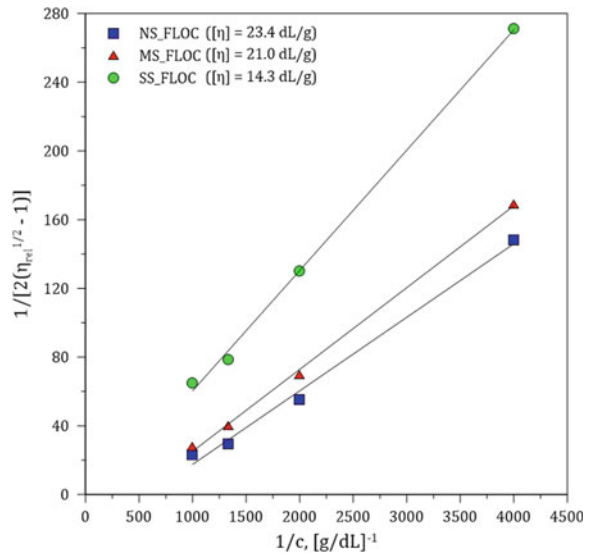


Fig. 2 FTIR spectrum of the sample of flocculant. (Color figure online)

obtained from method proposed by Fedors [8] as shown in Fig. 3. The insert shows the obtained intrinsic viscosities. As expected, shearing has a significant effect on the viscosity of the flocculant.

Fig. 3 Plots of the left side of Eq. 2 vs $1/c$ obtained for NS-PAM, MS-PAM, and SS-PAM. (Color figure online)



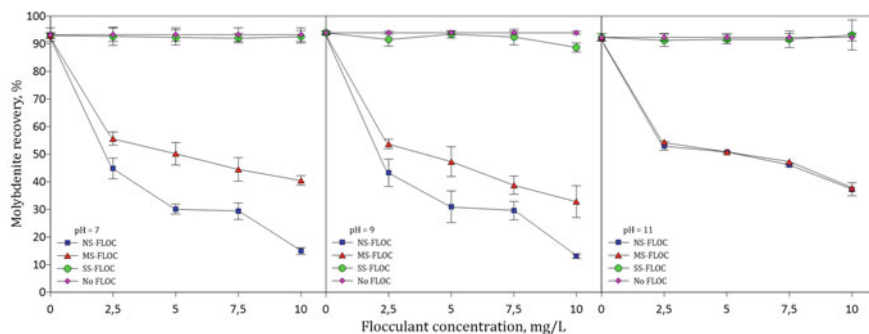


Fig. 4 Effect of flocculant concentration at different degradation conditions at pH of 7, 9, and 11 on the recovery of molybdenite. (Color figure online)

Microflotation

Figure 4 microflotation shows the recovery of molybdenite as a function of the concentration of flocculant NS-FLOC, MS-FLOC, and SS-FLOC at pH 7, 9, and 11. The results of molybdenite flotation in the presence of the PAM flocculant subjected to different degrees of mechanical shearing show that the NS-FLOC had the strongest depressing effect on molybdenite flotation followed by the MS-FLOC. The depressing effect of the SS-FLOC is minor.

Adsorption

Figure 5 shows the results of specific adsorption of NS-FLOC, MS-FLOC and SS-FLOC on molybdenite at different values of pH. The results show that the strongest the mechanical shearing of the PAM the more adsorption of the resulting molecules

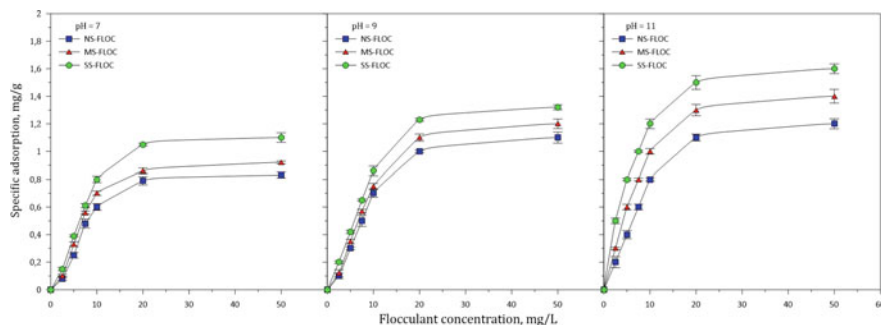


Fig. 5 Adsorption isotherms of NS-FLOC, MS-FLOC, and SS-FLOC on molybdenite at different values of pH. (Color figure online)

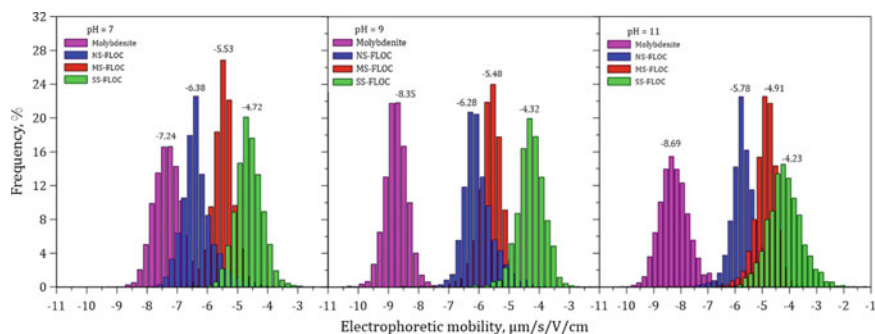


Fig. 6 Electrophoretic mobility distributions of particles of molybdenite in the presence of NS-FLOC, MS-FLOC, and SS-FLOC and at different values of pH. (Color figure online)

on the molybdenite surfaces. The adsorptions of flocculants on molybdenite tend to increase with pH.

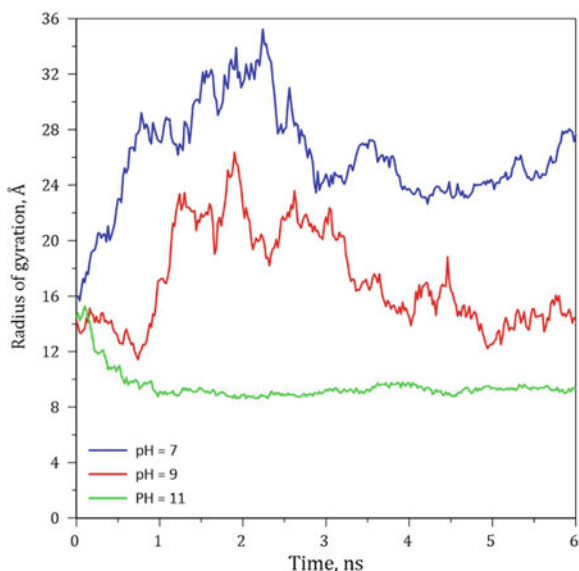
Electrophoretic Mobility

Figure 6 shows the results of electrophoretic mobility distributions of molybdenite in the absence and presence of flocculant, at pH 7, 9, and 11. The results show that the electrophoretic mobility distributions of molybdenite with no flocculant added move toward more negative values as the pH increases which agrees with previous studies [18]. In the presence of flocculant, the electrophoretic mobility distributions move toward less negative values. These experimental results indicate that that PAM flocculants obtained under different shearing conditions slightly reduce the negative surface charge of molybdenite, and that the more sheared the PAM the strongest the neutralizing effect.

Molecular Dynamics Simulation

Figure 7 shows the results of the radius of gyration $R_g = \left(\frac{\sum_i \|r_i\|^2 m_i}{\sum_i m_i} \right)^{1/2}$ of PAM calculated by molecular dynamic simulation at different PH values. The results show that when the pH is increased with NaOH, the radius of gyration of the PAM molecules decreases which agrees with previous studies [19].

Fig. 7 Radius of gyration of polyacrylamide in water at pH 7, 9, and 11. (Color figure online)



Discussion

The effect of different polymers on the flotation process is a subject which is under continuous research. Polymers of different nature and molecular weights have been used as dispersants/depressants, and polymers of high molecular weights have been usually used as flocculants in mineral processing plants. All these polymers are water soluble; thus, they are highly hydrophilic macromolecules which may affect the surface properties of different minerals.

Molybdenite particles are formed by non-polar and highly hydrophobic surfaces called faces and polar and highly hydrophilic surfaces called edges. Therefore, molybdenite can be described as an anisotropic mineral with varying surface properties on the edges and faces. Therefore, the negative surface charge of the molybdenite edges and faces increases with pH which agrees with the experimental data presented in Fig. 6 that show that the electrophoretic mobility distributions move to more negative values as pH is increased from 7 to 11. The microflotation results presented in Fig. 4 indicate that the depressing effect of the NS-FLOC and MS-FLOC on molybdenite flotation slightly increases with pH, which is in agreement with the theory raised regarding the possible interactions between polymers and the hydroxylated metallic sites existing on the mineral surfaces.

Figure 3 shows that shearing induces strong changes on the molecular weights of the flocculant as measured by their intrinsic viscosities. The flotation results presented in Fig. 4 indicate that molybdenite recovery is strongly depressed by the NS-FLOC, and to a lesser extent by MS-FLOC; however, molybdenite flotation is only slightly

affected by SS-FLOC. Castro and Laskowski [3] reported that molybdenite depression by a polyacrylamide flocculant of a DA of 18.1% occurs as other applications in which hydrophobic minerals are depressed by hydrophilic polymer. These authors also indicated that that when PAM molecules are mechanically sheared their depressing effect on molybdenite flotation is maintained and the ability to flocculate quartz particles is lost. The results obtained in this work show that the depressing effect of PAM on the flotation of molybdenite takes place only if this flocculant is sheared at moderate shearing conditions. At strongly shearing conditions, the PAM flocculant has almost no effect on molybdenite flotation.

The adsorption results presented in Fig. 5 indicate that the strongest the shearing the more the resulting molecules adsorb on molybdenite particles. Although the depressing effect of the SS-FLOC on molybdenite flotation is minor, the adsorption of these molecules on the mineral particles is high. In contrast, the adsorption of the NS-FLOC on molybdenite is lower than the adsorption of the MS-FLOC and SS-FLOC, but the observed depressing effect on molybdenite flotation is by far the strongest. The adsorption results correlate with the changes in the electrophoretic mobility distributions presented in Fig. 6 that show that the largest shifts of the distributions are obtained with the MS-FLOC and SS-FLOC.

Figure 7 shows that increasing the pH with NaOH the radius of gyration of the polyacrylamide molecules decreases. These results are a consequence of the neutralization of charges by the sodium ion in the polymer chains; this results in chains less extended and less negative. The simulation of radius of gyration results correlate with the changes in the electrophoretic mobility distributions presented in Fig. 6 that show less negative values with increasing pH.

Conclusions

Based our experimental observations, the following conclusions were drawn:

- Molybdenite flotation is strongly depressed by the NS-FLOC, and to a lesser extent by MS-FLOC; however, molybdenite flotation is only slightly affected by SS-FLOC.
- The results obtained in this work show that the depressing effect of PAM on the flotation of molybdenite takes place only if this flocculant is sheared at moderate shearing conditions. At strongly shearing conditions, the PAM flocculant has almost no effect on molybdenite flotation.
- The strongest the shearing of flocculant, the more the resulting molecules adsorb on molybdenite particles.
- The adsorption results correlate with the changes in the electrophoretic mobility distributions. when the pH is increased, the electrophoretic mobility of molybdenite tends to less negative values in the presence of flocculant.
- Molecular dynamics simulation shows that increasing the pH with NaOH the radius of gyration of the polyacrylamide molecules decreases.

Conflict of Interest The authors declare that they have no conflict of interest.

References

1. Romero H, Méndez M, Smith P (2012) Mining development and environmental injustice in the atacama desert of Northern Chile. *Environ Justice* 5(2):70–76. <https://doi.org/10.1089/env.2011.0017>
2. Oyarzún J, Oyarzún R (2011) Sustainable development threats, inter-sector conflicts and environmental policy requirements in the arid, mining rich, Northern Chile Territory. *Sustain Develop* 19(4):263–274. <https://doi.org/10.1002/sd.441>
3. Castro S, Laskowski JS (2015) Depressing effect of flocculants on molybdenite flotation. *Miner Eng* 74:13–19. <https://doi.org/10.1016/j.mineng.2014.12.027>
4. Arinaitwe E, Pawlik M (2009) A method for measuring the degree of anionicity of polyacrylamide-based flocculants. *Int J Miner Process* 91(1–2):50–54. <https://doi.org/10.1016/j.minpro.2008.12.002>
5. Owen AT, Fawell PD, Swift JD, Farrow JB (2002) The impact of polyacrylamide flocculant solution age on flocculation performance. *Int. J Miner Process* 67(1–4):123–144. [https://doi.org/10.1016/S0301-7516\(02\)00035-2](https://doi.org/10.1016/S0301-7516(02)00035-2)
6. Hogg R (2000) Flocculation and dewatering. *Int J Miner Process* 58(1–4):223–236. [https://doi.org/10.1016/S0301-7516\(99\)00023-X](https://doi.org/10.1016/S0301-7516(99)00023-X)
7. Scott JP, Fawell PD, Ralph DE, Farrow JB (1996) The shear degradation of high-molecular-weight flocculant solutions. *J Appl Polym* 62:2097–2106
8. Ghimici L, Popescu F (1998) Determination of intrinsic viscosity for some cationic polyelectrolytes by Fedors method. *Eur Polym J* 34(1):13–16. [https://doi.org/10.1016/S0014-3057\(97\)00072-4](https://doi.org/10.1016/S0014-3057(97)00072-4)
9. Klein J, Conrad KD (1978) Molecular weight determination of poly(acrylamide) and poly(acrylamide-co-sodium acrylate). *Die Makromol Chemie* 179(6):1635–1638. <https://doi.org/10.1002/macp.1978.021790624>
10. Ramirez A, Gutierrez L, Vega-Garcia LD, Reyes-Bozo L (2020) The depressing effect of Kaolinite on Molybdenite flotation in seawater. *Minerals* 10(6):578. <https://doi.org/10.3390/min10060578>
11. Ramirez A, Gutierrez L, Laskowski JS (2020) Use of ‘oily bubbles’ and dispersants in flotation of molybdenite in fresh and seawater. *Miner Eng* 148:106197. <https://doi.org/10.1016/j.mineng.2020.106197>
12. Ansari A, Pawlik M (2006) Floatability of chalcopyrite and molybdenite in the presence of lignosulfonates. Part I. Adsorption Studies *Miner Eng* 20(6):600–608. <https://doi.org/10.1016/j.mineng.2006.12.007>
13. Ansari A, Pawlik M (2007) Floatability of chalcopyrite and molybdenite in the presence of lignosulfonates. Part II. Hallimond tube flotation. *Miner Eng* 20(6):609–616. <https://doi.org/10.1016/j.mineng.2006.12.008>
14. Plimpton S (1997) Short-range molecular dynamics. *J Comput Phys* 117(6):1–42. <https://doi.org/10.1006/jcph.1995.1039>
15. Li P, Merz KM (2014) Taking into account the ion-induced dipole interaction in the nonbonded model of ions. *J Chem Theory Comput* 10(1):289–297. <https://doi.org/10.1021/ct400751u>
16. Sundaraganesan N, Puvvarasan N, Mohan S (2001) Vibrational spectra, assignments and normal coordinate calculation of acrylamide. *Talanta* 54(2):233–241. [https://doi.org/10.1016/S0039-9140\(00\)00585-3](https://doi.org/10.1016/S0039-9140(00)00585-3)
17. Deng Y, Dixon JB, White GN (2006) Adsorption of Polyacrylamide on Smectite, Illite, and Kaolinite. *Soil Sci Soc Am J* 70(1):297–304. <https://doi.org/10.2136/sssaj2005.0200>

18. Castillo I, Gutierrez L, Hernandez V, Diaz E, Ramirez A (2020) Hemicelluloses monosaccharides and their effect on molybdenite flotation. *Powder Technol* 373:758–764. <https://doi.org/10.1016/j.powtec.2020.07.032>
19. Hirst LS (2012) *Fundamentals of soft matter science*. CRC Press, Boca Raton

Part III
Thermodynamics on Metals and Slags
Processing

Modelling of Metal Loss in Ferromanganese Furnace Tapping Operations



Quinn Gareth Reynolds and Jan Erik Olsen

Abstract During the pyrometallurgical production of industrial metals such as ferromanganese in electric smelting furnaces, molten slag and alloy phases are removed from the unit by tapping at regular intervals. Intermixing of the two phases may occur during the latter stages of the tapping process, and if not carefully managed, it can result in significant alloy being lost to the waste slag by entrainment. This paper presents the results of a computational fluid dynamics study of the multiphase free surface fluid flow in tapping ladles, with a specific focus on the impact of various design and operational parameters on alloy losses to the slag.

Keywords Modelling · Pyrometallurgy · Ferromanganese

Introduction

Manganese is an important commodity with a wide range of applications in the production of clean steels, speciality alloys, and various battery technologies. It is produced commercially in the form of ferromanganese (FeMn) by chemical reaction of ores containing manganese and iron oxides with carbonaceous reductants. This is performed at temperatures in excess of 1400 °C, using blast furnaces or electric smelters [8]. At such temperatures the raw materials and products are in the molten state, and form immiscible metallic (alloy) and oxide-rich (slag) phases.

Smelting furnaces are typically emptied of molten products by a process called *batch tapping*. This involves periodically opening a channel (the tap-hole) in a dedi-

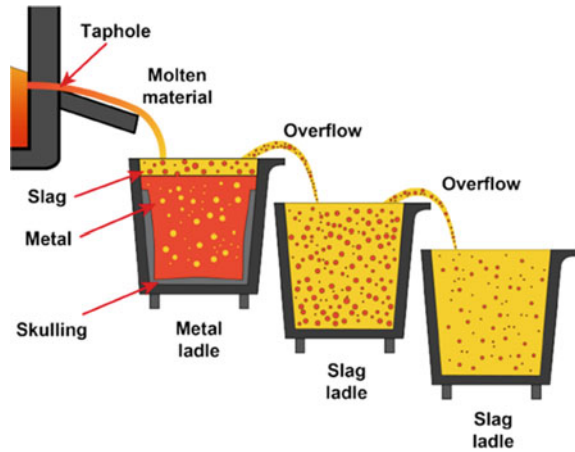
Q. G. Reynolds (✉)
Mintek, Private Bag X3015, Randburg 2125, South Africa
e-mail: quinnr@mintek.co.za

University of Stellenbosch, Private Bag X1, Matieland, Stellenbosch
7602, South Africa

J. E. Olsen
SINTEF Industri, P.O. Box 4760, Torgarden, Trondheim 7465, Norway
e-mail: jan.e.olsen@sintef.no

© The Minerals, Metals & Materials Society 2021
J. Lee et al. (eds.), *Materials Processing Fundamentals 2021*, The Minerals, Metals & Materials Series, https://doi.org/10.1007/978-3-030-65253-1_7

Fig. 1 Ferromanganese tapping process. (Color figure online)



cated section of the vessel sidewall, allowing the contents to drain out, and resealing it [11]. In FeMn processes, slag and alloy are tapped simultaneously through the same tap-hole. After exiting the tap-hole channel, the stream of molten material is directed along open launders and empties into a cascade of storage ladles. During this process, energy is imparted to the stream by turbulence in the flow and impact with solid and liquid surfaces. This causes break-up and intermixing of the slag–alloy phase interface, which is counteracted by settling and separation under gravity over time due to density differences between the slag and alloy phases. The tapping system is shown schematically in Fig. 1.

If too much mixing between the slag and alloy phases occurs, this may result in excessive quantities of valuable alloy product being discarded with the waste slag [1]. The presence of small alloy droplets in discarded slag may also pose environmental risks and can incur significant extra cost if treated downstream by crushing and separation. It is therefore preferable to achieve the best possible separation of the phases during the tapping operation, before they solidify.

Due to the hazardous nature of high-temperature processes, it is often difficult or impossible to obtain sufficient experimental data to perform effective design and optimisation. In this environment, computational modelling in the form of numerical experimentation and virtual prototyping is a particularly useful guidance tool to gain a deeper understanding of the problem, and assess the value of different changes to the design and operation of the tapping system.

A variety of computational fluid dynamics (CFD) methods are available for the study of dispersed multiphase flows such as those encountered in tapping systems. Perhaps the most commonly used are unresolved methods such as Eulerian models; in such methods, the phases are allowed to intermix, and small droplets with sizes below the mesh resolution are treated simply as part of the continuum. An alternative approach is to resolve small droplets directly via combined Eulerian–Lagrangian models; here, the bulk phases are treated as immiscible fluids, and small droplets

are modelled as discrete particles. It is important to note that both of these methods depend on the accurate specification of a number of empirical closure terms which determine how mass, momentum, and energy transfer between the dispersed and continuum phases.

Previous modelling work on ferroalloy tapping systems has focused mainly on fluid flow and associated effects in tap-holes [4, 6, 10], although some pioneering work was conducted on ladle flow modelling using particle tracking methods in [3].

The present paper documents the development and application of a high-resolution multiphase flow model capable of predicting overflow and entrainment effects in ladle flows. Heat transfer is quite naturally expected to play a large role in furnace tapping systems, especially with the formation of solid crusts and skulls as the slag and alloy cool to their freezing points. However due to many additional uncertainties in the parameters required to include heat transfer coupling, the decision was taken to focus on fluid flow effects only in the present work. Once a deeper understanding of this aspect of the problem has been gained, additional physics such as heat transfer and phase change will be integrated into the model at a later date.

Model Description

In order to study the cascade tapping problem, a multiphase CFD model was developed using the OpenFOAM® open-source computational mechanics platform [9]. The `multiphaseInterFoam` solver included in standard distributions of OpenFOAM® was modified with interfacial tension force smoothing techniques adapted from [2], to improve accuracy and performance of flow predictions for problems with high surface tension and a large degree of interface break-up. The resulting solver implements a segregated finite-volume solution scheme on arbitrary unstructured meshes and uses the volume-of-fluids formulation to track the phase interfaces.

Accuracy of the computational method relative to fundamental physical and empirical correlations has been presented previously in tapping system flow problems with similar materials [7, 10]; however, a more detailed experimental validation of the multiphase ladle flow model is currently underway and will be published in a forthcoming paper.

For each case studied, multiple versions of the model were simulated at progressively finer mesh resolutions. Phase interface surfaces from the previous step were then used to define mesh refinement regions for the next. This enabled relatively high resolutions of the order 5 mm to be reached in the regions of interest while avoiding the computational overhead of dynamic mesh refinement. The final high-resolution models typically contained between 1.8 and 2.5 million volume elements.

Alloy and slag flowrates at the ladle outlet boundary were monitored as functions of time over the duration of each simulation and used to estimate the mass fraction of alloy under different conditions. In order to estimate the dispersion of the alloy phase in the form of suspended droplets in the slag layer, the simulation results were post-

processed by filtering the volume elements in the mesh to a threshold determined by the alloy phase fraction field. A connectivity analysis was then performed on the remaining set of elements, with all elements forming part of a connected component assumed to represent a single droplet. Each droplet's diameter was then estimated by determining the quantity of alloy present in the connected component and relating it to a sphere of equivalent volume. Using all the droplets observed for a particular case, size distribution functions and average droplet diameters could be calculated. Droplet sizes are a useful proxy for the mixing energy imparted during the impact of the tapping stream and also give some indication of how long any subsequent settling and separation processes may take to complete.

Results and Discussion

Application of the model to the FeMn ladle flow problem was conducted, consisting of sensitivity studies and responses to operational variables relative to a base case parameter set.

Base Case Results

The geometry used for the full-scale ladle model is shown in Fig. 2. It consists of an open-topped vessel with an inflow stream and a gravity-driven outflow weir. The walls of the vessel are specified as no-slip boundaries, while the upper surface and ladle outlet are assumed to be open to atmosphere. The position, shape, and angle (from horizontal) of the inlet stream was determined using reduced-order models of the furnace tap-hole [7] and additional CFD simulations of the tapping runner channel. The complete set of parameters used for the model is shown in Table 1.

Simulations were run for 20 s, with average values taken using the final 10 s after the initial conditions had decayed. Visualizations of the slag isosurface at the end of the simulations are shown in Fig. 3.

It is interesting to see that the impact of the tapping stream on the slag–alloy interface is much more severe and turbulent than the flow behaviour at the surface of the slag; a ladle flow may therefore appear more quiescent than it actually is when observed visually. The impact of the tapping stream causes considerable mixing of the phases and a strong upwelling plume of mixed alloy and slag in the immediate vicinity of the ladle outlet. This arrangement, with the tapping stream in line with the ladle overflow, would therefore be expected to exacerbate losses by entrainment.

The evolution of the alloy mass fraction at the ladle outlet as well as the average diameter of the suspended droplets in the slag layer are shown in Fig. 4.

Significant variability is observed in both parameters even over the relatively short time scales modelled here. This indicates that ladle flows are strongly dynamic

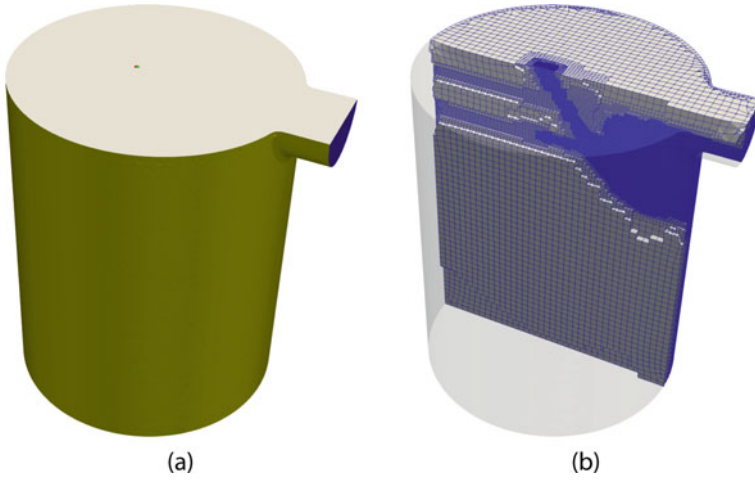


Fig. 2 **a** Ladle geometry, and **b** example computational mesh showing local refinements. (Color figure online)

Table 1 Base case ladle model parameters

Parameters	Values	Parameters	Values
Ladle height H_L	2.2 m	Ladle diameter D_L	2 m
Ladle offset y_i	0 m	Ladle angle α	0°
Outlet diameter d_o	0.6 m	Interfacial tension γ	0.5 N/m
Slag density ρ_s	3000 kg/m ³	Slag viscosity μ_s	0.1 Pa s
Alloy density ρ_m	6100 kg/m ³	Alloy viscosity μ_m	0.005 Pa s
Inlet slag flowrate \dot{m}_s	10 kg/s	Inlet alloy flowrate \dot{m}_m	10 kg/s
Inlet stream diameter d_i	0.0371 m	Inlet stream position x_i	-0.146 m
Inlet stream angle α_i	49°	Slag layer thickness h_s	0.3 m

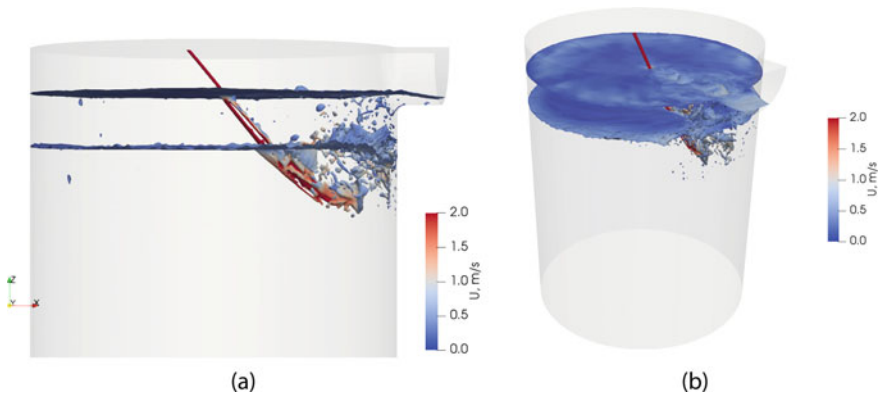


Fig. 3 Slag isosurface at $t = 20$ s, **a** side view, **b** isometric view. (Color figure online)

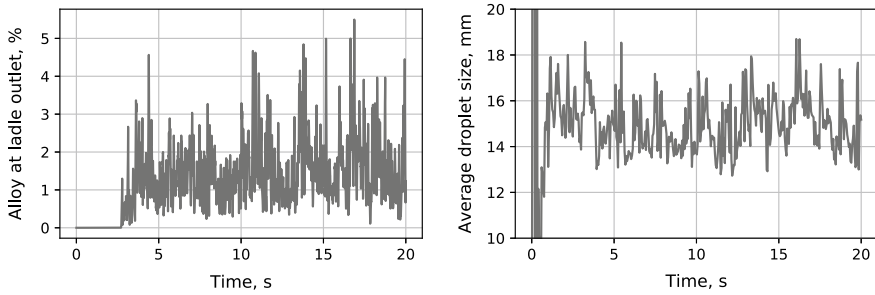


Fig. 4 Time series of outlet alloy fraction and average alloy droplet diameter, base case

phenomena, with the transient behaviour predominantly related to the impact and break-up of the incoming tapping stream as it contacts the alloy–slag interface.

Sensitivity to Fluid Properties

The model’s sensitivity to the properties of the materials being tapped was investigated by varying each property up and down by a factor of 25% relative to the base case while keeping the rest of the model parameters fixed and examining the effect on the alloy fraction at the ladle outlet as well as the average diameter of the suspended droplets. The parameter values used for the simulations are shown in Table 2.

From the results shown in Fig. 5, it can be seen that slag density has a disproportionately large effect on the behaviour of the model. Increased density significantly increases losses to the ladle overflow and vice versa. Similarly, increased density also results in larger alloy droplets in the slag phase. By contrast, the slag viscosity and interfacial tension appear to have relatively limited impact. This suggests that the larger scale features of the flow and interface break-up in FeMn tapping ladles are dominated by the momentum of the flow, as opposed to much slower settling and coalescence phenomena which would be expected to be strongly affected by viscosity (settling velocity) and interfacial tension (droplet shape, capillary drainage).

Quantification of actual expected ranges for the fluid phase properties in a ferromanganese operation is difficult due to the extreme conditions under which the process operates, but certain broad statements can be made. Properties are functions of both their chemical composition and temperature; since product compositions

Table 2 Changes to base case parameters for sensitivity study

Parameters	Values (–25%)	Values (+25%)
Slag density ρ_s	2250 kg/m ³	3750 kg/m ³
Slag viscosity μ_s	0.075 Pa s	0.125 Pa s
Interfacial tension γ	0.375 N/m	0.625 N/m

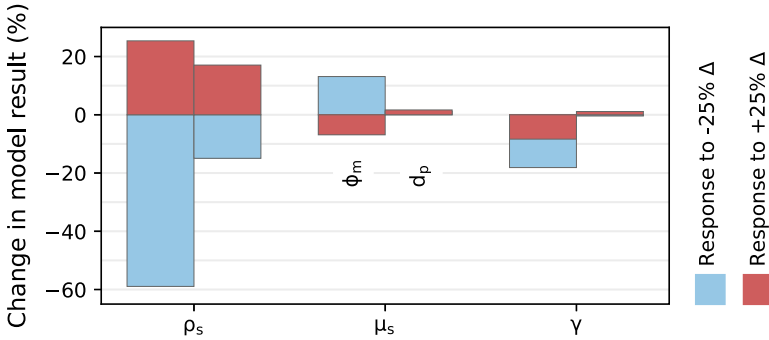


Fig. 5 Sensitivity of model to material properties (in each group the left column indicates relative change in alloy fraction ϕ_m in outlet stream, right column relative change in average droplet diameter d_p). (Color figure online)

are typically controlled tightly on any given furnace plant, the predominant effect is that of temperature of the tapping stream. The density range is proportional to the coefficient of expansion in the liquid state, which is usually small (of the order of $10^{-5}/K$). Viscosities generally obey Arrhenius or similar dependencies on temperature and may therefore vary more extensively particularly near to the freezing point of the material. Interfacial tension is more strongly affected by the presence of surface-active chemical components such as oxygen and sulphur than temperature. The publications of Mills and coworkers are recommended for further reading [5].

Effect of Operational Parameters

In order to assess the impact of operational changes to the ladle positioning and fill levels, a series of simulation sets was executed in which only the parameter of interest was varied relative to the base case.

In the first set the ladle was rotated relative to the tapping stream, so that the outlet was positioned at a different point on the ladle circumference. Rotations between 0° and 90° were considered. The results are given in Figs. 6a and 7 and demonstrate a consistent decrease in the alloy lost to the overflow as the ladle is rotated. The largest changes occur at small angles, in agreement with the results obtained in [3] using different modelling methods. This is consistent with the observation that the inlet stream causes a plume of mixed alloy and slag against the ladle sidewall—positioning the outlet further away from this plume therefore reduces entrainment losses. The effect on the size of the dispersed alloy droplets in the slag layer is statistically negligible, which is not unexpected given that rotating the ladle angle does not appreciably affect the geometry of the mixing zone.

In the second simulation set, the ladle was offset (moved sideways, in the y-direction) relative to the tapping stream. Offsets between 0 60cm were considered.

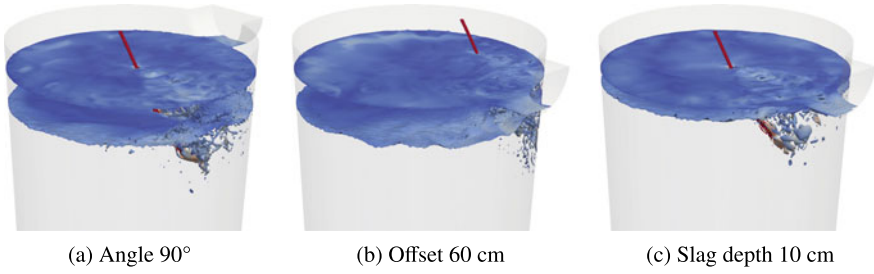


Fig. 6 Slag isosurfaces at $t = 20$ s for selected cases (velocity scale per Fig. 3). (Color figure online)

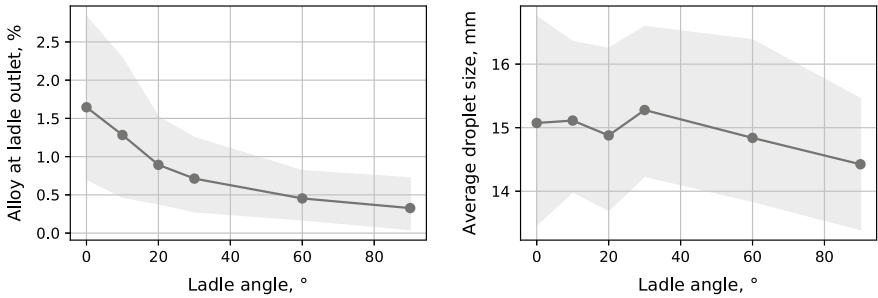


Fig. 7 Effect of ladle rotation angle relative to inlet stream (grey bands show 90% interval)

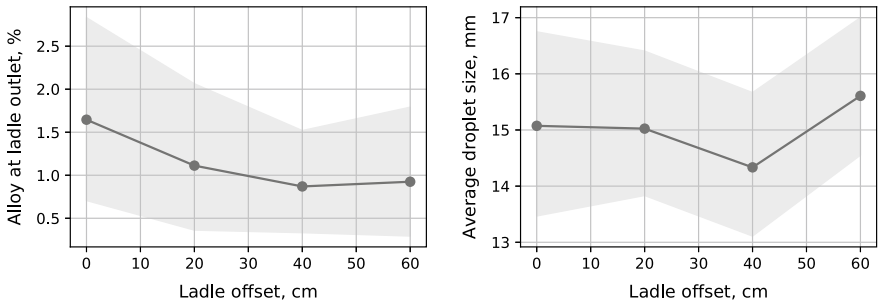


Fig. 8 Effect of ladle lateral offset relative to inlet stream (grey bands show 90% interval)

Figures 6b and 8 show the results, and again, the effect of moving the mixing plume away from the ladle outlet is seen to reduce alloy losses. However, this is only true up to a point, and when the ladle is offset too far, the tapping stream starts to impact much closer to the ladle sidewall. This generates more interfacial turbulence and mixing, as can be seen in the slight increase in alloy losses and the sharp increase in droplet sizes observed in 60cm simulation.

In the final simulation set, the thickness of the slag layer in the ladle was altered between 10 and 50 cm. Results are shown in Figs. 6c and 9, and show a dramatic impact on the alloy carry-over losses as the slag thickness decreases past 20 cm (note

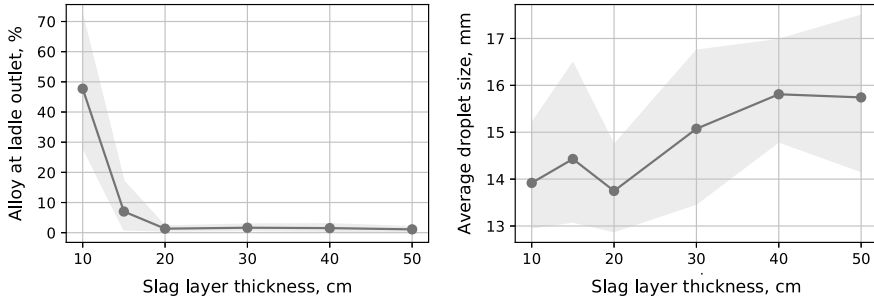


Fig. 9 Effect of slag layer thickness (grey bands show 90% interval)

the difference in scale compared to the previous two figures). This is due to a much larger and more alloy-dense portion of the mixing plume being exposed to the ladle overflow at shallower slag depths. The average droplet sizes also decrease slightly at lower slag depths—this seems somewhat counter-intuitive at first, but is most likely related to the reduced settling times for alloy droplets falling through the slag layer, which allows less time for smaller droplets to coalesce.

Conclusions

A high-resolution CFD model was successfully developed and used to study multiphase flows in ferromanganese furnace tapping ladles. The model showed that ladle flows are highly dynamic and that the momentum from the inlet tapping stream can cause significant large-scale mixing and flow structures at the alloy–slag interface.

The model was found to be most sensitive to the density of the tapped materials, with viscosity and interfacial tension playing a secondary role. The effect of the slag layer depth on alloy losses to the ladle outlet was found to be strong and highly non-linear, which is in line with current practices at many furnace plants which use this as a measure of when to stop a tap. It was also seen that small improvements in alloy losses could be achieved by altering the position and layout of the ladle cascade, although the practicalities of making such changes on working plants would need careful consideration.

A great deal of work still remains to be done on this topic. In particular, the use of more sophisticated multiphase flow methods which can account for the presence of very small (<5 mm) alloy droplets dispersed in the slag is suggested, since the behaviour of such small droplets cannot be accurately captured in the current model. In addition, the effect of ladle skulling and freeze linings which can appreciably affect the flow geometry should also be investigated; this will require full coupling of heat transfer and phase change to the CFD model. The monitoring of entrainment of the gas phase into the tapping ladle, particularly where there is contact between molten alloy and air, would be interesting to explore in the context of re-oxidation

losses. Finally, more experimental and problem-specific validation data is needed in order to assess the true accuracy and value of such models if they are to be used in virtual prototyping and digital twin applications in future.

Acknowledgements This paper is published by permission of Mintek and SINTEF. Project funding support from Mintek, and the Controlled Tapping project operated by the Research Council of Norway and the Norwegian Ferroalloy Producers Research Association, is acknowledged. Expenses for collaboration between the authors were supported by the INTPART Metal Production project funded by the Research Council of Norway. The authors acknowledge the Centre for High Performance Computing (CHPC), South Africa, for providing computational resources to this research project.

References

1. Eidem PA, Solheim I, Ringdalen E, Tang K, Ravary B (2015) Laboratory study of slag metal separation for HCFeMn. In: Proceedings of the fourteenth international ferroalloys Congress, pp 190–201, Kyiv, Ukraine, June 2015. Public Organization INFACON XIV
2. Heyns JA, Oxtoby OF (2014) Modelling surface tension dominated multiphase flows using the VOF approach. In: Proceedings of the jointly organized 11th World Congress on computational mechanics WCCM XI, 5th European Congress on computational mechanics ECCM V, and 6th European conference on computational fluid dynamics ECFD VI, pp 7082–7090, Barcelona, Spain, July 2014. CIMNE
3. Johansen ST, Ringdalen E (2018) Reduced metal loss to slag in HC FeCr production By redesign based on mathematical modelling. In: Proceedings of the furnace tapping 2018 conference, pp 29–38, Skukuza, South Africa, 2018. SAIMM
4. Kadkhodabeigi M, Tveit H, Johansen ST (2011) Modelling the tapping process in submerged arc furnaces used in high silicon alloys production. *ISIJ Int* 51(2):193–202
5. Mills KC, Yuan L, Jones RT (2011) Estimating the physical properties of slags. *J Southern African Inst Mini Metallurgy* 111:649–658
6. Muller J, Steenkamp JD (2013) Evaluation of HCFeMn and SiMn slag taphole performance using CFD and thermochemical property modelling for CaO-MnO-SiO₂-Al₂O₃-MgO slag. In: Proceedings of the thirteenth international ferroalloys Congress, pp 385–392, Almaty, Kazakhstan, June 2013. Public Association INFACON XIII
7. Olsen JE, Reynolds QG (2020) Mathematical modeling of furnace drainage while tapping slag and metal through a single tap-hole. *Metall Mater Trans B* 51(4):1750–1759
8. Olsen SE, Tangstad M, Lindstad T (2007) Production of manganese ferroalloys. Tapir Academic Press, Trondheim
9. OpenFOAM. OpenFOAM v6, July 2018
10. Reynolds QG, Olsen JE, Erwee MW, Oxtoby OF (2019) Phase effects in tap-hole flow - a computational modelling study. *J Southern African Inst Min Metall* 119:527–536
11. Steenkamp JD, Sutherland JJ, Hayman DA, Muller J (2016) Tap-hole life cycle design criteria: a case study based on silicomanganese production. *JOM* 68(6):1547–1555

Carbothermic Reduction of Brazilian Linz–Donawitz (LD) Steel Sludges



Mery C. Gómez-Marroquín, José Carlos D'Abreu, Enrique R. Dionisio-Calderón, Nilton Cárdenas-Falcón, Abraham J. Terrones-Ramirez, Jhony F. Huarcaya-Nina, Kim J. Phatti-Satto, and Fernando Huamán-Pérez

Abstract Carbothermic reduction was conducted using coarse (sample A) and fine (sample B) Brazilian Linz–Donawitz (LD) steel sludges and a sample of Peruvian anthracitic metallurgical coke (AMC) at 82.5% of fixed carbon. Specimens of 1 g of sample A and sample B preliminarily mixed with AMC at Fe/C: 1/2 were weighted. Sample A/AMC and sample B/AMC, reduction time and reduction temperature were identified as factors or independent variables. Conversions (α) or % reduction were selected as dependent variables. The values of weight ratios for sample A/AMC and sample B/AMC (3/7 and 7/3, respectively), reduction temperatures of 600 and 900 °C and reduction times lapses of 30 and 60 min, corresponding to their minimum as well as their maximum level of fluctuation respectively, were carried out via two design of experiments based in the factorial method 2^3 ; one for each sample (A and B); using

M. C. Gómez-Marroquín (✉) · A. J. Terrones-Ramirez · J. F. Huarcaya-Nina · K. J. Phatti-Satto · F. Huamán-Pérez
National University of Engineering, 210, Túpac Amaru Ave., Rímac LIMA 25, Lima, Perú
e-mail: mgomez@uni.edu.pe

A. J. Terrones-Ramirez
e-mail: abraham.terrones.r@uni.pe

J. F. Huarcaya-Nina
e-mail: jhuarcayan@uni.pe

K. J. Phatti-Satto
e-mail: kphattis@uni.pe

F. Huamán-Pérez
e-mail: fhuaman@uni.edu.pe

J. C. D'Abreu · E. R. Dionisio-Calderón
Pontifical Catholic University of Rio de Janeiro, 225, Marquês de SãoVicente Street, Gávea, RJ 22451-900, Brazil
e-mail: dabreu@puc-rio.br

E. R. Dionisio-Calderón
e-mail: enriquedionisio@puc-rio.br

N. Cárdenas-Falcón
Pontifical Catholic University of Peru, 1801, Universitaria Ave., San Miguel LIMA 32, Lima, Perú
e-mail: ncardenasf@pucp.edu.pe

a Brazilian statistics software called COLMEIA—Snedecor algorithm F in order to evaluate the effects simple, double and multiple of factors over the conversions (α) or % Reduction. Carbothermic reduction tests were performed at the optimal weight ratio (sample A/AMC: 3/7 and sample B/AMC: 3/7), reduction temperatures: 600, 700, 800 and 900 °C and reduction times: 20, 30, 40, 50 and 60 min in order to estimate k-specific reaction rate constant, E_a -apparent activation energy and the A-Arrhenius pre-exponential frequency factor. The kinetic models that better fitted to the conversions (α) of both samples (A and B) were: boundary chemical reaction model for spherical symmetry (BCRM-ss): $1 - (1 - \alpha)^{1/3} = kt$ and the model of simple exponential continuous reaction (MSECR): $-\ln(1 - \alpha) = kt$. The kinetic parameters obtained were: (1) sample A: $E_a = 7.45 - 8.08$ kJ/mol and $A = 0.009 - 0.032$ Hz for a linear correlation between 0.8241 and 0.8276 and (2) sample B: $E_a = 19.36 - 21.94$ kJ/mol and $A = 0.05 - 0.21$ Hz for a linear correlation between 0.9758 and 0.9777.

Keywords Carbothermic reduction · Linz–Donawitz (LD) · LD converter · BOF converter · Steel sludges · Converter process

Introduction

During the fabrication of steel, a considerably large amount of industrial waste is generated. Various solid wastes emerging from steel plants are in the form of sludge and slag, mainly blast furnace slag, blast furnace flue dust and slag, mill scale, mill sludge, etc. [1]. Linz–Donawitz (LD) sludges are the wastes extracted during the manufacture of steel in LD converter. Huge quantity of LD sludge is made per ton of steel produced [2]. The fine solid particles recovered after wet cleaning of the gas emerging from LD converters in the sludge form are termed as LD sludges. During this process, the furnace emits very fine iron oxide particles that are removed from the waste gases by a wet scrubbing process. This waste may contain high levels of CaO, Zn, Pb, etc., depending upon the type of limestone and chemistry of scrap used during the process of steelmaking. The sludge contains appreciable quantities of iron and lime, and it is, therefore, quite suitable for recycling in the sinter plant [3]. For example, the origination of these LD sludges in a Brazilian steelwork varied from 5.6 to 7.2 kg/t of crude steel for the basic oxygen furnace (BOF) coarse sludge and from 17.0 to 22.8 kg/t of crude steel for the fine sludge. Due to its content of total iron, ca 50–60%, these residues could be recycled into the production process of sinter [4]. The aim of this paper was to study the carbothermic reduction of mixtures of samples of LD steel sludges with a sample of anthracitic mineral coke (AMC). These experiments were performed using a design of experiments 2^3 that involved a factor treatment according to the COLMEIA Brazilian Statistic software. Other objectives were to evaluate the effect of factors or independent variables: sample A/AMC and sample B/AMC, reduction time and reduction temperature on the dependent variable: conversions (α) or % Reduction, the behavior of their carbothermic reduction

isotherms in different times and reduction temperature and to estimate their kinetic parameters corresponding using the kinetics model that presented the better fit of their conversions (α). These results will permit to avoid their accumulation and suggest a reuse in the steel plant itself. This reutilization would provide an added value to this material that until now is constituted as an environmental problem of considerable economic importance.

Experimental

Characterization of LD Steel Sludges

Chemical analysis was conducted using a 3.4-m Ebert Spectrograph (Jarrel Ash model) for determining elemental composition and an absorption spectrometer (model AA-7000) for estimating the main oxides. XRD analyses were performed using a D8 Discover diffractometer, Bruker, with a $\text{CuK}\alpha$ radiation ($\lambda = 1.5418 \text{ \AA}$), Ni filter and Lynxeye detector, operating at 40 mA and 40 kV. XRD patterns were recorded in the 2θ range from 10 to 90° with the increment of 0.02° . An energy discriminator was employed to reduce the iron fluorescence. The identification of the crystalline phases was carried out by comparison with standard patterns applying EVA module Bruker. The crystal structures of the most probable compounds were obtained from the Inorganic Crystal Structure Database (ICSD). The patterns were fitted by the Rietveld method with fundamental parameters using the TOPAS module Bruker.

A thermal analysis was performed using differential calorimetric scanning analysis—DSC, thermal differential gravimetric analysis—DTG and thermal gravimetric analysis—TG at 1000°C . The thermal characterization equipment, NETZSCH STA model 449 F3, is composed of combined techniques of DSC, TG and DTG, using the ASTM E1131-08 Standard. The tests were carried out using nitrogen atmospheres with a flow of 50 mL/min and a heating rate of 10 K/min.

Specific gravity and average particle size were determined. The specific gravity was calculated using the pycnometer method. The determination of the average particle size was obtained employing a series of ASTM meshes: m14, m20, m30, m50, m70, m100, m140, m200, m270, m400 and a background of under m400.

Preheating of Reactor and Crucibles

Carbothermic reduction of LD steel sludges (samples A and B) was processed in an electric furnace at 1000°C of maximum temperature. Various controls were made for ensuring the functioning of the electric furnace, i.e., (a) to prepare a profile of heating speeds of this reactor to be used for the tests, taking the temperatures and

times reached since room temperature until the maximum temperature of the test (900 °C) and (b) to preheat the new crucibles to 200 °C for about 3 h.

Preparation and Analysis of Carbon

Sequentially, a sample of anthracitic metallurgical coke-AMC was decreased of particle size using jaw crushers with 1/2", 1/3" and 1/8" aperture, respectively, to then grind and mechanically homogenize them in mortars until reaching a granulometry of approximately 100% – 100 mesh (about 0.149 mm). A carbon analysis was done in order to determine its humidity, volatile matter and fixed carbon according to ASTM standards: 7582, D2013 and D346, which consisted of heating 1 g of AMC in triplicate (three samples of AMC in their respective crucibles) and to heat them at 900 °C for 5 h into the electric furnace to eliminate not only all the humidity but also volatile matter present in the sample of AMC.

Design of Experiments and Experimental Planning

Specimens of 1 g of sample A and sample B were previously mixed with AMC weighted to a Fe/C: 1/2 ratio. Sample A/AMC and sample B/AMC, reduction time and reduction temperatures were identified as independent variables and: conversions (α) selected as dependent variable. Values of sample A/AMC and sample B/AMC were: weight ratios 3/7 and 7/3, reduction temperatures of 600 and 900 °C and reduction times of 30 and 60 min. These values correspond to the minimum and maximum levels of fluctuation. Two techniques of the design of experiments based in the factorial method 2^3 were used, one for each sample (A and B), using a COLMEIA Brazilian Statistic software based on the Snedecor algorithm F to evaluate the effects of simple, double and multiple factors over the conversions (α).

Carbothermic Reduction Tests

Experiences of carbothermic reduction of both samples (A and B) were carried out using the optimal weight ratio: sample A/AMC: 3/7 and sample B/AMC: 3/7, reduction temperatures of 600, 700, 800 and 900 °C and reduction times of 20, 30, 40, 50 and 60 min into the electric furnace in order to estimate k-specific reaction rate constant, E_a -apparent activation energy and A-Arrhenius pre-exponential frequency factor. The graphics % Reduction vs reduction time is called carbothermic reduction isotherms.

Conversions (α) Estimation

In order to obtain conversions (α), it is advisable to calculate the reducible oxygen content associated to all those phases present in LD steel sludges according to Eq. 1 [5]:

$$O_{\text{reducible}} = \%ZnFe_2O_4 \cdot \frac{M_0}{M_{ZnFe_2O_4}} + \%ZnO \cdot \frac{M_0}{M_{ZnO}} + \%Fe_3O_4 \cdot \frac{M_0}{M_{Fe_3O_4}} \quad (1)$$

Considering that the calculus of the mass of volatilized zinc contained in other mineralogical phases in both samples (A and B), Eq. 1 may be rewritten according to Eq. 2 [6]:

$$O_{\text{reducible}}, Zn_{\text{volatilized}} = \% FeO \cdot \frac{M_0}{M_{FeO}} + \% Fe_2O_3 \cdot \frac{M_0}{M_{Fe_2O_3}} \\ + \% ZnFe_2O_4 \cdot \frac{M_0}{M_{ZnFe_2O_4}} + \% ZnO \cdot \frac{M_0}{M_{ZnO}} + \% Fe_3O_4 \cdot \frac{M_0}{M_{Fe_3O_4}} \quad (2)$$

where:

M_o is the atomic mass of oxygen, M_o , Zn is the atomic mass of oxygen and zinc, M is the molecular mass, and $O_{\text{reducible}}$, $Zn_{\text{volatilized}}$ is the percentage of reducible oxygen and volatilized zinc.

Therefore, conversions (α) were calculated by weight difference, initial weight and the percentage of reducible oxygen and zinc, according to the Eq. 3 and Eq. 4 [6]:

$$\Delta W_t = W_i - W_t \quad (3)$$

$$\alpha = \left\{ \frac{100(\Delta W_t)}{\left[\left(\frac{16}{71.85} \right) \%FeO + \left(\frac{64}{231.55} \right) \%Fe_3O_4 + \left(\frac{129.38}{241.08} \right) \%ZnFe_2O_4 + \left(\frac{48}{159.79} \right) \%Fe_2O_3 + \%ZnO + \dots + \dots \right] (W_i)} \right\} \quad (4)$$

where:

W_i is the initial weight of the sample, W_t is the weight of the reduced sample at time t, ΔW_t is the weight loss of the reduced sample at time t, and α represents the conversions observed at time t.

To make more comfortable the use of practical method to compute the metallic iron and zinc volatilized via mass loss of LD steel sludges, Eq. 4 may be rewritten as Eq. 5 [7]:

$$\alpha = 100 \left(\frac{\Delta W_t}{W_i} \right) = \left(\frac{W_i - W_t}{W_i} \right) \quad (5)$$

Kinetic Parameters Estimation

The three kinetic models of reduction of iron oxides that better fit the conversions (α) were boundary chemical reaction model for spherical symmetry (BCRM-ss), which formula is written according to Eq. 6, boundary chemical reaction model for cylindrical symmetry (BCRM-cs) corresponding to Eq. 7 and the model of simple exponential continuous reaction (MSECR) obeying the Eq. 8 [6]:

$$1 - (1 - \alpha)^{1/3} = kt \quad (6)$$

$$1 - (1 - \alpha)^{1/2} = kt \quad (7)$$

$$-\ln(1 - \alpha) = kt \quad (8)$$

In addition, for estimating kinetic parameters— k -specific reaction rate constant, E_a -apparent activation energy and A -Arrhenius pre-exponential frequency factor—it was necessary to use the Arrhenius Equation according to Eq. 9 [6].

$$k = A \exp\left(\frac{-E_a}{RT}\right) \quad (9)$$

Results and Discussion

LD Steel Sludges Characterization

Table 1 summarizes physical and some chemical determinations, and mineralogical compositions of LD steel sludges (sample A and sample B).

Figure 1 shows a thermogravimetric analysis by DTG-DSC-TG at 1000 °C of LD steel sludges (sample A and sample B).

Table 1 Characterization of sample A and sample B

Sample	Physical determinations		Chemical and mineralogical compositions				
	Density, $\times 10^6$ g/m ³	Average particle size, mm	Fe Tot,%	Zn,%	FeO,%	ZnFe ₂ O ₄ ,%	Fe ₃ O ₄ ,%
A	4.72	0.146	77.5	0.5	36.0	5.9	– 2
B	3.67	0.120	51.4	1.7	55.1	5.3	14.8

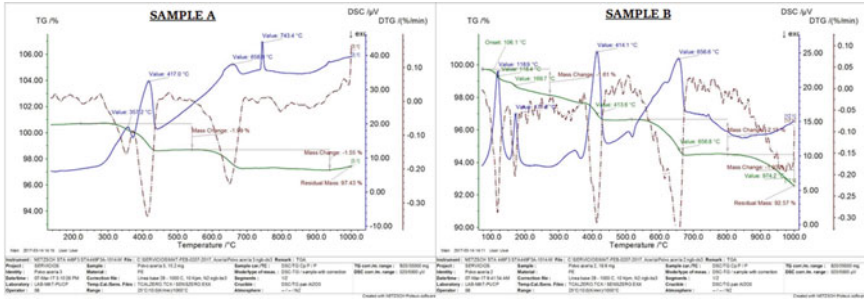


Fig. 1 Thermogravimetric analysis by DTG-DSC-TG at 1000 °C of LD steel sludges (sample A and sample B). (Color figure online)

Table 2 Carbon analysis of ACM

H ₂ O, %	Volatile matter, %	Ash, %	Fixed carbon, %
1.06	9.94	6.50	82.50

Carbon Analysis

Table 2, shows a carbon analysis of ACM.

Design Experiments and Experimental Planning

According to the methodology of design of experiments based on the factorial method 2³ that involved a factor treatment of the COLMEIA Brazilian Statistic software, Table 3 shows a random experimental planning of carbothermic reduction of sample A and sample B using as maximum fluctuation levels (A, B and C) and minimum fluctuation levels (a, b and c) of the factors or independent variables: sample A/AMC and sample B/AMC, reduction time and reduction temperature.

Table 4 shows the results of carbothermic reduction of sample A and sample B (conversions, α) according to the experimental planning shown in Table 3.

In Fig. 1, a thermogravimetric analysis by DTG-DSC-TG at 1000 °C exhibited a mass loss of 97.43% for the sample A and 92.57% for the sample B; however, the maximum conversion α or % Reduction observed in the preliminary design of experiments (Tables 3 and 4) was 67% that corresponds to factorial treatment BC for the sample B.

Table 5 shows a statistics analysis of effects of factors over conversions (α), according to experimental planning shown in Tables 3 and 4.

Table 5 is observed that the individual effects B and C were more significance than double or multiple synergies over % Reduction of sample A and % Reduction of sample B. Also, double synergy AB, AC and BC are not favorable over % Reduction

Table 3 Random experimental planning of carbothermic reduction of sample A and sample B according to the design of experiments based in factorial method 2³

Random order of realization of the experiences	Factor treatment according to the COLMEIA	Sample A/AMC and sample B/AMC	Reduction time, min	Reduction temperature, °C
8	<i>ABC</i>	7/3	60	900
6	<i>AC</i>	7/3	30	900
4	<i>AB</i>	7/3	60	600
2	<i>A</i>	7/3	30	600
7	<i>BC</i>	3/7	60	900
5	<i>C</i>	3/7	30	900
3	<i>B</i>	3/7	60	600
1	<i>I</i>	3/7	30	600

Table 4 Results of carbothermic reduction of sample A and sample B according to the experimental planning shown in Table 3

i	Factor treatment according to the COLMEIA	Levels of fluctuation of each independent variable, according to the nomenclature used by the factorial method			Conversions, α /% Reduction	
					Sample A	Sample B
1	<i>I</i>	<i>a</i>	<i>b</i>	<i>c</i>	29	26
2	<i>A</i>	<i>A</i>	<i>b</i>	<i>c</i>	15	22
3	<i>B</i>	<i>a</i>	<i>B</i>	<i>c</i>	48	53
4	<i>AB</i>	<i>A</i>	<i>B</i>	<i>c</i>	20	28
5	<i>C</i>	<i>a</i>	<i>b</i>	<i>C</i>	37	54
6	<i>AC</i>	<i>A</i>	<i>b</i>	<i>C</i>	15	30
7	<i>BC</i>	<i>a</i>	<i>B</i>	<i>C</i>	55	67
8	<i>ABC</i>	<i>A</i>	<i>B</i>	<i>C</i>	17	32

of sample A and % Reduction of sample B. However, triple or multiple synergy ABC represents certain increasing over % Reduction of sample B. This result permitted to conclude that as an increasing of reduction time (*B*) as reduction temperature (*C*) would increase the conversions (α) of LD steel sludges (sample A and sample B).

Carbothermic Reduction Tests

Figure 2 shows photos of samples A and B in crucibles after tests of carbothermic reduction which were carried out in different time and temperature of reduction,

Table 5 Statistics analysis of effects of factors over conversions (α) according to experimental planning

Sinergy	Statistics symbols of effects of factors according to the COLMEIA	Sample	Effect	Square mean	Prob F-Snedecor (%)
Single or simple	A	B	−22.00	13.1925	97.7882
		A	−25.50	33.4534	99.5561
	B	B	12.00	3.9250	88.1358
		A	11.00	6.2251	93.2876
	C	B	13.50	4.9676	91.0271
		A	3.00	0.4630	46.6437
Double	AB	B	−8.00	1.7445	−
		A	−7.50	2.8939	−
	AC	B	−7.50	1.5332	−
		A	−4.50	1.0418	−
	BC	B	−4.50	0.5520	−
		A	−1.00	0.0514	−
Triple or multiple	ABC	B	2.50	0.1704	−
		A	−0.50	0.0129	−

where can observe the volatilization of zinc and reduction of oxygen of their main oxides.

In Fig. 1, it is observable that the volatilization of zinc from franklinite and other volatile matters took place in the first ten minutes, whereas reduction simultaneously and rapidly occurred between iron oxides and reduction gases that were produced via intermediates reactions [8]. Also, according to the Boudouard reaction, the carbothermic reduction of wustite can produce only metallic iron in $PCO/PCO_2 = 1$ and temperatures higher than 600 °C. In addition, the reduction of franklinite occurred by instantaneous decomposition in its constituent oxides (zincite and hematite). Over 900 °C, the sequential reduction of zinc and iron oxides with gaseous intermediates took place [6].

Kinetic Parameters Estimation

Figure 3 shows carbothermic reduction isotherms of LD steel sludges (sample A and sample B). These experiments were carried out with the objective to evaluate the relation between % Reduction, reduction time and temperature with further estimation of the kinetic parameters using the Arrhenius equation.

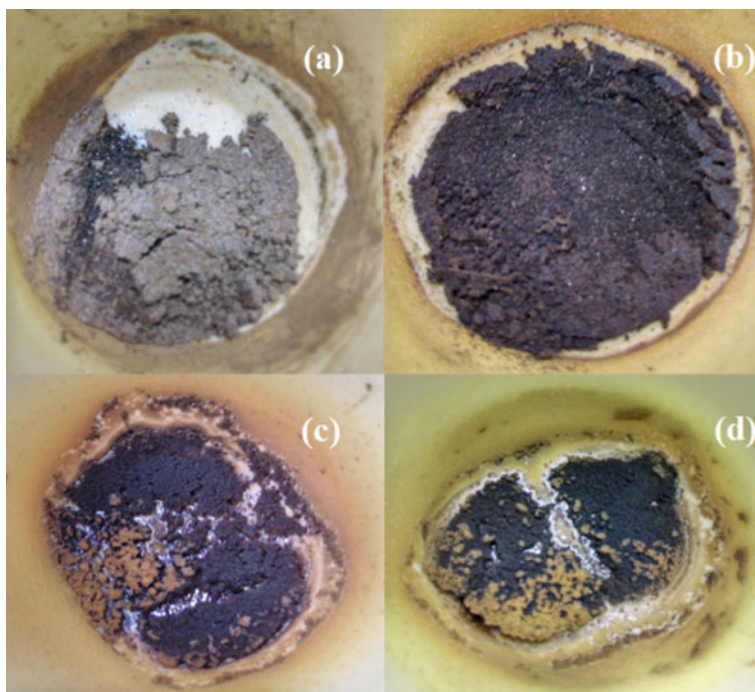


Fig. 2 Photos of samples of LD steel sludges after tests of carbothermic reduction: **a** sample A, $t = 60$ min and $T = 900$ °C **b** sample A, $t = 20$ min and $t = 900$ °C **c** sample B, $t = 20$ min and $t = 900$ °C **d** sample B, $t = 20$ min and $t = 900$ °C. (Color figure online)

In Fig. 3a, there is not an appreciable difference between the % Reduction for sample A and the % Reduction of sample B; however, in Fig. 3d it is notable that the % Reduction of sample A is higher than the % Reduction of sample B.

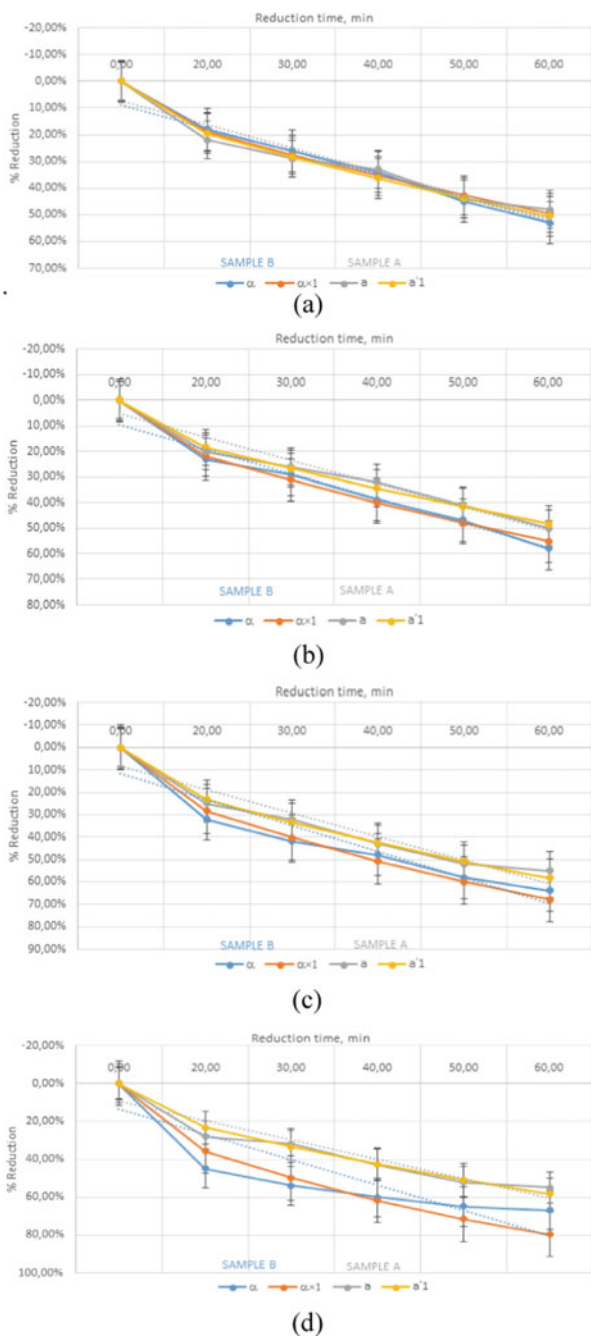
Figure 4 plots the Arrhenius adjustment of carbothermic reduction of LD steel sludges (sample A and sample B) mainly E_a -apparent activation energy and A-Arrhenius pre-exponential frequency factor in function to the linear correlation of $\ln(k)$ and $(1/T)$.

The kinetic models that better fit conversions (α) of carbothermic reduction of both samples (A and B) are the following: BCRM-ss: $1-(1-\alpha)^{1/3} = kt$, BCRM-cs: $1-(1-\alpha)^{1/2} = kt$, and MSECR: $-\ln(1-\alpha) = kt$. Kinetic parameters obtained from the models are shown in Table 6.

Conclusions

Design of experiments permitted to establish that simple synergy of B and C represented by the increasing of as reduction time (B) as reduction temperature (C) will

Fig. 3 Carbothermic reduction isotherms of LD steel sludges (sample A and sample B): **a** 600 °C, **b** 700 °C, **c** 800 °C and **d** 900 °C. (Color figure online)



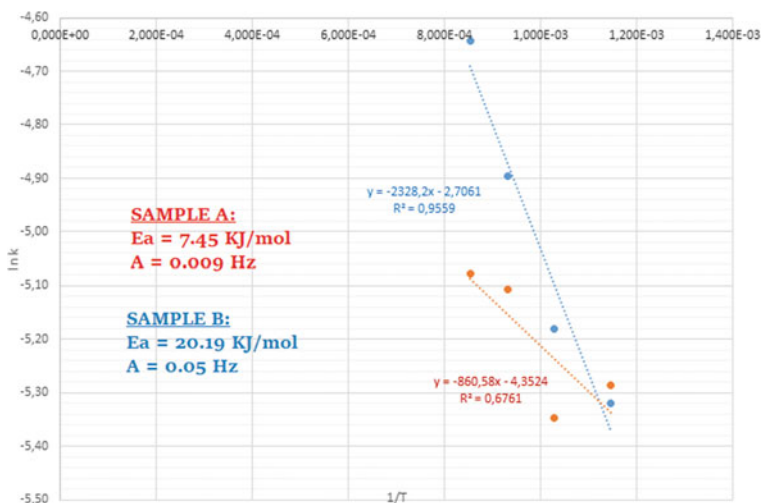


Fig. 4 Arrhenius adjustment in order to estimate kinetics parameters of carbothermic reduction of LD steel sludges (sample A and sample B). (Color figure online)

Table 6 Estimation of kinetic parameters of BCRM-ss, BCRM-cs and MSECR

Kinetic parameters	BCRM-ss		BCRM-cs		MSECR	
	Sample A	Sample B	Sample A	Sample B	Sample A	Sample B
E_a , KJ/mol	7.4518	20.1866	7.1548	19.3567	8.0819	21.9411
A, Hz	0.0092	0.0517	0.0129	0.0668	0.0324	0.2118
r-value	0.8241	0.9770	0.8223	0.9777	0.8276	0.9758

enhance the conversions (α) both in LD steel sludge samples (sample A and sample B). The kinetic models best fitted the carbothermic conversions of both samples (A and B) were: boundary chemical reaction model for spherical symmetry (BCRM-ss)—equation: $1 - (1 - \alpha)^{1/3} = kt$, while the model of simple exponential continuous reaction (MSECR) is in accordance to the equation: $-\ln(1 - \alpha) = kt$. The kinetic parameters estimated were: (1) sample A: $E_a = 7.45 - 8.08$ kJ/mol and $A = 0.009 - 0.032$ Hz for a linear correlation that is between 0.8241 and 0.8276 and (2) sample B: $E_a = 19.36 - 21.94$ kJ/mol and $A = 0.05 - 0.21$ Hz for a linear correlation that is between 0.9758 and 0.9777. Due to low values of E_a , it is possible to pre-terminate a diffusional control mechanism of LD steel sludges. The great similarity of the results obtained enables utilization of both residues in the case of an eventual addition of them as loading in shape of pellets or sinters in these reactors. Finally, this reutilization would provide an added value to these residues that until now is constituted as an environmental liability of considerable economic importance.

Acknowledgements The authors thank the Research Vice Rectorate and the College of Geological Mining and Metallurgical Engineering Research Institute of the National University of Engineering

for the financial assistance granted, without which these programmed experiences could not have been carried out, and thank the Brazilian Steelmaking Company for the background and the samples provided to this paper.

References

1. Drobíková K, Plachá D, Motyka O, Gabor R, Kutlákova KM, Vallová S, Seidlerová J (2016) Recycling of blast furnace sludge by briquetting with starch binder: waste gas from thermal treatment utilizable as a fuel. *Waste Manage* 48:471–477
2. Purohit A, Swain PTR, Patnaik PK (2020) Mechanical and sliding wear characterization of LD sludge filled hybrid composites. *Materials today: proceedings*
3. Das B, Prakash S, Reddy PSR, Misra VN (2007) An overview of utilization of slag and sludge from steel industries. *Resour Conserv Recy* 50(1):40–57
4. Cantarino MV (2011) Estudo da remoção de zinco e de álcalis contidos em lammas de aciaria LD. Master thesis, Federal University of Minas Gerais
5. Buboltz FF, Deves FB, Osorio E, Vilela FAC (2018) Carbothermic reduction of electric arc furnace dust via thermogravimetry. *Metallurgy Mater REM, Int Eng J Ouro Preto* 71(3):411–418
6. Gómez-Marroquín MC (2008) Caracterização e cinética da redução de ferrita de zinco presente em poeiras de aciaria por misturas de CO–CO₂. Doctoral thesis, Pontifical Catholic University of Rio de Janeiro
7. Zhang HN, Li JL, Xu AJ, Yang QX, He DF, Tian NY (2014) Carbothermic reduction of zinc and iron oxides in electric arc furnace dust. *J Iron Steel Res Int* 21(4):427–432
8. Chen SY, Fu XJ, Chu MS, Li XZ, Liu ZG, Tang J (2016) Carbothermic reduction mechanism of vanadium-titanium magnetite. *J Iron Steel Res Int* 23(5):409–414

Liquid–Liquid Extraction Thermodynamic Parameter Estimator (LLEPE) for Multicomponent Separation Systems



Titus Quah and Chukwunwike O. Iloeje

Abstract Gibbs energy minimization is a powerful tool for modeling liquid–liquid equilibrium (LLE) in multicomponent systems, but it requires key thermodynamic parameters that may not be readily available. Our earlier work demonstrated an approach for estimating these properties via regression to equilibrium isotherm data but identified limitations regarding applicability to higher-concentration systems, sensitivity to experimental data, and ease of implementation. To extend the accessibility and applicability of Gibbs energy minimization for modeling LLE, this study presents the open-source, liquid–liquid equilibrium parameter estimator (LLEPE) package for estimating thermodynamic parameters. LLEPE extends parameter estimation to include aqueous-phase Pitzer coefficients that capture the effects of ionic interactions and offers analysis and visualization tools that assess experimental data quality and model prediction accuracy. We apply LLEPE to a rare earth extraction case study where we incorporate data filtering and Pitzer parameter fitting to reduce the effect of outlier data, capture the contribution of ion interactions, and ultimately improve overall prediction accuracy for multicomponent data. Our results show that filtering data decreases the prediction error by removing outliers, and fitting Pitzer parameters increases overall prediction accuracy, especially for high-concentration systems. Iteratively fitting to a combined dataset increases prediction accuracy for multicomponent data for low to medium feed concentrations.

Keywords Solvent extraction · Parameter estimation · Thermodynamic modeling · Gibbs minimization · Rare earths

Introduction

Liquid–liquid extraction, also known as solvent extraction, is a technique that separates materials by exploiting their relative solubility in immiscible liquids, and is widely used in small- and large-scale continuous operations for hydrometallurgical

T. Quah (✉) · C. O. Iloeje
Energy Systems Division, Argonne National Laboratory, 9700 South Cass Avenue, Lemont, IL
60439-6903, USA
e-mail: titus.quah@gmail.com

© The Minerals, Metals & Materials Society 2021
J. Lee et al. (eds.), *Materials Processing Fundamentals 2021*, The Minerals, Metals
& Materials Series, https://doi.org/10.1007/978-3-030-65253-1_9

extraction, nuclear fuels reprocessing, biofuels processing, and wastewater treatment [1–5]. Gibbs Energy Minimization (GEM) can predict the extraction equilibrium by minimizing the system Gibbs energy with respect to quantities of each species in each phase. However, owing to limited availability of thermodynamic properties for certain organic-phase species in the literature, these properties must be estimated before GEM can be applied. Earlier studies [6, 7] proposed an estimation method for organic-phase species' missing thermodynamic properties based on regression to experimental equilibrium isotherm data. However, prediction accuracy was not uniform across data points, and not all datasets report measurement error, making it challenging to properly weight data.

To increase the accessibility and prediction accuracy of the thermodynamic parameter estimation method, this study introduces liquid–liquid equilibrium parameter estimator (LLEPE), a Python package that implements the estimation method, and explores strategies to reduce the model's prediction error. Three strategies are explored: filtering data points with outlier prediction error to eliminate model-skewing experimental data, fitting electrolyte Pitzer parameters to better model ionic interactions at higher concentrations, and iteratively fitting Pitzer and linear parameters for each species to fit to combined single- and multispecies datasets.

Methods

GEM Formulation

For a system with fixed temperature and pressure, the minimum Gibbs free energy with respect to molar quantities of each species in each phase represents the equilibrium criterion and is shown in Eqs. 1a, 1b:

$$\min(G) = \sum_p \sum_i n_{i,p} \left(\overline{G}_{i,p}^0 + RT \ln(\gamma_i m_i) \right) \quad (1a)$$

$$\text{st. } h(n_{i,p}) \leq d \quad (1b)$$

G is the Gibbs energy of the system; $n_{i,p}$ and $\overline{G}_{i,p}^0$ are the number of moles and partial standard molar Gibbs energy, respectively, for species i in phase p ; and R , T , γ_i , m_i are, respectively, the universal gas constant, temperature, and species i activity coefficient and molality. Equation 1b represents equality and inequality constraints such as mole, species, elemental, and non-negativity balances [8]. Solving Eqs. 1a, 1b predicts the phase compositions at equilibrium. The activity model for γ_i in the aqueous phase uses Pitzer equations, which account for nonideal behavior due to ion-ion and ion–solvent interactions [9]. In the organic phase, we model the solution

as ideal ($\gamma_i = 1$) and assume the mixing model indirectly captures nonideal interactions [7]. To model the partial standard molar Gibbs energy $\overline{G}_{i,p}^0$ in the aqueous phase, we use the Helgeson–Kirkham–Flowers equation of state (EoS) to compute species standard partial molar property values as a function of pressure and temperature [10]. Data for $\overline{G}_{i,p}^0$ in the organic phase for many extractants and organo-metal complexes are not readily available in the literature, so we need to estimate them by regression to experimental data.

LLEPE Implementation

Figure 1 illustrates the overall structure of the LLEPE Python package [11]. It comprises three main modules: inputs, the LLEPE object, and outputs. The input module includes experimental equilibrium isotherm data and an XML file with EoS and thermodynamic data definitions, formatted to provide inputs to Cantera™ [6, 7]. This input information is used to instantiate a LLEPE object, which contains the standard parameter estimator method that handles parameter fitting. The outputs module handles all post-processing analysis and visualization. The basic fit method comprises the standard parameter estimator and the linear parameter estimator.

Standard Parameter Estimator

This model estimates the standard species Gibbs free energy by minimizing the difference between predicted and experimental isotherms. It directly estimates the species standard enthalpy (H^0) and obtains G^0 from the relation $G^0 = H^0 - TS^0$. The standard entropy, S^0 , is estimated using the Glasser and Jenkins [12] correlation. Figure 2a illustrates the estimation logic.

The estimator starts by creating an input file and populating it with EoS and Pitzer parameters, as well as initial guesses for extractant and organo-metal complex standard enthalpies. Then, the model reads in data from the input file, as well as experimental feed concentrations, and uses the Gibbs minimization algorithm implemented in Cantera [13] to predict equilibrium compositions. Next, it compares these predictions with equilibrium data from the experiments and minimizes the log mean squared

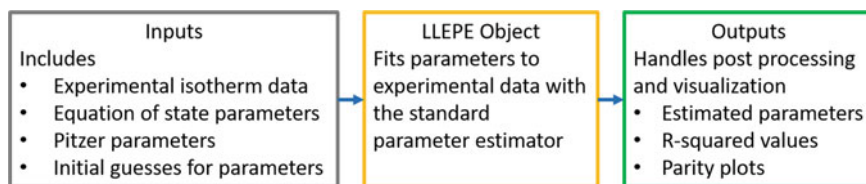


Fig. 1 LLEPE package structure illustrating key modules. (Color figure online)

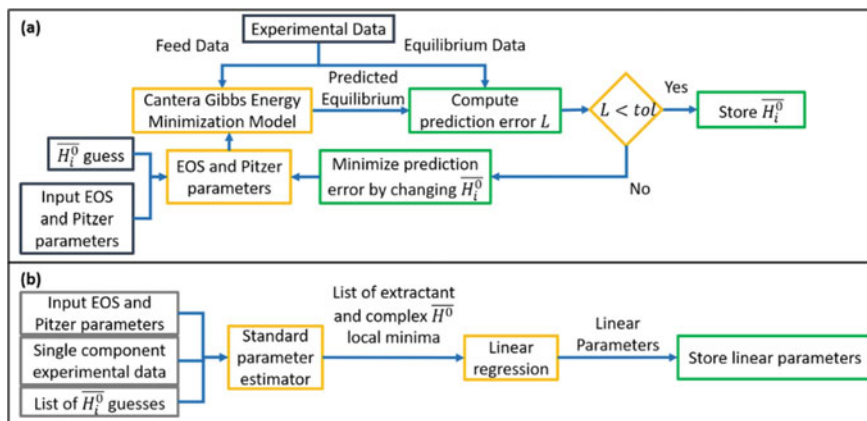


Fig. 2 Logic for **a** the standard parameter estimator and **b** the linear parameter estimator implemented in the LLEPE package. (Color figure online)

error (LMSE), L , described in Eq. 2a, by updating standard enthalpy estimates until L falls below the set tolerance.

$$L = \frac{1}{N} \sum_N \left(\log_{10}(\tilde{D}_{pred}) - \log_{10}(\tilde{D}_{meas}) \right)^2 \quad (2a)$$

$$\tilde{D} = \frac{n_{j,org} + \epsilon}{n_{j,aq} + \epsilon} \quad (2b)$$

N is the number of experimental data points; \tilde{D}_{pred} and \tilde{D}_{meas} are the predicted and measured perturbed distribution ratios described in Eq. 2b; $n_{j,org}$ and $n_{j,aq}$ are the number of moles of the extracted species in the organic and aqueous phase, respectively; and ϵ is a very small number to avoid division by zero.

Linear Parameter Estimator

Fitting to multicomponent data is challenging, since there are $N + 1$ unknown variables where N is the number of organo-metal complexes. Previous work established a linear relationship between extractant and complex standard enthalpies [6], which eliminates the dependent complex enthalpies, reducing the dimension of the parameter-fitting problem to $(N + 1) - N$. Figure 2b illustrates the logic for estimating the linear parameters using data for each single-component system. For each extracted species, we use the standard parameter estimator on the single-component data with a set of complex and extractant enthalpy initial guesses. This procedure returns a set of complex and extractant enthalpy values that describe the locus of locally optimal solutions that are used to fit linear parameters a and b in Eq. 3, where

H_{com}^0 and H_{ext}^0 are the complex and extractant standard enthalpies, respectively.

$$H_{com}^0 = aH_{ext}^0 + b \quad (3)$$

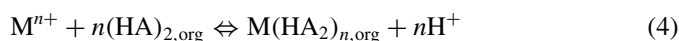
The linear parameter estimator returns the linear parameters a and b to relate each extracted species complex standard enthalpy to the extractant standard enthalpy.

Basic Fit Method

The basic fit method combines the standard parameter estimator with the linear parameters obtained from the linear parameter estimator. The model is fit to a combined dataset using the basic parameter estimator by fitting only the extractant standard enthalpy. The complex standard enthalpies are computed using the linear relationship. All relevant source code and data are available in the package's repository [11].

Case Study

We illustrate the applicability of this package with a case study on rare earth extraction equilibrium. For the experimental data, multiple extraction isotherm equilibrium datasets for rare earth-HCl-PC88A systems over ranges of feed pH, PC88A concentration, and rare earth concentration were gathered from the literature [14–21]. The dataset includes single-component data for neodymium (Nd), praseodymium (Pr), cerium (Ce), lanthanum (La), dysprosium (Dy), samarium (Sm), and yttrium (Y) and multicomponent combinations of Nd, Pr, Ce, and La. The aqueous phase is an H₂O-HCl-rare earth system, and the organic phase is a dodecane-PC88A-rare earth complex system. The extraction reaction is shown in Eq. 4, where M^{n+} represents the rare earth ion, $n(\text{HA})_{2,\text{org}}$ represents the extractant, and $M(\text{HA}_2)_{n,\text{org}}$ represents the rare earth-extractant complex.



This case study explores the effectiveness of three strategies—outlier filtering, Pitzer parameter fitting, and iterative fitting—for improving prediction accuracy using the datasets described above.

Outlier Filtering

We start with the hypothesis—based on observation—that some experimental data points unduly skew the model, causing an overall decrease in prediction accuracy. Then, for each single-component dataset, we implement the outlier filtering logic

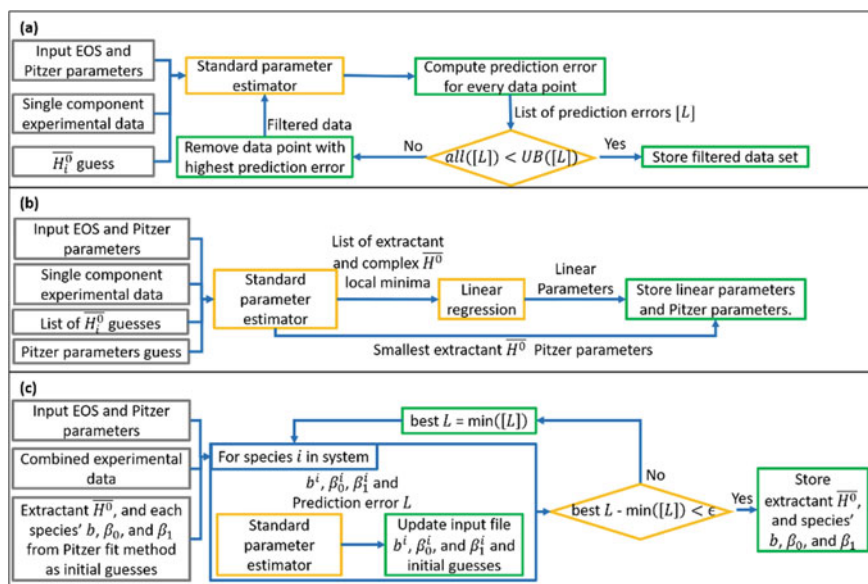


Fig. 3 Strategies to improve the basic fit method: **a** outlier filtering, **b** pitzer parameter fitting, and **c** iterative fitting. (Color figure online)

illustrated in Fig. 3a, which removes data points with high prediction error and returns a fit based on the resulting filtered dataset. After the estimator converges, it computes the prediction error for each data point and compares it to the upper bound, UB , estimated from Eq. 5, where LQ and UQ are, respectively, the lower and upper quartiles of the prediction error from the entire dataset.

$$UB = UQ + 3(UQ - LQ) \quad (5)$$

Data points with error greater than UB (extreme outliers) are removed [22], and the process repeats until there are no more outlier data points. The filtered single-component datasets are then used to estimate the linear parameters, allowing us to express the organo-metal complex enthalpies in terms of the extractant enthalpy. The final step then fits the extractant enthalpy using an unfiltered combined dataset.

Pitzer Parameter Fitting

Figure 3b illustrates the Pitzer parameter fitting strategy, an approach for estimating the Pitzer parameters for the metal chloride. For each species, we fit Pitzer coefficients— β_0 , β_1 , and C^ϕ —with initial guesses from May et al. [23] and linear parameters to the unfiltered single-component datasets. Unfiltered data are used because the Pitzer parameters account for interactions that may accurately predict previously

high-error data points. Our preliminary work showed that using Pitzer coefficients found at the local optima with the minimum extractant standard enthalpy yields the highest accuracy, so those Pitzer coefficients and obtained linear parameters are used in the basic estimator method to estimate the extractant standard enthalpy.

Iterative Fitting

As Fig. 3c illustrates, this approach sequentially fits the extractant enthalpy and linear and Pitzer parameters to the combined dataset for each species while keeping other species parameters constant. It iterates over this sequential loop until the difference between the last iteration and the lowest recorded prediction error value is greater than the tolerance ϵ . Experiments showed that species values for C^ϕ and the slope a should be kept at the values found in with the Pitzer parameter fitting strategy, leaving the fitting parameters to be the extractant enthalpy, intercepts, β_0 , and β_1 . We also tested a variant of this strategy that uses mean squared error (MSE) as the prediction error function. The initial guesses for this variant are the solutions found using iterative fitting with LMSE as the prediction error function.

Results

This case study compared the predictive accuracy of the three strategies—outlier filtering, Pitzer parameter fitting, and iterative fitting—with extraction equilibrium data for rare earth-HCl-PC88A systems. We observed that outlier filtering decreases the overall prediction error by reducing the skewing effect of outlier data points. We also found that fitting Pitzer parameters reduces prediction errors for most data points, especially those with higher feed concentrations. The iterative fitting strategy decreases the prediction error for multicomponent datasets but significantly increases the error for single-component datasets. This section highlights results for Pr, La, and Ce, but additional results and figures for Nd, Dy, Sm, and Y can be found in the repository [11].

Basic Fit Method Underpredicts Cases with High Feed Concentrations

To establish a baseline for the three strategies, the GEM-based thermodynamic parameter fitting method was implemented in Python and applied to the rare earth equilibrium dataset. For Pr predictions, the basic fit method (Fig. 4a) works well for data points with feed rare earth concentrations less than 0.05 mol/L, as the absolute

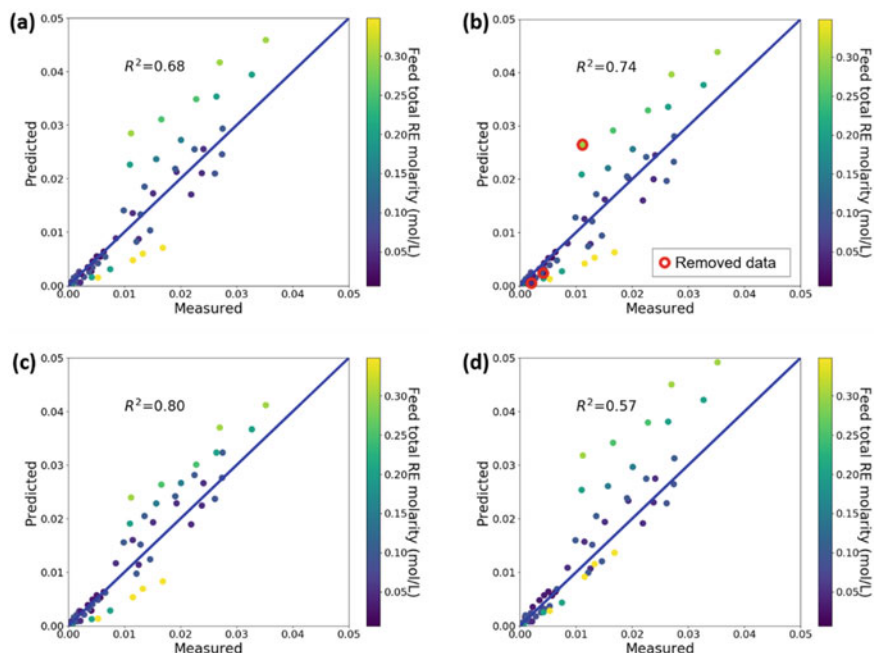


Fig. 4 Parity plots for predicted Pr organic-phase molarity over rare earth concentrations with different feeds, using the **a** basic fit method, **b** outlier filtering strategy, **c** Pitzer parameter fitting strategy, and **d** iterative fitting strategy. (Color figure online)

mean error is 0.001 mol/L. However, for feed concentrations above 0.05 mol/L, we observe that the prediction errors increase to an absolute mean error of 0.007 mol/L. Another issue is that the model typically overpredicts the organic-phase equilibrium concentration, with 14% more overpredicted than underpredicted points and 70% higher average overpredicted errors compared to underpredicted errors.

Outlier Filtering Improves Prediction Accuracy

To test the hypothesis that outlier data points partially explain the prediction error for the basic fit case, we applied outlier filtering while fitting to the single-component data by removing data points with high outlier prediction error. Three and one data points were removed from the Pr and Nd datasets, respectively. The outlier filtering strategy's prediction accuracy for Pr concentrations (Fig. 4b) increases the most, with the R-squared value increasing by 8%. R-squared values for Ce, Nd, and La insignificantly increase. Dy, Sm, and Y only have single-component data and therefore are not affected. By eliminating the outlier data points, the model predicts slightly higher

equilibrium concentrations for all the data points, as the two underpredicted points that were removed had pulled the model to predict lower values.

Pitzer Parameter Fitting Increases Prediction Accuracy for High Feed Concentrations

The basic fit method and outlier filtering strategy only account for electrolyte binary interaction parameters, since including reported metal chloride interaction parameters worsened the fits. Here we explore whether fitting interaction parameters for the metal ions would improve prediction accuracy. Results show that R-squared values for Pr, La, Dy, Sm, and Y increase by 18%, 10%, 22%, 6%, and 13%, respectively, compared to the basic fit method. The R-squared value for Ce decrease by 7% and for Nd, the change is insignificant. The Pr concentration parity plot (Fig. 4c) shows a larger reduction in prediction errors for high-feed rare earth concentrations (above 0.05 mol/L) with a 15% reduction in mean absolute error. Lower feed concentrations (below 0.05 mol/L) show a 9% reduction in mean absolute error.

However, the pitzer parameter fitting parity plot for La (Fig. 5a) shows that the model consistently underpredicts La concentrations for multicomponent datasets. The pitzer parameter fitting parity plot for Ce (Fig. 5b) shows that the model can predict the Kim dataset [16] relatively well but does poorly when predicting the Formiga dataset [17]. Examining the data, we noticed that the multicomponent data had feed concentration ranges (pH from 0.5 to 1 and PC88A concentrations from 0.1 to 2 mol/L) outside of the single-component data ranges (pH from 0.9 to 1 and one PC88A concentration at 1 mol/L). Since Pitzer and linear parameters are only fit to single-component data, these parameters had not been fitted to multicomponent ranges.

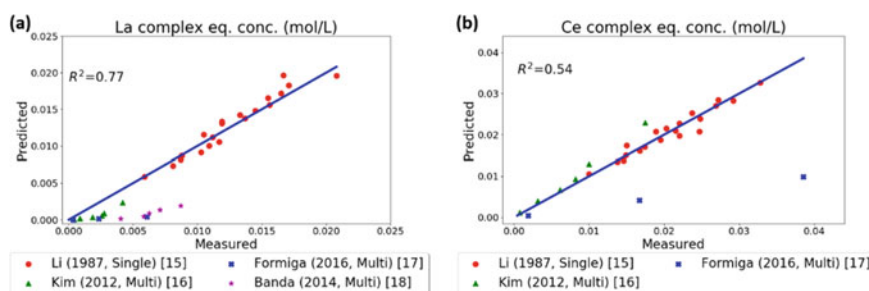


Fig. 5 Parity plots for organic-phase molarities, predicted by the Pitzer parameter fitting strategy, for **a** La and **b** Ce, labeled by experimental dataset and single- or multicomponent data. (Color figure online)

Iterative Fitting Increases Prediction Accuracy for Multicomponent Datasets

To decrease prediction error in multicomponent data, we implemented an iterative fitting strategy that fits extractant enthalpy, Pitzer parameters, and linear parameters to the combined dataset. However, the prediction error increased after applying this strategy. Results show that R-squared values for Pr and Ce decrease by 29%, 2% respectively, compared to the pitzer parameter fitting strategy. For La, the R-squared value is negative, suggesting a worse fit than the mean. The changes for Nd, Dy, Sm, and Y are less than 4% increase. The Pr parity plot (Fig. 4d) shows that the prediction error increases over all feed concentrations, with a 2% and 34% increase in mean absolute errors for low and high feed concentrations, respectively. This strategy decreases the multicomponent prediction errors by 29% but increases single-component prediction errors by 46%.

This strategy highlights two issues with using LMSE (Eqs. 2a, 2b) as the prediction error function. First, the function penalizes underpredictions more than overpredictions and results in more overpredictions. Second, the function computes relative error and thus weights big differences between large true and predicted values the same as small differences between small true and predicted values. Since the multicomponent Pr measurements are on average 70% smaller compared to single-component Pr measurements, fitting to multicomponent data results in large prediction error for high Pr measurements.

For the La parity plot (Fig. 6a), the model decreases the prediction error for both the Kim and Banda datasets [16, 18], but increases prediction error for the single-component Li dataset [15]. The parity plot for Ce (Fig. 6b) shows a relatively good fit to all the data except for the Formiga dataset [17].

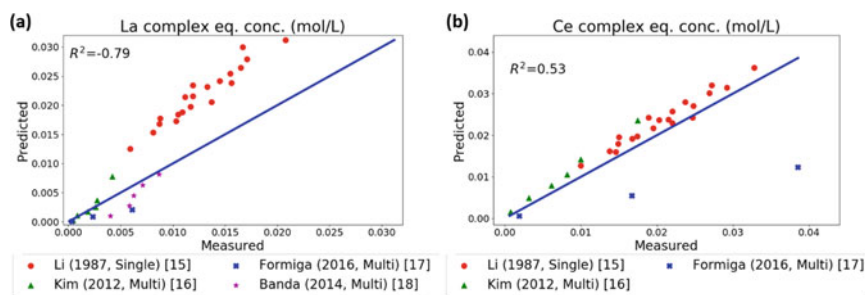


Fig. 6 Parity plots for organic-phase molarities, predicted by the iterative fitting strategy, for **a** La and **b** Ce, labeled by experimental dataset and single- or multicomponent data. (Color figure online)

Iterative Fitting with Mean Squared Error Increases Overall Prediction Accuracy

Since the prediction error function, Eqs. 2a, 2b, weights relative error, we explored the effect of changing the prediction error function to MSE, which penalizes absolute error but has fewer regions with a gradient and thus is more difficult to optimize. Our results show that R-squared values generally increase. The Ce R-squared value increases the most, becoming 54% greater compared to the Pitzer parameter fitting strategy, while Nd, Pr, Dy, and Y increase by 2–3%. R-squared values for La and Dy did not change much (0.9% and 0.4% decrease respectively). The organic-phase Pr, La, and Ce concentration parity plots (Fig. 7) show that the iterative fitting strategy with MSE gives similar fits to the Pitzer parameter fitting strategy, except for Ce (Fig. 7c), which shows decreased prediction error for the Formiga dataset [17]. Using the MSE also removes the penalty differences between over- and underprediction, resulting in 6% higher average underpredicted errors compared to overpredicted errors with Pr predictions. However, prediction errors for multicomponent La data are still high.

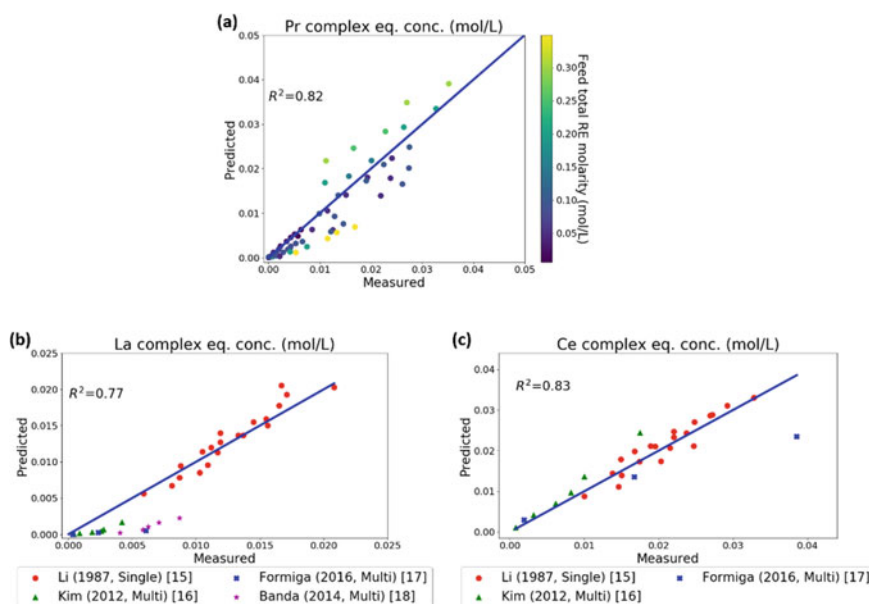


Fig. 7 Parity plots for organic-phase molarities, predicted by the iterative fitting strategy with MSE, for **a** Pr with various feed RE concentrations, **b** La by experimental dataset, and **c** Ce by experimental dataset. (Color figure online)

Discussion

In this study, we introduced LLEPE, a Python package for thermodynamic parameter estimation, and used it to comparatively assess the prediction accuracies of three strategies for GEM-based thermodynamic parameter estimation. Our results show that (a) applying the outlier filtering strategy increases the model's overall prediction accuracy by removing outlier data, (b) fitting metal chloride Pitzer parameters increases the prediction accuracy of the method, with prediction accuracy increasing more for data points with higher rare earth concentrations, and (c) while the iterative fitting strategy increases the prediction accuracy for multicomponent datasets, it decreases the prediction accuracy for single-component datasets. We find that changing the prediction error function in the iterative fitting strategy from LMSE to MSE further increases the prediction accuracy compared to the Pitzer parameter fitting strategy.

The results from the iterative fitting strategy suggest there are assumptions in the model that lead to prediction errors. One factor that was not considered is the effect of NaCl on the system. Some experiments, such as those underlying the Formiga dataset [17], used NaOH to adjust the pH, and others, like those underlying the Kim dataset [16], used a constant concentration of NaCl. Pfennig and Schwerin [24] showed that electrolytes have a significant impact on partition coefficients in liquid-liquid extraction, and Lee et al. [14] showed that in saponification, sodium will form a complex with the extractant. Thus, to accurately model the system, the solvation, binary interaction effects, and additional chemistry associated with the addition of NaCl should be included in the model.

Conclusion

In summary, the LLEPE package provides an accessible method for estimating thermodynamic parameters and offers helpful visualizations and analysis such as the parity plots and R-squared values. Using this package, the present study shows that the strategies explored—filtering outlier data, fitting Pitzer parameters, and iteratively fitting to data—are effective in increasing the prediction accuracy of the parameter estimation method and may be useful for future estimation of thermodynamic parameters for solvent extraction. Furthermore, iterative fitting with the MSE prediction error function is shown to have a high overall prediction accuracy.

Since the LLEPE package currently handles two-phase systems, future work could explore generalizing LLEPE to handle multiple phases, as well as other multicomponent separations applications beyond rare earth systems. Improvements to the model include accounting for electrolyte effects such as complex formation and binary interactions.

Acknowledgements The submitted manuscript has been created by UChicago Argonne LLC, Operator of Argonne National Laboratory (“Argonne”). Argonne National Laboratory’s work was

supported by the U.S. Department of Energy, Office of Energy Efficiency and Renewable Energy (EERE), under contract DE-AC02-06CH11357. The U.S. Government retains for itself, and others acting on its behalf, a paid-up nonexclusive, irrevocable worldwide license in said article to reproduce, prepare derivative works, distribute copies to the public, and perform publicly and display publicly, by or on behalf of the Government. The Department of Energy will provide public access to these results of federally sponsored research in accordance with the DOE Public Access Plan. This research used resources of the Argonne Leadership Computing Facility, which is a DOE Office of Science User Facility.

Conflict of Interest All the authors declare no conflict of interest.

References

1. Sharmila S, Rebecca LJ, Chandran PN et al (2015) Extraction of biofuel from seaweed and analyse its engine performance. *Int J Pharm Technol* 7:8870–8875
2. Paiva AP, Malik P (2004) Recent advances on the chemistry of solvent extraction applied to the reprocessing of spent nuclear fuels and radioactive wastes. *J Radioanal Nucl Chem* 261:485–496. <https://doi.org/10.1023/B:JRNC.0000034890.23325.b5>
3. Yang C, Qian Y, Zhang L, Feng J (2006) Solvent extraction process development and on-site trial-plant for phenol removal from industrial coal-gasification wastewater. *Chem Eng J* 117:179–185. <https://doi.org/10.1016/j.cej.2005.12.011>
4. Xie F, Zhang TA, Dreisinger D, Doyle F (2014) A critical review on solvent extraction of rare earths from aqueous solutions. *Miner Eng* 56:10–28
5. Mihaylov I (2003) Solvent extractants for nickel and cobalt: new opportunities in aqueous processing. *JOM* 55:38–42
6. Iloeje CO, Jové Colón CF, Cresko J, Graziano DJ (2019) Gibbs energy minimization model for solvent extraction with application to rare-earths recovery. *Environ Sci Technol* 53:7736–7745
7. Jové Colón CF, Moffat HK, Rao RR (2013) Modeling of liquid-liquid extraction (LLE) equilibria using gibbs energy minimization (GEM) for the system TBP–HNO₃–UO₂–H₂O–diluent. *Solvent Extr Ion Exch* 31:634–651
8. Rossi C, Cardozo-Filho L, Guirardello R (2009) Gibbs free energy minimization for the calculation of chemical and phase equilibrium using linear programming. *Fluid Phase Equilib* 278:117–128
9. Pitzer KS (1991) Ion interaction approach: theory and data correlation. *Acta Coeff Electrolyte Solut* 2:75–153
10. Helgeson HC, Kirkham DH (1974) Theoretical prediction of the thermodynamic behavior of aqueous electrolytes at high pressures and temperatures; I, Summary of the thermodynamic/electrostatic properties of the solvent. *Am J Sci* 274:1089–1198
11. Quah T, Iloeje CO (2020) LLEPE. <https://github.com/ANL-CEEESA/LLEPE.git>. Accessed 7 Sep 2020
12. Glasser L, Jenkins HDB (2004) Standard absolute entropies, S 298, from volume or density: part II organic liquids and solids. *Thermochim Acta* 414:125–130
13. Goodwin DG, Speth RL, Moffat HK, Weber BW (2018) Cantera: an object-oriented software toolkit for chemical kinetics, thermodynamics, and transport processes
14. Lee M-S, Lee J-Y, Kim J-S, Lee G-S (2005) Solvent extraction of neodymium ions from hydrochloric acid solution using PC88A and saponified PC88A. *Sep Purif Technol* 46:72–78
15. Li H, Chen Z, Meng S (1987) Extraction equilibria of individual rare earth in HEHEHP–kerosene–HCl–RECl₃ system. *J Chin Rare Earth Soc* 3
16. Soo Kim J, Nagaphani Kumar B, Lee JY et al (2012) Separation and recovery of light rare-earths from chloride solutions using organophosphorus based extractants. *Sep Sci Technol* 47:1644–1650

17. Formiga TS, de Morais CA (2016) Cerium separation from light rare earth concentrate by liquid-liquid extraction. *World J Eng Technol* 4:129–137
18. Banda R, Jeon HS, Lee MS (2014) Separation of Ce and La from synthetic chloride leach solution of monazite sand by precipitation and solvent extraction. *Metall Mater Trans B* 45:2009–2017
19. Lyon KL (2016) Separation of adjacent rare earth elements using solvent extraction. University of Idaho
20. Lyon KL, Utgikar VP, Greenhalgh MR (2017) Dynamic modeling for the separation of rare earth elements using solvent extraction: predicting separation performance using laboratory equilibrium data. *Ind Eng Chem Res* 56:1048–1056
21. Lee MS, Liu Y, Jeon HS (2016) Solvent extraction of Pr and Nd from chloride solution by mixtures of acidic extractants and LIX 63. *Korean J Met Mater* 54:592–597. <https://doi.org/10.3365/KJMM.2016.54.8.592>
22. Devore JL (2011) *Probability and statistics for engineering and the sciences*. Cengage Learning
23. May PM, Rowland D, Hefter G, Königsberger E (2011) A generic and updatable Pitzer characterization of aqueous binary electrolyte solutions at 1 bar and 25 C. *J Chem Eng Data* 56:5066–5077
24. Pfennig A, Schwerin A (1998) Influence of electrolytes on liquid–liquid extraction. *Ind Eng Chem Res* 37:3180–3188. <https://doi.org/10.1021/ie970866m>

Thermodynamic Modeling of Iron-Copper-Sulfuric Acid Solutions During Solvent Extraction and Electrowinning for Copper Production



Jiahao Xu and Guikuan Yue

Abstract Solvent extraction and electrowinning (SX/EW) play an important role during the hydrometallurgical production of copper for low-grade ores. To better understand the rapid Cu extraction/strip kinetics for producing a high-purity $\text{CuSO}_4\text{-H}_2\text{SO}_4$ electrolyte and elucidate the method to maximize current efficiency by preventing leach carryover to electrolyte during SX and minimizing the iron concentration, a detailed speciation study is required to quantitatively describe the iron and copper distribution in the SX/EW solutions. In the present study, by virtue of our previous modeling work, thermodynamic modeling of the SX/EW solutions is carried out to quantify the distribution of iron (in the form of ferric and ferrous), copper, and sulfuric acid. The developed model provides a mathematical tool capable of quantifying the concentrations of free ions and complexes in terms of temperature (25–60 °C) and solution composition under simulated industrial conditions. Finally, oxidation reduction potential measurements are employed to validate the model.

Keywords Speciation · Iron · Copper · Sulfuric acid · Solvent extraction · Electrowinning · Redox potential

Introduction

Hydrometallurgical processing of copper ores accounts for around 20% of global primary copper production. The production via this method is about 4.5 million tons in 2010 and is steadily increasing due to the associated advantages such as the possibility of treating low-grade ores (increasingly more abundant in the case of copper) [1–3]. Pregnant leaching solution (PLS) generated by leaching during the process is purified and upgraded by solvent extraction (SX) to provide sufficiently conductive

J. Xu (✉) · G. Yue (✉)

Department of Metallurgical, Materials and Biomedical Engineering, The University of Texas at El Paso, 500 W University Ave, El Paso, TX 79968, USA

e-mail: jxu3@miners.utep.edu

G. Yue

e-mail: gyue@utep.edu

electrolyte (45–55 g/L Cu, 175–190 g/L H_2SO_4) for the following electrowinning (EW) where high-purity cathode copper is electrodeposited. The combined technology of SX-EW makes hydrometallurgical process as a commercial alternative to pyrometallurgical process, and becomes more and more important as more copper is being produced by the leaching of much lower grade copper ores [1].

To produce high-purity copper cathode and increase the current efficiency in EW, impurities (such as Fe, Mn, and Cl) in the electrolyte provided by SX must be minimized by appropriate extractant that are very selective for Cu over other cations, especially Fe [1, 3]. Current efficiency is one of the key parameters for maximizing copper plating rate and minimizing electrical energy consumption and ranges from 85–95% in modern Cu EW plants [4]. Typically, the reduction of ferric ion at the EW cathode lowers the current efficiency for plating of copper by 2.5% for each 1 g/L Fe, and 5 g/L ferric ion in the EW electrolyte can make the current efficiency drop to as low as 80% [5, 6].

Clearly, a better understanding for iron (ferrous and ferric) and copper distribution in solutions during SX/EW is very important for the production of high-purity $\text{CuSO}_4\text{--H}_2\text{SO}_4$ electrolyte and for minimizing iron concentration. Hence, a detailed speciation study is required to quantitatively describe the species distribution in SX/EW solutions.

In a previous work, a thermodynamic model was developed and proved to reliably simulate the speciation of $\text{H}_2\text{SO}_4\text{--Fe}_2(\text{SO}_4)_3\text{--FeSO}_4\text{--H}_2\text{O}$ system through a wide range of solution compositions and temperatures related to leaching [2]. The model was validated by accurate prediction of measured redox potential, and a novel redox potential equation (shown in the following section) was also developed. Additionally, when CuSO_4 is further dissolved in the acidic iron sulfate solution, species such as Cu^{2+} , CuSO_4° , CuHSO_4^+ will be formed according to the literature [7–9]. Hence, the related thermodynamic data were collected and reviewed for model calculation [7–12]. Especially, in our previous publication, thermodynamic modeling of $\text{Fe(II)–Fe(III)–Cu(II)–H}_2\text{SO}_4\text{–H}_2\text{O}$ system was carried out under conditions most relevant to the copper electrorefining [12].

The current work aims to extend the broader range of applicability of the previous developed model of $\text{Fe(II)–Fe(III)–H}_2\text{SO}_4\text{–H}_2\text{O}$ and $\text{Fe(II)–Fe(III)–Cu(II)–H}_2\text{SO}_4\text{–H}_2\text{O}$ systems to solutions during SX/EW. It is also of interest to determine whether developed ORP equation remains applicable under those conditions. It is expected that this speciation work will facilitate the development of combined SX-EW technology to achieve higher current efficiency.

Model Development

As mentioned in the previous section, thermodynamic modeling of $\text{Fe(II)–Fe(III)–H}_2\text{SO}_4\text{–H}_2\text{O}$ system and $\text{Fe(II)–Fe(III)–Cu(II)–H}_2\text{SO}_4\text{–H}_2\text{O}$ system has been carried out under conditions related to leaching and electrorefining [2, 12]. In this work,

Table 1 Standard and calculated equilibrium constants for the main species in aqueous Fe(II)–Fe(III)–H₂SO₄–H₂O Solutions in the range of 25–60 °C by Criss–Cobble method

Species and Formation Reactions	Log K_f° 25 °C	Log K_f° 35 °C	Log K_f° 40 °C	Log K_f° 45 °C	Log K_f° 50 °C	Log K_f° 55 °C	Log K_f° 60 °C
$H^+ + SO_4^{2-} \leftrightarrow HSO_4^-$	1.98	2.13	2.20	2.27	2.34	2.41	2.49
$Fe^{2+} + H^+ + SO_4^{2-} \leftrightarrow FeHSO_4^+$	1.08	1.42	1.59	1.75	1.91	2.07	2.22
$Fe^{2+} + SO_4^{2-} \leftrightarrow FeSO_4^\circ$	2.25	2.33	2.37	2.42	2.46	2.50	2.54
$Fe^{3+} + H^+ + SO_4^{2-} \leftrightarrow FeHSO_4^{2+}$	2.48	2.90	3.11	3.30	3.50	3.68	3.87
$Fe^{3+} + 2SO_4^{2-} \leftrightarrow Fe(SO_4)_2^-$	5.38	4.29	4.78	5.26	5.73	6.18	6.62
$Fe^{3+} + SO_4^{2-} \leftrightarrow FeSO_4^+$	4.04	4.35	4.50	4.65	4.79	4.94	5.08
$Cu^{2+} + SO_4^{2-} \leftrightarrow CuSO_4^\circ$	2.36	2.46	2.52	2.57	2.62	2.67	2.72
$Cu^{2+} + H^+ + SO_4^{2-} \leftrightarrow CuHSO_4^+$	2.34	2.69	2.86	3.02	3.18	3.34	3.49

we will further employ the methods developed previously to evaluate the possibility of extending its applicability to conditions most relevant to the industrial SX/EW process. Details for the model development could be found in the previous publication. Only the key additional information will be provided in the following.

The calculated equilibrium formation constants of main reactions in this study from 25 to 60 °C were shown in Table 1. Information such as species concentrations and redox potentials can thus be obtained or calculated [2, 12].

Additionally, an expression Eq. (1) was developed to accurately predict redox potential in the H₂SO₄–Fe₂(SO₄)₃–FeSO₄–H₂O solutions only based on nominal ferric/ferrous ratio and temperature. From previous results, it seems that this new expression could be extended to more complicated acidic iron sulfate solutions with or without copper [2, 13, 14]. Thus, this expression was applied to compare calculated potentials with experimental potentials in this work.

$$E(\text{mV}) = -1 \times 10^{-3} \times [T(K)]^2 + 0.91 \times T(K) + \frac{2.303R}{nF} \times T(K) \times 10^3 \times \log \frac{C_{\text{ferric, nominal}}}{C_{\text{ferrous, nominal}}} + 492 \quad (1)$$

Table 2 Compositions of synthetic SX solution, g/L

Sample	[H ₂ SO ₄]	[Fe ³⁺]	[Fe ²⁺]	[Cu ²⁺]	Nominal [Fe ³⁺]/[Fe ²⁺]
#1	200	0.01	1	0	0.01
#2	200	1	1	0	1
#3	200	0.01	1	30	0.01
#4	200	0.01	1	40	0.01
#5	200	1	1	30	1
#6	200	1	1	40	1

Table 3 Compositions of synthetic EW solution, g/L

Sample	[H ₂ SO ₄]	[Fe ³⁺]	[Fe ²⁺]	[Cu ²⁺]	Nominal [Fe ³⁺]/[Fe ²⁺]
#7	180	3.5	1	0	3.5
#8	180	2.4	0.4	0	6
#9	180	3.5	1	45	3.5
#10	180	3.5	1	50	3.5
#11	180	3.5	1	55	3.5
#12	180	2.4	0.4	45	6
#13	180	2.4	0.4	50	6
#14	180	2.4	0.4	55	6

Experimental

Electrolyte Preparation

In the present study, the overall composition of both synthetic SX solutions and Cu EW solutions was determined according to the operating conditions of industrial processes. The detailed information is shown in Tables 2 and 3. The nominal ferric/ferrous ratio in this paper is the ratio of the initial total ferric to initial total ferrous added when preparing the solution. The real ferric/ferrous ratio in the electrolyte is typically lower than its corresponding nominal ferric/ferrous ratio after speciation calculation, and details for this could be found in our previous publication [2].

Electrochemical Measurement

Details on the redox potential measurement by electrochemical method (including the procedure and potential correction) can be found in previous publication [2, 12–14].

Results and Discussion

Calculated Species Distribution in Fe(II)–Fe(III)–H₂SO₄–H₂O System from 25 to 60 °C

The results of the aqueous speciation (expressed as the percentage of the total ferric or ferrous) in aqueous Fe(II)–Fe(III)–H₂SO₄ solution from 25 to 60 °C are presented in Fig. 1. The results of species distribution for the solutions with four different nominal Fe³⁺/Fe²⁺ ratios are similar to each other. Fe(II) species mainly distribute as free Fe²⁺ cations which account for 73.5–77.7% of the total Fe(II). FeHSO₄⁺ is in the smallest proportion 3.8% at 25 °C, and then gradually increases up to 16.3% at 60 °C. FeSO₄⁰ is the second dominant species at 25 °C initially (about 19.2%), and then decreases to about 10.1% eventually at 60 °C.

For Fe(III) species, free Fe³⁺ accounts for only 2.1–7.6%. The percentage of FeHSO₄²⁺ ranges from 14.4% to 34.3%. The percentage of Fe(SO₄)₂⁻ is around 0.4%–11.9%. However, the distribution of this species strongly is dependent on temperature and total amount of Fe(III). Similar observation was also found in the published literature [2, 8, 9, 12]. FeSO₄⁺ is the predominant species for Fe(III) and takes the proportion of 58.4–73.4% of total Fe(III).

Additionally, the predominant species of Fe(II) and Fe(III) are free Fe²⁺ and FeSO₄⁺, which is similar to the results from the literature published previously [2, 12].

Calculated Species Distribution in Fe(II)–Fe(III)–Cu(II)–H₂SO₄–H₂O System from 25 to 60 °C

Figure 2 shows the results of the aqueous speciation in Fe(II)–Fe(III)–Cu(II)–H₂SO₄–H₂O solutions for synthetic SX from sample #3 to sample #6 and for synthetic EW from sample #9 to sample #14 with various solution composition from 25 to 60 °C. It shows that the overall percentage trend of each Fe(II) and Fe(III) species does not have any substantial change after CuSO₄ was added. The percentage of free ferrous cations is within 67.7–74.2%, which is slightly lower than that in Fe(II)–Fe(III)–H₂SO₄–H₂O system. The proportion of FeHSO₄⁺ is within 3.9–16.3% which is nearly equal to that of Fe(II)–Fe(III)–H₂SO₄–H₂O solution. The percentage of FeSO₄⁰ is in the range of 12.6–26.7% and is slightly larger than that in the Fe(II)–Fe(III)–H₂SO₄–H₂O system.

For Fe(III) species, free ferric cations and FeHSO₄²⁺ only account for a minor proportion, about 1.3–6.1% and 10.8–29.5%, which are slightly lower than those in Fe(II)–Fe(III)–H₂SO₄–H₂O system. FeSO₄⁺ remains the predominant species of Fe(III), with a percentage of 61.6–79.8%. The percentage of Fe(SO₄)₂⁻ is in the range of 0.5–19.3%, which is similar to the results from the literature published previously [2, 12].

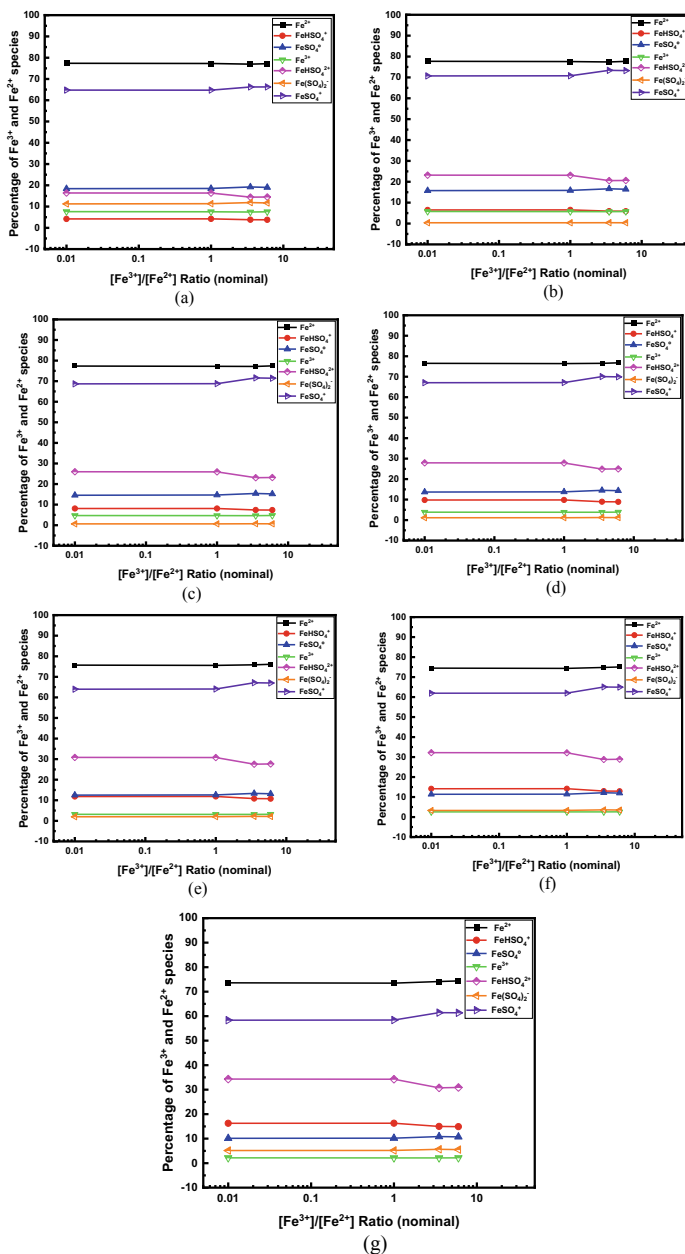


Fig. 1 Calculated aqueous speciation diagram of the main ferric and ferrous species in the Fe(II)–Fe(III)–H₂SO₄–H₂O solutions for synthetic SX with sample #1, sample #2 and for synthetic EW with sample #7, sample #8 in the temperature range from 25 °C to 60 °C with **a** temperature 25 °C; **b** temperature 35 °C; **c** temperature 40 °C; **d** temperature 45 °C; **e** temperature 50 °C; **f** temperature 55 °C; and **g** temperature 60 °C. Please note that the sum of the percentage values of both Fe(II) species (filled symbols) and Fe(III) species (half-filled symbols) are 100%. (Color figure online)

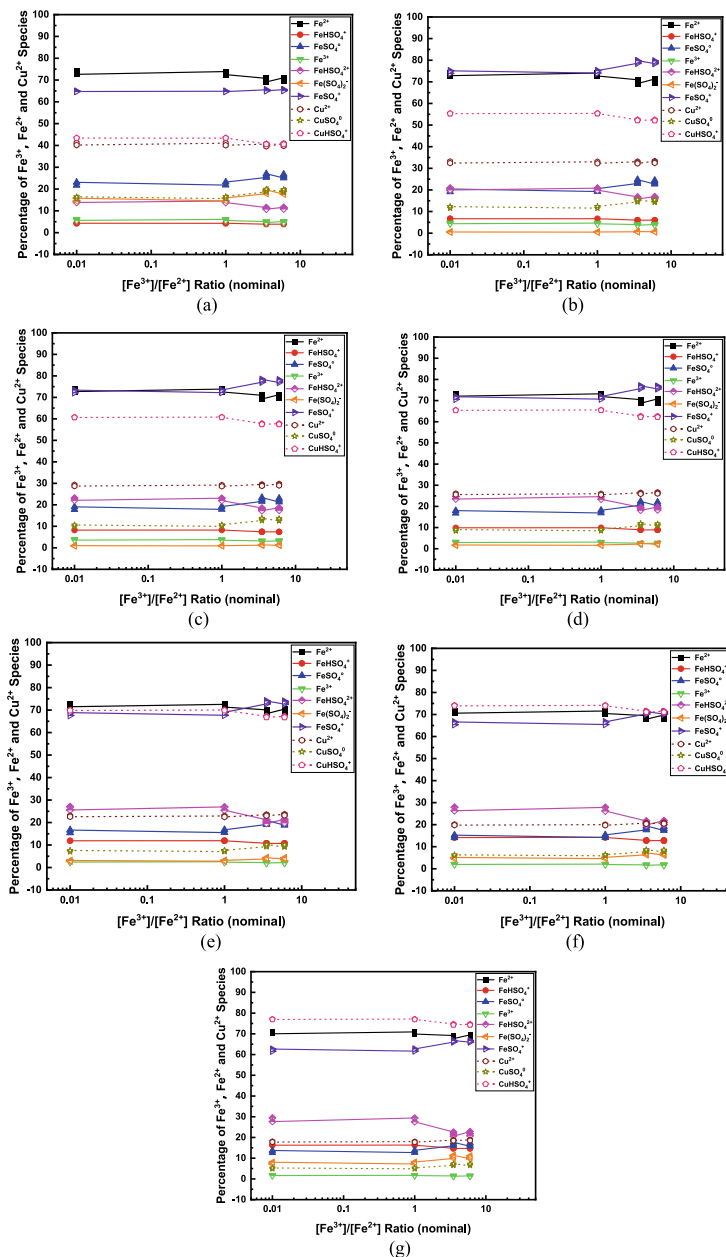


Fig. 2 Calculated aqueous species distribution diagram in the Fe(II)–Fe(III)–Cu(II)– H_2SO_4 – H_2O solutions for synthetic SX from sample #3 to sample #6 and for synthetic EW from sample #9 to sample #14 with **a** temperature 25 °C; **b** temperature 35 °C; **c** temperature 40 °C; **d** temperature 45 °C; **e** temperature 50 °C; **f** temperature 55 °C; and **g** temperature 60 °C. Please note that the sum of the percentage values of Fe(II) species (filled symbols), Fe(III) species (half-filled symbols), and Cu(II) species (unfilled symbols) are 100%. (Color figure online)

Cu(II) species mainly distributes as Cu^{2+} , CuSO_4^0 , and CuHSO_4^+ , with the proportion of 17.7%–41.7%, 4.9%–19.9%, and 40.5%–77.1%, respectively. CuSO_4^0 is the least abundant species and its proportion decreases when increasing temperature. The second most abundant Cu(II) species is free Cu^{2+} and its percentage decreases when increasing temperature. A considerable proportion of Cu(II) exists as CuHSO_4^+ and its proportion increases with temperature.

Comparison of Redox Potential Between Model Result and Experimental Measurement from 25 to 60 °C

A comparison of the reversible potentials between experimental measurement and model calculation was employed to validate the model. As shown in Figs. 3a and 4a, the redox potentials predicted by the model and measured by experiment are in good agreement under different nominal $\text{Fe}^{3+}/\text{Fe}^{2+}$ ratios in both synthetic Fe(II)–Fe(III)– H_2SO_4 – H_2O solution and Fe(II)–Fe(III)–Cu(II)– H_2SO_4 – H_2O solution from 25 to 60 °C. The difference between experimental and calculated values was typically around ± 5 mV depending on solution composition and temperature. This proves that the model is qualitatively and quantitatively validated. Therefore, a conclusion can be drawn that the predicted species distribution are correct for both Fe(II)–Fe(III)– H_2SO_4 – H_2O and Fe(II)–Fe(III)–Cu(II)– H_2SO_4 – H_2O solutions in the temperature and composition ranges investigated in the present work.

In addition, Eq. (1) has been proved to accurately predict redox potential in Fe(II)–Fe(III)– H_2SO_4 – H_2O system over a wide range of solution composition [2, 14]. The comparison of measured potential by experiment and calculated potential by Eq. (1) in the present study are employed to validate its broad applicability as well. Figures 3b

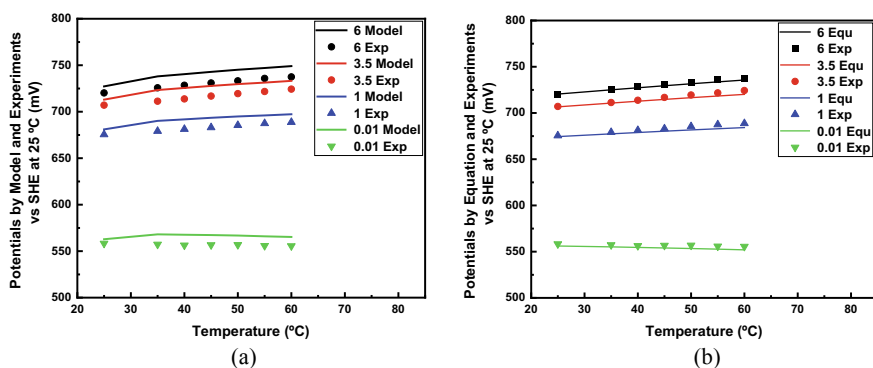


Fig. 3 Comparison of potentials **a** calculated by thermodynamic modeling and measured by experiment, and **b** calculated by Eq. (1) and measured by experiment vs SHE at 25 °C with various nominal $\text{Fe}^{3+}/\text{Fe}^{2+}$ ratios and temperature from 25 to 60 °C in Fe(II)–Fe(III)– H_2SO_4 – H_2O solutions (for synthetic SX and EW conditions). (Color figure online)

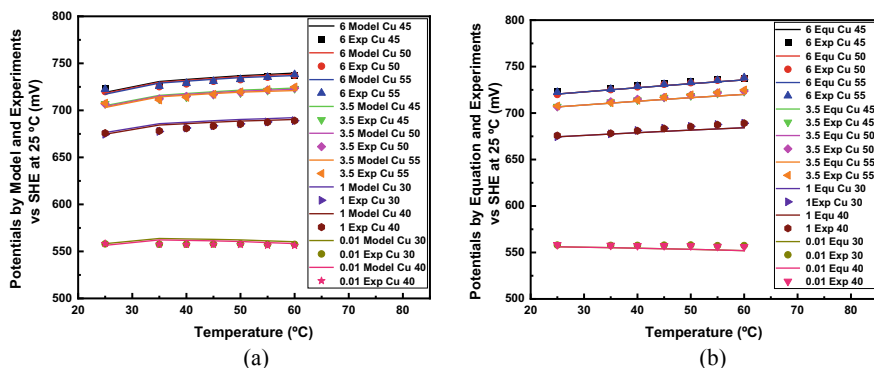


Fig. 4 Comparison of potentials **a** calculated by thermodynamic modeling and measured by experiment, and **b** calculated by Eq. (1) and measured by experiment vs SHE at 25 °C with various nominal $\text{Fe}^{3+}/\text{Fe}^{2+}$ ratios and temperature from 25 °C to 60 °C in $\text{Fe(II)-Fe(III)-Cu(II)-H}_2\text{SO}_4\text{-H}_2\text{O}$ solutions (for synthetic SX and EW conditions). (Color figure online)

and 4b show that the experimental potentials in the present study are in an excellent agreement with those calculated by Eq. (1). The potential difference is generally less than 1.5 mV under nominal $\text{Fe}^{3+}/\text{Fe}^{2+}$ ratios ranging from 0.01 to 6 with the concentrations of copper and sulfuric acid varying from 0 to 55 g/L and from 180 to 200 g/L, respectively. Therefore, a conclusion could be drawn that the expression developed previously can also be employed to accurately predict the redox potential in complicated solutions for SX/EW in this work.

Conclusions

The speciation of $\text{Fe(II)-Fe(III)-H}_2\text{SO}_4\text{-H}_2\text{O}$ and $\text{Fe(II)-Fe(III)-Cu(II)-H}_2\text{SO}_4\text{-H}_2\text{O}$ solutions was investigated by thermodynamic modeling under conditions related to SX/EW. Results reveal that most of the Fe(III) is distributed as complexes and the free Fe^{3+} accounts for only a minor percentage, whereas a large amount of Fe(II) exists in the form of free Fe^{2+} . The Cu(II) species mainly distributes as Cu^{2+} , CuSO_4^0 , and CuHSO_4^+ , and a considerable proportion of Cu(II) exists as CuHSO_4^+ . The validity of the proposed model was confirmed by reliable prediction of measured redox potential from 25 to 60 °C. The fact that there exists an excellent agreement between the redox potential calculated by previously developed equation and measured by this work, further extends its applicability and provides an alternative method of predicting redox potential. It is expected that the findings in this work will facilitate the development of combined SX/EW technology to achieve higher current efficiency.

Acknowledgements The authors acknowledge the financial support of The University of Texas at El Paso, Engineering STARs Program Funding from The University of Texas System, and Freeport-McMoRan Inc.

Conflict of Interest The authors declare that they have no conflict of interest.

References

1. Schlesinger ME, King MJ, Sole KC, Davenport WG (2011) Extractive metallurgy of copper. Elsevier, Amsterdam
2. Yue G, Zhao L, Olvera OG, Asselin E (2014) Speciation of the $\text{H}_2\text{SO}_4\text{-Fe}_2(\text{SO}_4)_3\text{-FeSO}_4\text{-H}_2\text{O}$ system and development of an expression to predict the redox potential of the $\text{Fe}^{3+}/\text{Fe}^{2+}$ couple up to 150 °C. *Hydrometallurgy* 147–148:196–209
3. ICSG (2010) Directory of copper mines and plants 2008–2013. Lisbon, Portugal: International Copper Study Group. <https://www.icsg.org>
4. Robinson T et al. (2008) Copper solvent extraction 2007 world operating data. Paper presented at International solvent extraction conference ISEC 2008, Tucson, Arizona, USA, 15–19 Sept 2008
5. Dew DW, Philips CV (1985) The effect of Fe(II) and Fe(III) on the efficiency of copper electro-winning from dilute acid Cu (II) sulphate solutions with the chemelec cell. *Hydrometallurgy* 14:331–367
6. Moats M, Khourabchia Y (2009) Effective diffusivity of ferric ions and current efficiency in stagnant synthetic copper electro-winning solutions. *Miner Metall Process* 26(4):179–186
7. Casas JM, Alvarez F, Cifuentes L (2000) Aqueous speciation of sulfuric acid-cupric sulfate solutions. *Chem Eng Sci* 55:6223–6234
8. Casas JM, Etchart JP, Cifuentes L (2003) Aqueous speciation of arsenic in sulfuric acid and cupric sulfate solutions. *AIChE J* 49(8):2199–2210
9. Cifuentes L, Casas JM, Simpson J (2006) Temperature dependence of the speciation of copper and iron in acidic electrolytes. *Chem Eng Res Des* 84(A10):965–969
10. Powell KJ, Brown PL, Byrne RH, Gajda T, Hefter G (2007) Chemical speciation of environmentally significant metals with inorganic ligands part 2: the $\text{Cu}^{2+}\text{-OH}^-$, Cl^- , CO_3^{2-} , SO_4^{2-} , and PO_4^{3-} systems. *Pure Appl Chem* 79(5):895–950
11. Akilan C (2008) Thermodynamic and related studies of aqueous copper(II) sulfate solutions. Ph.D. thesis. Murdoch University, West Australia
12. Dong Y et al (2019) Speciation of iron-arsenic-copper-sulfuric acid solution during copper electrorefining from 25 to 70 °C. Paper presented at the COM 2019, Vancouver, BC, Canada, 21–23 Aug 2019
13. Yue G, Guezennec A, Asselin E (2016) Extended validation of an expression to predict ORP and iron chemistry: application to complex solutions generated during the acidic leaching or bioleaching of printed circuit boards. *Hydrometallurgy* 164:334–342
14. Xu J et al. (2019) Extended validation of an expression to predict ORP: application to pregnant leaching solution generated during heap leaching and copper electro-winning solution. Paper presented at the COM 2019, Vancouver, BC, Canada, 21–23 Aug 2019

Part IV
Metal Processing and Manufacturing

An Experimental Study on the Melting Temperature of Mould Flux Under Electromagnetic Field



Yijia Wang, Mingxing Wang, Li Zhao, and Yu Wang

Abstract The silicate-based molten slag plays a crucial role in the process of continuous casting as functional materials. In the present study, the influences of electromagnetic field intensity and frequency on melting temperature of mould flux are revealed by an experimental method. To achieve this, a conductivity electrode and a measurement device are implemented to measure the melting temperatures under various magnetic field intensities and frequencies. The tested results show that with the increasing of magnetic field intensity (0–30 mT), the melting temperature of mould flux increases by 11–12 K. When the magnetic field intensity is 20 mT, the frequency increases by 6 Hz, and the melting temperature of the slag is increased by 0.4–1.6 K. Additionally, it is found that according to the melt solidification theory, the potential barrier requires to be overcome when the flux melts from liquid phase to solid phase, and the barrier can be weakened when electromagnetic force is applied.

Keywords Mould flux · Electromagnetic field intensity · Frequency

Introduction

Electromagnetic fields have been widely used in the continuous casting process, especially for the electromagnetic stirring technology [1, 2]. Electromagnetic force can lead to the directional flow or turbulent flow, which causes the change in the flow and temperature fields. Therefore, the electromagnetic fields play a crucial role in improving the surface quality and the internal quality of beam blank. On the other hand, the mould flux is a typical silicate structure, which displays the electrical conductivity to some extent under high-temperature condition. As the result, the ion arrangement and distribution in the mould flux would be changed due to the applied external electromagnetic fields [3], which affects the performances, including the heat transfer and the lubrication, during the continuous casting process.

Y. Wang · M. Wang · L. Zhao · Y. Wang (✉)

College of Materials Science and Engineering, Chongqing University, Chongqing 400044, China
e-mail: wangyu@cqu.edu.cn

© The Minerals, Metals & Materials Society 2021

J. Lee et al. (eds.), *Materials Processing Fundamentals 2021*, The Minerals, Metals & Materials Series, https://doi.org/10.1007/978-3-030-65253-1_11

Table 1 Basic chemical composition of the mould flux and basicity

CaO/%	SiO ₂ /%	Al ₂ O ₃ /%	MgO/%	CaF ₂ /%	Na ₂ O/%	MnO/%	FeO/%	R
39.57	39.49	3.33	4.84	4.29	5.41	2.96	0.12	1.00

Table 2 Chemical composition of mould flux with varying basicity in the experiment (wt%)

NO	CaO	SiO ₂	Al ₂ O ₃	MgO	CaF ₂	Na ₂ O	MnO	FeO	R	Basicity
R-1	39.92	39.08	3.23	4.89	4.35	5.46	2.95	0.12	1.02	1.18
R-2	40.27	38.73	3.23	4.89	4.35	5.46	2.95	0.12	1.04	1.20
R-3	40.65	38.35	3.23	4.89	4.35	5.46	2.95	0.12	1.06	1.22
R-4	41.02	37.98	3.23	4.89	4.35	5.46	2.95	0.12	1.08	1.24

According to the study of Xingjuan Wang et al. [4], the high-frequency electromagnetic field had a significant effect on the overall morphology of the mould flux film. The mould flux film has changed from the original two-layer structure form of crystalline layer–glass layer to a three-layer structure form of crystalline layer–glass layer–crystalline layer which influences the melting temperature of mould flux. In this study, an experiment was performed at the self-developed test system to identify the influence of the magnetic field intensity and frequency on the melting temperature of the mould flux. Furthermore, the content of CaO/SiO₂ was adjusted in each test to evaluate the role of the basicity on the melting temperature of the mould flux.

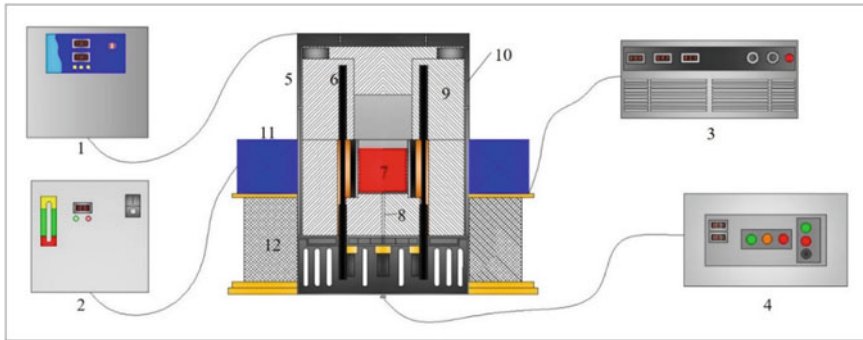
Experimental Details

Materials of the Mould Flux

Based on the previous research basis of our group, the mould flux used in the process of producing slabs was applied in the present experiment. The chemical composition is listed in Table 1. The chemical compositions of the mould flux with various basicity, which can be achieved by adjusting the content of CaO/SiO₂, in the current experiment are summarized in Table 2.

Test System

Figure 1 shows the schematic of the performance test system for the mould flux considering magnetic field. The crucible furnace and the electromagnetic stirring device are curial, where the crucible furnace is used to heat the slag and the electromagnetic stirring device is used to generate the alternating magnetic field.



1 - Crucible furnace water cooler; 2 - Electromagnet water cooler; 3 - Electromagnet power supply; 4 - Crucible furnace control cabinet; 5 - Furnace wall; 6 - Silicon molybdenum rod; 7 - Crucible; 8 - Thermocouple; 9 - Insulation layer; 10 - Water cooling layer; 11 - Electromagnet; 12 - Electromagnet

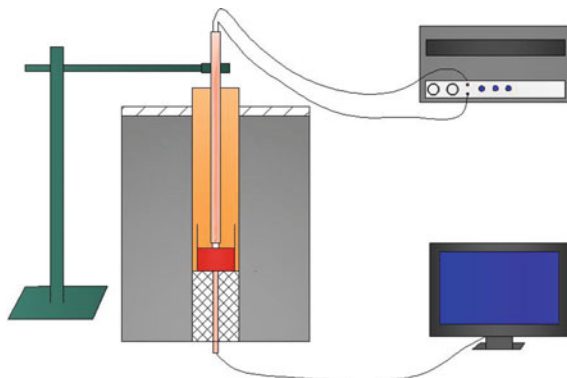
Fig. 1 Schematic of the performance test system for mould flux considering alternating magnetic field. (Color figure online)

Test Method

In the present test, the conductance electrode method [5] was adopted to measure the melting temperature of the mould flux. The schematic of the test device is depicted in Fig. 2. It is noteworthy that the measuring principle of conductance electrode method is based on the ionic properties of the melting at different temperatures and electrical conductivities of the mould flux. Additionally, the generated electrical signals during the test may be interfered by the electromagnetic fields. Therefore, it is necessary to perform a preliminary experiment to analyse the magnitude of the effect of the electromagnetic field on the measurements for the conductance electrode method.

Based on our preliminary experiment, in order to eliminate the interference of electromagnetic field, the maximum and minimum voltages fluctuations at each temperature were recorded separately, and the recorded values were drawn and fitted

Fig. 2 Device diagram of conductance electrode method. (Color figure online)



to calculate the corresponding temperature. Let E_{\max} and E_{\min} denote the electrode voltages of start and end measurement, respectively. Based on the abovementioned measurement principle, the relationship between the voltage and the temperature is plotted in Fig. 3. The relationship between the voltage and the temperature can be fitted as the following expression, and the fitting factor $R^2 = 0.91853$.

$$E = -505.81488 + 3.6163T - 0.00212T^2 \quad (1)$$

As shown in Fig. 3, the melting temperature is the x-coordinate where the slope is highest, which is when the conductivity changes most rapidly. Subsequently, the melting temperature can be defined as the following expression

$$T_c = f\left(\frac{E_{\max} - E_{\min}}{2}\right) \quad (2)$$

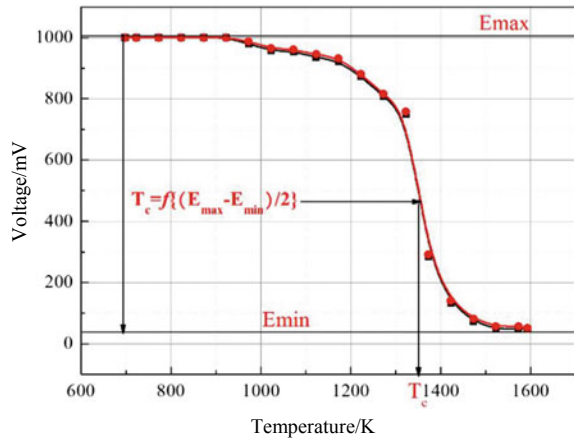
$$f = 1463.48 + 0.7026E - 0.00129E^2 \quad (3)$$

Results and Discussion

Effects of the Magnetic Field Intensity

Figures 4 and 5 show the effect of different magnetic field intensity and basicity on the melting temperature of the mould flux at a frequency of 8 Hz. The magnetic field is generated by alternating current through the coil, and the magnetic intensity is adjusted by adjusting the current. The melting temperature increased about 11–12 K

Fig. 3 Relationship between the voltage and the temperature. (Color figure online)



(100.76–100.90%) with the magnetic field intensity increasing from 0 to 30mT at different basicity. The increment of the melting temperature with the basicity ranges from 1.06 to 1.08 is larger than that with the basicity ranges from 1.02 to 1.04 and from 1.04 to 1.06, revealing that the increased magnitude of the melting temperature raises with the increasing basicity of the mould flux. The effect of magnetic field intensity on melting temperature is less than that of basicity.

As shown in Fig. 5, the melting temperature of the mould flux gradually increases with the increase of the basicity. The melting temperature is risen about 48–49 K with the basicity increasing from 1.02 to 1.08 at different magnetic field intensities. The increasing trend of the melting temperature of mould flux is approximately identical with the increasement of the magnetic field intensity. This is because that the CaO of mould flux is prone to combine with other components to generate crystalline mineral with high melting point (such as anorthite and dicalcium silicate), thereby resulting the rise of melting temperature [6].

Fig. 4 Effects of the magnetic field intensity on the melting temperature of the mould flux under different basicity. (Color figure online)

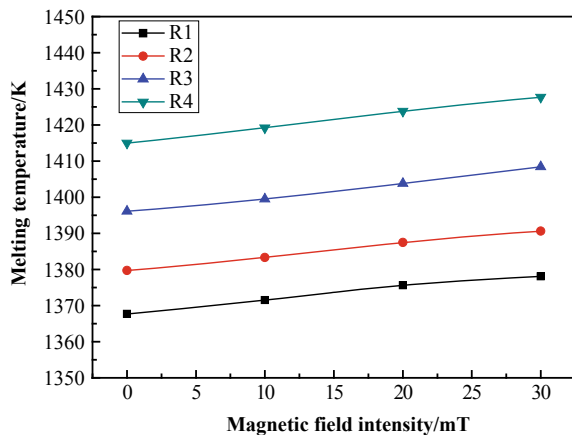
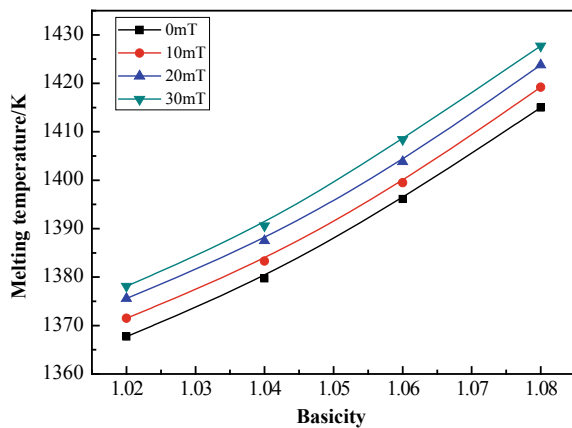


Fig. 5 Effects of the basicity on the melting temperature of the mould flux under different magnetic field intensities. (Color figure online)



Effects of the Magnetic Field Frequency

The effects of the magnetic field frequency and basicity on the melting temperature of the mould flux when the magnetic field intensity is 20 mT are shown in Figs. 6 and 7, respectively. Although the melting temperature of the mould flux slightly increases with the increase of the magnetic field frequency, it basically tends to be flat, as shown in Fig. 6. For the mould fluxes with different basicity, the melting temperature increases around 0.41–1.6 K when the magnetic field frequency increases from 6 to 12 Hz. When the basicity raises from 1.06 to 1.08, the increment of the melting temperature is greater than that when the basicity increases from 1.02 to 1.04 and 1.04 to 1.06, indicating that the increasing magnitude of the melting temperature of the mould flux rises with the increase in the basicity.

As demonstrated in Fig. 7. The melting temperature of the mould flux increases with the increase of basicity. Furthermore, Fig. 7 shows the melting temperature of

Fig. 6 Effects of magnetic field frequency on melting temperature of the mould flux under different basicity. (Color figure online)

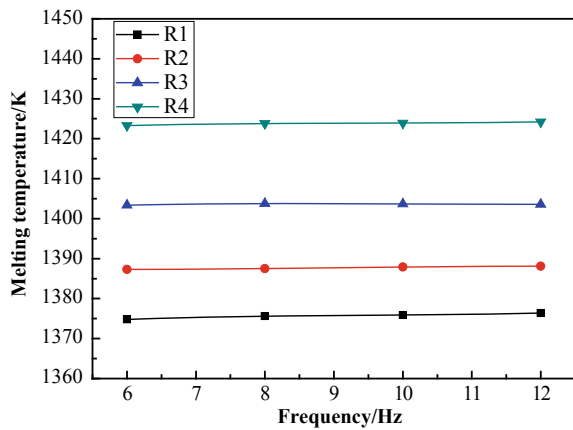
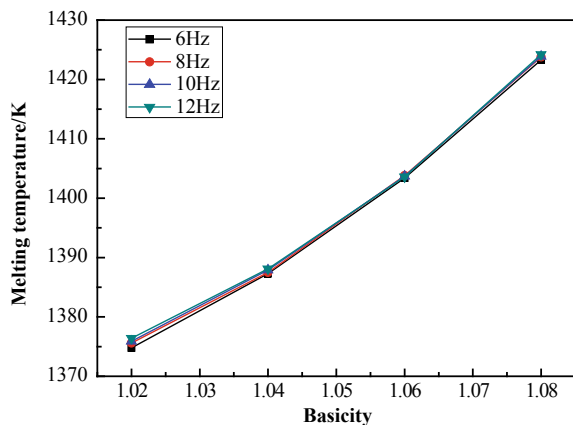


Fig. 7 Effects of the basicity on the melting temperature of the mould flux under different magnetic field frequencies. (Color figure online)



the mould flux which increases about 48 K as the basicity of mould flux increases from 1.02 to 1.08 under different magnetic field frequencies. It is evident that the increasing trend of the melting temperature of the mould flux is basically the same when the frequency varies from 6 to 12 Hz. The reason for the abovementioned results may be that the changing magnitude of the field frequency is relatively small, thereby resulting in the limited effect on the melting temperature among various magnetic field frequencies.

Conclusion

In this paper, an experimental study was performed to explore the effects of the magnetic field intensity and frequency on the melting temperature of the mould flux during continuous casting process under different basicity. Based on the experimental observations, the following conclusions can be drawn:

- (1) In the present experiment, the melting temperature of the mould flux gradually increases with the increasing magnetic field intensity and frequency. More specifically, when the frequency and intensity of the magnetic field equal 8 Hz and 30 mT, respectively, the melting temperature of the mould flux increases around 11–12 K. When the frequency and intensity of the magnetic field equal 6 Hz and 20 mT, respectively, the melting temperature of the mould flux increases around 0.4–1.6 K.
- (2) Compared with the magnetic field intensity, the melting temperature of the mould flux is less sensitive to the magnetic field frequency. The melting temperature of the mould flux is increased with the increase in the basicity. Furthermore, the applied alternating magnetic field can facilitate in reducing the barrier when the mould flux transforms from liquid phase to solid phase.

Acknowledgements This work was financially supported by National Natural Science Foundation of China (project No. 50274078) and Sharing Fund of Large Scale Equipment, Chongqing University (project No. 201512150025).

References

1. Ren ZM, Deng K, Jiang GC (2002) Development of electromagnetic continuous casting processing with soft-contact mold. *J Iron and Steel Res* 14(1):58–63
2. Nakata H, Inoue T, Mori H (2002) Improvement of billet surface quality by ultra-high-frequency electromagnetic casting. *ISIJ Int* 42(3):264
3. Mills KC, Fox AB (2003) The role of mould fluxes in continuous casting so simple yet so complex. *ISIJ Int* 43(10):1479–1486
4. Wang X, Jin H, Zhu L, Liu R, Song T (2020) Effect of high-frequency electromagnetic field on microstructure of mold flux. *High Temp Mater Processes* 39(1)

5. Xiuli Z (2006) Research on the melting temperature of mold powder measured with electrode. Dongbei University
6. XingJuan W, Liguang Z, Ran L, Xiangming J (2013) Viscosity properties of flux under high frequency electromagnetic field. Iron Steel Vanadium Titanium 34(02):79–83

Effect of Dissolution of Titanium Ions on Ti Alloys Electrodeposition from EMIC-AlCl₃ Ionic Liquid at Low Temperature



Pravin S. Shinde and Ramana G. Reddy

Abstract In this work, the dissolution of Ti ions from a sacrificial Ti anode during electrolysis on the reduction behavior of Ti–Al alloy electrodeposits from a Lewis acidic eutectic mixture of 1-ethyl-3-methylimidazolium chloride (EMIC) and a 0.667-mol fraction of aluminum chloride (AlCl₃) is investigated. The Ti ions are dissolved in EMIC–AlCl₃ ionic liquid (IL) by potentiostatic and galvanostatic electrolysis using chronoamperometry (CA) and chronopotentiometry (CP) techniques, respectively. At the same time, the electrodeposition of the Ti–Al alloy is accomplished on the copper cathode electrode at 383 K using the Ti anode. The dissolution, concentration, and deposition of Ti species are controlled by varying the electrolysis current, potential, and the electrolysis duration (1–3 h). The electrochemical reduction behavior of Ti and Al ions is studied on all Pt wire electrodes using cyclic voltammetry (CV). SEM studies revealed homogeneous and crystalline Ti–Al electrodeposits for CP-electrolysis. EDS and XRD revealed 16 at % Ti with a cubic Ti_{0.12}Al_{0.88} phase of Ti–Al alloy obtained from 1 h CP-electrolysis. The Ti content in Ti–Al alloy decreased with an increase in electrolysis time.

Keywords Ti alloy · Electrodeposition · EMIC–AlCl₃ ionic liquid · Electrochemistry · CV · CA · CP

Introduction

Titanium (Ti), because of its highest strength-to-weight ratio, is an essential alloying agent with many metals, including aluminum, molybdenum, and iron. Such alloys find larger applications, including aircraft, spacecraft, and missiles. Because of the excellent corrosion-resistant property, Ti is widely used in medical industries, especially for bone compatibility and surgeries. Ti production by the Kroll process invented in the 1940s has been the known primary method [1]. Despite excellent thermomechanical and corrosion-resistance properties, Ti production is expensive and

P. S. Shinde · R. G. Reddy (✉)

Department of Metallurgical and Materials Engineering, The University of Alabama, Tuscaloosa, AL 35487, USA

e-mail: reddy@eng.ua.edu

© The Minerals, Metals & Materials Society 2021

J. Lee et al. (eds.), *Materials Processing Fundamentals 2021*, The Minerals, Metals & Materials Series, https://doi.org/10.1007/978-3-030-65253-1_12

141

difficult to extract and machine [2]. Electrochemical synthesis from low-temperature ionic liquid (IL) electrolytes is one of the fascinating methods of producing Ti metal or its alloys [3]. Unfortunately, the electrochemical mechanism for pure titanium deposition is more complicated than other metals such as aluminum because of its different oxidation states (II, III, and IV). Therefore, it is often electrodeposited in the form of alloys, such as titanium aluminide (Ti–Al). The electrodeposition of Ti and Ti–Al alloys has been performed via an energy-efficient and cost-effective extraction process using the molten chloride salt electrolytes [4–8]. Understanding the electrochemistry of Ti ions in the IL can provide ways to improve the Ti-rich deposition of Ti–Al alloy. The electrochemical studies of TiCl_4 in a strongly Lewis acidic room-temperature molten salt showed that Ti^{4+} is reducible to Ti^{3+} and Ti^{2+} in two steps with one-electron charge transfer each, while Ti^{3+} was deposited at the electrode as a passivating dark thin film layer, mostly as TiCl_3 organic salt [9]. Alternatively, Stafford et al. [10] studied the electrochemistry of titanium using a $2\text{AlCl}_3\text{-NaCl}$ electrolyte in which the oxidation of titanium yielded Ti(II), Ti(III), and Ti(IV) complexes. The divalent species Ti(II) led to electrodeposit Ti–Al alloys, while the trivalent species are sparingly soluble. Despite several attempts to deposit phase-pure Ti, it only resulted in the co-deposition of Al and Ti. Nevertheless, the low-temperature electrochemical synthesis of Ti–Al alloys using IL is not only energy-efficient but also eliminates high-temperature melting and consolidation processes.

The electrodeposition of Ti alloys from chloroaluminate-based alkyl imidazolium chloride IL electrolyte is very challenging because of complex Ti electrochemistry and passivation of electrode surface with the TiCl_3 layer [11–15]. For instance, in an IL of EMIC and AlCl_3 , several anion species such as $[\text{AlCl}_4]^-$, $[\text{Al}_2\text{Cl}_7]^-$, and $[\text{Al}_2\text{Cl}_{10}]^-$ with different concentrations are in equilibrium for a given mole fraction (X_{Al}) of AlCl_3 . The amount of X_{Al} dictates the acidity or basicity of electrolyte and impacts the electrodeposition conditions. At higher AlCl_3 ($X_{\text{Al}} > 0.5$), the electrolyte mainly possesses AlCl_4^- and Al_2Cl_7^- species exhibiting Lewis acidic properties primarily due to coordinately unsaturated Al_2Cl_7^- species [16]. The electrochemical deposition of Al from such chloroaluminate ILs has been reported to be mainly due to contribution from the diffusion of Al_2Cl_7^- species [12, 17, 18]. The electrochemical process of reduction of Al-species in the ILs is relatively well studied. Acidic IL compositions are active for Al plating and stripping at the anode, according to the reversible redox reaction given below [12, 19].



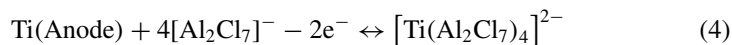
We previously electrodeposited Ti–Al alloys from BMIC- AlCl_3 - TiCl_4 (1:2:0.019 molar ratio) at different applied potentials and temperatures (343–398 K) using Ti foils as cathode and anode, and Ti wire as a reference electrode [20]. The possible reactions are given by Eqs. (2–5).

Cathode reactions:





Anode reactions:



The composition of a solvent-fused salt has a dramatic influence on electrodeposition process of titanium [21–23]. The deposition of pure Ti or its alloy from inorganic and organic melts and ILs is encountered with obstacles of controlling the electrolytes made by dissolving the titanium salts. Addition of salts like TiCl_4 involves its sublimation at elevated temperatures, unwanted disproportionation reaction of titanium ions and formation of passivating TiCl_3 layer resulting into titanium oxide deposition.

To counter most of the mentioned issues, titanium ions can be incorporated into EMIC- AlCl_3 IL by electrochemically controlled dissolution. So far, there are no reports on electrochemical studies on the behavior of dissolution and deposition of Ti species to deposit Ti–Al alloy without the addition of TiCl_4 . In our previous work, the potentiostatic electrodeposition of smooth, compact, and dendrite-free growth of Ti–Al alloy on the copper substrate was demonstrated at -1.3 V versus Ti for 1 h using BMIC- AlCl_3 IL ($X_{\text{Al}} = 0.667$) at low temperature [18]. However, the effect of higher concentrations of Ti species on the Ti–Al deposit compositions was not studied. Furthermore, only the potentiostatic mode was used to dissolve and electrodeposit the Ti–Al alloy.

In this work, it is demonstrated how the dissolution of Ti ions from sacrificial Ti anode during electrolysis and their concentration in the Lewis acidic eutectic ionic liquid mixture of 1-ethyl-3-methylimidazolium chloride and aluminum chloride (EMIC- AlCl_3) affects the electrodeposition behavior of Ti–Al alloy. Then, the electrochemical reduction behavior of Ti and Al ions on Pt wire electrodes is studied using the CV technique by varying the CA and CP-electrolysis durations. The objectives of this research work are to investigate the dissolution and solubility of Ti ions in EMIC- AlCl_3 IL and to determine the underlying reduction mechanism and to characterize surface morphology and composition of the Ti–Al electrodeposits.

Experimental

Preparation of EMIC- AlCl_3 Ionic Liquid

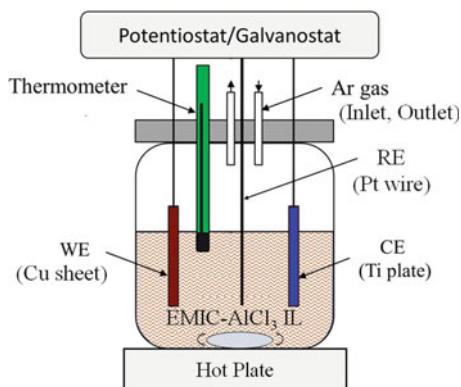
The chemicals such as anhydrous AlCl_3 (95+%, Alfa Aesar) and organic chloride salt 1-ethyl-3-methylimidazolium chloride (EMIC, 95%, Sigma-Aldrich) were

purchased and used without further treatment. The Pt wire (0.5 mm diameter, 99.99%) was obtained from Sigma-Aldrich company. Pure titanium sheet (2 mm thick, 99.99%) was obtained from Alfa Aesar[®]. The ultrahigh pure (UHP) Argon gas (99.999%) was obtained from Airgas. All chemical reagents were handled in a dry atmosphere. The eutectic mixture of Lewis acidic EMIC- AlCl_3 IL was prepared by mixing a 1:2 molar ratio (AlCl_3 mole fraction, $X_{\text{Al}} = 0.667$) of EMIC and AlCl_3 in a pyrex beaker at room temperature under constant stirring for 30 min until a clear homogeneous solution was obtained. $X_{\text{Al}} = 0.667$ was chosen to maximize the concentration of Al_2Cl_7^- anion species crucial for metal electrodeposition from the EMIC- AlCl_3 IL. The desired amount of clear IL solution is then transferred to the 50 mL electrochemical Pyrex cell placed on a hot plate, and IL was stirred for several minutes using a magnetic stirrer at 60 RPM to achieve a stable temperature of 383 K for further electrochemical studies.

Electrochemical Measurements

All electrochemical measurements were performed from EMIC- AlCl_3 IL at 383 K using cyclic voltammetry (CV), chronoamperometry (CA), and chronopotentiometry (CP) techniques with the help of an EG&G PARC model 273A potentiostat/galvanostat workstation controlled by Power Suite software. The electrochemical cell for the measurements consisted of a 40 mL Pyrex[®] glass beaker fitted with Teflon/Perspex cover, which has provisions for inserting the electrodes, thermometer, and inert gas inlet/outlets, as shown schematically in Fig. 1. A conventional three-electrode cell (Fig. 1) was used for these measurements. The Ti ions are hard to dissolve in EMIC- AlCl_3 ionic liquid even after putting a Ti slab in it at 383 K. Therefore, the electrolysis approach was chosen to dissolve Ti ions from the metallic Ti counter electrode as a sacrificial anode electrode and incorporate in the EMIC- AlCl_3 IL. The dissolution of Ti ions to deposit Ti-Al alloy was performed by potentiostatic

Fig. 1 Schematic of the experimental setup for CA- and CP-electrolysis from EMIC- AlCl_3 IL. (Color figure online)



(constant potential) and galvanostatic (constant current) electrolysis for different durations (1, 2, and 3 h) using CA and CP techniques, respectively. For electrolysis, copper sheet ($2 \times 2 \times \sim 0.25$ cm, 99%, Sigma-Aldrich) served as working electrode (WE), Ti plate ($2 \times 2 \times \sim 2$ cm, 99.99%, Sigma-Aldrich) served as the counter electrode (CE), and Pt wire (0.05 cm diameter, >99.99%, Alfa Aesar) as a quasi-reference electrode (q-RE). The CV measurements were performed before and after CA-electrolysis, and after CP-electrolysis using all Pt electrodes as WE, CE, and q-RE. The working distance between WE and CE was 2 cm. The temperature was controlled by a hot plate and was precisely monitored by the inserted thermometer. The Ar gas flow was continuously maintained through the alumina tube during the experiment.

Before electrochemical measurements, all the electrodes were polished with 800-grit SiC abrasive paper, rinsed thoroughly with deionized water, cleaned in an ultrasonic bath for 5 min, and dried by air to remove any residual impurities. The height of the electrodes immersed in the IL was measured after each experiment. Ti–Al alloy was deposited on copper plate by CA-electrolysis from EMIC- AlCl_3 ($X_{\text{Al}} = 0.667$) IL electrolyte at 383 K at a fixed applied potential of -1.5 V versus Pt and by CP-electrolysis at 10 mA cm^{-2} for 1, 2, and 3 h durations. The electrodeposited Ti–Al alloy electrodes were characterized using structural, morphological, and compositional techniques such as scanning electron microscopy (SEM) on Thermo Scientific™ Apreo scanning electron microscope equipped with energy dispersive spectroscopy (EDS), and X-ray diffraction (XRD) on a Bruker D8 Discover X-ray diffractometer with GADDS by employing monochromatic $\text{Co K}\alpha$ radiation.

Results and Discussion

Cyclic Voltammetry of Ti-Free EMIC- AlCl_3 IL

The cyclic voltammetry is used to study the electron transfer process for Al deposition from freshly prepared EMIC- AlCl_3 IL at different scan rates before potentiostatic CA-electrolysis to dissolve Ti ions. A standard three-electrode configuration cell with three Pt wires was used as working, counter, and quasi-reference electrodes.

Figure 2a shows a typical CV recorded from EMIC- AlCl_3 IL ($X_{\text{Al}} = 0.667$) on a polished Pt wire electrode at 383 K. The potential is swept at 300 mV s^{-1} from open-circuit potential (OCP) to -2.0 V versus Pt, where Al (III)-complex $[\text{Al}_2\text{Cl}_7]^-$ ions are reduced to Al (0) and then reversed back to OCP. The electrodeposition (reduction) of Al commences at -1.34 V versus Pt and reaches the maximum current at -1.75 V. After this peak potential, the current decreases until the reversal of potential, indicating the drop in the concentration of electroactive Al_2Cl_7^- species near the electrode. During the anodic potential sweep, the occurrence of a broad stripping peak at -0.64 V corresponds to the oxidation of the Al (0) electrodeposited during the cathodic sweep. Additionally, the CV shows the distinct redox peaks in

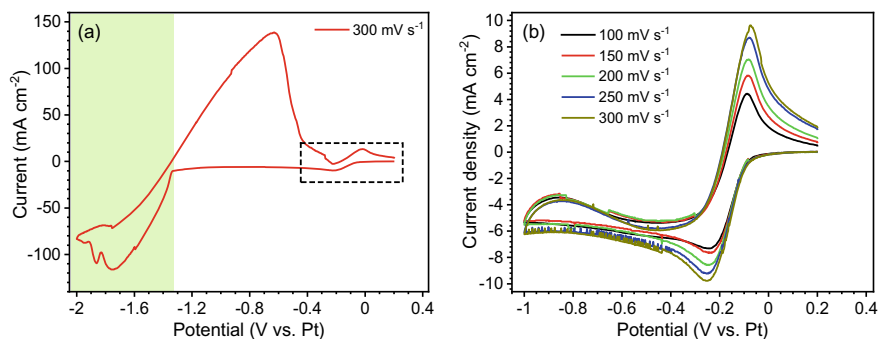


Fig. 2 **a** A typical CV recorded on polished Pt wire from EMIC- AlCl_3 IL at the scan rate of 300 mV s^{-1} at 383 K showing cathodic deposition of Al and its subsequent anodic stripping during the reverse direction. **b** CV curves recorded in the potential range from OCP to -1 V versus Pt at different scan rates ($100\text{--}300 \text{ mV s}^{-1}$), indicating UPD deposition and stripping of Al. (Color figure online)

the potential range from 0 to -0.8 V . It is reported that Ti can be reduced (from Ti^{4+} to Ti^{2+}) from Ti-containing chloroaluminate ionic liquid in the potential from 0 to -1.0 V versus Pt [24]. Hence, the CV curves were recorded from EMIC- AlCl_3 IL with and without Ti ions dissolved electrochemically by CA and CP modes at different hours. Figure 2b shows the CV curves recorded from Ti-free EMIC- AlCl_3 IL at different scan rates ($100\text{--}300 \text{ mV s}^{-1}$) at 383 K. Please note that these CVs were recorded before recording the extended CV shown in Fig. 1a. The potential is varied from open-circuit potential to -1.0 V versus Pt. The CVs show a cathodic peak at -0.25 V versus Pt, which can be ascribed to the underpotential deposition (UPD) of aluminum, and its corresponding counterpart anodic peak on the reverse scan at -0.08 V versus Pt is attributed to stripping of UPD Al. Similar UPD behavior is observed by several researchers [25–27]; however, the mechanism of UPD is still unclear. It is reported that UPD is responsible for nanocrystalline growth of Al, while the broader redox peaks followed by UPD are responsible for microcrystalline or bulk growth of Al in the electrodeposit [26].

Electrochemical Dissolution of Ti Ions by CA-Electrolysis

After recording CVs from EMIC- AlCl_3 IL, the Ti ions were incorporated into it employing electrolysis using a pure Ti plate as anode and Cu sheet as a cathode. The two methods of electrolysis, potentiostatic chronoamperometry (CA) and galvanostatic chronopotentiometry (CP), were employed at different durations. The cathode and anode electrodes were weighed before and after each electrolysis to account for the amount of Ti ions stripped from the Ti anode and the amount of Ti–Al material deposited onto the Cu cathode electrode.

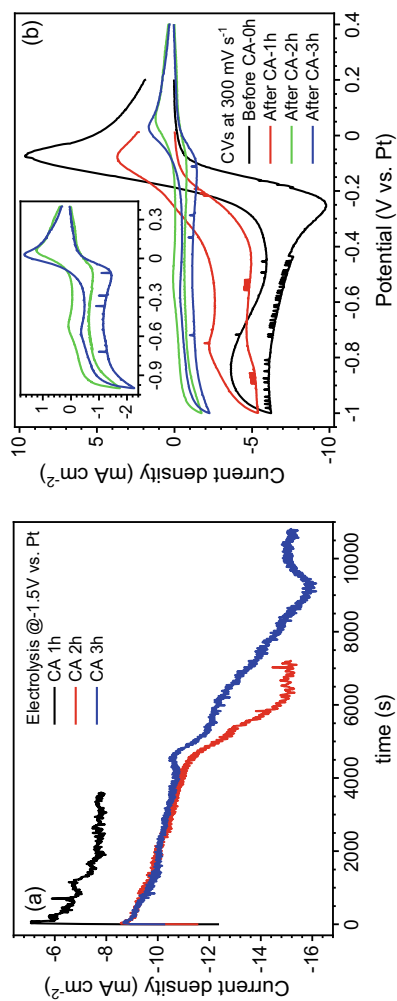


Fig. 3 **a** CA-electrolysis curves for 1, 2, and 3 h durations on Cu cathode at -1.5 V versus Pt. **b** Overlay of representative CVs recorded before and after CA-electrolysis for different durations at 300 mV s^{-1} at 383 K . The inset shows the magnified view of CV curves recorded for 2 and 3 h CA-electrolysis time. (Color figure online)

Table 1 Weight gain and loss of Cu cathode and Ti anode electrodes during CA and CP-electrolysis at different times

Electrolysis mode	Duration (h)	Weight gain of Cu cathode due to Ti–Al deposition (Wt.%)	Weight loss of Ti anode due to the stripping of Ti ions (Wt.%)
CA	1	0.25	0.57
CA	2	2.34	2.05
CA	3	3.05	3.40
CP	1	0.89	0.78
CP	2	2.85	1.82
CP	3	2.97	2.90

Figure 3a shows CA-electrolysis curves for 1, 2, and 3 h durations carried out independently with identical experimental conditions. The current density increases over time. The current density rises sharply after about 75 min as seen for 2 and 3 h CA-electrolysis. Electrolyte temperature plays role in shifting the deposition potential to less negative values. Rise in temperature of the EMIC-AlCl₃ IL causes increase in mobility of the electroactive [Al₂Cl₇][−] and Ti[(Al₂Cl₇)₄]^{2−} species toward the Cu cathode electrode surface leading to an increase of the reaction rate. The reason for temperature rise due to exothermic electrochemical reactions during higher electrolysis durations needs to be investigated. In general, the conductivity and viscosity of ionic liquids are strongly dependent on temperature [28]. The weight loss and gain percentages of Ti anode and Cu cathode with varying CA-electrolysis time are shown in Table 1. The wt. % of Cu cathode increases with electrolysis time, due to the Ti–Al deposition. At the same time, the Ti ions released by Ti anode in EMIC-AlCl₃ IL increases with time as indicated by wt. % loss of Ti anode.

Figure 3b shows the representative CVs recorded in separate experiments before and after CA-electrolysis for different durations at 300 mV s^{−1} at 383 K. Before CA-electrolysis, the typical UPD redox peaks are seen. However, with the increasing duration of CA-electrolysis, the current density of UPD peaks decreases. Moreover, new redox peaks emerge in the potential range from −0.9 to −0.7 V versus Pt, which corresponds to the deposition of Ti species (reduction of Ti₄₊ to Ti₂₊). The current density for Ti peaks (along with UPD Al) decreases with CA-electrolysis time despite the continuous release of Ti ions in IL, suggesting a saturation limit to form the Ti complex with [Al₂Cl₇][−] ions. As a result, despite the higher concentration of Ti ions released in IL by Ti anode, significantly less Ti[(Al₂Cl₇)₄]^{2−} ions are available for co-electrodeposition of Ti along with Al. The primary electrodeposition process proceeds at more negative potentials to deposit microcrystalline or bulk Al (around −1.5 V vs. Pt).

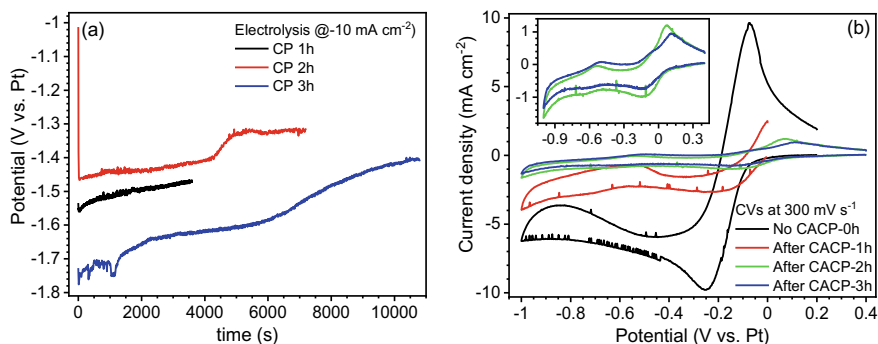


Fig. 4 **a** CP-electrolysis curves for 1, 2, and 3 h durations on Cu cathode at a constant current density. **b** Overlay of representative CVs recorded before and after CA-electrolysis for different durations at 300 mV s^{-1} at 383 K . The inset shows the magnified view of CV curves recorded for 2 and 3 h CP-electrolysis time. (Color figure online)

Electrochemical Dissolution of Ti Ions by CP-Electrolysis

After recording CA-electrolysis, the CP electrolysis was performed from Ti-enriched EMIC- AlCl_3 IL using a fresh Ti plate as anode and Cu sheet as a cathode.

Figure 4a shows the CP-electrolysis curves for 1, 2, and 3 h durations carried out independently with identical experimental conditions. The potential fluctuates initially in the range of -1.45 and -1.75 V versus Pt and decreases over time as the more Ti-Al gets deposited on the Cu cathode. Figure 4b shows the representative CVs recorded in separate experiments before and after CA and CP-electrolysis for different durations at 300 mV s^{-1} at 383 K . Similar to CA-electrolysis, the current density of UPD Al and Ti decreases with the increasing duration of CP-electrolysis. However, the Ti redox peaks are more evident in the potential range from -0.9 to -0.7 V versus Pt (see inset of Fig. 4b). Again, a drop in current density could be due to the availability of limited concentration of $\text{Ti}[(\text{Al}_2\text{Cl}_7)_4]^{2-}$ ions, and CP electrolysis is driven mainly by Al deposition at higher electrolysis time.

Morphological and Compositional Analysis by SEM-EDS

SEM and EDS analyses were performed to examine the morphology and chemical composition of the electrodeposits. Figure 5abc shows SEM images of Ti-Al electrodeposits obtained from CA-electrolysis. For 1 h, the Ti-Al electrodeposit shows uniform coverage of large grains with several cracks. With increasing time, the crack disappears, forming a continuous layer. Homogeneous and smooth deposits are seen for 3 h. The morphology of Ti-Al deposits obtained by CP-electrolysis is compact and crystalline (Fig. 5def). Ti-Al deposit from 3 h CP-electrolysis reveals $2\text{--}3 \mu\text{m}$ size

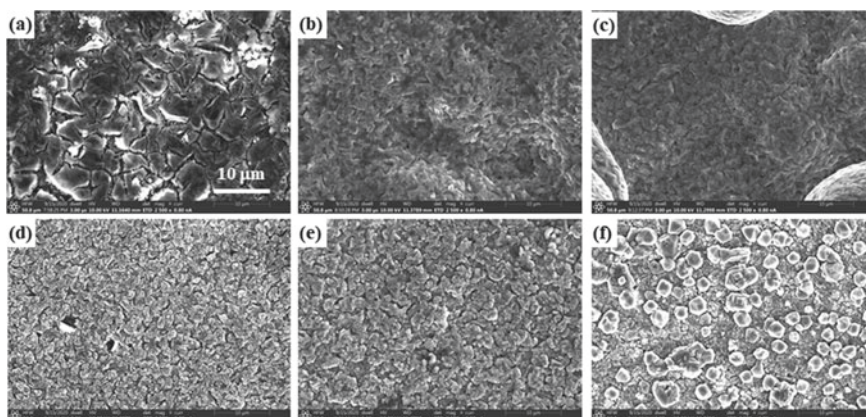


Fig. 5 Surface morphologies of Ti–Al alloys on Cu substrate by potentiostatic electrodeposition for **a** 1 h, **b** 2 h, and **c** 3 h, and galvanostatic electrodeposition for **d** 1 h, **e** 2 h, and **f** 3 h. Magnification: 2500X

grains crystallized on top of the continuous Ti–Al layer. Such crystallization could be due to a rise in temperature of the EMIC–AlCl₃ IL due to exothermic reaction.

Figure 6 shows the EDS spectra obtained from a selected area (2500X) of Ti–Al electrodeposits obtained from CA- and CP-electrolysis for different durations. As

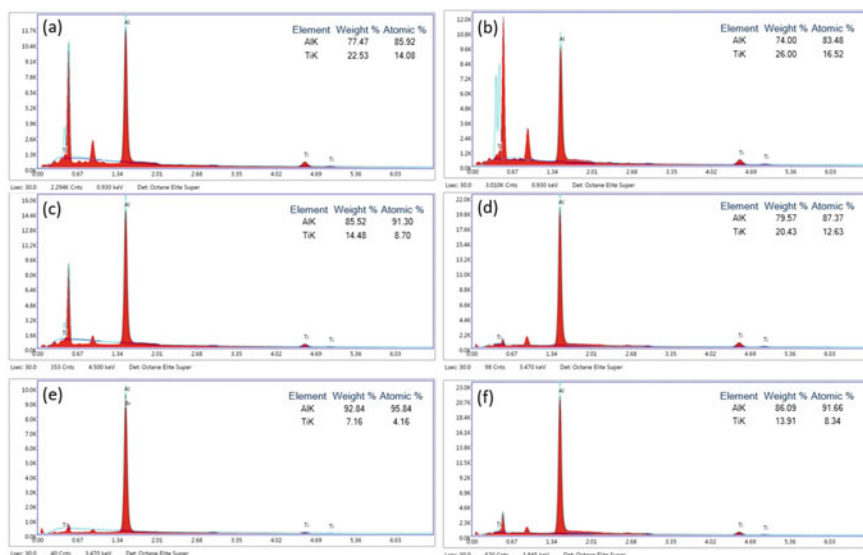


Fig. 6 EDS analysis on a selected area (2500X magnification) of Ti–Al electrodeposits obtained from CA-electrolysis for **a** 1 h, **c** 2 h, and **e** 3 h and from CP-electrolysis for **b** 1 h, **d** 2 h, and **f** 3 h. The inset shows the percentage composition of Ti and Al elements. (Color figure online)

seen from Fig. 6ace, the chemical compositions of Ti and Al in Ti–Al electrodeposit from 1 h CA-electrolysis are 14 at.% and 86 at.%, respectively. The atomic percentage of Ti goes on decreasing with increasing CA-electrolysis time. Ti–Al electrodeposits obtained by CP-electrolysis show relatively higher concentrations of Ti (16.5 at.%), understandably due to the higher concentration of Ti ions dissolved in EMIC- AlCl_3 . However, Ti concentration goes on decreasing with increasing CP-electrolysis time. The decrease in Ti concentration in the EDS spectrum at higher CA- and CP-electrolysis time agrees with the drop in the current density for UPD Al and Ti peaks, as discussed earlier in the CV section.

Structural Analysis by XRD

The Ti–Al electrodeposits were further characterized using XRD. Figure 7 shows the normalized XRD patterns of Ti–Al electrodeposits obtained on Cu substrate from CA-electrolysis (CA1, CA2, and CA3) and CP-electrolysis (CP1, CP2, and CP3). XRD of all the electrodeposits shows five distinct crystallographic peaks of Ti–Al identified according to PDF4+ card (ICDD#:04-016-6423), while the rest of the peaks are due to copper substrate. The five crystallographic planes (111), (200), (220), (311), and (222) belongs to the cubic $\text{Ti}_{0.12}\text{Al}_{0.88}$ phase (space group: $\text{Fm}\bar{3}m$ (225)) of Ti–Al alloy. No other peaks of metallic elements are detected. The atomic percentage composition observed from XRD agrees with the EDS studies. The intensity of (220) and (311) planes increases with increasing electrolysis time for CA as well as CP-electrolysis. The Ti–Al (CP3 sample) electrodeposit obtained

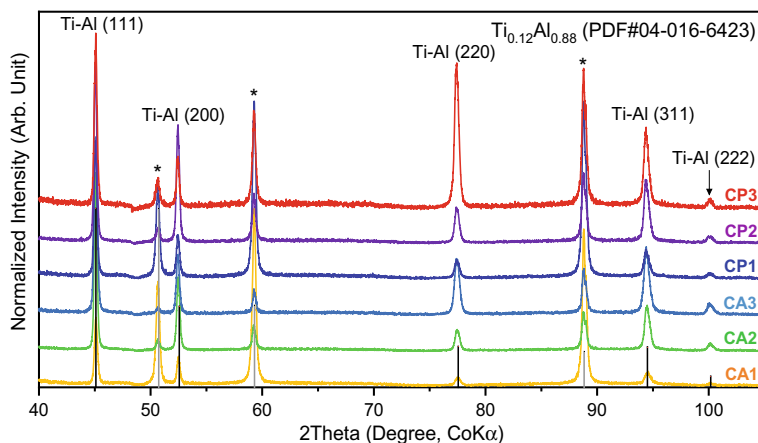


Fig. 7 XRD patterns of Ti–Al electrodeposits obtained from EMIC- AlCl_3 on the copper substrate by CA-electrolysis (1–3 h) and CP-electrolysis (1–3 h). The vertical lines represent the lines from standard diffraction patterns of Ti–Al alloy ($\text{Ti}_{0.12}\text{Al}_{0.88}$) and Cu(*). (Color figure online)

from CP-electrolysis for 3 h shows the highest crystallinity and agrees with the morphological SEM study.

Thus, through this work, we demonstrated that it is feasible to synthesize Ti–Al alloy by dissolving Ti ions in the ionic liquid from Ti anode during electrolysis. It is crucial to investigate the solubility limitations in the reduction of Ti complex ions at higher electrolysis duration. More work is needed to understand the Ti electrochemistry and the disproportionate behavior of Ti ions. Future work is to improve the Ti content in Ti–Al alloy by tailoring the CA and CP-electrolysis parameters.

Conclusions

The dissolution of Ti ions from Ti anode in EMIC- AlCl_3 (with a 0.667-mol fraction of AlCl_3) ionic liquid at 383 K is investigated. The simultaneous dissolution of Ti ions and electrodeposition of Ti–Al alloy on the copper cathode is accomplished by controlled electrolysis using chronoamperometry and chronopotentiometry techniques at different durations. The electrochemical reduction behavior of Ti and Al ions is studied on all Pt wire electrodes using cyclic voltammetry. The reduction of Ti ions commences along with the underpotential deposition of Al. The Ti content in Ti–Al alloy goes on decreasing with higher electrolysis time using CA and CP methods. This indicates that the reduction current of Ti ions is limited by the formation of Ti complex with $[\text{Al}_2\text{Cl}_7]^-$ anions present in the EMIC- AlCl_3 ionic liquid. The Ti–Al electrodeposits obtained from CP-electrolysis are homogeneous and crystalline. One-hour CP-electrolysis yields a Ti–Al alloy with 16 at.% Ti with a cubic $\text{Ti}_{0.12}\text{Al}_{0.88}$ phase.

Acknowledgements The authors acknowledge the financial support from the National Science Foundation (NSF) award number 1762522 and ACIPCO for this research project. The authors also thank the Department of Metallurgical and Materials Engineering, The University of Alabama, for providing the experimental and analytical facilities.

References

1. Kroll W (1940) The production of ductile titanium. *Trans Electrochem Soc* 78:35
2. Crowley G (2003) How to extract low-cost titanium. *Adv Mater Processes* 161:25–27
3. Zhang M, Kamavaram V, Reddy RG (2006) Ionic liquid metallurgy: novel electrolytes for metals extraction and refining technology. *Mining Metall Explor* 23:177–186
4. Fung KW, Mamantov G (1972) Electrochemistry of titanium (II) in AlCl_3 -NaCl melts. *J Electroanal Chem* 35:27–34
5. Girginov A, Tzvetkoff TZ, Bojinov M (1995) Electrodeposition of refractory-metals (Ti, Zr, Nb, Ta) from molten-salt electrolytes. *J Appl Electrochem* 25:993–1003
6. Rolland W, Sterten A, Thonstad J (1987) Electrodeposition of titanium from chloride melts. *Proc Electrochem Soc* 7:775–785

7. Head RB (1961) Electrolytic production of sintered titanium from titanium tetrachloride at a contact cathode. *J Electrochem Soc* 108:806–809
8. Stafford GR (1994) The electrodeposition of Al_3Ti from chloroaluminate electrolytes. *J Electrochem Soc* 141:945–953
9. Carlin RT, Osteryoung RA, Wilkes JS, Rovang J (1990) Studies of titanium (IV) chloride in a strongly Lewis acidic molten-salt-electrochemistry and titanium NMR and electronic spectroscopy. *Inorg Chem* 29:3003–3009
10. Stafford GR, Moffat TP (1995) Electrochemistry of titanium in molten $2\text{AlCl}_3\text{-NaCl}$. *J Electrochem Soc* 142:3288–3296
11. Koronaios P, King D, Osteryoung RA (1998) Acidity of neutral buffered 1-Ethyl-3-methylimidazolium chloride- AlCl_3 ambient-temperature molten salts. *Inorg Chem* 37:2028–2032
12. Jiang T, ChollierBrym MJ, Dubé G, Lasia A, Brisard GM (2006) Electrodeposition of aluminium from ionic liquids: part I—Electrodeposition and surface morphology of aluminium from aluminium chloride (AlCl_3)–1-ethyl-3-methylimidazolium chloride ([EMIm]Cl) ionic liquids. *Surf Coat Technol* 201:1–9
13. Kamavaram V, Mantha D, Reddy RG (2005) Recycling of aluminum metal matrix composite using ionic liquids: effect of process variables on current efficiency and deposit characteristics. *Electrochim Acta* 50:3286–3295
14. Liao Q, Pitner WR, Stewart G, Hussey CL, Stafford GR (1997) Electrodeposition of aluminum from the aluminum chloride-1-methyl-3-ethylimidazolium chloride room temperature molten salt + benzene. *J Electrochem Soc* 144:936–943
15. Zhao Y, VanderNoot T (1997) Electrodeposition of aluminium from room temperature $\text{AlCl}_3\text{-TMPAC}$ molten salts. *Electrochim Acta* 42:1639–1643
16. Karpinski ZJ, Osteryoung RA (1984) Determination of equilibrium-constants for the tetra-chloroaluminate ion dissociation in ambient-temperature ionic liquids. *Inorg Chem* 23:1491–1494
17. Pradhan D, Reddy RG (2014) Mechanistic study of Al electrodeposition from EMIC- AlCl_3 and BMIC- AlCl_3 electrolytes at low temperature. *Mater Chem Phys* 143:564–569
18. Tang J, Azumi K (2011) Optimization of pulsed electrodeposition of aluminum from $\text{AlCl}_3\text{-1-ethyl-3-methylimidazolium chloride}$ ionic liquid. *Electrochim Acta*. 56:1130–1137
19. Wilkes JS, Levitsky JA, Wilson RA, Hussey CL (1982) Dialkylimidazolium chloroaluminate melts—a new class of room-temperature ionic liquids for electrochemistry, spectroscopy, and synthesis. *Inorg Chem* 21:1263–1264
20. Pradhan D, Reddy RG (2009) Electrochemical production of Ti-Al alloys using $\text{TiCl}_4\text{-AlCl}_3\text{-1-Butyl-3-Methyl imidazolium chloride}$ (BmimCl) electrolytes. *Electrochim Acta* 54:1874–1880
21. Song J, Wang Q, Wu J, Jiao S, Zhu H (2016) The influence of fluoride ions on the equilibrium between titanium ions and titanium metal in fused alkali chloride melts. *Faraday Discuss* 190:421–432
22. Song J, Xiao J, Zhu H (2017) Electrochemical behavior of titanium ions in various molten alkali chlorides. *J Electrochem Soc* 164:E321
23. Song Y, Jiao S, Hu L, Guo Z (2016) The cathodic behavior of Ti (III) Ion in a NaCl-2CsCl Melt. *Metall Mater Trans B* 47:804–810
24. Endres F, Zein El Abedin S, Saad AY, Moustafa EM, Borissenko N, Price WE, et al. (2008) On the electrodeposition of titanium in ionic liquids. *PhysChemChemPhys* 10:2189–2199
25. Bakkar A, Neubert V (2015) A new method for practical electrodeposition of aluminium from ionic liquids. *Electrochem Commun* 51:113–116
26. Zein El Abedin S, Giridhar P, Schwab P, Endres F (2010) Electrodeposition of nanocrystalline aluminium from a chloroaluminate ionic liquid. *ElectrochemCommun* 12:1084–1086
27. Böttcher R, Valitova A, Ispas A, Bund A (2019) Electrodeposition of aluminium from ionic liquids on high strength steel. *Trans IMF* 97:82–88
28. Okoturo OO, VanderNoot TJ (2004) Temperature dependence of viscosity for room temperature ionic liquids. *J Electroanal Chem* 568:167–181

Effect of ZrO₂ Filters on Inclusions in Steel



Ming Li, Biao Tao, Huajie Wu, and Yanhui Sun

Abstract The ZrO₂ ceramic filter in the steelmaking plant in Nanjing Iron and Steel United Co., Ltd. was studied. Samples were taken from the tundish that ceramic filter installed. The total oxygen content and the type, shape, size, and composition of the non-metallic inclusions in steel were analyzed. Then the inclusion-removing capability of the tundish ceramic filter was evaluated. The results indicate that the effect of the ceramic filter on the filtration of inclusions is striking. The inclusion removal rate was 41.6% when the diameter of inclusions was more than 30 μm. The tundish guaranteed the production of high-quality steel. However, the calcium treatment process should be reasonably controlled to decrease secondary oxidation and improve the cleanliness of molten steel.

Keywords Ceramic filter · Tundish · Inclusions · Calcium treatment

Introduction

The molten steel filter, a new technology that has been developed in recent years, is simple to operate and has good ability to purify molten steel. The technology removes part of the non-metallic inclusions in molten steel through the filter placed in the tundish to obtain relatively clean molten steel, thereby improving the quality of a slab and providing significant economic benefits. It has been suggested that the removal rate of inclusions is related to the filter material, mesh diameter, thickness, and molten steel flow rate [1]. The main types of steel water filters include ceramic foam filters, porous filter plates, and filter tubes. Its material is mainly CaO, Al₂O₃, ZrO₂, ZrO₂-Al₂O₃, mullite, MgO, and Al₂O₃-C. Studies show that large inclusions are basically removed by the filter and Al₂O₃ has decreased significantly [2, 3]. When

M. Li · H. Wu (✉) · Y. Sun
Collaborative Innovation Center of Steel Technology, University of Science and Technology
Beijing, Beijing 100083, China
e-mail: wuhujie@ustb.edu.cn

M. Li · B. Tao · Y. Sun
Research Institute Nanjing Iron and Steel United Co., Ltd., Nanjing, Jiangsu 210035, China

Ansteel's No. 3 Steelmaking Plant installed quality CaO rectangular ceramic filters in the 48-ton slab continuous casting tundish, the average amount of inclusions in the tundish steel samples reduced by 14.42%. There are significant effects of CaO ceramic filters to remove inclusions of Al_2O_3 and SiO_2 [4]. A CaO straight hole filter was tested in Liugang Steelmaking Plant, and the inclusions in the steel reduced by 20% [5]. After adopting a magnesium through-hole filter in Benxi Steel, the mass fraction of inclusions in the finished billet reduced by more than 50% [6].

Experimental Procedure

Experimental conditions: A 5-stream continuous casting machine was used. The tundish capacity was 35 ton, and section size of billet is $150 \text{ mm} \times 150 \text{ mm}$. The casting speed was 2.0 m/min while the top to top time was about 45 min. The experimental samples were grade 50CrVA steel. The steel was a high-grade spring, which has an important use, with a large cross section and a high load, and a valve spring, a piston spring, and a safety valve spring with an operating temperature of less than $300 \text{ }^\circ\text{C}$. The steel had good toughness, high proportional and strength limits after heat treatment, and high fatigue strength. The experiment used a ZrO_2 foam ceramic filter. An O–N analyzer, direct reading spectrometer, optical microscope, and SEM–EDS were used for analysis.

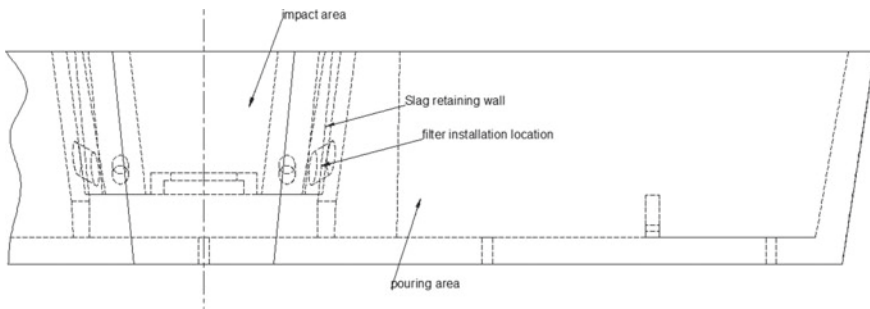


Fig. 1 Profile of the tundish and the filter installation position

Fig. 2 Schematic of the filter structure

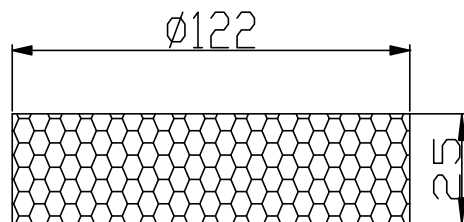


Figure 1 shows the tundish structure and filter installation location. Figure 2 shows a schematic of the foam ceramic filter structure whose thickness and diameter are 25 mm and 122 mm, respectively. The main composition of the 0.787 mm cellular foam ceramic is ZrO₂. The sample has a cylindrical shape with a diameter of 30 mm and a height of 45 mm. The sample was taken from the first five furnaces using the same pouring time required to take a bucket sample. The sampling time was 15–20 min for each furnace steel. The sampling position of the tundish was the impact and pouring area, and two bucket samples were taken each for a total of ten bucket samples. A 15 mm high cut was made on each sample for high magnification analysis and 50 fields of view observed using an optical microscope at 100 × magnification. The number of inclusions of 10–20, 20–30, and >30 μm was counted. Furthermore, a scanning electron microscope was used to analyze the energy spectrum of typical inclusions and an inductively coupled plasma (ICP) chemical method used to analyze the mass fractions of Al_T (total aluminium content), Al_S (aluminat content), and Ca. Then the remaining 30 mm high cylindrical samples were forged into 60-mm-long rod samples for total oxygen analysis.

Results and Discussion

Total Oxygen Mass Fraction Analysis

During the experiment, bucket samples were taken 15 min after the first five furnaces were loaded using the same pouring time. The sampling position was 40 cm below the liquid level near the long nozzle of the tundish impact zone and the outlet of the diversion hole of the tundish filter.

An O–N analyzer was used to measure the total oxygen mass fraction ($\omega([\text{O}])$) of the molten steel samples in the impact and pouring zones of different tundishes. The results are shown in Fig. 3. Further, $\omega([\text{O}])_1$ is the total oxygen mass fraction sampled in the impact zone of the tundish while $\omega([\text{O}])_2$ is the total oxygen mass fraction sampled in the pouring zone. As can be seen from the test data, the highest $\omega([\text{O}])$ value in the molten steel impact zone is 0.0038%, the lowest value is 0.0024%, and the average value is 0.0031%; the highest $\omega([\text{O}])$ in the pouring area is 0.0035%, the lowest value is 0.0022%, and the average value is 0.00278%. After the steel in the tundish passes the filter, the average value of $\omega([\text{O}])$ drops to 0.0032% and a decrease of 10.3%.

Analysis of Aluminum and Calcium Mass Fraction

Direct reading spectroscopy and ICP chemical methods were used to determine the mass fraction of total aluminium Al_T, acid soluble aluminium Al_S, and Ca in

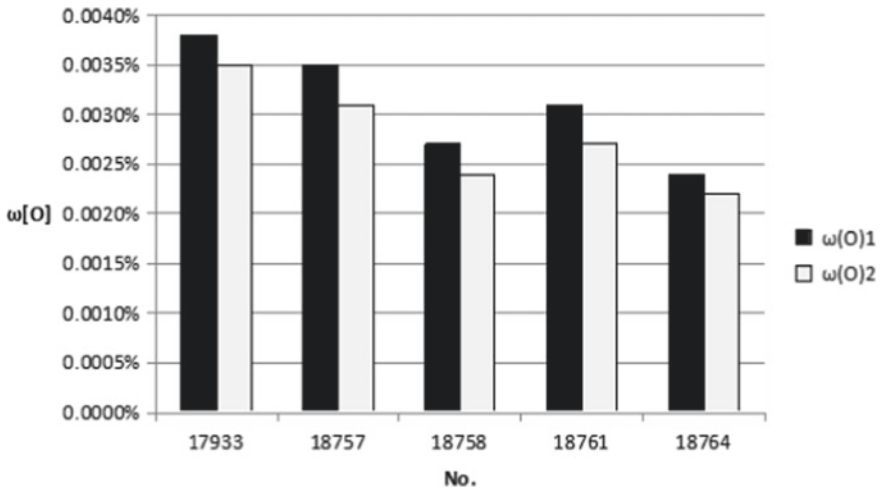


Fig. 3 Total oxygen content variation of tundishes

molten steel. The results are shown in Table 1. The results of Al_T and Al_S analysis of the samples in the impact zone and the pouring zone show that relative to the impact zone, the pouring zone $\omega(\text{Al}_S)/\omega(\text{Al}_T)$ generally increases by 0–9%, and the mass fraction of the aluminum-containing inclusions decreases. The Al_S of the furnace numbers 18758, 18,761, and 18,764 are relatively high, ranging from 0.016 to 0.028%, corresponding to $\omega(\text{[O]})$ ranging from 0.0022 to 0.0027%.

Research has shown that when $\omega(\text{Ca})/\omega(\text{Al}_S) \geq 0.09$ in steel, inclusions are mostly deformed into $12\text{CaO} \cdot 7\text{Al}_2\text{O}_3$ low-melting point calcium aluminate inclusions [7]. To obtain a good calcium treatment effect, higher calcium to aluminum ratio is conducive to the removal of particulate inclusions. In this experiment, the fluctuation range of $\omega(\text{Ca})/\omega(\text{Al}_S)$ is relatively large. The first two furnaces have low Al_S, and the latter three furnaces have a low $\omega(\text{Ca})/\omega(\text{Al}_S)$ of 0.05–0.068. Therefore, the calcium treatment is not ideal.

Optical Microscope Analysis

The sample was analyzed at high magnification. It is difficult to count inclusions under 10 μm with an optical microscope at 100 magnification. In this experiment, 50 fields of view at 100 \times magnification with the optical microscope were used. The number of inclusions of various sizes was counted at 30 μm . The results are shown in Table 2.

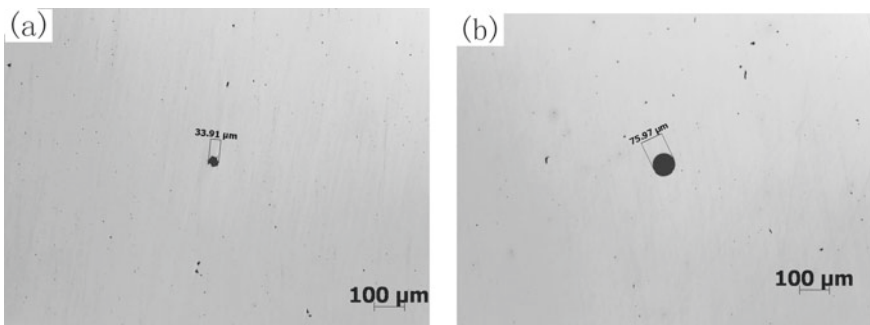
It can be seen from Table 2 that before and after molten steel filtration, the removal rate of inclusions below 10–20 μm is 14.1%, the removal rate of inclusions between 20 and 30 μm is 23.4%, and the average removal rate of inclusions above 30 μm

Table 2 Comparison of quantities and sizes of inclusions in the samples

No.	Position	Number of inclusions with different particle sizes		
		10–20 μm	20–30 μm	>30 μm
17,933	Impacting zone	94	24	3
	Pouring zone	85	22	2
18,757	Impacting zone	103	33	2
	Pouring zone	92	24	1
18,758	Impacting zone	82	19	2
	Pouring zone	62	15	2
18,763	Impacting zone	73	31	3
	Pouring zone	69	19	1
18,765	Impacting zone	102	30	2
	Pouring zone	82	25	1
Average removal rate of inclusions		14.1%	23.4%	41.7%

is 41.7%. Figure 4 shows typical inclusions of different sizes in molten steel in the impacting zone and pouring zone of furnace number 18,758, and the inclusions are all spherical.

When the melt passes through the ceramic filter, the physical separation of coarse particles by the filter first happens and the inclusions are intercepted at different positions of the filter according to the size of the particles. The second separation involves entrapment of small blocky particles on the interior surface of the filter. The material, porosity, and interior surface roughness of the filter influence the filtration efficiency of different mechanisms [13].

**Fig. 4** Morphology of inclusion in the samples: **a** impacting zone; **b** pouring zone

SEM-EDS Analysis

Electron microscope observation and energy spectrum analysis were carried out on the sample from furnace number of 1863. The sampling locations were the impacting and pouring areas. The typical inclusions in the tundish from SEM energy spectrum analysis are shown in Table 3, and their morphologies are shown in Figs. 5 and 6.

It can be seen from Table 3 that the inclusions in the tundish were CaO–Al₂O₃–SiO₂–MnO which are mainly refining deoxidation products. After the molten steel passed through the filter, the average mass fraction of Al₂O₃ in the inclusions reduced from 32 to 15%. $\omega(\text{CaO})/\omega(\text{Al}_2\text{O}_3)$ was 0–0.9, which indicates that the calcium treatment was insufficient, and that it was a high-melting point inclusion. The source of MgO in the inclusion was the corrosion resistance of the material, and MnO was a secondary oxidation product [8].

Research shows that after calcium treatment, the calcium–aluminum ratio of calcium–aluminate inclusions in molten steel was 1.17–1.86, and the types of inclusion were 12CaO·7Al₂O₃ and 3CaO·Al₂O₃ [9]. Such inclusions have lower-melting points. Moreover, its smaller density is beneficial to the removal of inclusions. The large particles formed during refining and deoxidation are important sources of inclusions in steel. In order to promote the floating of inclusions and to improve tundish metallurgy, the next step required is to improve the structure and distribution of filter pores and give full play to the physical ability of the filter to remove inclusions [10–12].

Experimental results show that nitrogen inclusions can also be removed by adhering to the surface of the filter [13, 14]. Different particle removal methods are related to the properties and sizes of particles as well as the character of the filter. Some research suggests that the higher the alumina amount on the surface in the filter system, the more alumina-based non-metallic inclusions get trapped on the filter surface. This confirms the dependence of filtration efficiency on the chemistry of non-metallic inclusions as well as the filter material [15–17]. The proposed mechanisms for the removal of non-metallic inclusions in the filtration mode are (1) collisions with walls and the interception effect and (2) the formation of both intermetallic and non-metallic inclusion bridges during filtration. Fluid dynamics modeling of inclusion attachment to the filter walls showed that most inclusions, especially those with larger sizes, are trapped at the upper part of the filter, whereas smaller inclusions are well dispersed throughout the filter [18]. The number of inclusions was substantially reduced in molten steel by filtering the melt through alumina-based ceramic media with monolithic extruded and tabular granules. Inclusion removal efficiencies ranged between 45 and 100% depending on (a) melt velocity through the filter, (b) height of the filter, and (c) inclusion size [19]. It was found that casting rate and inclusion density play minor roles in the capture ratio while inclusion size was the most influential variable [20].

Table 3 Energy spectrum analysis of the type of inclusions in steel

Position	EDS	O	Al	Si	Ca	Mg	Mn	Type of inclusion
Impacting zone	1	35.14	16.13	29.16			12.46	28%Al ₂ O ₃ -57%SiO ₂ -15%MnO
	2	28.07	17.14	32.2			14.7	
	3	30.44	16.12	26.55			19.53	
	1	33.7	17.64	16.46	12.15		6.63	18%CaO-35%Al ₂ O ₃ -37%SiO ₂ -9%MnO $\omega(\text{CaO})/\omega(\text{Al}_2\text{O}_3) = 0.51$
	2	31.52	47.31	4.39	8.73			
	3	27.52	24.79	16.06	13.58		11.05	
Pouring zone	1	41.47	11.7	27.44	14.55	4.85	5.07	18%CaO-20%Al ₂ O ₃ -7%MgO-54%SiO ₂ $\omega(\text{CaO})/\omega(\text{Al}_2\text{O}_3) = 0.9$
	2	36.00	11.4	29.14	15.06	3.32	5.07	
	3	32.05	10.7	25.81	20.06	3.91	7.47	10%Al ₂ O ₃ -64%SiO ₂ -26%MnO
	4	33	10.18	28.68	16.44	3.77	5.44	
	1	32.66	6.51	36.02			24.63	
	2	30.97	8.07	37.89			23.08	
	3	30.71		39.81			29.48	
4	26.01	8.36	35.6			30.03		

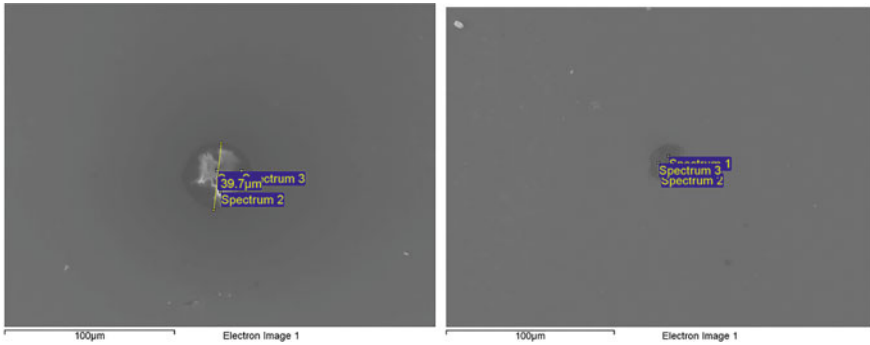


Fig. 5 Morphology of inclusions in steel in the impacting areas. (Color figure online)

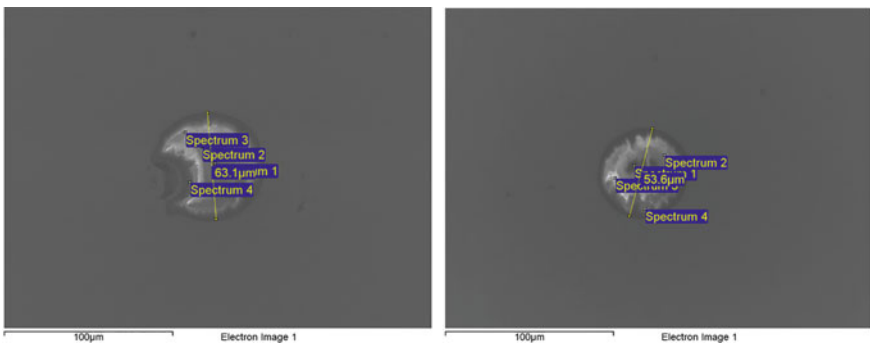


Fig. 6 Morphology of inclusions in steel in the pouring areas. (Color figure online)

Conclusions

In this experiment, a bucket sampler was used for sampling. Analysis showed that the molten steel $\omega([O])_1$ averaged 0.0031% while the pouring area of $\omega([O])_2$ averaged 0.00278%. After the tundish molten steel passed through the filter, the average value of $\omega([O])$ decreased to 0.0032%, a decrease of 10.3%.

According to the analysis results of Al_T and Al_S in the impact and pouring zones, relative to the impact zone, the pouring zone $\omega(Al_S)/\omega(Al_T)$ increased by 0–9% while the mass fraction of aluminum-containing inclusions decreased. $\omega(Ca)/\omega(Al_S)$ was 0.05–0.068, indicating that the calcium treatment was not ideal.

After the molten steel was filtered using the foam ceramic filter, inclusions of different sizes were reduced. The removal rate of inclusions below 10–20 μm and 20–30 μm was 14.1% and 23.4%, respectively. Inclusions above 30 μm generally reduced; their average removal rate was 41.7%. The inclusions in the impact and pouring zones were all spherical.

After the molten steel passed through the filter, the mass fraction of Al_2O_3 in the inclusions reduced from 32% to 15%, and $\omega(\text{CaO})/\omega(\text{Al}_2\text{O}_3)$ was ≤ 0.9 , indicating that the calcium treatment was insufficient, and there were high-melting point inclusions. The source of MgO in the inclusions was corrosion resistance caused by MnO as a secondary oxidation product.

References

1. Kang JG, et al (11 November, 2009) The study of the result of inclusion's filtration with filters in tundish of continuous casting of baosteel. Paper presented at the 7th China iron and steel annual conference, Beijing
2. Zhao XY, Zhang JM, Wu SZ, et al. (2011) Non-temperature simulation of inclusions in filtered tundish water. *Chinese J Eng* 33(5):539
3. Miu CF, Kang JG, Lv XY et al (2009) Study on application effect of T-shape Tundish's filter. *China Metall* 19(10):19
4. Lu YQ, Zhang CM, Dai YD et al (2003) Effect of Tundish CaO ceramic filter on inclusion removal. *Energy Metall Ind* 22(6):9
5. Zhou ZZ, Dong LR (1996) Filtration of liquid steel in tundish by a lime filter. *Chinese J Eng* 18(2):163
6. Liu J, Xue WH (2005) Development and application of the weirs with holes installed in tundish for continuous casting. *Shanghai Metals* 27(1):55
7. Zhang J, Jiang JP (2000) Effect of ladle feeding CaSi wire on the deformation of inclusions in steel. *Steelmaking* 16(2):26
8. Peng QC, Zhao JT, Chen LP, et al. (2011) Study on inclusions of DC04 steel in the process of continuous casting. *China Metall* 21(6):5
9. Guo YM, Xu ZB, Wang HT (2007) Research on inclusions in Al-killed steel during LF refining iron steel vanadium titanium 28(3):14
10. Dai BY, Ma RD, Shang JL (2007) Effect of foam ceramic filtration on inclusions in 42CrMo. *Steel Foundry Technol* 28(3):409
11. Zhao XY, Zhang JM, Wu SZ (23 September, 2009) Influence of filter in structure T tundish on inclusion-removal. Paper presented at 2009 special steel annual conference. Qingdao, Shandong
12. Wang YC, Zhang JQ (2015) Key technologies of cleanliness and homogeneity control for high-speed heavy rail steel. *China Metall* 25(4):9
13. Chen FW, Huang XB, Wang Y et al (1998) Investigation on foam ceramic filter to remove inclusions in revert superalloy. *Mater Lett* 34(3–6):372–376
14. Wetzig T, Baaske A, Karrasch S et al (2018) Development and testing of carbon-bonded alumina foam filters for continuous casting of steel. *Ceramics Int* 44(18):23024–23034
15. Wang Q, Liu Y, Huang A, Yan W et al (2020) CFD investigation of effect of multi-hole ceramic filter on inclusion removal in a two-strand tundish. *Metall Mater Trans B* 51(1):276–292
16. Yang Y, Nomura H, Takita M (1996) Inclusion removal using ceramic foam filters and filter size estimation. *Int J Cast Met Res* 9(1):27–35
17. Emmel M, Aneziris CG, Schmidt G et al (2013) Influence of the chemistry of surface functionalized ceramic foam filters on the filtration of alumina inclusions in steel melts. *Adv Eng Mater* 15(12):1188–1196
18. Damoah LNW, Zhang LF (2010) Removal of inclusions from aluminum through filtration. *Metall Mater Trans B* 41(4):886–907
19. Apelian D, Mutharasan R, Ali S (1985) Removal of inclusions from steel melts by filtration. *J Mater Sci* 20(10):3501–3514
20. Davila-Maldonado O, Adams A, Oliveira L et al (2008) Simulation of fluid and inclusions dynamics during filtration operations of ductile iron melts using foam filters. *Metall Mater Trans B* 39(6):818–839

Part V
Poster Session

A Hybrid Model for Predicting the End-Point Phosphorus Content of Electric Arc Furnace



Chao Chen, Nan Wang, and Min Chen

Abstract A hybrid model based on the combination of k -means method, BP neural network and decision tree algorithm is proposed for predicting the end-point phosphorus content of electric arc furnace. The industrial data from electric arc furnace is filtered firstly by the box-plot method, and the processed data of end-point phosphorus content is classified into three clusters by k -means analysis method. Then, three BP neural networks with different parameters for each cluster are established to deal with the data overlapping problem and increase the model accuracy. In order to obtain the optimum prediction result, a new method combined with the posterior knowledge of dephosphorization ratio and the decision tree algorithm is employed. With this method, the results predicted, respectively, by the three different BP neural networks are merged according to the merging rule set established by decision tree algorithm and the identified result is taken as the final end-point phosphorus content. In comparison with the traditional BP neural network and deep layer neural network, the hybrid model increases the prediction accuracy of end-point P content to 97.8% with $\pm 0.006\%$ error range, and meanwhile for the error ranges of $\pm 0.005\%$ and $\pm 0.004\%$, the prediction accuracy is 94.2% and 83.0%, respectively.

Keywords End-point phosphorus content · BP neural network model · K -means method · Data overlapping · Decision tree algorithm

Introduction

The end-point phosphorus (P) content is one of the main targets in steelmaking process due to its significant influence on the steel product. With the increasing demand for low and ultra-low phosphorus steels, many steel plants apply high-efficiency dephosphorization technology into the converter [1]. However, in view of the fact that most process parameters are correlative with each other, it is difficult to control the end-point phosphorus content with a high accuracy degree, and thus,

C. Chen · N. Wang (✉) · M. Chen
School of Metallurgy, Northeastern University, Shenyang, Liaoning 110819, China
e-mail: wangn@smm.neu.edu.cn

numerous researches have been carried out to realize the precise controlling of the end-point P content through the intelligent models [2–5]. However, due to the limited experience knowledge of the operators, machine error, and other uncertain factors, the industrial data shows complex patterns, which is the significant factor to affect the model effectiveness. Thus, in this paper, a hybrid model to stabilize the prediction result is established according to the different data patterns.

In recent years, electric arc furnace is widely used in China. Compared with the BOF converter, electric arc furnace possesses more advantages such as higher production quality, easily controlling and higher energy efficiency. In light of the fact that some high steel grades like high-pressure boiler tube steel needs to have low phosphorus content, it is of significance to establish a prediction model to control the end-point phosphorus content precisely in electric arc furnace. In this paper, the industrial data of electric arc furnace is preprocessed by utilizing the box-plot method to drop out the exceptional data. And then, in order to achieve more optimum prediction result, a deep layer neural network is established based on the reference model of BP neural network. Furthermore, in order to eliminate the data overlapping problem, the k-means method is employed to investigate the data pattern, and the corresponding BP neural network model is established for different data patterns. Finally, the decision tree model is used to formulate the rule set to determine the optimum output for the end-point P content.

Data Collection and Preprocess

The industrial data from the electric arc furnace production process, about 1258 heats, are collected from a steel plant in China. According to the dephosphorization thermodynamics and the actual operation in electric arc furnace, the end-point phosphorus content of electric arc furnace is mainly determined by 18 process variables, including the chemical composition of hot metal, hot metal weight, scrap weight, lime weight, dolomite weight, carbon weight, limestone weight, smelting cycle, oxygen consumption, natural gas consumption, electricity consumption, tapping weight, end-point C content, and end-point temperature. The box-plot method is employed in this work to filter the exceptional data out, and the data samples after processing are reduced from 1258 to 1114 heats.

Neural Network Model for End-Point Phosphorus Content

Reference Model Based on BPNN Neural Network

The neural network model possesses the superior property to fit the complex non-linear relationship, and thus, many researchers choose this type of model to fit the

relationship between the input and output variables [6, 7]. BPNN is a multi-layer feed-forward artificial neural network, which is trained by error back propagation algorithm proposed by Rumelhart [8]. The BP neural network is a typical three-layer BPNN neural network. By applying the BP neural network, a basic reference model in this work is constructed to predict the end-point phosphorus content. For the reference model, the main parameters are selected as the followings.

Step 1: Taking Eq. (1) as the normalization formula, which can eliminate the errors from different dimensions, and the transformed data of each covariate would meet the Gaussian distribution with the expectations of 0 and the variance of 1.

$$x_{\text{norm}} = \frac{x - x_{\text{mean}}}{x_{\text{var}}} \quad (1)$$

where x_{norm} is the normalized data; x_{mean} is the mean value of variable x ; x_{var} is the standard deviation.

Step 2: Taking Rectified Linear Units (ReLU) function as the activation function [9].

Step 3: Taking Mean Square Error (MSE) function as the loss function [10].

All the preprocessed data of electric arc furnace is divided into two parts, i.e., training set and test set, and the ratio of the two sets is 8:2. For the three-layer neural network, in order to obtain the optimal node number in the hidden layer, the circulation method is adopted to set the node number from 1 to 200 to search the optimum node number, and finally, the structure of the reference model is determined to be $18 \times 8 \times 1$. The prediction hit rate of the BP neural network model is 96.9% with $\pm 0.006\%$ error range, whereas the hit rates are 91.1%, 82.5%, and 65.2%, respectively, for the error ranges of $\pm 0.005\%$, $\pm 0.004\%$, and $\pm 0.003\%$. But with the increasingly higher product quality demand, it is essential to develop other methods to predict the end-point phosphorus content with higher precision.

Deep Layer Neural Network Prediction Model

To obtain a higher prediction precision, the deep layer neural network is employed, which possesses more complex structure and higher fitting capacity. However, it is well known that the deep layer neural network is easy to over-fit the training data, leading to a poor prediction result in test set. Thus, the circulation method is employed in each layer in this work, and the parameter of next layer is searched for based on the previous parameter when the optimum node in one layer is determined. Meanwhile, the test set is used to evaluate the model parameter to avoid the over-fitting in each

circulation. By constantly increasing the amount of hidden layer data and comparing its prediction results, the prediction accuracy is fluctuant with the increasing hidden layer number, and when the hidden layer number is selected as 6, the prediction accuracy is the optimum one. Finally, the structure of the deep layer neural network is determined as $18 \times 8 \times 5 \times 7 \times 18 \times 13 \times 8 \times 1$.

By setting the maximal circulation number in each layer, the optimum structure is determined, and the hit rate of the deep layer neural network model is 97.3% with $\pm 0.006\%$ error range, whereas the hit rates are 92.9%, 79.9%, and 65.6%, respectively, for the error ranges of $\pm 0.005\%$, $\pm 0.004\%$, and $\pm 0.003\%$, indicating that the deep layer neural network has higher prediction accuracy compared with BP neural network.

A Hybrid Prediction Model for End-Point Phosphorus Content

Data Pattern Analysis by k-means Method

Although the deep layer neural network presents higher prediction accuracy than the traditional three-layer BP neural network, the prediction accuracy with $\pm 0.005\%$ error range is insufficient at some data points. In order to construct a model with high precision, a further investigation should be carried out on the data pattern by using *k*-means method. In this work, the dephosphorization ratio defined in Eq. (2) is used to induce the construction of the hybrid model, with an assumption that the values of dephosphorization ratio are different even though the values of end-point P contents are the same.

$$\eta = \frac{|P_0 - P|}{P_0} \times 100\% \quad (2)$$

where η is the dephosphorization ratio of electric arc furnace, P_0 stands for the original phosphorus content, P is the end-point phosphorus content.

The *k*-means method, namely an unsupervised method [11], is used to find the potential data pattern for the dephosphorization ratio and end-point P content. Through the calculation, the value of K value in *k*-means method is taken as 3, indicating that three data patterns are included in the end-point P content and the dephosphorization ratio. Thus, the processed data are segmented to three clusters, namely class 1, class 2, and class 3, as shown in Table 1. It can be noted that the value range of dephosphorization ratio is different for different clusters, but the data overlapping problem is found for the end-point P contents with the three value ranges of 0.004%–0.013%, 0.007%–0.013%, and 0.01%–0.018%, respectively, which would increase the burden of modeling process.

Table 1 Distribution situation of each class

Class	End-point P content (%)	Dephosphorization ratio (%)	Data samples
Class 1	0.004–0.013	92–97	380
Class 2	0.007–0.018	87–92	552
Class 3	0.01–0.018	78–87	182

Data Experiment with Multiple BP Neural Network Model

In terms of the aforementioned k-means analysis, the data is segmented into three classes and the data overlapping problem is found to exist among the whole data. This paper firstly makes an experiment for each class, namely establishing the BP neural networks model between input variable and output variable in each class. And then, the data of each class is all inputted into the established three BP neural networks to predict the end-point P content of electric arc furnace. The error range within $\pm 0.005\%$ is shown in Fig. 1. In Fig. 1, the denotations of (1–1), (1–2), and (1–3) represent that the data from class 1 is input into the BP neural network established by class 1, class 2, and class 3, respectively. Similarly, other subgraphs have same implication. By comparing the results, the predicted accuracy within $\pm 0.005\%$ error range of (1–1), (2–2), and (3–3) is found to be higher than others subgraph of their own row. It is obvious that when the data is input into a model that established by its

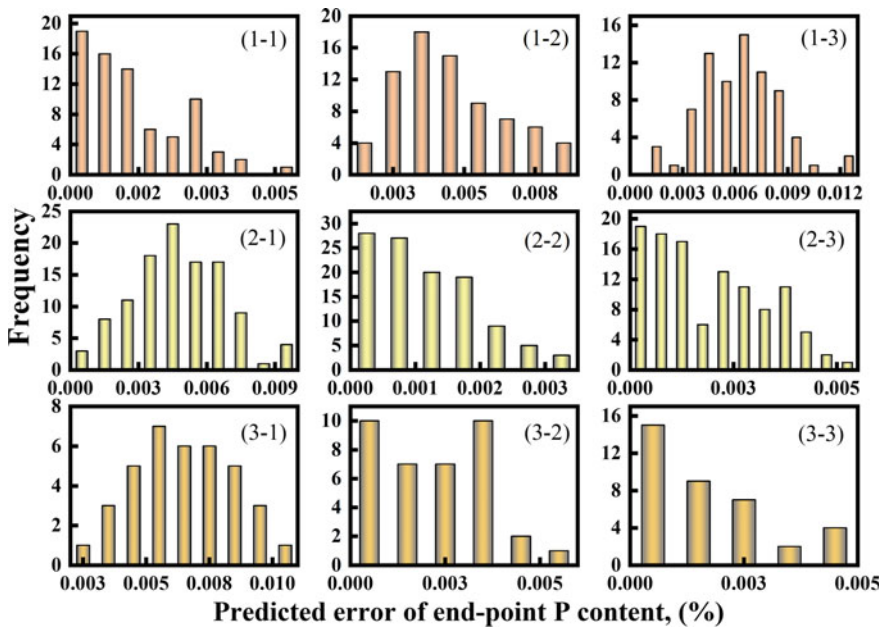


Fig. 1 Cross result of the three BP neural networks. (Color figure online)

own class, the accuracy is higher than when it is input into a model that established by other class data.

Through the above experiment, we make an assumption that when a group of data from the electric arc furnace process is input into three BP network, respectively, there must exist one prediction result with higher accuracy than others, and if we reasonably merge them as the final prediction result, it may possess higher accuracy.

A Hybrid Prediction Model Based on Multiple BP Neural Network and Decision Tree Model

On the basis of k -means method and BP neural network, three BP neural networks with different parameters are established, and the predicted results based on the three models, respectively, present high accuracy. Thus, it can be inferred that the model accuracy would be certainly improved by merging all the predicted results reasonably. So, this paper presents a hybrid prediction model that by establishing three BP neural networks for the three different data clusters classified by k -means method, and the final end-point P content is predicted by merging the three predicted results reasonably.

Owing to its excellent ability of classification and generalization, the decision tree algorithm is used to establish the new data subset [12]. So, the decision tree model is employed to merge the result from three BP neural networks. Firstly, according to Eq. (3), the predicted dephosphorization ratio is determined.

$$\eta_{\text{predict}} = \frac{|Q - P_i|}{P_i} \quad (3)$$

where η_{predict} is the predicted dephosphorization ratio, Q represents the predictive result from the different BP neural network models, P_i represents the input hot metal [P] content.

Next, we transform the η_{predict} from each BP neural networks to 0 or 1, and the transforming criteria is shown as the following:

1. For the result 1, if η_{predict} is greater than 92%, result 1 is set to 1, and otherwise, it is set to 0;
2. For the result 2, if η_{predict} is less than 92% and greater than 87%, result 2 is set to 1, and otherwise, it is set to 0;
3. For the result 3, if η_{predict} is less than 87%, result 3 is set to 1, and otherwise, it is set to 0.

After being transformed, the continuous data is transformed to discrete data. It is benefit for establishing decision tree model. Then, the decision tree model is used to segment the transformed data, and the results are shown in Fig. 2. It is noted that the training data is divided into five data subsets and the corresponding outputs are

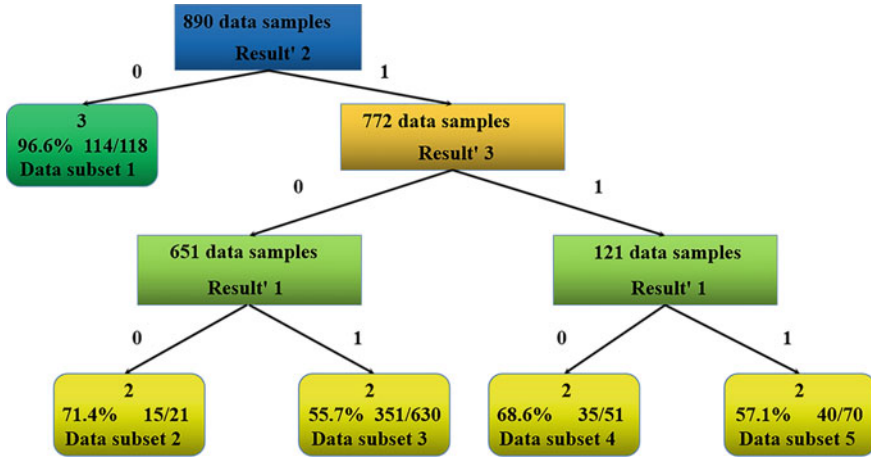


Fig. 2 Classification of train data by decision tree algorithm. (Color figure online)

formulated for each subset, as shown in Table 2. In particular, for the training data subsets 1, 2, and 3, two output rules are formulated to improve the output accuracy, expressed by Eqs. (4) and (5), respectively.

$$R_{\text{predict}} = \frac{(\text{result 1} + \text{result 2} + \text{result 3})}{3} \tag{4}$$

where R_{predict} presents the final predicted end-point P content, result 1, result 2 and result 3 are the predicted results by BP neural network 1, BP neural network 2 and BP neural network 3, respectively.

$$R_{\text{predict}} = \text{tree 1} \times \text{result 1} + \text{tree 2} \times \text{result 2} + \text{tree 3} \times \text{result 3} \tag{5}$$

where tree 1, tree 2, and tree 3 are the probability value of classification by decision tree method.

Table 2 Generation rule of training data subset

Rule	Content
R1	If Result' 2 = 0, then result 3 is output
R2	If Result' 2 = 1, Result' 1 = 0 and Result' 3 = 0, then result 2 is predicted
R3	If Result' 2 = 1, Result' 3 = 0 and Result' 1 = 1, then the output result is formulated by Eq. (5)
R4	If Result' 2 = 1, Result' 3 = 1 and Result' 1 = 0, then result 2 is predicted
R5	If Result' 2 = 1, Result' 3 = 1 and Result' 1 = 1, then the output result is formulated by Eq. (4)

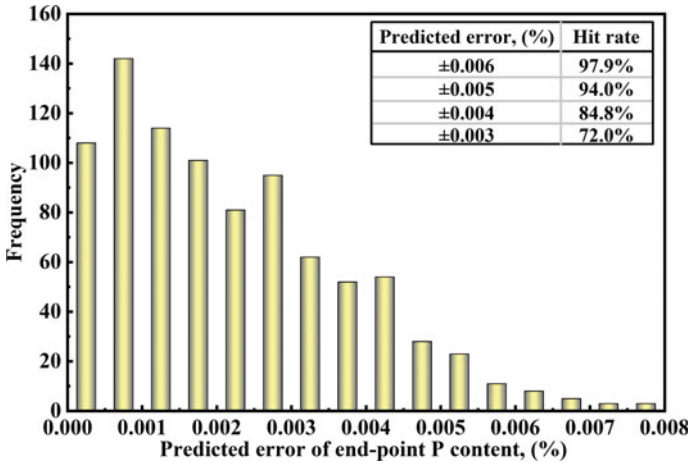


Fig. 3 Frequency distribution of predictive errors in train data by the hybrid prediction model. (Color figure online)

Figure 3 shows the training result by the hybrid model. It is obvious that the hit rate of the hybrid model is 97.9% within $\pm 0.006\%$ error range, whereas the hit rates are 94.0%, 84.8%, and 72.0% when the error ranges are within $\pm 0.005\%$, $\pm 0.004\%$, and $\pm 0.003\%$, respectively, from Fig. 3. Compared with the deep layer neural network, it is obvious that the high error problem is improved well.

Effectiveness of the Hybrid Prediction Model

Through the test set, verification of the hybrid model is discussed. As shown in Fig. 4, the hit rate of the hybrid model is 97.8% with $\pm 0.006\%$ error range, whereas the hit rates are 94.2%, 83.0%, and 68.8%, respectively, when the error ranges are within $\pm 0.005\%$, $\pm 0.004\%$, and $\pm 0.003\%$. Compared with the results in Figs. 3 and 4, it is obvious that the hybrid model possesses better generalization and prediction ability.

Conclusion

In this paper, a hybrid model is established to predict the end-point phosphorus content of electric arc furnace. The following conclusions can be drawn:

1. By analyzing the process parameters which affect the end-point phosphorus content in electric arc furnace, the three-layer BP neural network and deep layer neural network model to predict the end-point phosphorus content are established, and

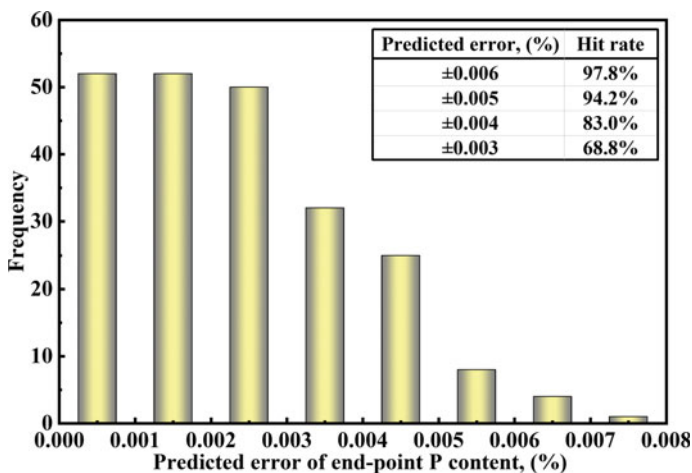


Fig. 4 Frequency distribution of predictive errors in test data by the hybrid prediction model. (Color figure online)

the corresponding hit rates are 91.1% and 92.9%, respectively, with $\pm 0.005\%$ error range, indicating that the model prediction accuracy can be enhanced by increasing the hidden layer number.

- By combining the statistics analysis and k -means method, three data pattern of actual production data from electric furnace are found, meanwhile there is data overlapping phenomenon in each pattern which enhance the burden of model.
- A hybrid model for predicting the end-point P content in electric arc furnace is established based on multiple BP neural network and decision tree algorithm. The hit rate of the hybrid model is 97.8% with $\pm 0.006\%$ error range, whereas the hit rates are 94.2%, 83.0%, and 68.8%, respectively, for the error ranges of $\pm 0.005\%$, $\pm 0.004\%$, and $\pm 0.003\%$, which is higher than the traditional BP neural network and deep layer neural network.

Acknowledgements This work was supported by the National Key R&D Program of China (Grant numbers 2017YFB0304201, 2017YFB0304203, and 2016YFB0300602).

Conflict of Interest The authors declare that they have no conflict of interest.

References

- Wang M, Du J, Deng Q et al (2015) The effect of phosphorus on the microstructure and mechanical properties of ATI 718Plus alloy. *Mater Sci Eng a* 626:382–389
- Wang HB, Xu AJ, Ai LX et al (2012) Prediction of end-point phosphorus content of molten steel in BOF using weighted k -means and GMDH neural network. *J Iron Steel Res Int* 19:11–16

3. Liu H, Wang B, Xiong X (2014) Basic oxygen furnace steelmaking end-point prediction based on computer vision and general regression neural network. *Optik* 125:5241–5248
4. Pal S, Halder C (2017) Optimization of phosphorous in steel produced by basic oxygen steel making process using multi-objective evolutionary and genetic algorithms. *Steel Res Int* 88:1600193
5. He F, Zhang L (2018) Prediction model of end-point phosphorus content in BOF steelmaking process based on PCA and BP neural network. *J Process Control* 66:51–58
6. Zhou Y, Li S (2020) BP neural network modeling with sensitivity analysis on monotonicity based Spearman coefficient. *Chemomet Intell Laborat Syst* 200:103977
7. Zou XF, Hu YJ, Long XB et al (2020) Prediction and optimization of phosphorus content in electroless plating of Cr12MoV die steel based on PSO-BP model. *Surfaces Interfaces* 18:100443
8. Rumelhart DE, Hinton GE, Williams RJ (1986) Learning representations by back propagating errors. *Nature* 323:533–536
9. Glorot X, Bordes A, Bengio Y (2011) Deep sparse rectifier neural networks. *J Mach Learn Res* 15:315–323
10. Aguel S, Meddeb Z, Jeday MR (2019) Parametric study and modeling of cross-flow heat exchanger fouling in phosphoric acid concentration plant using artificial neural network. *J Process Control* 84:133–145
11. Hofmeyr DP (2020) Degrees of freedom and model selection for k-means clustering. *Comput Stat Data Anal* 149:106974
12. Barsacchi M, Bechini A, Marcelloni F (2020) An analysis of boosted ensembles of binary fuzzy decision trees. *Expert Syst Appl* 154:113436

Considerations of Removing Arsenic from Molten Steel by Adding Rare Earth Elements



Yu Peng, Hongpo Wang, and Silu Jiang

Abstract Cleanliness control in steel has always been a topic discussed by researchers. Many methods were used to remove residual elements from steel. Adding rare earth elements to molten steel is one of the potential ways. However, to remove arsenic from steel using lanthanum, many issues need considerations. The effects of steel-crucible reactions, vaporation, and slags on the removal of arsenic from the molten steel were investigated. The results show that using the alumina crucible is more conducive to removing arsenic from the molten steel by rare earth elements, because LaAlO_3 can inhibit the further reactions between lanthanum and the crucible. Magnesia crucible, however, does not have similar effects. BN crucibles drop powders and decrease the cleanliness of steel. Besides, when the concentration of arsenic is low, arsenic can be barely removed by volatilizing under normal pressure. Furthermore, due to the existence of the interfacial tension, the molten slag is easy to separate from the molten steel and makes the fluidity of slag become worse. Although the molten slag can remove arsenic from the molten steel to some extent, it also has harmful corrosion effects on the crucibles.

Keywords Arsenic · Rare earth · Crucible · Vapor pressure · Slag

Introduction

The residual elements in steel, including arsenic, tin, antimony, etc., are difficult to be removed in the conventional steelmaking process. These elements usually segregate to grain boundaries and phase boundaries and cause serious harm to the mechanical properties of steel products. To improve the cleanliness of steel, decreasing the content of the residual elements is of great significance. The recycling of a large number of scrap steel leads to the enrichment of residual arsenic in steel. To effectively remove arsenic from steel, many methods have been tried. Because of very active chemical activity, rare earth elements (REEs) have great potential to remove

Y. Peng · H. Wang (✉) · S. Jiang

College of Materials Science and Engineering, Chongqing University, Chongqing 400044, China
e-mail: wanghp@cqu.edu.cn

© The Minerals, Metals & Materials Society 2021

J. Lee et al. (eds.), *Materials Processing Fundamentals 2021*, The Minerals, Metals & Materials Series, https://doi.org/10.1007/978-3-030-65253-1_15

177

and stabilize arsenic in steel. The main roles of REEs in steel are purifying molten steel, modifying inclusions [1–5], and microalloying [6–9]. Generally speaking, REEs preferentially react with oxygen and sulfur in steel to form La_2O_3 and $\text{La}_2\text{O}_2\text{S}$ first [10], and followed by La–S–As, as well as LaAs [11].

Owing to the extremely strong chemical activity of REEs, considerations need to be noticed when REEs are used to remove arsenic from molten steel: First is the reactions between REEs in molten steel and refractories, especially for small-scale experiments in the laboratory, and second is the reactions between REEs in molten steel and slags. REEs can also react with oxides in the slag that dramatically decreases the effective content of them. Third, the evaporation of arsenic also needs to be taken into account.

This paper focuses on the above-mentioned three issues that need considerations when REEs are used to remove residual element arsenic from molten steel.

Materials and Methods

Pre-melt refining slags were used in this work. Pure reagents CaO , SiO_2 , Al_2O_3 , and MgO are mixed according to the proportion of 55%, 9%, 30%, and 6%, respectively. We used GCr15 bearing steel and high carbon steel as the raw materials. Their chemical compositions are shown in Table 1. 500–600 g raw materials without and with a 5% refining slag were added into the alumina crucibles. The steelmaking process was carried out in an induction furnace with high-purity argon protection. After vacuuming, we used argon gas to fill the furnace tube. We gradually increased the output power to control the temperature of the induction furnace and measure the temperature with a thermocouple at the bottom of the crucible. It takes about 45 min to reach the target temperature (1600 °C for high carbon steel and 1570 °C for GCr15 bearing steel) from room temperature. After it melted totally for 10 min, high-purity arsenic particles were added. Ten minutes after adding arsenic, lanthanum metal was added. The induction furnace power was turned off after another 20 min, and the liquid steel was furnace cooled to room temperature. Similarly, the same steps are adopted when using magnesia crucible and BN crucible. In the same way, the same steps are adopted to add different lanthanum contents to the slag. The sampling time and alloy adding time during the smelting process are shown in Fig. 1.

The equipment used to observe the types of inclusions in steel was a scanning electron microscope. From the initial sampling to final ingot, concentrations of arsenic and lanthanum were measured with Optima 8000, an inductively coupled plasma

Table 1 Chemical compositions of the raw materials (mass %)

Elements	C	Si	Mn	P	S	Al	O	As
High carbon steel	0.79	0.21	0.61	0.011	0.015	0.001	0.0024	0.005
GCr15	0.96	0.23	0.33	0.014	0.002	0.012	≤0.001	0.002

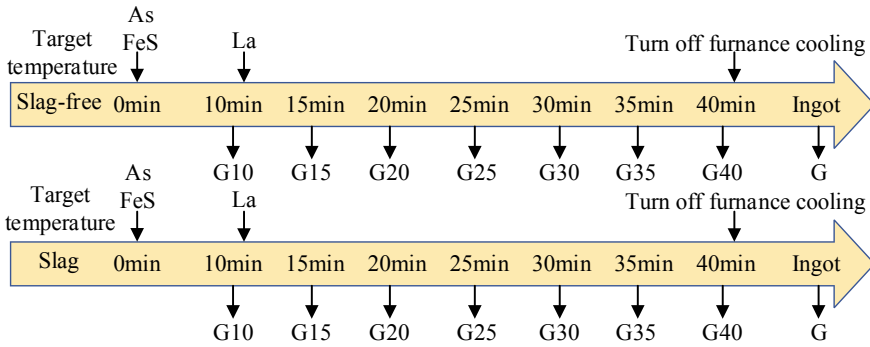


Fig. 1 Experimental detail of adding lanthanum, sulfur, and arsenic, and sampling. (Color figure online)

optical emission spectrometer. The compositions of inclusions were identified with an energy dispersive spectrometer.

Results and Discussion

Reactions Between REEs and Crucibles

After the molten steel was cooled to room temperature, no adhesion was found between the steel ingot and the alumina crucible, and a layer of substance is found in the contact surface of the alumina crucible and steel ingot, as shown in Fig. 2. It can be seen from Fig. 2 that adding 0.15% lanthanum into the high carbon steel reacted with the alumina crucible. LaAlO_3 and La_2O_3 were discovered in the surface layer of steel ingot, resulting from the reactions of lanthanum with alumina crucible, as shown by Eq. (1) and (2) [12, 13]. Meanwhile, La_2O_3 can afford heterogeneous nucleation cores for the formation of LaAlO_3 . Therefore, La_2O_3 and $\text{La}_2\text{O}_3\text{-LaAlO}_3$ complex inclusions were found at the surface of the ingot, which has a certain inhibitory effect on the continuous reaction between La and the crucible [14].



When magnesia crucibles were employed, only La_2O_3 was found on the contact surface between high carbon steel ingot and the crucible, as shown in Fig. 3. On the one hand, because magnesium has active chemical properties when lanthanum reacts with magnesia crucible to generate magnesium (Eq. (3)), magnesium reacts

Fig. 2 Interface of the ingot of high carbon steel and the alumina crucible. (Color figure online)

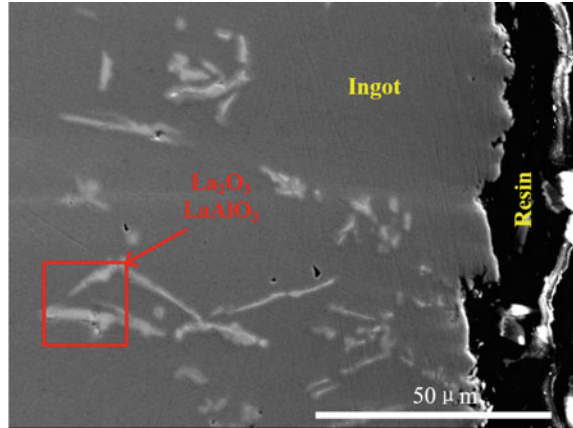
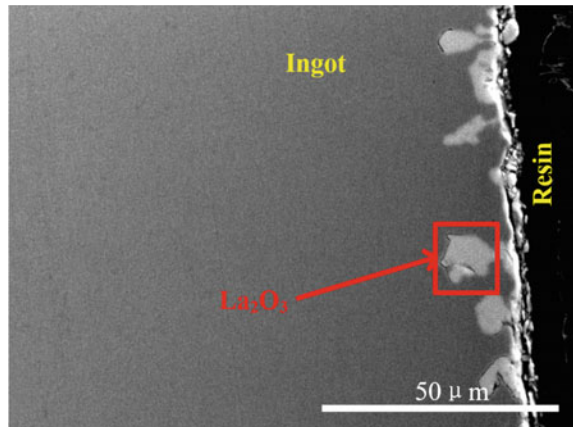
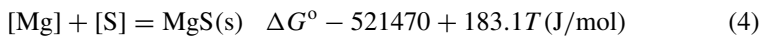
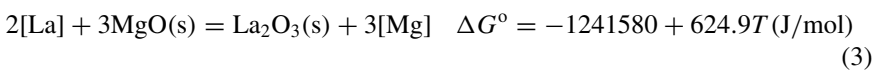


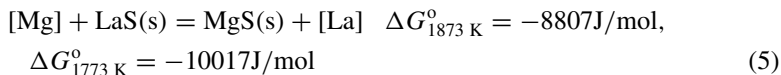
Fig. 3 Side surface of ingot when melting high carbon steel in the magnesia crucible with 0.15% La. (Color figure online)



with other inclusions in liquid steel to generate inclusion containing magnesium; on the other hand, the dissolved magnesium may transform into gas and escape from the molten steel owing to low vapor pressure, improving the continuous reactions between lanthanum and the magnesia crucible. This reduces the effective content of effective lanthanum to remove arsenic.

Besides, magnesium reacts with sulfur (Eq. (4)) and LaS (Eq. (5)) in molten steel, decreasing the effective sulfur content for the formation of La–S–As and its removal [15].





For the GCr15 bearing steel, the ingot tightly adheres to the magnesia crucible that shows severe reactions between La and magnesia, as shown in Fig. 4.

Boron nitride (BN) crucibles were also used to remove arsenic from the molten GCr15 bearing steel using lanthanum addition. Although lanthanum does not react with BN crucible, BN powders were discovered on the surface of the BN crucible after the melting process, illustrated in Fig. 5a, and many powders were also found in the ingot, as shown in Fig. 5b, c. Therefore, BN crucibles are not suitable for the steelmaking process.

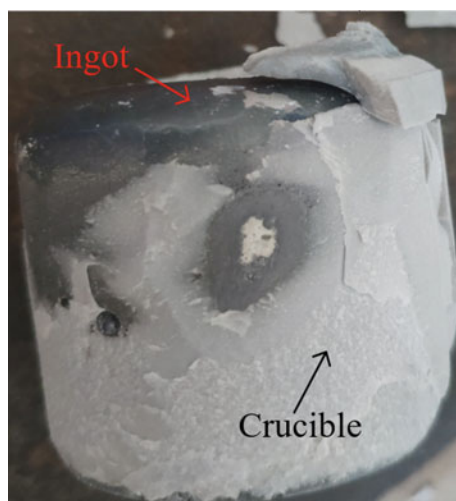


Fig. 4 GCr15 bearing steel ingot in the magnesia crucible with 0.1% La. (Color figure online)

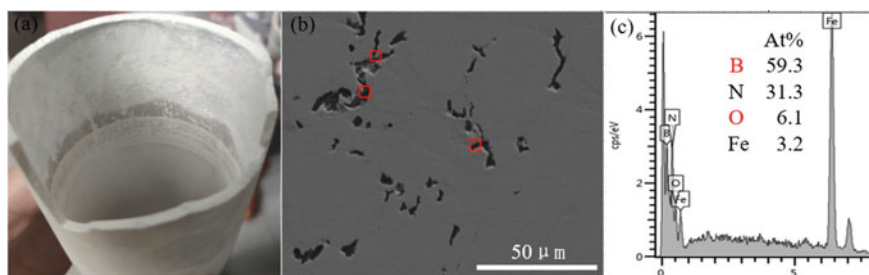


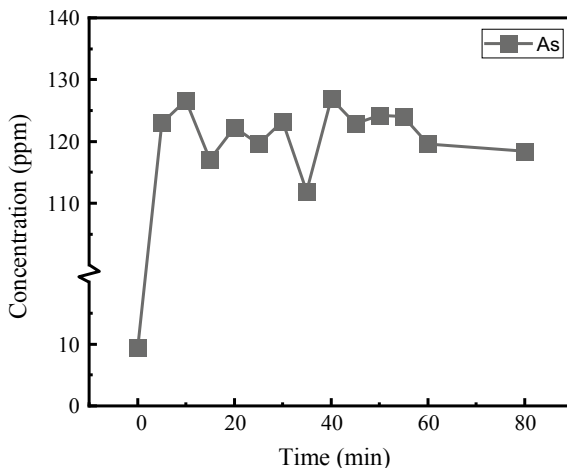
Fig. 5 BN crucible and ingot for smelting GCr15 bearing steel with 0.15% La. **a** The inner side of the BN crucible; **b** morphologies of BN powders; **c** chemical compositions of BN powders. (Color figure online)

In summary, the crucible used in the laboratory is relatively small and has a large specific surface area. The reactions between REEs and crucibles need considerations. The alumina crucible reacts with lanthanum to form La_2O_3 at first. As the heterogeneous nucleation cores of LaAlO_3 , La_2O_3 accelerates the generation of La_2O_3 – LaAlO_3 composite inclusion that inhibits the continuous reactions of lanthanum with the alumina crucible. The magnesia crucible will react severely with REEs, and the generated magnesium will react with sulfur in molten steel, which is not conducive to the generation of LaS , La-S-As , and cannot achieve a good arsenic removal effect. However, in industrial production, the specific surface area of crucibles (ladles) is very small, and the reaction between REEs and refractories can be ignored when the concentration of REEs is low. Due to having fallen powder with BN crucibles are not suitable for the steelmaking process. Therefore, it is more beneficial to investigate the removal of arsenic from steel by using alumina crucible to add rare earth in the laboratory.

Arsenic Volatilization

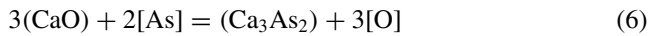
In theory, the vapor pressure of the arsenic element is very large, making it possible to remove arsenic by volatilization, but it turns out that arsenic does not volatilize much during the steelmaking process under the protection of argon. When the initial arsenic content was 0.012% in the molten GCr15 bearing steel, the arsenic content is 123 ppm in 5 min and 120 ppm in the ingot (Fig. 6).

Fig. 6 Volatilization of arsenic in the molten GCr15 bearing steel with melting time



The Reaction Between Rare Earth Element and Slag

The increasing REEs content has no obvious effect on the arsenic content in the molten steel when slags were added, as shown in Fig. 7a. At the same time, the arsenic content in molten steel increases slightly after adding La for 5 min. We think that the used high-basicity slags have a certain adsorption effect on arsenic. After adding La, because of its active chemical properties, it will react with the slag, resulting in a decrease in arsenic content of the slag and an increase in the molten steel. The adsorption of arsenic by the slag is due to the removal of arsenic from the molten steel by calcium-based materials [16]. In this paper, CaO content in the slag accounts for 55% that is beneficial to arsenic removal (Eq. (6)) [17]. The core theory of arsenic removal is the generation of La-S-As [18]. That the arsenic content in the molten steel does not decrease with the increase of lanthanum content here results from a low sulfur concentration of 20 ppm.



When the sulfur concentration increases from 20 to 100 and 150 ppm, the arsenic content in molten steel only decreases slightly after adding La for 5 min, as shown in Fig. 7b. This is because sulfur will react with high-basicity slags first [17], leading to the effective sulfur concentration lower for the removal of arsenic. Besides, the reactions between lanthanum and slags may also be a factor that decreases the removal effect of arsenic.

Before the addition of the slag, the arsenic content in the molten steel is about 120 ppm; after adding the slag, the arsenic content decreased to 100 ppm. It was reported that the high-basicity slag under normal pressure had a 10–15% rate of the arsenic removal in the molten steel [17], which is in accordance with this research.

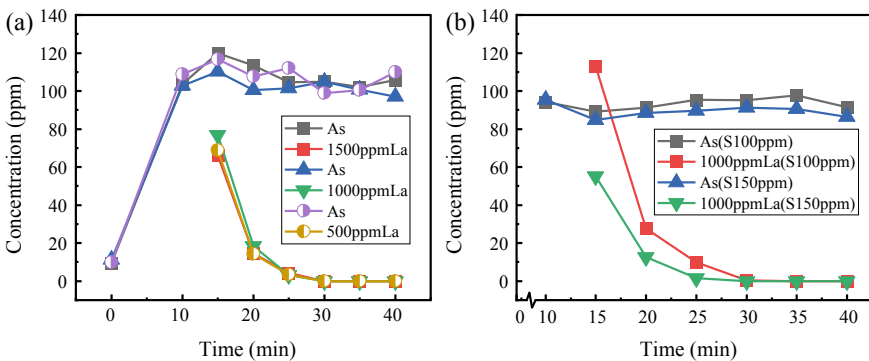
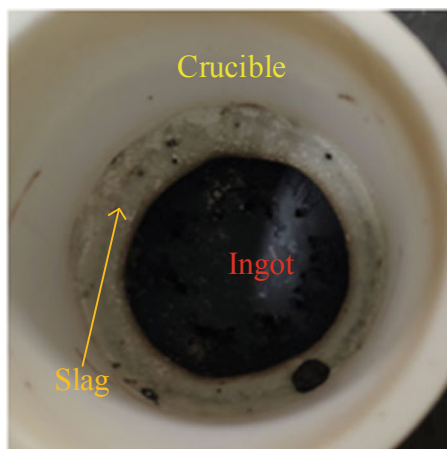


Fig. 7 Changes of lanthanum and arsenic content with slag and sulfur content in the steelmaking process. **a** Effect of slag with different lanthanum content on arsenic content in the steel; **b** effect of sulfur content in slag on lanthanum and arsenic content in the steel. (Color figure online)

Fig. 8 Morphologies of ingot and refining slag. (Color figure online)



After adding lanthanum, it will react with the alumina crucible to increase the aluminum content in the molten steel. As the aluminum content in molten steel increases, it will promote the removal of arsenic from the molten steel by high-basicity slag [19]. At the same time, the initial high sulfur content of the molten steel also promotes the removal of arsenic from the molten steel by slag.

It is worth noting that due to the existence of interfacial tension of the slag and the alumina crucible, the slag adheres to the wall of the alumina crucible, as shown in Fig. 8, resulting in poor fluidity of slag and reducing the absorption of arsenic removal products by slag.

In summary, in the laboratory, in order to reduce the influence factors of rare earth on the residual element arsenic in steel, the first consideration can be the case of not adding slag.

When sulfur with different lanthanum contents is added without slag, the arsenic content in molten steel decreases greatly within 5 min after adding 0.1% lanthanum, and arsenic returns after adding lanthanum for 10 min, as is shown in Fig. 9. After adding lanthanum for 30 min, the arsenic content in molten steel with an initial sulfur content of 150 ppm is lower than that with an initial sulfur content of 100 ppm. It is concluded that a suitable initial sulfur content is beneficial to the removal of arsenic.

Conclusions

1. The reactions between rare earth elements in the molten steel and crucibles are inevitable, especially in laboratory melting, because of the large contact area between the molten steel and crucible per unit mass. Alumina crucibles are more conducive to investigate the influence of rare earth elements on the removal of arsenic from the liquid steel.
2. Arsenic barely volatilizes under normal pressure smelting condition.

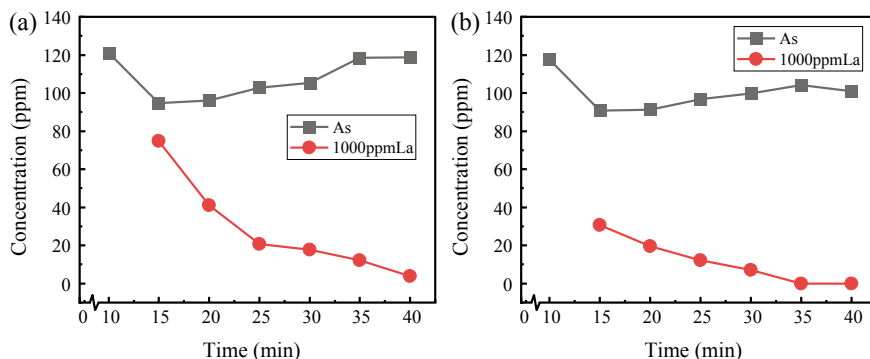


Fig. 9 Changes of lanthanum and arsenic content with and without slags and sulfur content in the steelmaking process. **a** Slag-free and with 100 ppm sulfur; **b** slag-free and with 150 ppm sulfur. (Color figure online)

3. High-basicity slags can remove arsenic in steel to some extent, but also react with the added rare earth.
4. In the crucible-scale steelmaking process, the existence of interfacial tension leads to poor fluidity of slags and reduces their absorption effect on the dearsenification products.

Acknowledgements This research is financially supported by the National Natural Science Foundation of China (No. 51704051).

References

1. Peng HB, Chen WQ, Chen L, Guo D (2015) Effect of rare earth yttrium on hot ductility of 20CrMnTi steel with 0.05% Tin. *Metall Res Technol* 112(3):307
2. Sun GL, Song B, Tao SF, Cai ZY (2015) Effect of manganese sulphide size on the precipitation of tin heterogeneous nucleation in as-cast steel. *High Temp Mater Proc* 34(3):251–256
3. Sun GL, Song B, Yang LZ, Tao SF, Yang Y (2014) Effect of manganese sulfide on the precipitation behavior of tin in steel. *Int J Min Met Mater* 21(7):654–659
4. Zhu YZ, Li JC, Xu JP (2012) Macroscopic distribution of residual elements As, S, and P in steel strips produced by compact strip production (CSP) process. *Metall Mater Trans A* 43a(7):2509–2513
5. Zhu YZ, Zhu Z, Xu JP (2012) Grain boundary segregation of minor arsenic and nitrogen at elevated temperatures in a microalloyed steel. *Int J Min Met Mater* 19(5):399–403
6. Adabavazeh Z, Hwang WS, Su YH (2017) Effect of adding cerium on microstructure and morphology of Ce-based inclusions formed in low-carbon steel. *Sci Rep* 7:46503
7. Torkamani H, Raygan S, Mateo CG, Rassizadehghani J, Vivas J, Palizdar Y, San-Martin D (2017) The influence of La and Ce addition on inclusion modification in cast niobium microalloyed steels. *Metals* 7(9):377
8. Xu YW, Song SH, Wang JW (2015) Effect of rare earth cerium on the creep properties of modified 9Cr-1Mo heat-resistant steel. *Mater Lett* 161:616–619

9. Yu Z, Liu CJ (2019) Modification mechanism of spinel inclusions in medium manganese steel with rare earth treatment. *Metals* 9(7):804
10. Das G, Lencka MM, Eslamimanesh A, Anderko A, Riman RE (2017) Rare-earth elements in aqueous chloride systems: thermodynamic modeling of binary and multicomponent systems in wide concentration ranges. *Fluid Phase Equilib* 452:16–57
11. Yang C, Luan Y, Li D, Li Y (2019) Effects of rare earth elements on inclusions and impact toughness of high-carbon chromium bearing steel. *J Mater Sci Technol* 35(7):1298–1308
12. Wang HP, Yu P, Jiang SL, Bai B, Sun LF, Wang Y. (2020) Evolution of inclusions in steelmaking process of rare earth steels containing arsenic with alumina crucibles. *Metals* 10(2):275
13. Kim HJ, Jun JH, Choi DJ (2008) Characteristics of La_2O_3 thin films deposited using metal organic chemical vapor deposition with different oxidant gas. *Ceram Int* 34(4):953–956
14. Kwon SK, Park JS, Park JH (2015) Influence of refractory-steel interfacial reaction on the formation behavior of inclusions in Ce-containing stainless steel. *Isij Int* 55(12):2589–2596
15. Wang HP, Yu P, Jiang SL, Wang Y (2020) Effect of heterogeneous nucleation on removal of arsenic from molten steel by rare earth addition. *Metals* 10(5):664
16. Noboru Hayashi HK, Teruo T (1971) Method for removing arsenic from metals or alloys. *US*, 3622302 11–23
17. Liu S, Sun S (2001) A study on dearsenication of molten iron and liquid steel with Ca–Si alloy. *Spec Steel* 22(5):12–15
18. Wang H, Jiang S, Yu P, Bai B, Sun L, Wang Y (2020) Distribution of arsenic inclusions in rare earth steel ingots. *Metals* 10(1):146
19. Liu S, Sun S, Zhang B, Wen G (2001) Arsenic removal from alkaline molten iron slag. *J Chongqing University (Nat Sci Edn)* 24(4):106–110

Containerless Materials Processing for Materials Science on Earth and in Space



Jonghyun Lee, Sai Katamreddy, Yong Chan Cho, Sooheyong Lee,
and Geun Woo Lee

Abstract Electromagnetic and electrostatic levitation techniques have been utilized for the last few decades to process metastable and highly reactive materials. Main fields of application include thermophysical properties, solidification, and transport phenomena of molten metals, which are of critical importance to better understand and control manufacturing processes dealing with molten metals, such as casting, welding, and additive manufacturing. This paper addresses part of our international collaborative work with NASA, European Space Agency, German Aerospace Center, and Japanese Aerospace Exploration Agency to support containerless experiments aboard the International Space Station. Along with space experiments, our recent work using an electrostatic levitator to unveil the liquid structure of aqueous sodium sulfate solutions (the most damaging salt to civil structures) is also introduced.

Keywords Containerless processing · Electrostatic levitation · Electromagnetic levitation · Thermophysical properties · Solidification · Convection in melts · Space experiments · Crystallization of salt solutions

J. Lee (✉) · S. Katamreddy
Department of Mechanical Engineering, Iowa State University, Ames, IA 50011, USA
e-mail: jolee@iastate.edu

J. Lee
Division of Materials Science and Engineering, Ames Laboratory, Ames, IA 50014, USA

Y. C. Cho · S. Lee · G. W. Lee
Center for Convergence Property Measurement, Korea Research Institute of Standards and Science, Daejeon 34113, Republic of Korea
e-mail: gwlee@kriss.re.kr

G. W. Lee
Department of Nano Science, University of Science and Technology, Daejeon 34113, Republic of Korea

Introduction

Containerless processing has been playing important roles in research on highly reactive materials, especially at high temperatures. Removing container walls allows access to a metastable state that cannot be reached by conventional container-based methods. For instance, an Fe–Co sample can be undercooled by more than 100 K and such a deep undercooling allows the study of multipath solidification phenomena of molten metallic alloys and the measurement of thermophysical properties over a much wider range of temperatures covering deep undercooling through superheating [1, 2]. On the other side, research is being carried out to unveil the liquid structure of quasicrystal and glass forming metals using containerless processing [3, 4]. Recently, an electrostatic levitator (ESL) was extended to study the change in molecular structure in a deep supersaturated state and its crystallizing phases [5]. By virtue of such unique advantages, the containerless processing community is expanding continuously. ESL was first developed by Dr. Won-Kyu Rhim at Jet Propulsion Laboratory in 1993 [6]. NASA Marshall Space Flight Center, Washington University in St. Louis, and Iowa State University followed in the USA. German Aerospace Center (DLR) has also joined this wave. Later, Japan, South Korea, and China developed their own ESL facilities. Electromagnetic levitator (EML) is relatively simpler in structure and operation and is being operated by more institutions than ESL all over the world. This paper gives several examples of how containerless processing has been applied to materials research. In the first section, the principles of EML and ESL that are being used both on eEarth and in space are described. From the second to fourth section, examples of application of EML and ESL to metals research are discussed. The topics in these three sections include phase selection during solidification of molten metallic alloys, convection in molten metals, and thermophysical properties of molten metals. These three topics are complementary to each other. In the fifth section, recent extension of ESL to process aqueous solution and colloidal suspension is introduced along with the potential applications of low-temperature ESL.

Electromagnetic and Electrostatic Levitators

There are several existing ways of achieving levitation of materials: electrostatic [6, 7], electromagnetic [8, 9], aerodynamic [10, 11], and acoustic [9, 12] methods are relatively widely utilized. This section briefly describes the principles and applications of ESL and EML to materials research on Earth and in space. The first column in Fig. 1 shows a 1-g EML where 1-g means gravity. This EML is installed and used on Earth counteracting gravity. EML uses a set of water-cooled copper tubes wound to form a cylindrical or conical shape. It can be noticed in the first column that the lower part has more turns of copper tube in order to generate an upward resultant force equivalent to the weight of a conductive sample. The size of a sample ranges from 5 to 7 mm in diameter and the weight is around 1 g. An alternating current


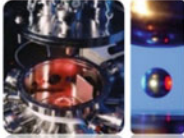
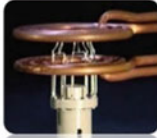

	1-g EML	1-g ESL	Space EML	Space ESL
Appearance				
Levitation Method	EM force induced by alternating current through coils	Charged sample supported by strong electric field	No gravity	No gravity
Pressure	~ 1 atm	Vacuum ($\sim 10^{-7}$ torr)	~ 1 atm	~ 1 atm
Advantages	Negligible mass evaporation Simple facility	Spherical sample Non-conducting materials	Negligible mass evaporation Spherical sample	Ceramics processing Negligible mass evaporation
Drawbacks	Deformed sample	Significant mass evaporation Complicated facility	Complicated facility High operation cost	Complicated facility High operation cost
Flow	Turbulent ($Re \sim 3000$)	Laminar ($Re \sim 100$)	Laminar - Turbulent	Laminar ($Re \sim 100$)

Fig. 1 EML and ESL on earth and in space. (Color figure online)

provided through the coils generates an electromagnetic force field which levitates and heats up the sample simultaneously. Heating was enabled by the combination of induced eddy current and the resistance of the sample. As levitation force and heating power is coupled, an inert gas such as helium or argon is flown over the sample in order to control the sample temperature. Helium provides a higher cooling effect due to its higher thermal conductivity. In a molten sample, electromagnetic forces not only induce convection but also deform the sample into a shape of a flipped egg. For 1-g EML, a minimum amount of current to counteract gravity is large enough to induce turbulence of $Re \sim 3000$ [13]. Such high convection limits the application of 1-g EML. For instance, when viscosity is measured by the oscillating droplet method which will be elaborated later in this paper, it must be ensured that the convection in the sample stays in the laminar regime. Otherwise, the measured viscosity is the turbulent viscosity which is the property of the flow not the fluid. Meanwhile, one of the space experiments is to investigate the influence of convection in a molten metal on phase selection during solidification. In order to collect a set of meaningful data, solidification must be observed under various convection conditions covering from laminar to turbulent regimes, which cannot be accessed using 1-g EML. This is a part of reasons why the EML shown in the third column is being operated in the International Space Station (ISS). This ISS-EML was built by a German aerospace company, Airbus, in collaboration with the European Space Agency and German Aerospace Center. US investigators are also participating in this large internationally collaborative research program with support from NASA. As can be seen in the third column of Fig. 1, the upper and lower coils have the identical number of turns as there is no need to cancel gravity. The coil set for ISS-EML is called SUPOS coil as two superimposed currents at different frequencies are provided through the coils

concurrently [14]. The positioner current at 150 kHz generates a quadrupole EM field to hold the sample near the center of the coils. The heater current at 350 kHz forms a dipole field to heat up and melt the sample. In the reduced gravity condition, the minimum magnitude of the positioning current can be lowered significantly, and it allows access to laminar, transition, and turbulent flows. This capability makes the ISS-EML a unique and powerful containerless tool when melt convection-related research is pursued. Reduction in the coil current thanks to the absence of gravity also decreases the amount of sample deformation during processing. An ISS-EML sample is processed in a vacuum chamber which is at times filled with helium or argon up to the half of atmospheric pressure depending on the purpose of experiments. Pressurizing the chamber is not allowed due to risk of gas leak which may jeopardize the health of astronauts. An inert gas(es) in the chamber helps control the melt temperature during processing and also reduces the amount of mass evaporation of a molten metal sample by several orders of magnitude. Eighteen samples are loaded in a sample holder cartridge per batch. As of August 2018, batch 1 processing has finished, and batch 2 experiments are being prepared.

ESL has a pair of vertical electrodes which generate an electrostatic field to levitate a charged sample in between. The electric potential difference between the vertical electrodes can be as high as 20 kV which is large enough to arc in a medium gas. Therefore, a 1-g ESL needs a vacuum chamber. Vacuum processing increases the rate of mass evaporation of molten metals considerably, especially for metals with high vapor pressure, such as iron, chromium, or manganese. For instance, an $\text{Fe}_{50}\text{Co}_{50}$ (at.%) sample held at 80 K above the melting temperature ($T_m = 1850$ K) for 85 s lost 9.2% of its mass. Fe concentration shifted from 0.4911 to 0.4744 (1.67%pt) as iron has higher vapor pressure than cobalt [15]. In this case, both mass change and composition shift must be tracked during processing and reflected in the course of data analysis for thermophysical properties measurements. In ESL, there are two additional pairs of electrodes on the horizontal plane which stabilize the sample by a proportional-integral-differential (PID) control loop based on the signal from a position-sensitive diode (PSD). Once the sample is levitated and stabilized, a heating laser(s) is applied to the sample. Nd:YAG, CO_2 , or diode laser of 60–200 W is (are) used for this purpose. With a 200 W Nd:YAG laser, a tungsten sample could be melted in several seconds. Sample temperature is continuously monitored using an optical pyrometer which detects the wavelength of light emitted from the sample and converts it into temperature data. Laser heating often generates temperature difference on the surface of the sample even up to 29 K [16]. Along the surface of a 2 mm sample, the temperature gradient can become as large as $9231 \text{ K}\cdot\text{m}^{-1}$ which induces a Marangoni flow. However, the magnitude of this surface flow is small in the magnitude with $\text{Re} \sim 100$ [16]. With ESL, only laminar convection can be obtained on the sample surface. In order to reduce the effect of thermal gradient induced by localized heating, the laser is often split into multiple paths and the sample is heated from two to four different angles. Theoretically, ESL can process almost all kinds of materials in the periodic table. However, ceramic materials are typically more difficult to be levitated stably as they tend to lose their surface charge upon heating

more easily. In order to minimize the mass evaporation and process the difficult-to-levitate materials, largely ceramics, the Japanese Aerospace Exploration Agency developed an ESL called ‘Electrostatic Levitation Furnace (ELF)’ which is installed in the Japanese KIBO deck in the ISS [17, 18]. As one of the ELF projects, the interfacial behavior between molten steel and molten slag is being investigated. A brief description on this project is provided in the following section.

Thermophysical and Thermomechanical Properties

Measuring accurate thermophysical properties has been an important issue in casting industry where casting simulation has become a standard process. For the last few decades, theoretical framework and numerical schemes to predict the convection during various casting processes have been improved significantly. The accuracy of numerical prediction tends to be determined more dominantly by the integrity of thermophysical properties. Metal additive manufacturing such as powder-bed fusion or direct energy deposition involves melting and solidification of a micron-sized metal particles in a timescale of microseconds. Localized heating by a laser or an electron beam may raise the temperature of a melt pool in the vicinity of a heat source up to 2300 K (Inconel 718 [19]) or even higher depending on materials. Such extreme conditions limit the roles of experimental investigation and the importance of computational approach keeps increasing. For successful physics-based simulations of additive manufacturing processes, accurate thermophysical properties measured over a wide range of temperature are strongly demanded.

Thermophysical properties, such as density [20–22], viscosity [23, 24], and surface tension [25, 26] of molten metals can be measured over a range of temperature covering deep undercooled through superheated regions using containerless processing facilities listed in Fig. 1. For the density measurement using ESL, a material of target composition is melted typically using an arc-melter into a near-spherical shape of 2–3 mm in diameter. Once a sample is levitated stably, it is heated with a heating laser. In general, for density measurement, the sample is put to one full melt cycle—heating from a solid, melting, superheating, free cooling, solidification, and cooling as a solid. During a thermal cycle, the silhouette of the sample is captured by a high-speed camera at a frame rate of 30 fps. The video data, combined with pyrometer data, is used to calculate the change in volume of the sample as a function of temperature. The mass of the sample before and after arc-melting and processing is measured to calculate the mass loss due to mass evaporation. The mass evaporation of the sample along the thermal cycle is also tracked analytically [15]. Mass loss and composition shift due to evaporation are reflected in the calculation of density. A thermal cycle for viscosity and surface tension measurement is identical to that for density measurement up to superheating. After a desired level of superheating is reached, laser power is regulated to put the sample into a thermal hold on the planned measurement temperature. During this thermal hold, the sample is excited either by a superimposed electrostatic field alternating at a frequency near the natural frequency

of the sample for the case of ESL or by an electromagnetic impulse for EML. Once the desired amount of deformation is achieved, the sample is let to dampen freely. High-speed video data (1000 fps) of an oscillating silhouette was image processed to extract the change in projected area as a function of time, which is in turn Fourier-transformed onto the frequency domain. The viscosity of the sample is calculated using damping time by the Lamb's equation (Eq. (1) [27]). Longer damping time gives lower viscosity. In a similar way, surface tension can be determined by the Rayleigh equation (Eq. 2 [28]) using the extracted oscillation frequency. Higher oscillation frequency results in larger surface tension.

$$\tau = \frac{\rho R_0^2}{(l-1)(2l+1)\mu} \quad (1)$$

$$f = \sqrt{\frac{l(l-1)(l+2)\gamma}{3\pi m}} \quad (2)$$

In the Lamb's equation, τ is the damping time which gives the viscosity, μ with known density (ρ) and radius (R_0) of the oscillating sphere. The Rayleigh equation determines the surface tension (γ) by the measured oscillation frequency (f) with known sample mass (m). l in both equations is mode number of oscillation.

One apparent way to increase the thermodynamic efficiency of energy conversion systems is to raise operating temperatures, which is generally restricted by materials. Recently, refractory materials whose melting point is higher than 2500 °C have been being developed. If the operating temperature is above the 50% of the melting point in K, creep becomes an important design factor. Conventional creep tests are contact-based methods where the specimen is in contact with grips, which limits the maximum testing temperature below 1700 °C. Beyond this limit, a chemical reaction can happen at the interface between the specimen and the grips. If the creep resistance of a material with a high melting point (>2500 °C) is to be tested by a contact-based method, it may take weeks or even months to see meaningful amount of creep deformation. In order to help accelerate the development and application of new high-temperature materials, a new creep test method that could be applied at temperatures higher than the current limit was strongly demanded. With this motivation, Lee et al. [29, 30] developed a new contactless method to measure the creep resistance of niobium using a 1-g ESL. A niobium sample was machined into a high-precision sphere of 2 mm in diameter. Once the sample is levitated, a heating laser is applied slightly off the center of the sample. Due to photon pressure exerted by the heating laser, the sample began rotating at an acceleration of approximately 780 rps-hr⁻¹. During this acceleration, the temperature of the sample was held at 1985 °C. Without gas drag in a vacuum chamber, the angular velocity at the end of test (420 min) reached 4878 rps (Fig. 2). By the combination of high temperature and high rotation rate, the sample showed noticeable creep deformation at about 250 min. The deforming sample was captured using a high-speed camera, and the deformed shape was numerically correlated to the creep constant (2.48 ± 0.12 , stress exponent in the Norton creep model). The creep constant was also measured by the

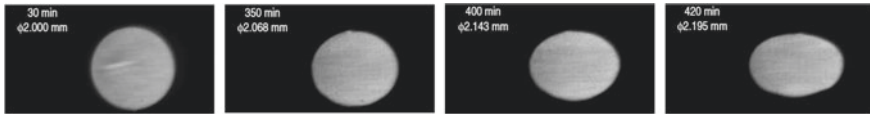


Fig. 2 Creep deformation of a high-precision niobium sphere processed by ESL at 1985 °C

conventional creep test (2.4 ± 1.0). The ESL test yielded a close result to that from the convectional creep test even with the higher precision by an order of magnitude. The developed method has been utilized to measure the creep resistance of newly developed high-temperature materials in funded collaboration with NASA, General Electric, US Air Force, and Aerojet Rocketdyne. The nickel-based superalloy tested with Aerojet Rocketdyne was applied to the nozzle extension of the J2X engine for the next-generation spacecraft.

Multi-pathway Solidification

Depending on the degree of undercooling and composition, a molten metal may solidify into a metastable phase first and then transform into a stable phase. Such a phenomenon is referred to as two-step solidification, and its resulting microstructure is quite different from the one formed by one-step solidification (liquid to stable phase). The chemical and mechanical properties of the solidified metals differ significantly depending on the paths they took during solidification. For instance, when steel (FeCrNi) solidifies in a two-step manner, the secondary dendritic arms of the metastable FCC phase formed during the first solidification are melted again by absorbing latent heat ejected from the solidifying stable BCC phase. Remelting of the first metastable phase results in smaller, more homogeneous, and more globular grains than those formed by one-step solidification [31].

As a molten metal undercools, its density and structure change. In this undercooled state, nuclei form and melt away continuously. According to the classical nucleation theory, the interfacial free energy between the nuclei and molten metal is the major contributor to the nucleation barrier. As the similarity in density and structure between the nuclei and molten metal increases, interfacial energy (nucleation barrier) decreases and the probability of forming a critical nucleus increases. Some metallic alloy systems such as Fe–Co [1, 2], Fe–Cr–Ni [31, 32], and Ti–Zr–Ni [4] solidify in a two-step manner when undercooled below a certain threshold temperature. The reason for this two-step solidification has not been understood completely. One strong hypothesis is that a molten metal first solidifies into a metastable solid phase which has more similar crystal structure (smaller nucleation barrier) to that of the undercooled molten metal. After a certain amount of delay time, this metastable phase transforms into a stable solid phase. The delay time, the time duration between the two solidification events, can range from the order of milliseconds to several

seconds depending on the degree of undercooling and composition. Such a two-step solidification phenomenon is observed even in aqueous salt solutions, proteins, and colloidal suspensions. Understanding the phase selection during solidification should allow a better control over the microstructure and property of a product made by casting or additive manufacturing.

The influence of melt convection on the phase selection of Fe–Co and Fe–Cr–Ni during solidification is being studied using the ISS-EML. As mentioned in the previous section, the ISS-EML is the only facility that allows access to melt convection in the laminar through turbulent regimes. A 1-g ESL is also being used to collect reference data and measure thermophysical properties for thermodynamic analysis and computational fluid dynamic models. A magnetohydrodynamic model was developed to predict the level of convection as a function of test parameters of ISS-EML, positioner, and heater currents [33]. The results of numerical simulations were used to determine the test parameters in order to induce and maintain the desired level of convection under which various solidification behaviors of the molten metal sample was observed. The details of the experiments can be found elsewhere [34–36].

Mass Transport Phenomena

Understanding and controlling of melt convection is important for a successful casting process. Convection affects cavity filling, cooling rate, warpage, and eventually the properties of a cast product. As discussed in the section above, melt convection may alter the resulting microstructure considerably. Convection also plays an important role in the formation of amorphous metals or quasicrystals. The basic idea of making an amorphous metal is rapid cooling from a molten state in order not to allow enough time for the atoms to rearrange themselves and form a crystal structure. A high shear rate may hinder this rearranging motion of the atoms and thus enhance its glass formability. Convection in the EM-levitated molten metal droplet has been studied for more than thirty-six years by a number of research groups. Due to its extreme conditions, e.g., high temperature, high reactivity, and metastable state, experimental characterization of convection in an EM-levitated metal droplet is an extremely challenging task. This is why most research groups have adopted analytical and numerical approaches.

With the ISS-EML, various compositions of metallic alloys are being tested. Approximate cost to process one sample is one million US dollars. PIs already spent several years to prepare their space experiments. Knowing that the melt convection affects the space experiments, there was a strong need to have an experimentally validated model that can predict the convection inside an EM-levitated molten metal droplet. Under such circumstances, Lee et al. [33] developed a magnetohydrodynamic (MHD) model. For the validation purpose, a $\text{Co}_{16}\text{Cu}_{84}$ sample was levitated by EML. If this sample is undercooled below 1468 K, it shows spinodal decomposition due to its large miscibility gap and separates into Co-rich and Cu-rich liquid phases. Due to difference in emissivity between the two separated phases, Co-rich

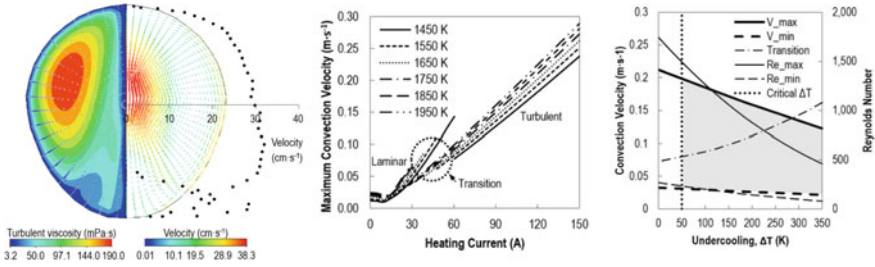


Fig. 3 Left [33]: Convection velocity field in an EM-levitated Co–Cu droplet. Black dots indicate surface convection velocity along the meridian. Convection velocity near the equator is predicted as $\sim 30\text{ cm}\cdot\text{s}^{-1}$; middle [37]: numerically predicted maximum convection velocity as a function of heater current in a Fe–Co droplet processed using the ISS-EML; right [31]: predicted accessible range of convection (gray parallelogram) in a Fe–Co sample during ISS-EML processing. (Color figure online)

phases looked brighter in the captured high-speed video. These Co-rich particles were drifting along the streamline of the Cu-rich liquid. The particle velocity near the equator was measured as $\sim 30\text{ cm}\cdot\text{s}^{-1}$. The convection velocity at the similar location predicted by the developed MHD model was $28.6\text{--}32.5\text{ cm}\cdot\text{s}^{-1}$. The difference between the observed and predicted convection velocities is less than 8.3%, which is excellent agreement considering the flow is turbulent. This was the first-ever quantitative experimental validation of a MHD model of convection in an EM-levitated molten metal droplet. The developed model is being utilized to predict the convection pattern, convection velocity field, accessible convection range, and convection status in the flight samples for the ISS-EML [36, 37].

In order to know when laminar to turbulent transition (LTT) happens as indicated in Fig. 3b, the Reynolds number at LTT must be known. LTT is also important when viscosity is measured as mentioned in the section above. LTT in a molten metal is also investigated using the ISS-EML. In the previous space experiment, Hyers et al. [38] observed a turbulent transition phenomenon in a molten Pd–Si sample. Under a constant EM field generated by the TEMPUS coils, the convection in the sample accelerates. With a high heater current, the resultant EM force pushes the molecules from the surface to the center along the equatorial plane forming one large toroidal flow in the upper and lower hemispheres. The two toroidal flows form a stagnation line along the equator on the surface. As soon as the Pd–Si sample melted, tracer particles quickly drifted toward the equator and accumulated along the stagnation line. The agglomeration of the tracer particles began oscillating forming a sinusoidal curve upon the flow acceleration. As the convection accelerates further, the amplitude of the sinusoidal curve increases gradually and the curve eventually breaks into multiple small pieces, which is an apparent indication of turbulence. The Reynolds number at LTT was determined to be 600. A similar transition phenomenon has also been observed for the Ni–Al system. In this case, the particles come from the poles down to the equator and disappear into the center instead of accumulating along the stagnation line. The tracer particles used for the Pd–Si sample were made of ceramics which

have much lower density than Pd–Si. For the case of Ni–Al, tracer particles were not added and the observed particles could be some of intermetallics which have a higher melting point but similar density to the molten part. Small or even possibly negligible density difference must have enabled the particles to follow the flow into the center instead of floating on the surface along the stagnation line (Stokes number $\ll 1$). A numerical model is being developed to reconstruct the accelerating flow in the molten Ni–Al under a constant EM field. This model is expected to shed more light on the LTT phenomena in molten metals.

In a continuous casting process, molten steel is fed into a tundish which in turn feeds the molten steel down to a water-cooled mold where continuous solidification occurs. Slags are added to the tundish to absorb impurities from the molten steel and reduce the amount of oxidation by covering the exposed surface of the molten steel. Due to the momentum carried by the molten steel fed into the tundish, mixing between the molten steel and molten slag often happens. Some of the mixed molten slag can be emulsified into the molten steel and leave in the final cast steel resulting in a low-quality product. In order to control the slag and steel mixing and slag emulsification, the interfacial phenomena are being studied using the ELF aboard the ISS [39]. As the first step, interfacial tension between molten steels and molten slags is being measured [39]. A concentric compound droplet of molten steel (core) and molten slag (shell) is levitated and excited to induce oscillation. Different from the single phase droplet described in the section above, due to the presence of the core, two oscillation frequencies are extracted from the time-oscillation curve. Interfacial tension can then be calculated analytically using the two extracted oscillation frequencies [40, 41]. During the experiments, the core oscillation cannot be directly observed as the molten slag is not transparent. By the help of a computational fluid dynamic model, the oscillation behavior of both the core and shell can clearly be visualized, which will help facilitate the design of space experiments [42]. This oscillation behavior has been modeled numerically. This model allows researchers to investigate the influence of core–shell radii ratio, in-phase and out-of-phase oscillation, and rotation of the droplet on the measured interfacial tension. The developed model will also be used to interpret the results of the ELF experiments.

Low-Temperature ESL

Recently, Lee et al. [43] developed an ESL optimized to process liquid at low temperatures. With the low-temperature ESL, they investigated the multipath crystallization of potassium dihydrogen phosphate (KDP) solutions [5]. An injection needle attached to the bottom electrode injects the KDP solution within the ES field. There is competition between the electrostatic (ES) force which tries to levitate the injected droplet and the surface tension force which tries to hold the blown droplet at the tip of the needle. The droplet can be levitated when the ES force becomes slightly larger than the surface tension force. A Teflon-coated needle makes more hydrophobic surface

and helps reduce the surface tension force and facilitate the detachment of the droplet from the needle tip.

Once the solution droplet is levitated, the similar PSD and PID control schemes are used to keep the sample levitated stably. The size of the droplet is typically 2–3 mm in diameter. As soon as the solution leaves the needle tip, it evaporates and the droplet size decreases. An LED back light is used to capture the silhouette of the sample as a function of time from the opposite side of the sample. This silhouette data is also used to calculate the volume and concentration (supersaturation) of the sample assuming only water leaves the sample by evaporation. With this facility, the KDP solution could be brought up to unprecedentedly deep supersaturation with a supersaturation ratio over 4. Note the deepest supersaturation ratio reported was less than 2. The supersaturation ratio is defined as the ratio of the concentration of a solution to the saturated concentration at a given temperature. Under such deep supersaturation, the number of water molecules surrounding KDP ions (hydration number) decreases significantly and the molecules and ions behaves differently, which changes the nucleation and crystallization paths. A Raman spectrometer combined with the ESL allows to trace the change in molecular structure during evaporation. Raman shift gives clues to detect polymerization or phase transition. The solution ESL was also combined with a synchrotron x-ray facility to measure molecular structure before, during, and after crystallization. Using the solution ESL combined with a Raman spectrometer and a synchrotron x-ray, an experimental evidence of two-step crystallization in an aqueous KDP solution was clearly demonstrated.

The solution ESL shown in Fig. 4 is also being used to study the assembly of colloidal particles. Controlling the way of particle assembly may allow for the production of various kinds of functional materials. So far, the assembly of colloidal particles has been experimentally studied mostly in two-dimensional spaces, where the effect of the walls cannot be neglected. The low-temperature ESL extends the colloidal assembly to three-dimensions which is more relevant to large-scale manufacturing

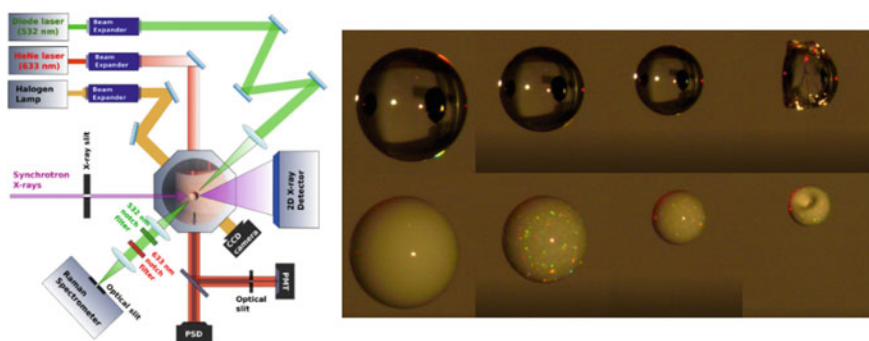


Fig. 4 Left [5] Solution ESL; top right: levitate sodium sulfate solution evaporates and eventually crystallizes; bottom right: levitated colloidal suspension (1 mm polystyrene particles in water) dries by evaporation. (Color figure online)

and also allows observation of pure interactions among particles by removing undesired wall effects. The application of the low-temperature ESL can also be farther extended to investigate the crystallization of medicines, proteins, optical filters, polymers, and other biological materials.

Summary

Containerless processing has been utilized to study physical phenomena in metastable or highly reactive materials. The areas of main applications include measurement of thermophysical and themomechanical properties of molten materials at high temperatures, multistep solidification in metallic alloys, and mass transport phenomena in molten metals and ceramics. Recently, ESL has been extended to levitate and process aqueous solutions and colloidal suspensions. The low-temperature ESL has good potential to be applied to crystallization of medicine, proteins, and other biological materials. Overall, containerless processing community which began to form in the USA is still being expanded all over the world. Japan and South Korea are running multiple ESL and EML facilities. China also recently developed ESL. Hong Kong is also developing ESL. With such expansion of the containerless processing, much work which has not been possible is expected to be done and new areas of science would be opened up in near future.

Acknowledgements This research has been supported by NASA under grant NNX14AH85G.

References

1. Rodriguez JE, Kreischer C, Volkman T, Matson DM (2017) *Acta Mater* 122:431–437
2. Rodriguez JE, Matson DM (2015) *CALPHAD: Comput. Coupling Phase Diagrams Thermochem* 49:87–100
3. Kim TH, Lee GW, Gangopadhyay AK, Hyers RW, Rogers JR, Goldman AI, Kelton KF (2007) *J Phys: Condens Matter* 19:455212
4. Lee GW, Gangopadhyay AK, Kelton KF (2011) *Acta Mater* 59:4964–4973
5. Lee S, Wi HS, Jo W, Cho YC, Lee HH, Jeong S-Y, Kim Y-I, Lee GW (2016) *Proc Natl Acad Sci USA* 113:13618–13623
6. Rhim W-K, Chung SK, Barber D, Man KF, Gutt G, Rulison A, Spjut RE (1993) *Rev Sci Instrum* 64:2961–2970
7. Rulison A, Watkins JL, Zambrano B (1997) *Rev Sci Instrum* 68:2856–2863
8. Peifer WA (1965) *J Met* 17:487–493
9. Brandt EH (1989) *Science* 243:349–355
10. Enderby JE, Ansell S (1997) *Appl Phys Lett* 71:116–118
11. Saboungi ML, Enderby JE, Glorieux B, Schnyders H, Sungaila Z, Krishnan S, Price DL, Non-Cryst J (2002) *Solids* 312–314:294–298
12. Gammel PM, Croonquist AP, Wang TG (1988) *J Acoust Soc Am* 83:496–501
13. Lee J, Xiao X, Matson DM, Hyers RW (2013) *Proc. TMS* 2013, pp 469–476. San Antonio, TX

14. Lohoefer G, Piller J (2002) The new ISS electromagnetic levitation facility: "MSL-EML". In: 40th AIAA aerospace sciences meeting and exhibit, pp AIAA 2002-0764. Reno, NV
15. Lee J, Matson DM (2014) *Int J Thermophys* 35:1697-1704
16. Hyers RW (2005) *Meas Sci Technol* 16:394-401
17. Murakami K, Koshikawa N, Shibasaki K, Ishikawa T, Okada J, Nakamura T, Yamaura Y, Arai T, Funino N, Tankada T (2013) *Adv Astronaut Sci* 146:705-708
18. Tamaru H, Koyama C, Saruwatari H, Nakamura Y, Ishikawa T, Takada T (2018) *Microgravity Sci Technol*
19. Li S, Xiao H, Liu K, Xiao W, Li Y, Han X, Mazumder J, Song L (2017) *Mater Des* 119:351-360
20. Lee J, Rodriguez JE, Hyers RW, Matson DM (2015) *Metall Mater Trans* 46B:2470-2475
21. El-Mehairy AE, Ward RG (1963) *Trans Metall Soc AIME* 227:1226-1229
22. Paradis P-F, Yu TIJ, Aoyama T, Yoda S, Weber JKR (2003) *J Cryst Growth* 249:523-530
23. Hyers RW, Bradshaw RC, Rogers JR, Rathz TJ, Lee GW, Gangopadhyay AK, Kelton KF (2004) *Int J Thermophys* 25:1155-1162
24. Rhim W-K, Ohsaka K, Paradis P-F, Spjut RE (1999) *Rev Sci Instrum* 70:2796-2801
25. Bakhtiyarov SI, Overfelt RA (2002) *Ann N Y Acad Sci* 974:132-145
26. Egrý I, Lohoefer G, Seyhan I, Schneider S, Feuerbacher BF (1999) *Int J Thermophys* 20:1005-1015
27. Lamb H (1881) *Proc London Math Soc* 13:51-66
28. Rayleigh L (1879) *Proc R Soc London* 29:71-97
29. Lee J, Bradshaw RC, Hyers RW, Rogers JR, Rathz TJ, Wall JJ, Choo H, Liaw PK (2007) *Mater Sci Eng, A* 463:185-196
30. Lee J, Hyers RW, Rogers JR, Rathz TJ, Wall JJ, Choo H, Liaw PK (2015) *Meas Sci Tech* 26:015901
31. Hanlon AB, Matson DM, Hyers RW (2006) *Phil Mag Lett* 86:165-174
32. Matson DM, Hyers RW (2006) *Phil Mag Lett* 86:3795-3807
33. Lee J, Matson DM, Binder S, Kolbe M, Herlach D, Hyers RW (2014) *Metall Mater Trans* 45B:1018-1023
34. Matson DM, Xiao X, Rodriguez JE, Lee J, Hyers RW, Shuleshova O, Kaban I, Schneider S, Karrasch C, Burggraaf S, Wunderlich R, Fecht H-J (2017) *JOM* 69:1311-1318
35. Lee J, SanSoucie MP (2017) *JOM* 69:1298-1302
36. Lee J, Hyers RW (2015) *Int J Microgravity Sci Appl* 32:320105
37. Lee J, Xiao X, Matson DM, Hyers RW (2015) *Metall. Mater Trans* 46B:199-207
38. Hyers RW, Trapaga G, Abedian B (2003) *Metall. Mater Trans* 34B:29-36
39. Watanabe M, Onodera K, Ueno S, Tsukada T, Tanaka T, Tamaru H, Ishiwawa T (2016) 10th international conference on molten slags, fluxes and salts, pp 1245-1252. Seattle, WA
40. Egrý I (2002) *Zeitschrift für Metalkunde* 93:528-531
41. Egrý I, Ratke L, Kolbe M, Chatain D, Curiotto S, Battezzati L, Johnson E, Pryds N (2010) *J Mater Sci* 45:1979-1985
42. Sumaria K, Hyers RW, Lee J (2017) *Proc. TMS 2017*, pp 65-72. San Diego
43. Lee S, Jo W, Cho YC, Lee HH, Lee GW (2017) *Rev Sci Instrum* 88:055101

Effect of Nitrogen on Weldability and the Microstructure in Laser Beam Welding of Duplex Stainless Steel



Yunxing Xia, Kenshiro Amatsu, Fumikazu Miyasaka, and Hiroaki Mori

Abstract Due to unbalanced phases' contents in welds of duplex stainless steel, their mechanical properties and corrosion resistance should be remarkably degraded from base metals' ones. It is reported that both the precipitation and growth of the austenite phase in the welds are affected by the nitrogen content as well as thermal cycles of welding. Especially, in the case of laser beam welding (LBW), these effects might be drastically changed as compared with them in conventional welding methods. From the microstructure observation in the LB welds using argon shield gases varied with nitrogen contents of 0, 10, and 20%, austenite phases growth at grain boundaries are promoted by the increase in nitrogen content in the shield gases. Based on elements' distributions measured in the previous report by an EPMA analysis, nitrogen is powerfully concentrated in austenite in each case. In addition, the in-situ observation by the micro-focused X-ray transmission imaging system revealed that porosity in the LB welds is suppressed by the increase of nitrogen in argon shield gases. These results suggested that under suitable thermal history conditions, the addition of nitrogen in argon shield gas for LBW might be effective to increase in austenite contents in welds of duplex stainless steels.

Keywords Laser beam welding · Nitrogen · Precipitation behavior · Phase ratio · Duplex stainless steels · X-ray transmission

Introduction

Duplex stainless steel has attracted extensive attention due to its high strength and corrosion resistance. Moreover, due to the price increase of raw materials, a low nickel type of duplex stainless steel is developed to replace the traditional stainless steel like

Y. Xia (✉) · K. Amatsu · H. Mori
Management of Industry and Technology, Graduate School of Engineering, Osaka University, 2-1 Yamadaoka, Suita 565-0871, Osaka, Japan
e-mail: xsia-y18@mit.eng.osaka-u.ac.jp

F. Miyasaka
Department of Adaptive Machine Systems, Graduate School of Engineering, Osaka University, 2-1 Yamadaoka, Suita 565-0871, Osaka, Japan

© The Minerals, Metals & Materials Society 2021
J. Lee et al. (eds.), *Materials Processing Fundamentals 2021*, The Minerals, Metals & Materials Series, https://doi.org/10.1007/978-3-030-65253-1_17

201

SUS304 and SUS316. It is widely used in many industrial products such as marine infrastructure equipment, bridges, and heat exchangers in recent years. Nevertheless, during the processing, especially welding, it is difficult to maintain duplex steel characteristics because the thermal history will change the amount of the phase ratio between the ferrite and austenite in welds. Due to the phase ratio changes after welding, weld metal of duplex stainless steels causes performance differences with the base metal [1]. Therefore, it is vital to understand the effect of thermal history on alloy diffusion and overall solidification. Many research studies have demonstrated that in welds of duplex stainless steel, both the precipitation and growth of the austenite phase are dependent on nitrogen diffusion [2, 3]. Particularly when applying laser beam welding, the absorption and escape of nitrogen in the welds during laser beam welding can also have a massive impact on the welds' microstructure. Also, the rapid cooling causes the diffusion rate of elements to become more critical. This will determine whether they could complete diffusion before the end of solidification.

Therefore, the purpose of this study is to compare the effect of applying 100% argon shield gas, Ar–10%N₂ shield gas, and Ar–20%N₂ shield gas on the microstructure in welds during full penetration laser beam welding and confirm the influence of thermal history on the ultra-thin plate (0.6 mm) thickness during lap-welding by microstructure observation. The study also compared the effect of argon shield gas and nitrogen shield gas on molten pool and bubble generation during the laser welding process in real-time via X-ray transmission in-situ observation. After analyzing the nitrogen content in the weld metal, we sorted out the relationship between nitrogen escape and laser welding velocities, and clarified the relationship between the nitrogen and the precipitation and growth behavior in the weld's microstructure of the duplex stainless steel via microstructure observation.

Experimental

Material

In this experiment, the duplex stainless steel (S82031) is subjected to a lap-welding by laser beam welding. The specification of the sheet is 100 mm (Length) × 100 mm (Width) × 0.6 mm (Thickness), and the chemical composition thereof is shown in Table 1.

Table 1 Chemical compositions of materials used (mass %)

Material	C	Mn	Ni	Cr	Mo	N
S82031	≤0.05	≤2.50	2.0–4.0	19.0–22.0	0.60–1.40	0.14–0.24

Table 2 Processing conditions of the laser beam welding for microstructure observation

		Laser output	Velocity (mm/min)	Focus distance	Shield gas
Laser beam weld	No. 1	1750 w	2000	31.4 mm (J.F.)	100%Ar(a)
	No. 2		4000		Ar-10%N ₂ (b)
	No. 3		6000		Ar-20%N ₂ (c)

Laser Beam Welding Condition and Shield Gas

Process parameters for laser beam welding are shown in Table 2. For comparing the effect of heat input (laser output/velocity) on the microstructure, we have chosen various welding velocities and constant laser output with full penetration-type lap-welding by the laser beam. Further, the effect of two types of argon–nitrogen-mixed shield gas and pure argon shield gas on precipitation and growth of austenite under each welding velocities were compared. There are nine kinds of welding conditions totally.

X-Ray Transmission Imaging System

In this experiment, the observation is performed using the microfocus X-ray fluoroscopic imaging system developed by the Joining and Welding Research Institute of Osaka University [4]. The experimental setup is shown in Fig. 1. This device is a microfocus X-ray tube (160 kV, 1 mA), worktable, X-ray image intensifier, high-speed video camera (maximum shooting speed: 400 f/s, or 40,500 f/s), and X-ray protection box. The laser head is also fixed so that the sample is irradiated with light at a predetermined point.

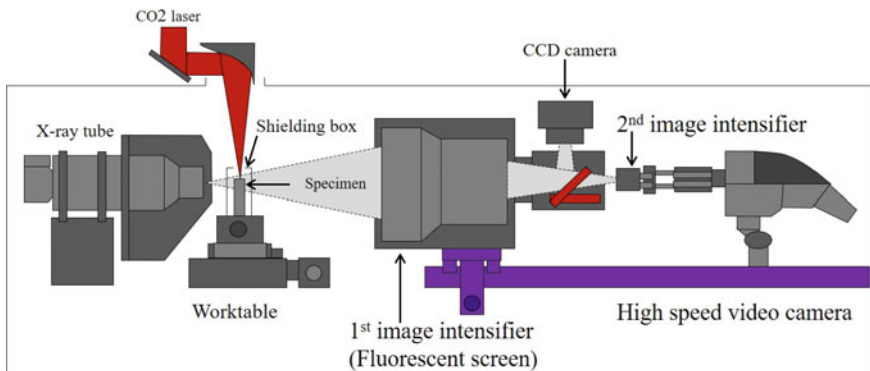


Fig. 1 Schematic arrangement of X-ray transmission imaging system for observation of keyhole behavior, bubble generation, and porosity formation. (Color figure online)

Table 3 Processing parameters of welding conditions for X-ray transmission imaging system

	Laser output	Velocity (mm/min)	Focus distance	Shield gas
Laser beam weld	2000 w	1000	31.4 mm (J.F.)	100%Ar 100%N ₂
		1500		
		2000		

Table 3 shows the process parameters when using direct observation of keyhole behavior through the X-ray transmission imaging system . These experiments were performed to observe and study the relationship between the welding velocities and the bubble production under the difference in nitrogen/argon shield gas with six welding conditions.

Results and Discussion of the Effect of Nitrogen on Weldability and Microstructure of Welds

In-Situ Observation

To investigate the effect of nitrogen shield gas on the weldability during laser beam welding in welds of duplex stainless steel, the real-time observation is performed applying a microfocus X-ray fluoroscope. Figure 2 shows the X-ray transmission experiments concept and the actual observation result with the welds of duplex stainless steel during the laser beam welding. The image shows the size of the keyhole and the generation of bubbles during the welding process and without using tracer for interface tracking.

The in-situ observation experiments used 100% Ar shield gas and 100% N₂ shield gas for observation and comparison. The observation results of different welding velocities are shown in Fig. 3. Whether the nitrogen or argon shield gas, under the

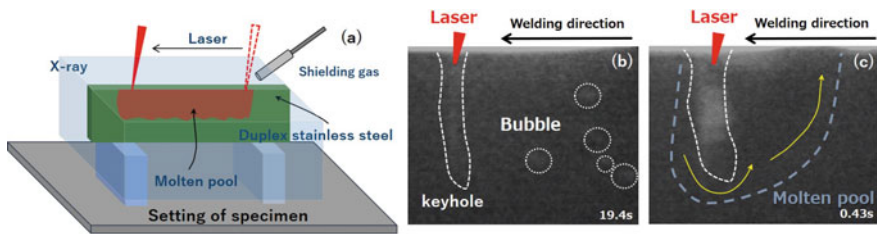


Fig. 2 X-ray transmission experiments concept and the actual observation result. **a**: Schematic diagram of the laser beam welding process in X-ray transmission imaging system **b**: keyhole and bubbles observed through X-ray transmission imaging system **c**: Schematic diagram of molten pool and flow during laser beam welding in X-ray transmission imaging system). (Color figure online)

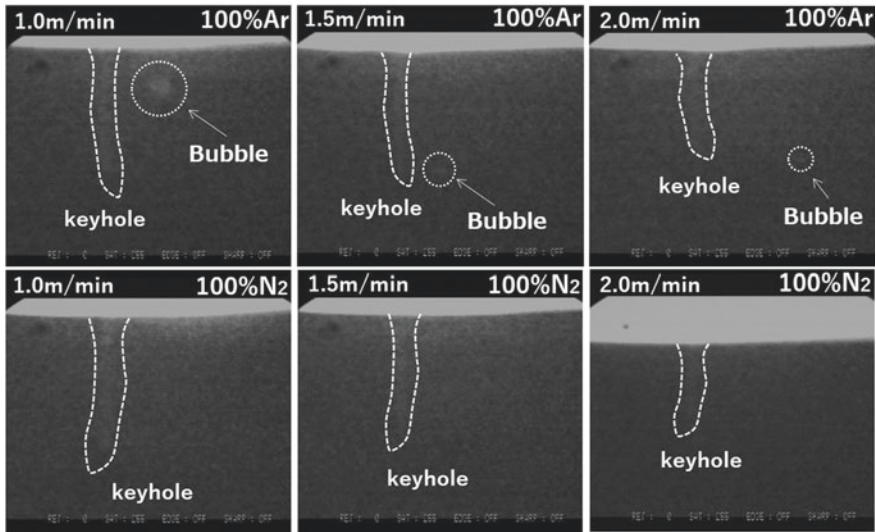


Fig. 3 Observation and comparison of Ar and N₂ shield gas under different welding conditions

same laser beam welding output, the length of the keyhole becomes shorter as the welding velocity increases, and the penetration ability of laser welding is reduced. Under argon shield gas at various welding velocities, bubbles are generated in the molten pool. The slower the speed, the larger the bubble formation and depending on the welding velocity, the floating position of the bubble also changes. In particular, in the case of fast welding, the bubbles are difficult to float up; they are basically parallel to the top of the keyhole's tip. As the welding velocity decreases, the bubbles can float up to the top in one moment and finally return to the middle location because of the molten pool's vortex. These bubbles remain during the solidification process and form the porosity of the welds. On the other hand, when nitrogen shield gas is applied, the formation of bubbles is obviously suppressed. In the case of slow welding velocity, almost no bubbles are observed. It can be presumed that nitrogen is soluble in the molten pool of duplex stainless steel and absorbed into the welds' microstructure during solidification, so it does not even leave porosity in the welds.

Microstructural Characteristics in the Welds

Figure 4 shows the microstructure in the welds of duplex stainless steel by lap-welding with argon shield gas. The top of the row is a full view of the welds, and the bottom row is a zoom-in view of the middle position of the welds. These three welding conditions with different velocities have penetrated the plate and formed a stable weld shape. Due to the heat input's influence, as the welding velocity increases, the welds' area becomes narrow, the microstructure of the weld has also changed.

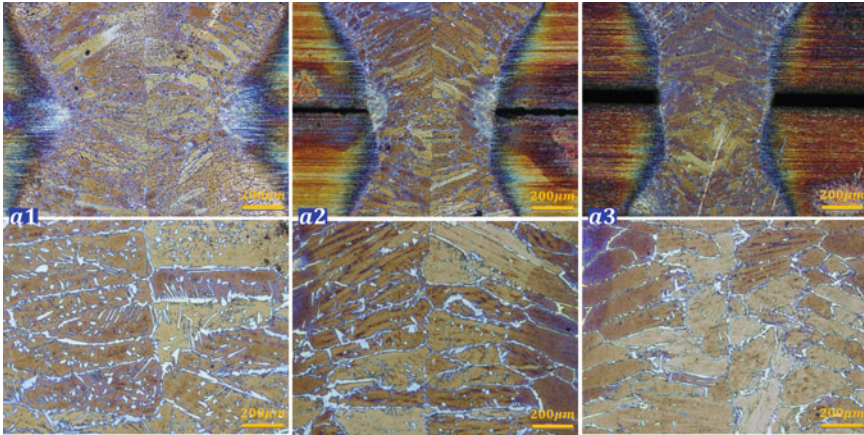


Fig. 4 Effect of laser beam welding velocities on microstructure of S82031 in welds (**a1**: 2000 mm/min, **a2**: 4000 mm/min, **a3**: 6000 mm/min). (Color figure online)

The faster the welding velocity, the more obvious the reduction of segregation in the welds, especially under the rapid cooling effect of laser beam welding. After 10% KOH corrosion, the austenite appears white. In Fig. 4a1, the precipitation of austenite is mainly based on the grain boundary and intragranular, and near the grain boundaries, many Widmanstätten-austenite can be observed. They grow along the austenite grain boundary into the ferrite matrix. With the decrease of the heat input, the Widmanstätten-austenite and intragranular austenite precipitation also decrease simultaneously. Previous research and literature search results show that the diffusion of nitrogen in the welds plays a decisive role in the behavior of austenite precipitation in the welds of duplex stainless steel. As an interstitial atom, nitrogen has a faster diffusion rate than a substitution atom. Even under laser welding with a high-speed cooling rate, a certain amount of diffusion can be achieved.

In this experiment, by adding nitrogen to the shield gas, the total nitrogen content of the welds increased while improving the precipitation of austenite. Due to lap-welding, even when pure argon shield gas is used, there is almost no residual porosity observed in the welds. Most bubbles, except those that rise and grow, are formed at the tip of the keyhole and remain in the solidification process. When the welds are penetrated like lap-welding, the bubbles escape to the external environment.

Figure 5 shows the microstructure in welds by welding with nitrogen and argon mixed gas and pure nitrogen at different welding velocities. Comparing Fig. 5a1, b1, c1 shows that when the heat input is relatively large, the amount of austenite precipitation in the welds increases with the rise of the nitrogen content in the shield gas. Also, the increasing precipitation morphology of austenite is mainly intergranular precipitation. With the increase of laser welding velocity, Ar-N₂ mixed shield gas has no effect on austenite precipitation in the welds. There is almost no difference with the microstructure under the 100% argon shield gas. These results can be presumed

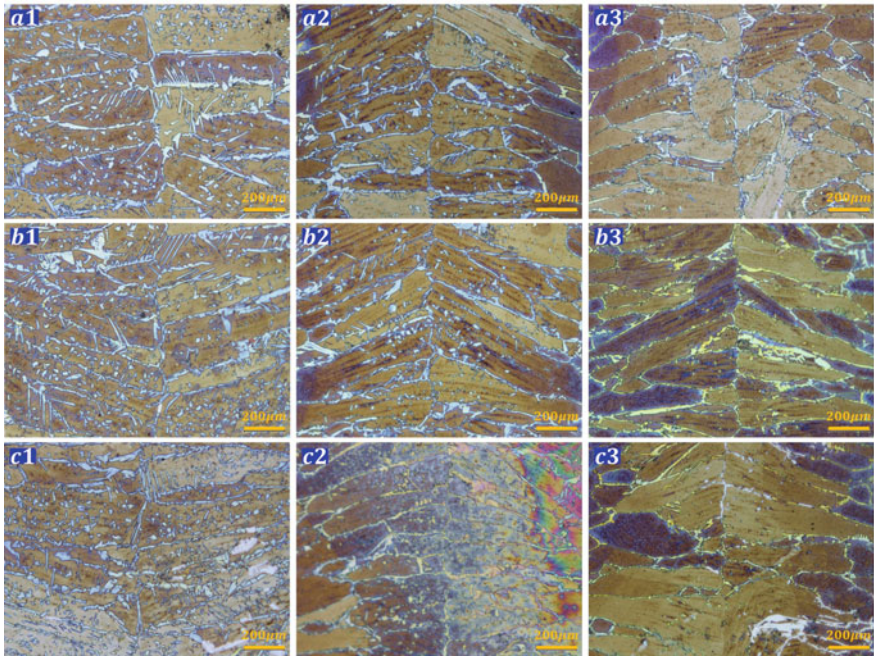


Fig. 5 Effect of laser beam welding velocities and shield gas on the microstructure of S82031 in welds (1: 2000 mm/min, 2: 4000 mm/min, 3: 6000 mm/min, **a**: 100%Ar, **b**: Ar10%N₂, **c**: Ar.20%N₂). (Color figure online)

due to the amount of escaped nitrogen at different welding velocities and the solid solubility limit of nitrogen in austenite under the effect of different heat histories.

The Amount of Escaped Nitrogen and the Solid Solution Limit of Nitrogen

The analysis result of the nitrogen content of the weld metal part is shown in Table 4. These results only consider the influence of nitrogen content in base metal on the escape of nitrogen during laser beam welding, so the shield gas is argon. By

Table 4 Nitrogen content analysis of weld metal (mass %)

Nitrogen content	BM	WM (1000 mm/min)	WM (2000 mm/min)
	0.18	0.15 (-16%)	0.16 (-11%)
	0.215	0.18 (-22%)	0.19 (-16%)
	0.31	0.24 (-16%)	0.26 (-12%)

comparing three types of commercially available duplex steels with different nitrogen content, the higher the nitrogen content in the base metal, the more nitrogen escaped. However, in comparison with the microstructure of welds at different welding velocities, it can be found that the amount of nitrogen escaped under laser welding has a minimal influence on the amount of austenite precipitated in welds. What is even more interesting is that under welding conditions with a large amount of nitrogen escape, the amount of austenite precipitation is much more than that of welding conditions with a small amount of nitrogen escape. When the welding velocity drops from 2 to 1 m/min, the weld metal's nitrogen content is reduced by about 5%.

It has been known from previous studies that the solubility of nitrogen in austenite increases as the content of chromium and manganese increases [5, 6]. During the solidification process, it is predicted that nitrogen's solubility will decrease due to the diffusion of chromium and manganese content in the austenite of welds. As a substitution atom diffusion is slow, chromium and manganese are almost incapable of diffusion in welds when they achieve influence from rapid laser solidification. But with the welding velocity increases, the size of the cylindrical crystals in welds become small. Finally, the solid solubility limit of nitrogen in ferrite is increased. In the relationship between the solid solution limit and the crystal grains, a relatively small crystal grain has a larger solid solution limit [7].

Conclusions

The influence of nitrogen on the welds of duplex stainless steel is summarized as follows.

The precipitation of austenite in the welds of duplex stainless steel mainly depends on nitrogen diffusion; this is due to the substitutional atoms that cannot get the corresponding diffusion under the rapid solidification of laser beam welding: the greater the heat input, the more obvious the precipitation of austenite, when the heat input is small, austenite is only precipitated at the grain boundaries. Also, the nitrogen of the base metal is escaped when using laser beam welding. The escape amount is different for each welding velocity.

After mixing nitrogen with the argon shield gas, as the nitrogen content increases, the austenite precipitation in the welds is promoted by large heat input welding conditions. However, due to the effect on nitrogen solid solution limit in the welds, in low heat input welding conditions, the amount of austenite precipitation hardly changes.

References

1. Fukui F (1981) Weldability duplex stainless steel. *J Japan Welding Soc* 50(3):235–240. <https://doi.org/10.2207/qjjws1943.50.235>

2. Kokawa H, Okada J, Kuwana T (1993) Nitrogen absorption and microstructure of duplex stainless steel weld metal. *Weld Int* 7(5):384–389
3. Omura T, Kushida T, Komizo Y (1999) Nitrogen distribution on rapid solidification in laser welded duplex stainless steels. *Q J Japan Welding Soc* 17(3):448–455
4. Seto N, Katayama S, Matsunawa A (2003) Porosity formation mechanism and suppression procedure in laser welding of aluminum alloy. *Weld Int* 17(6):431–437
5. Kikuchi M, Tanaka R (1975) Activity of nitrogen in austenitic steels. *Tetsu-To-Hagane* 61(13):2892–2903
6. Mori T, Shinmyo K, Ichise E, Morooka A (1963) Effects of chromium and manganese on the activity of nitrogen in austenite. *J Japan Instit Metals Mater* 27(2):49–53
7. Lagerberg G, Wolff EG (1958) The effects of grain size and texture on the internal friction in α -iron due to interstitial solutes. *Acta Metall* 6(2):136–137

Experimental Measurements and Optimized Iida Model Estimations of Viscosity in Vanadium Slag with Different FeO Content



Lingxi Zhang and Min Chen

Abstract The viscosity evolution of vanadium slag using photovoltaic cutting waste as a reductant during the pre-reduction process was very important to kinetic condition and separation of Fe. However, there was little work reported on viscosity and model of FeO–SiO₂–V₂O₃–CaO–MnO–Cr₂O₃–TiO₂ system for the pre-reduction process of vanadium slag. In this study, the viscosity of FeO–SiO₂–V₂O₃–CaO–MnO–Cr₂O₃–TiO₂ system was experimentally measured by the cylinder method, and the Iida model was optimized by fitting experimental viscosity data. The results showed that the viscosity of the slag system increased from 0.120 to 0.473 Pa s as the FeO mass fraction decreased from 37 to 11% at 1873 K. Besides, the optimized Iida model estimated the viscosity, which had an average error value (Δ) of less than 11.40% from the experimentally measured viscosity, and the optimized Iida model also well predicted its subsidiary system of FeO–SiO₂–V₂O₃–TiO₂–Cr₂O₃ and FeO–SiO₂–V₂O₃–TiO₂, with Δ below 13.62% and 11.25%, respectively. For the vanadium slag with Cr₂O₃ mass% less than 5, the optimized Iida model could provide theoretical viscosity and it had a satisfactory agreement with experimentally measured results.

Keywords Vanadium slag · Reduction · Viscosity · Iida model · Optimize

Introduction

The production process of FeV alloy from vanadium slag included oxidizing roasting, leaching, second roasting and aluminothermic or silicothermic reduction, which was long and high cost [1, 2]. Therefore, Tang and other researchers tried to directly produce FeV alloy using vanadium slag as starting materials by a two-step reduction. Silicothermic pre-reduction was to enrich vanadium, and then the pre-reduced slag

L. Zhang · M. Chen (✉)
School of Metallurgy, Northeastern University, Shenyang 110819, China
e-mail: chenm@smm.neu.edu.cn

was finally reduced by aluminothermic reduction [3, 4]. However, during the pre-reduction using silicon metal as a reductant, the problem with cost and resource waste was serious.

As well known photovoltaic cutting waste (PCW) was a by-product during silicon wafer slicing for solar cell fabrication, it mainly consisted of 40.0–61.5% Si and 20.5–27.5% SiC with the price of only a quarter of metal silicon [5]. Therefore, the selection of PCW as a reductant for the pre-reduction of vanadium slag was a promising method to solve the above-mentioned problems.

The viscosity of slag influenced the kinetic condition and the separation of hot metal during pre-reduction, and it was a key aspect of the pre-reduction process for enrichment of vanadium slag [6]. But till now, there was little work reported on the viscosity of FeO–SiO₂–V₂O₃–CaO–MnO–Cr₂O₃–TiO₂ system. Besides, the Iida model was considered as one of the most reliable on estimations of viscosity, and it worked well for slags including waste disposal slags and synthetic slags [7, 8]. However, the Iida model of the present slag system had not been investigated. Therefore, the experimental measurement and Iida model estimations of viscosity were indispensable.

In the present study, the viscosity of FeO–SiO₂–V₂O₃–CaO–MnO–Cr₂O₃–TiO₂ slag system was investigated by the cylinder method, and the Iida model was optimized by fitting experimental viscosity data. Besides, the average error values (Δ) of the slag system and its subsidiary system of FeO–SiO₂–V₂O₃–TiO₂–Cr₂O₃ and FeO–SiO₂–V₂O₃–TiO₂ would also be investigated to further indicate the prediction effect using the optimized Iida model.

Experimental Procedures

Viscosity Measurement

Based on the typical compositions of the vanadium slag and PCW (as shown in Tables 1 and 2), the slag samples with composition were shown in Table 3. Reagent-grade powders (>99.50 wt%) as raw materials including FeC₂O₄, Cr₂O₃, V₂O₃, MnO, TiO₂, SiO₂ and CaCO₃ were used. After drying and mixing, 180 g of the samples

Table 1 Chemical compositions of vanadium slag, wt%

Compositions	FeO	V ₂ O ₃	SiO ₂	MnO	Cr ₂ O ₃	TiO ₂
wt%	41.16	14.24	19.35	11.15	4.92	9.18

Table 2 Chemical compositions of PCW, wt%

Compositions	Si	SiC	SiO ₂
wt%	59.19	25.85	14.96

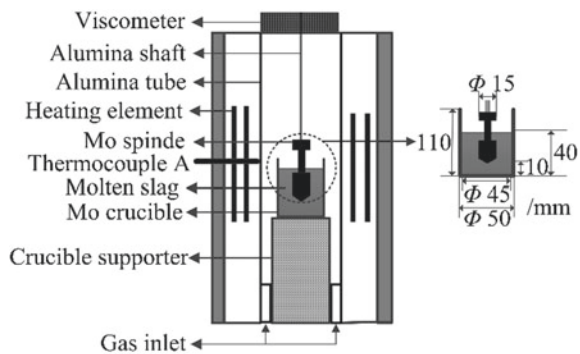
Table 3 Chemical compositions of investigated slag system, wt%

Slag No.	Reduction degree of FeO [%]	w(FeO)	w(V ₂ O ₃)	w(SiO ₂)	w(MnO)	w(Cr ₂ O ₃)	w(TiO ₂)	w(CaO)
S1	0	37	13	17	11	5	9	8
S2	20	30	14	22	11	5	9	9
S3	40	24	14	27	11	5	9	10
S4	60	18	15	32	11	5	9	10
S5	80	11	16	37	11	5	9	11

were placed in a Mo crucible (an inner diameter of 45 mm and a height of 110 mm), and they were soaked at 873 K and 1173 K for 2 h to ensure the decomposition of FeC₂O₄ and CaCO₃, respectively. Whereafter, to ensure the cations existing in desired valency, namely in the occurrence state of Fe²⁺, V³⁺, Ti⁴⁺ and Cr³⁺, the slag samples were soaked at 1873 K for 8 h to ensure the above cations reach equilibrium. Finally, the crucible was rapidly taken out of the furnace and quenched in liquid nitrogen, after separation of the slag sample and crucible, the pre-melted slag was prepared.

The viscosity of slag at elevated temperature was measured using the rotating cylindrical method [9, 10], and the experimental apparatus for viscosity measurements was shown in Fig. 1. 180 g of the pre-melted slag sample was put into a Mo crucible and soaked at 1873 K for 2 h to ensure the sample completely melted. For each sample, the viscosity was measured from 1873 K with temperature dropping rate of 2 K/min. Besides, the gas mixture of CO₂/CO with the volume proportion (V(CO₂)/V(CO)) of 1:4.124 was as protective gas, and the flow rate was kept at 1.2 L/min to ensure the oxygen partial pressure (atm) at 10⁻⁸ during the whole heating, cooling and the viscosity measurement process.

Fig. 1 Experimental apparatus for viscosity measurements



Iida Model

Based on the Iida model, the viscosity of slag was shown in Eq. (1), where A is pre-exponential factor, E is activation energy, and B_i is the slag basicity index. B_i is expressed by Eq. (2), where α is characteristic parameter, ω is mass fraction of the components, subscript A represents basic oxides, and subscript B represents acidic oxides.

$$\ln \eta_{\text{measure}} - \ln \eta_0 = \ln A + E/B_i \quad (1)$$

$$B_i = \frac{\sum (\alpha_i \omega_i)_A}{\sum (\alpha_i \omega_i)_B} = \frac{\alpha_{\text{CaO}} \omega_{\text{CaO}} + \alpha_{\text{MnO}} \omega_{\text{MnO}} + \alpha_{\text{FeO}} \omega_{\text{FeO}} + \alpha_{\text{TiO}_2} \omega_{\text{TiO}_2}}{\alpha_{\text{SiO}_2} \omega_{\text{SiO}_2} + \alpha_{\text{V}_2\text{O}_3} \omega_{\text{V}_2\text{O}_3} + \alpha_{\text{Cr}_2\text{O}_3} \omega_{\text{Cr}_2\text{O}_3}} \quad (2)$$

Besides, η_0 is the theoretically calculated viscosity of slag as shown in Eq. (3), where n is the number of slag components, X_i is mole fraction of the components, η_{0i} is the hypothetic viscosities of the components, M_i is mole mass, T_m is melting temperature, and V_m is mole volume. H_i is melting enthalpy of individual components “ i ”, which was expressed by Eq. (4). Based on the experimental viscosity data and theoretical computations of η_0 and B_i , the optimized Iida model was established by fitting technique. The parameters A and E were optimized to make it adequate for a given temperature range and for a definite group slag.

$$\eta_0 = \sum_i^n \eta_{0i} X_i = \sum_i^n \left\{ 1.8 \times 10^{-7} \frac{[M_i(T_m)_i]^{1/2} \exp(H_i/RT)}{(V_m)_i^{2/3} \exp[H_i/R(T_m)_i]} X_i \right\} \quad (3)$$

$$H_i = 5.1 \times (T_m)_i^{1.2} \quad (4)$$

Results and Discussion

Experimental Measurements of Viscosity of Vanadium Slag with Different FeO

Figure 2 shows the effect of temperature and FeO mass fraction on the viscosity behavior of the FeO–SiO₂–V₂O₃–CaO–MnO–Cr₂O₃–TiO₂ slag system. It is observed from Fig. 2a that the viscosity decreased with increasing temperature from 1723 to 1848 K in the specific slag system, and then the viscosity remained stable with further increasing temperature to 1873 K. The viscosity of S1, S3 and S5 decreased from 0.655 Pa s, 1.015 Pa s and 1.555 Pa s to 0.125 Pa s, 0.245 Pa s and 0.475 Pa s when the temperature increased from 1723 K to 1848 K, respectively. Whereafter, with the temperature further increasing to 1873 K, the viscosity of S1,

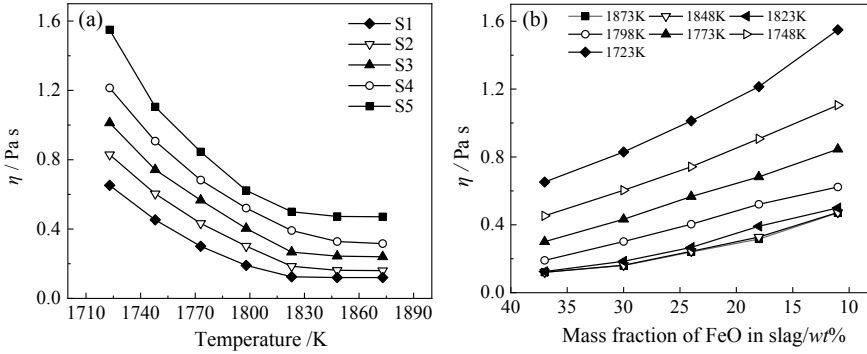


Fig. 2 Effect of temperature and mass fraction of FeO on the viscosity: **a** temperature; **b** mass fraction of FeO in slag

S3 and S5 slowly decreased to 0.120 Pa s, 0.240 Pa s and 0.471 Pa s, respectively. The viscosity decreased with the increase of temperature due to the depolymerization of the complex polymers in slag. But when the depolymerization of the complex polymers was finished and the simple structures with stability were regenerated, thereby the viscosity was closed to a constant value.

In addition, from Fig. 2b it is observed that the viscosity increased with the decrease of FeO mass fraction at the specific temperature. The viscosity of slag increased from 0.652 Pa s to 1.549 Pa s and 0.120 Pa s to 0.473 Pa s as the FeO mass fraction decreased from 37 to 11% at 1723 K and 1873 K, respectively. Therefore, the viscosity of slag increased gradually with the decrease of FeO mass fraction, namely with reduction reaction proceeding.

Optimization of Iida Model

Table 4 shows calculation parameters of Iida model in Eqs. (2) and (3), and in Table 5 there are presented calculation values of basicity index B_i in experimental slag system.

Based on the above calculation parameters and experimental viscosity data, the relationship between model parameters A and E and temperature T is shown in Fig. 3. The results of curve fitting showed that the parameters A and E were a second-order function of the temperature and presented in Eqs. (6) and (7). Therefore, an optimized Iida model was straightforward established for calculating the viscosity of FeO–SiO₂–V₂O₃–CaO–MnO–Cr₂O₃–TiO₂ slag system.

$$A = 6.12465 \times 10^{-7}T^2 - 0.00252T + 2.58385 \tag{6}$$

$$E = 8.07453 \times 10^{-6}T^2 - 0.02925T + 27.2654 \tag{7}$$

Table 4 Calculation parameters of Iida model

Component	T/K	M/10 ⁻³ kg/mol	V/10 ⁻⁶ m ³ /mol	η _{0i} /Pa s	α
SiO ₂	2001	60.08	27.29	0.13170exp (5613.8/T)	1.48
V ₂ O ₃	2243	149.90	31.23	0.18902exp (6438.1/T)	0.11
TiO ₂	2108	79.90	21.03	0.18045exp (6027.0/T)	0.36
CaO	2873	56.10	23.49	0.13712exp (8664.9/T)	1.53
MnO	1923	70.90	8.91	0.30212exp (5352.2/T)	1.03
FeO	1642	71.80	12.90	0.24021exp (4428.0/T)	0.96
Cr ₂ O ₃	2538	151.99	29.12	0.19708exp (7467.1/T)	0.13

Table 5 Calculation value of basicity index B_i in experimental slag system

Slag No.	S1	S2	S3	S4	S5
B _i	2.288	1.644	1.255	0.949	0.734
1/B _i	0.437	0.608	0.797	1.053	1.362

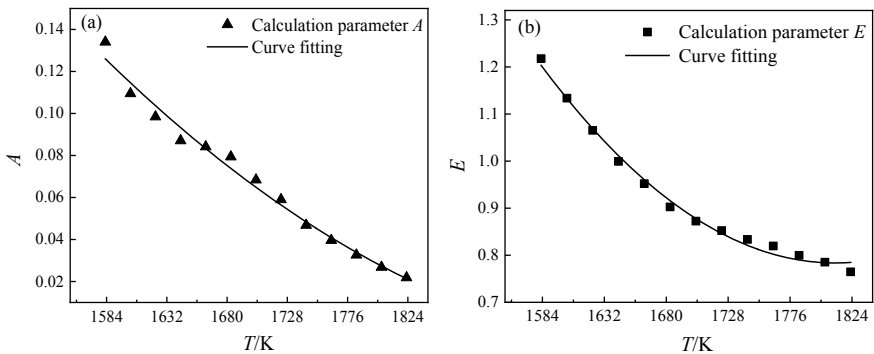


Fig. 3 Relationship between model parameters A and E and temperature T: **a** parameters A and T; **b** parameters E and T

Application of the Optimized Iida Model

The viscosity prediction effects of FeO–SiO₂–V₂O₃–Cr₂O₃–TiO₂ and FeO–SiO₂–V₂O₃–MnO–TiO₂ system were investigated using the optimized Iida model. The deviation between the experimental data and optimized Iida model was calculated by the following formula:

$$\Delta = \frac{1}{N} \sum_{n=1}^N |\delta_n| 100\% = \frac{1}{N} \sum_{n=1}^N \left| \frac{\eta_{\text{calculation}} - \eta_{\text{measure}}}{\eta_{\text{measure}}} \right| 100\% \quad (8)$$

where δ_n is the percentage difference of the calculated and measured viscosity values and Δ is an average error which is calculated by taking the summation of all absolute values of δ_n and dividing by the number of all data.

The average error Δ for FeO–SiO₂–V₂O₃–CaO–MnO–Cr₂O₃–TiO₂ system at different temperatures is given in Table 6. For all the calculated viscosities of S1 to S5, the average error Δ was below 11.40% between 1623 and 1873 K. Besides, comparisons between measured and estimation viscosity for subsidiary system are shown in Fig. 4. According to viscosity data from Huang WJ et al. [11] for FeO–SiO₂–V₂O₃–TiO₂–Cr₂O₃ system, it is observed from Fig. 4a that for Cr₂O₃ content of 0–5%, the average error Δ was less than 13.62% with good prediction effect, while $wf(\text{Cr}_2\text{O}_3)$ exceeded 10% with the average error Δ above 50% and poor prediction effect. Furthermore, according to viscosity values about FeO–SiO₂–V₂O₃–TiO₂ system by Liu S et al. [12], the average error Δ was less than 11.25% and the optimized Iida model had a satisfactory agreement with experimentally measured results, as shown in Fig. 4b.

Table 6 Δ for FeO–SiO₂–V₂O₃–CaO–MnO–Cr₂O₃–TiO₂ system

T/K	1873 (%)	1823 (%)	1773 (%)	1723 (%)	1673 (%)	1623 (%)	Δ (%)
S1	13.01	13.52	12.56	5.47	11.39	6.02	10.33
S2	10.56	6.57	9.04	10.18	7.59	8.23	8.69
S3	12.82	9.56	10.26	8.12	13.05	14.59	11.40
S4	13.21	12.91	7.38	11.80	11.11	10.12	11.08
S5	9.81	5.57	8.25	2.80	8.75	5.89	6.85

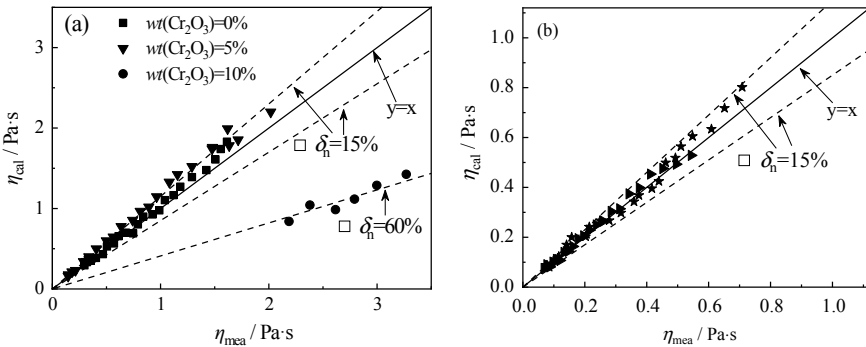


Fig. 4 Comparisons between measured and estimation viscosity by optimized Iida model: **a** Huang; **b** Liu

Conclusions

The viscosity evolution of vanadium slag during the pre-reduction process was experimentally measured by the cylinder method, and the Iida model was optimized by fitting experimental viscosity data. The following results had been obtained.

- (1) The viscosity of $\text{FeO}-\text{SiO}_2-\text{V}_2\text{O}_3-\text{CaO}-\text{MnO}-\text{Cr}_2\text{O}_3-\text{TiO}_2$ slag system increased from 0.652 Pa s to 1.549 Pa s and 0.120 Pa s to 0.473 Pa s as the FeO mass fraction decreased from 37 to 11% at 1723 K and 1873 K, respectively.
- (2) For $\text{FeO}-\text{SiO}_2-\text{V}_2\text{O}_3-\text{TiO}_2-\text{Cr}_2\text{O}_3$ and $\text{FeO}-\text{SiO}_2-\text{V}_2\text{O}_3-\text{TiO}_2$ system, the average error was below 13.62% and 11.25% using estimations viscosity by the optimized Iida model, respectively.
- (3) For the vanadium slag with Cr_2O_3 mass% less than 5, the optimized Iida model could provide theoretical viscosity and it had a satisfactory agreement with experimentally measured results.

Acknowledgements The authors gratefully acknowledge the National Natural Science Foundation of China (Grant numbers 517740735177407251974080), the National Key R&D Program of China (2017YFB03042012017YFB0304203), and the Basic Science Research Fund in Northeastern University (Grant numbers N182506005) which has made this research possible.

References

1. Andersson JO (1983) A thermodynamic evaluation of the iron-vanadium system. *Calphad* 7(4):305–315
2. Swinbourne DR, Richardson T, Cabaltega F (2016) Understanding ferrovanadium smelting through computational thermodynamics modelling. *Min Proc Ext Metall* 125(1):45–55
3. Tang J, Chu MS, Feng C, Tang YT, Liu ZG (2016) Melting separation behavior and mechanism of high-chromium Vanadium-bearing Titanomagnetite metallized pellet got from gas-based direct Reduction. *ISIJ Int* 56(2):210–219
4. Xiang JY, Huang QY, Lv W, Pei GS, Lv XW, Bai CG (2018) Recovery of tailings from the vanadium extraction process by carbothermic reduction method: thermodynamic, experimental and hazardous potential assessment. *J Hazard Mater* 357:128–137
5. Drouiche N, Cuellar P, Kerkar F, Medjahed S, Boutouchent-Guerfi N, Hamou MO (2014) Recovery of solar grade silicon from kerf loss slurry waste. *Renew Sustain Energy Rev* 32:936–943
6. Mills KC (1993) The influence of structure on the physico-chemical properties of slags. *ISIJ Int* 33(1):148–155
7. Forsbacka L, Holappa L, Iida T, Kita Y, Toda Y (2003) Experimental study of viscosities of selected $\text{CaO}-\text{MgO}-\text{Al}_2\text{O}_3-\text{SiO}_2$ slags and application of the Iida model. *Scand J Metall* 32(5):273–280
8. Forsbacka L, Holappa L (2004) Viscosity of $\text{CaO}-\text{CrO}_x-\text{SiO}_2$ slags in a relatively high oxygen partial pressure atmosphere. *Scand J Metall* 33(5):261–268
9. Sukhanovsky AN (2011) Formation of differential rotation in a cylindrical fluid layer. *Fluid Dyn.* 46:158–168
10. Wu T, Zhang YL, Yuan F, An ZQ (2018) Effects of the Cr_2O_3 content on the viscosity of $\text{CaO}-\text{SiO}_2-10\text{PctAl}_2\text{O}_3-\text{Cr}_2\text{O}_3$ quaternary slag. *Metall Mater Trans B* 49:1719–1731

11. Huang WJ, Zhao YH, Yu S, Zhang LX, Ye ZC, Wang N, Chen M (2016) Viscosity property and structure analysis of FeO–SiO₂–V₂O₃–TiO₂–Cr₂O₃ slags. *ISIJ Int* 56(4):594–601
12. Liu S, Wang L, Chou K (2018) Viscosity measurement of FeO-SiO₂-V₂O₃-TiO₂ slags in the temperature range of 1644–1791 K and modelling by using ion-oxygen parameter. *Ironmaking Steelmaking* 45(07):641–647

Influence of Cr₂O₃ Content on Phase of Chromium-Containing High-Titanium Blast Furnace Slag



Ding Yang, Hanghang Zhou, Jian Wang, and Guibao Qiu

Abstract The presence of high content of Cr₂O₃ introduces a major impact on the smelting reduction and slagging processes in the blast furnace process. Therefore, the effect of Cr₂O₃ content on the phase of chromium-containing high-titanium blast furnace slag has been investigated in this work via XRD. The results show that when the added amount of Cr₂O₃ was a minimum of 1.5 wt.%, perovskite and spinel phases were formed in slag, resulting in increased viscosity. For good fluidity and thermal stability of blast furnace slag, the content of Cr₂O₃ in blast furnace slag should not exceed 0.5 wt.%.

Keywords Cr₂O₃ · Blast furnace slag · Phase · Perovskite phase · Spinel phase

Introduction

Panzhuhua-Xichang area is the largest vanadium-titanium magnetite base in China [1], and vanadium-titanium magnetite is the main iron-bearing raw materials for smelting molten iron in Panzhuhua Iron & Steel Co. Ltd., China [2], which is divided into high-chromium vanadium-titanium magnetite and ordinary vanadium-titanium magnetite according to the content of chromium. The ordinary vanadium-titanium magnetite has been rapidly consumed because of its use in smelting for many years, thus the high-chromium vanadium-titanium magnetite will be developed and utilized in the future. The Hongge ore found in the Panzhuhua-Xichang area (China) is a typical high-chromium vanadium-titanium magnetite [3]. However, the presence of a high content of TiO₂ and Cr₂O₃ has a major impact on smelting reduction and slagging processes, which are part of the blast furnace process. Therefore, it is of great

D. Yang · H. Zhou · J. Wang · G. Qiu (✉)

Chongqing Key Laboratory of Vanadium-Titanium Metallurgy and Advanced Materials,

Chongqing University, Chongqing 400044, China

e-mail: qjuguibao@cqu.edu.cn

College of Materials Science and Engineering, Chongqing University, Chongqing 400044, China

© The Minerals, Metals & Materials Society 2021

J. Lee et al. (eds.), *Materials Processing Fundamentals 2021*, The Minerals, Metals & Materials Series, https://doi.org/10.1007/978-3-030-65253-1_19

221

significance to fully understand the physical and chemical properties of chromium-containing high-titanium blast furnace slag for the large-scale development and utilization of Hongge ore.

The research on the viscous flow characteristics of TiO_2 -bearing blast furnace slag has been relatively mature. Gao et al. [4] found that a certain degree of reduction was beneficial to the viscosity of the slag, and the viscosity of the slag was the smallest when the degree of reduction was 0.2–0.3, which also indicated that TiO_2 reduction could reduce the viscosity of the slag in the case of a small amount of TiO_2 reduction. Zhang et al. [5] proved that Ti_2O_3 can also reduce the viscosity of the slag and achieve a better effect. If the reduction continues and $\text{Ti}(\text{C},\text{N})$ is generated, the viscosity will be greatly increased. Bai et al. [6], Xu et al. [7] found that Ti-bearing blast furnace slag is formed as a kind of high-temperature hydrophilic colloid in the blast furnace, which leads to the sharp increase of slag viscosity. Due to the presence of Cr_2O_3 , the slag system will become more complicated, and the viscous flow characteristics of the slag will directly affect the normal production of blast furnace smelting, which has not been investigated so far. In the present work, the effect of Cr_2O_3 content on the phase structure of chromium-containing high-titanium blast furnace slag was further investigated via XRD, which may provide guidance for the utilization of high-chromium vanadium-titanium magnetite ore.

Experimental

To perform this study, the rotating cylinder method was used to measure the viscosity of slag samples, the rotating viscosity test system comprises a Si-Mo furnace, a Brookfield viscometer, temperature control system and a computer. Figure 1 is the schematic diagram of the device. The molybdenum crucible (D: 46, H: 120 mm) and molybdenum bob (D: 15, H: 20 mm) used in the experiment are shown in Fig. 2. A total of six slag samples were prepared by the external distribution method in the laboratory, which are listed in Table 1. A pure chemical reagent was used to prepare the samples. Before preparation, the reagent was dried for 5 h at the 130 °C to remove any moisture. The chemical composition of the plant slag of Panzhihua steel was obtained through the composition analysis of the plant slag, as presented in Table 2. Experimental slag samples were prepared based on the plant slag. Group A focused on the effect of Cr_2O_3 while keeping the proportions of other components constant, which fixed the basicity (CaO/SiO_2) of 1.10, TiO_2 content of 22 mass pct.

In this study, the experimental slag sample should be kept at 1500 °C for 2 h to ensure the slag composition and temperature uniformity. After that, the slag was quickly taken out of the viscosity furnace for water quenching. The glassy slag after water quenching was ground into a fine powder of more than 200 mesh.

Fig. 1 Experimental apparatus for the slag viscosity measurements. (Color figure online)

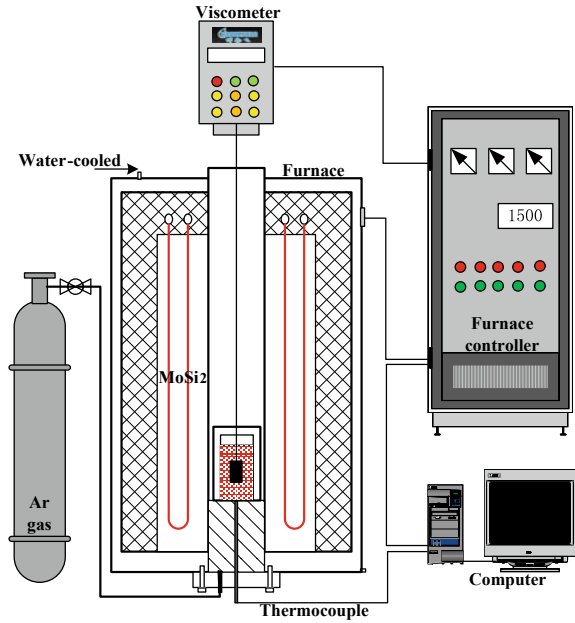
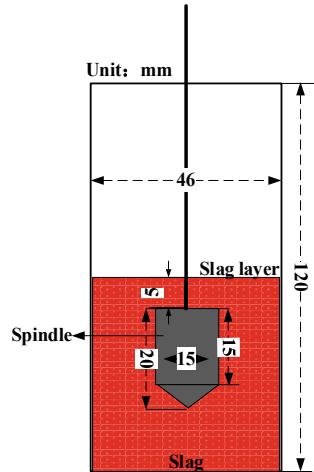


Fig. 2 Dimensions of the molybdenum crucible and bob. (Color figure online)



Results and Discussion

The formation of phase with high-melting point will seriously affect slag viscosity and make slag thicken. X-ray diffraction (XRD) is a common means to detect the slag. XRD was used to detect its phase and Jade 6.5[®] software was used to analyze the test results. Figure 3 shows the XRD test results. It can be seen from Fig. 3 that

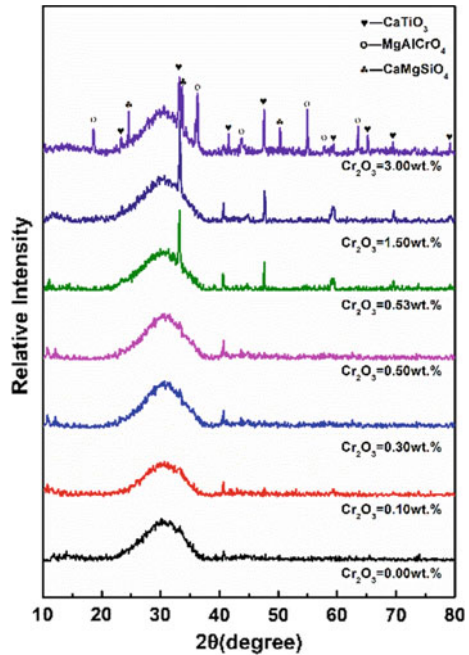
Table 1 Chemical composition of experimental slags, wt.%

Slag	CaO	SiO ₂	MgO	Al ₂ O ₃	TiO ₂	Cr ₂ O ₃	C/S
A1	28.29	25.71	9.00	15.00	22.00	0.00	1.10
A2	28.26	25.69	8.99	14.99	21.98	0.10	1.10
A3	28.20	25.64	8.97	14.96	21.93	0.30	1.10
A4	28.14	25.59	8.96	14.93	21.89	0.50	1.10
A5	27.87	25.33	8.87	14.78	21.67	1.50	1.10
A6	27.46	24.97	8.74	14.56	21.36	3.00	1.10

Table 2 Chemical composition of BF slag from Panzhihua Iron and Steel Corporation, wt.%

CaO	SiO ₂	MgO	Al ₂ O ₃	TiO ₂
25.88	24.91	9.25	14.69	21.58

Fig. 3 XRD pattern of slag system (CaO–SiO₂–AlO₃–MgO–TiO₂–Cr₂O₃) with different content of Cr₂O₃. (Color figure online)



when the addition amount of Cr₂O₃ is less than 0.5 wt.%, the test result shows the steamed bread peak, there was no obvious crystallization peak, which indicates that no solid phase is formed in the slag; when the addition amount of Cr₂O₃ is greater than 0.5 wt.%, an obvious crystallization peak begins to appear, indicating that solid-phase particles begin to form in slag; with the increase of Cr₂O₃ content, the strength

of crystal peak increases and the peak position changes, which indicate that Cr₂O₃ has an obvious effect on slag phase.

According to Fig. 3, when the content of Cr₂O₃ increased to 1.5 wt.%, the crystallization peak of the perovskite (CaTiO₃) was strong, which indicates that perovskite has been precipitated out of the slag at 1500°C. When the content of Cr₂O₃ was increased to 3.0 wt.%, high-melting point solid particles of magnesia-chrome-aluminum spinel phase were formed in slag. The test results also showed that olivine phase (CaMgSiO₄) precipitated from slag, and it was the precipitation of these solid-phase particles that led to the rise in slag viscosity.

Conclusions

The effect of Cr₂O₃ on the phase of chromium-containing high-titanium blast furnace slag has been investigated in this work via XRD. No solid phase was generated in the slag when the added amount of Cr₂O₃ was less than 0.5 wt.%. When the addition of Cr₂O₃ was greater than 0.5 wt.%, solid particles began to form in the slag.

References

1. Qiu G, Chen L, Zhu J et al (2015) Effect of Cr₂O₃ addition on viscosity and structure of Ti-bearing blast furnace slag. *ISIJ Int* 55(7):1367–1376. <https://doi.org/10.2355/isijinternational.55.1367>
2. Deng J, Xue X, Liu GG (2007) Status and development of comprehensive utilization of vanadium-titanium magnetite resources in Pangang. *J Mater Metall* 83–86+93. <https://doi.org/10.3969/j.issn.1671-6620.2007.02.001>
3. Du HG (1996) Blast furnace smelting principle for vanadium titanium magnetite. Science Press, Beijing, p 278
4. Gao GQ, Yang YC, Yang DX (1987) Measurement of the viscosity and melting point of titanium slag. *Steel Vanadium Titanium*, 51–55+66. CNKI:SUN:GTFT.0.1987-01-009
5. Zhang L, Jahanshahi S (2004) Modelling viscosity of TiO₂ containing silicate melts. In: The seventh international conference on molten slags, fluxes and salts, pp 51–56
6. Bai CG, Pei HN, Zhao SJ, Zhou PT (1995) Study on the relationship between the size of Ti(C,N) and slag viscosity. *Steel Vanadium Titanium* 6–9
7. Xu CD, Lin R (1980) Important physical and chemical problems in high temperature reduction of Panzhihua vanadium titanium magnetite. *Iron Steel Vanadium Titanium* 1-10. CNKI:SUN:GTFT.0.1980-Z1-001

Influence of Natural Convection Caused by Slag Density Difference on Temperature and Solidification of Molten Slag



Chunming Zhang, Nan Wang, and Min Chen

Abstract The temperature and heat loss of molten slag during transportation has guiding significance for molten slag heating and heat preservation. In the present work, the effects of the thickness of a solidified slag layer and heat-dissipating caused by natural convection were numerically simulated. The results showed that the temperature of molten slag decreased and the slag density increased near the pot wall. Slag with higher density flowed down the pot wall and the slag with lower density flowed up to the slag surface, respectively. Circulation was formed between the pot wall and the center, which caused the higher temperature by ~ 200 K in the middle part of pot wall than the bottom. The maximum thickness of the slag layer ~ 28 mm appeared at the bottom, much higher than the thicknesses of 16.6 mm on the side. The slag upper surface is the main path of the energy dissipation and accounts for 81% of the total.

Keywords Molten slag · Slag pot · Temperature distribution · Heat loss

Introduction

A huge amount of solid waste is generated in the process of steel production, among which high-temperature molten slag accounts for a relatively high proportion, which is about 12–20% of steel output [1]. The molten slag temperature up to 1600 °C, which carries a great deal of high-grade heat accounting for 10% of waste energy in steel industry and 35% of high-temperature waste heat. However, the waste heat is not effectively used and a lot of high-value energy is wasted. Therefore, the waste heat recovery and resource utilization of molten slag are of great significance to the energy saving of China's steel industry, which attracts intense attention of researchers worldwide to develop various heat recovery technologies from molten slag [2–6].

The slag pot is an important device for storing and holding heat for molten slag during the waste heat recovery process of molten slag. In the actual production of

C. Zhang · N. Wang (✉) · M. Chen
School of Metallurgy, Northeastern University, Shenyang 110819, Liaoning, China
e-mail: wangn@smm.neu.edu.cn

steel plants, the temperature of molten slag decreases rapidly. Generally, it takes 10–20 min to transport molten slag from steel mills to slag dumps. During this period, the heat loss is very serious and the slag surface forms a layer. The thicker solidified layer may even stick on the slag pot, causing difficulty in the slag dumping process. More importantly, the heat loss from high-temperature slag is substantial [7, 8]. There are two main reasons for the heat loss from molten slag: one is the large temperature difference between molten slag and external environment; the other reason is the structure of slag pot, and the heat loss of molten slag occurs mainly through the outlet of slag pot. Metallurgists have done a lot of research on the utilization of slag waste heat. Using waste heat to generate electricity is considered an effective way to increase energy efficiency [9]. At present, some waste-heat power generation technologies have been applied in steel manufacturing process and play an energy saving effect [10–12]. These technologies are mainly by steam expanding to generate electricity [13], which means they need relatively large and complex equipment and can only make use of high-temperature heat [14]. Therefore, in order to make better use of the waste heat of molten slag, it is necessary to make heat preservation before transported. The temperature change of molten slag during natural cooling has guiding significance for molten slag surface heating and heat preservation process.

The heat transfer of molten slag is a complicated and composite process that includes convection and heat transfer of molten slag, fluid–solid coupled heat transfer between molten slag and wall, heat conduction of slag pot, and convection and radiation of surfaces. There have been many numerical studies on heat transfer of molten slag, but few researchers have considered coupled heat transfer of wall and molten slag, and they neglected the flow of molten slag or assumed that there is no natural convection inside the molten slag [15]. The impact degree of these assumptions is not evaluated. So, to more accurately represent heat dissipation behavior of molten slag, the overall heat transfer of slag pot with molten slag and the natural convection inside the molten slag needs to be considered.

On the basis of above analysis, a mathematical model that describes the natural convection and heat transfer of molten slag as well as the heat dissipation from pot wall and slag is established in this paper. In addition, the effect of natural convection on temperature change during molten slag cooling process and the heat-dissipating behavior of surfaces were obtained. The results lay the foundation for the adjustment of heat preservation and preheating slag pot process parameters.

Research Method

Geometrical Description

The study takes the actual slag pot of the factory as the prototype. The slag pot is made of cast iron. The total capacity of the slag pot is 75t. 25t molten slag is added to the slag pot and used as the research object. The height of the slag pot is 3.65 m,

Table 1 Physical properties of the molten slag and pot

Parameters	Pot	Slag	
Density/kg m ⁻³	7700	-0.36 T + 3567	
Thermal expansion coefficient/K ⁻¹	-	1 × 10 ⁻⁵	
Viscosity/Pa s	-	0.1	
Thermal conductivity/W m ⁻¹ K ⁻¹	25	-2.71 × 10 ⁻³ T + 5.18	T ≥ 1173 K
		2	T < 1173 K
Specific heat capacity/J kg ⁻¹ K ⁻¹	460	1600	
Emissivity/-	0.8	0.8	
Solidus temperature/K	-	1573	
Liquidus temperature/K	-	1673	

with an outside diameter of 4.31 m at the top. The pot is filled with molten slag up to the height of 1.7 m from the inside bottom wall, equivalent to 25t. The side wall of the pot with the thickness of 0.11 m. The physical properties of the molten slag and pot used in calculation are listed in Table 1.

Mathematical Model

Basic Assumptions

The governing equation was formulated based on following assumptions:

- (1) the materials of the pot wall are homogeneous and the temperature-dependence of material parameter is not considered, as shown in Table 1.
- (2) The effect of natural convection was considered in the present calculation.
- (3) The radiation effect was incorporated as boundary condition in the present model.
- (4) Ignore thermal resistance between slag and wall of the slag pot.

Fluid Flow Model

The continuity equation and transient Navier–Stokes equation for momentum conservation can be expressed as:

$$\frac{\partial \rho}{\partial t} + \nabla \cdot (\rho v) = 0 \quad (1)$$

$$\frac{\partial}{\partial t}(\rho v) + \nabla \cdot (\rho v v) = -\nabla p + \nabla \cdot ((\mu_l + \mu_t)\nabla \cdot v) + \rho g + S \quad (2)$$

where ρ is density of molten slag, v is the flow velocity, p is the static pressure, g is gravity, μ_l is the laminar viscosity, μ_t is the turbulent viscosity, respectively.

$$S = \frac{(1 - f_l)^2}{(f_l^3 + \xi)} A_{\text{mush}} (v - v_{\text{pull}}) \quad (3)$$

where, ξ is a small number (>0), used to prevent zero in the denominator. A_{mush} is a mushy zone constant.

The turbulence kinetic energy, k , and its rate of dissipation, ε [16], are given as follows:

$$\rho \frac{\partial k}{\partial t} + \nabla \cdot (\rho k v) = \nabla \cdot \left[\left(\mu_l + \frac{\mu_t}{\sigma_k} \right) \nabla k \right] + G - \rho \varepsilon + S_k \quad (4)$$

$$\rho \frac{\partial \varepsilon}{\partial t} + \nabla \cdot (\rho \varepsilon v) = \nabla \cdot \left[\left(\mu_l + \frac{\mu_t}{\sigma_\varepsilon} \right) \nabla \varepsilon \right] + C_{1\varepsilon} \frac{\varepsilon}{k} G - C_{2\varepsilon} \rho \frac{\varepsilon^2}{k + \sqrt{v\varepsilon}} + S_\varepsilon \quad (5)$$

where G represents the generation of turbulence kinetic energy due to the mean velocity gradients, $C_{1\varepsilon}$, $C_{2\varepsilon}$ and C_μ are constants, σ_k and σ_ε are respectively the turbulent Prandtl numbers for k and ε . The recommended values for $C_{1\varepsilon}$, $C_{2\varepsilon}$, σ_k and σ_ε are, respectively, 1.44, 1.92, 1.0, and 1.3 [17].

Heat Transfer and Solidification Equations

For solidification process, energy conservation equation is given as:

$$\rho \frac{\partial H}{\partial t} + \rho \nabla \cdot (vH) = \nabla \cdot (k_{\text{eff}} \nabla T) + Q_L \quad (6)$$

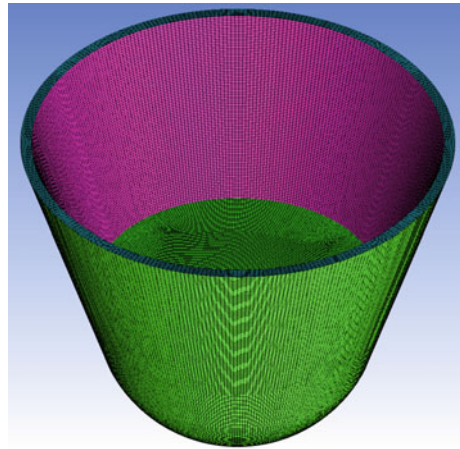
$$H = h_{\text{ref}} + \int_{T_{\text{ref}}}^T c_p dT + f_l L \quad (7)$$

$$Q_L = \rho L \frac{\partial(1 - f_l)}{\partial t} + \rho L v_{\text{pull}} \cdot \nabla(1 - f_l) \quad (8)$$

where, k_{eff} is effective thermal conductivity. H is total enthalpy, h_{ref} is the reference enthalpy, T_{ref} is the reference temperature, c_p is the specific heat, f_l is the liquid fraction and L is the latent heat. Q_L is the source term. The liquid fraction (f_l) can be calculated by determining the temperature as:

$$f_l = \begin{cases} 0 & T < T_{\text{solidus}} \\ \frac{T - T_{\text{solidus}}}{T_{\text{liquidus}} - T_{\text{solidus}}} & T_{\text{solidus}} < T < T_{\text{liquidus}} \\ 1 & T > T_{\text{liquidus}} \end{cases} \quad (9)$$

Fig. 1 Structure and computational mesh of the molten slag and the pot. (Color figure online)



Boundary Conditions and Numerical Methods

The convective and radiative heat loss boundary condition was considered for outside surface of molten slag and pot. The initial temperatures of molten slag and pot were considered to be 1773 K and 300 K respectively. The commercial software ANSYS FLUENT 16.0 was used in this study. The numerical simulations were carried out based on around 1.3 million grid cells to guarantee the grid independent solution. The structural mesh is used to divide the solid and fluid domain, as shown in Fig. 1.

Results and Discussion

Flow Characteristics of Molten Slag

Figure 2 shows the flow field of molten slag at 5 min and 20 min respectively. As shown in Fig. 2a, the convection of molten slag is significant at 5 min and the natural convection is fully developed. Due to the larger heat flux of inner side wall, the temperature of side part falls faster. The low-temperature molten slag flow toward bottom of pot, so the lower part has a lower temperature. The upper surface of molten slag has a large heat flux, and the temperature falls faster. The high-temperature molten slag in the center flows to the upper surface. After the molten slag flows to the bottom of pot, a part stays at the bottom and the other part flows upward with the heat flow in the center. A circulation inside the slag pot is formed and the maximum velocity is about 0.0048 m/s. As shown in Fig. 2b, after 20 min, the natural convection is not significant and only little molten slag flows upward the top surface. At the same time, the internal temperature of molten slag is more uniform, and the flow state and velocity of molten slag present a steady state.

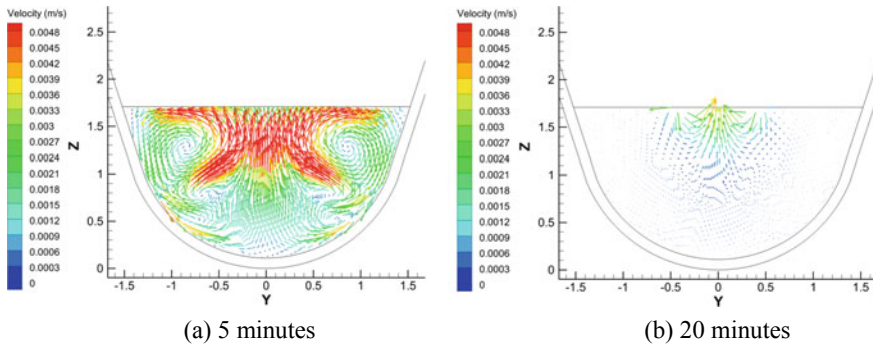


Fig. 2 Flow field of molten slag at different time. (Color figure online)

Temperature Characteristics of Molten Slag and Pot

Figure 3 shows the temperature distribution of molten slag and pot at different time. It can be observed that the temperature distribution of slag pot and molten slag varies with time significantly. At the initial stage, such as the time is 5 min, the slag temperature falls faster near the side wall and the edge corner of slag surface. The internal temperature of slag pot rises faster. At the same time, there has a large temperature gradient between the inner and outer surface of slag pot, and the heat is not conducted to the pot outer surface completely. As heat is dissipated over time, the temperature of slag pot is gradually uniform. The temperature near the bottom and edge corner of slag surface falls faster than that near the side wall, as shown at 30 min.

In order to better analyze the temperature distribution of slag pot and molten slag, which varies with time, different positions are selected as temperature monitoring points, as shown in Fig. 4. P1 to P3 and P4 to P6 are the monitoring points on the

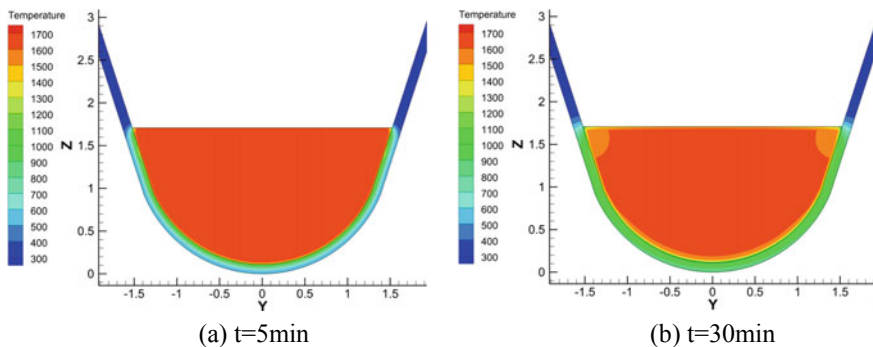


Fig. 3 The temperature distribution of molten slag and pot at different time. (Color figure online)

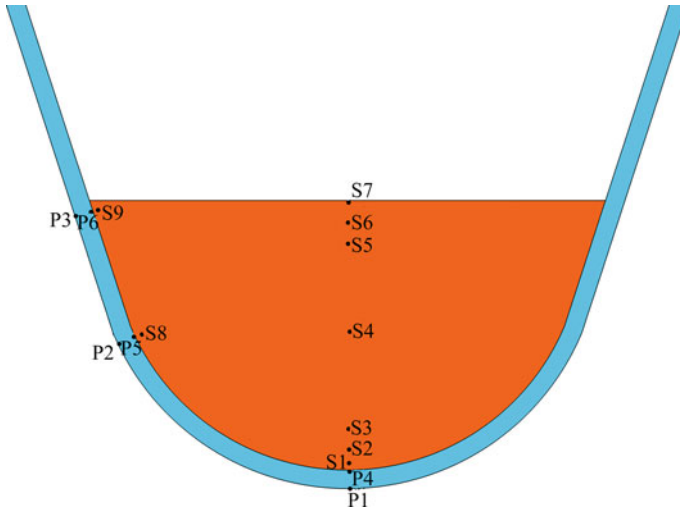


Fig. 4 Schematic diagram of monitoring points location. (Color figure online)

outer and inner surfaces of slag pot, respectively. S1 to S9 are the monitoring points inside the molten slag.

Figure 5 shows the temperature of monitoring points at different time. It can be observed that the temperature at P1-3 is increased consistently and the the temperatures at P4-6 first increased, decreased and then increased. The temperature difference at different points is increased with time. As shown in Fig. 5a, at 30 min, the temperature at bottom of slag pot (P1) is 849 K, which is 169 K higher than that near the slag surface corner (P3). The temperature at sidewall (P2) is higher than other parts, about 909 K. The inner surface temperature at bottom and slag surface corner are 987 K and 839 K, respectively. The temperature at sidewall is about 1115 K.

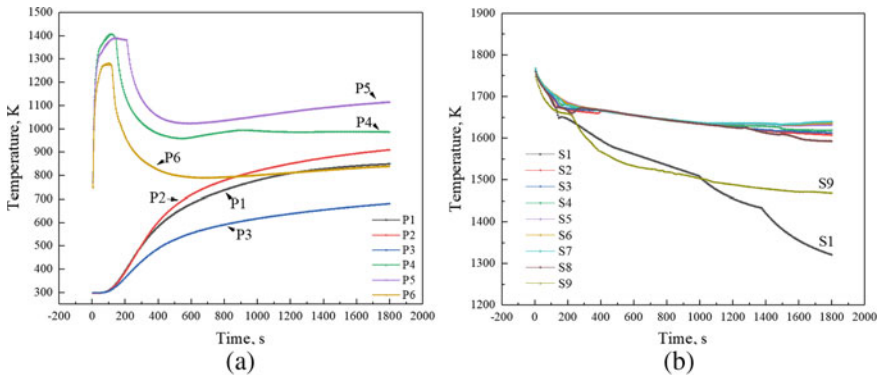


Fig. 5 The temperature of monitoring points at different time. (Color figure online)

Figure 5b shows the temperature of monitoring points at different time inside the molten slag. It can be observed that the temperature of different of monitoring points are gradually decreased with time. At 30 min, the temperature at bottom of slag (S1) is 1320 K, which is lower than other parts. The temperature at the slag surface corner (S9) and the sidewall (S8) are 1467 K and 1592 K respectively. The temperature of other parts is close, between 1600 and 1650 K.

Solidification Characteristics of Molten Slag

Figure 6 shows the liquid fraction of slag at different time, it is assumed that the slag is solid when the liquid fraction is less than 0.3. As shown at 5 min, a solid layer appears on the side of slag. The slag layers at surface corner and bottom of slag are thicker than that at sidewall. However, there is no solidification inside and on the upper surface of slag. The thickness of slag layers at different positions gradually increase with time. At 30 min, the upper surface of slag has been completely solidified, and inside the slag is the solid-liquid phase region. The thickness of solid layers at upper surface corner and bottom of slag increase significantly. The thickness solid layers at sidewall increase slowly, as shown in Fig. 6b.

As shown in Fig. 7a, at 5 min, there is no solidification on the slag upper surface, and the thickness of the bottom slag layer is about 9.6 mm. The thickness of slag layer gradually increases over time. At 30 min, the thickness of slag layer at bottom and top is 28.8 mm and 16.0 mm, respectively. At 5 min, the thickness of slag layer at the sidewall is thinner than the bottom, about 5.5 mm. At 30 min, the thickness of slag layer at the sidewall is 16.6 mm, as shown in Fig. 7b.

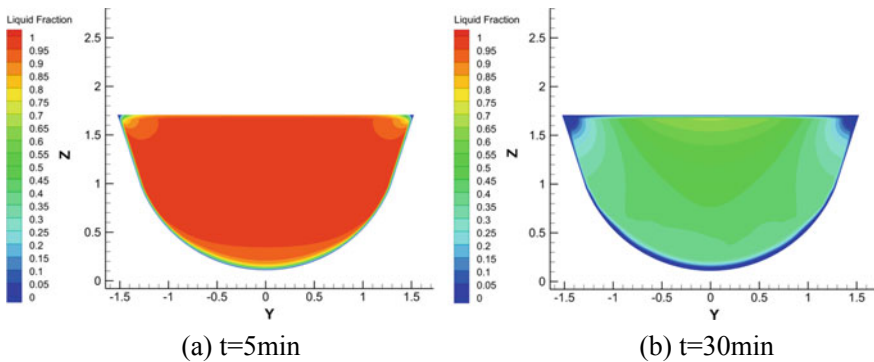


Fig. 6 Liquid fraction of slag at different time. (Color figure online)

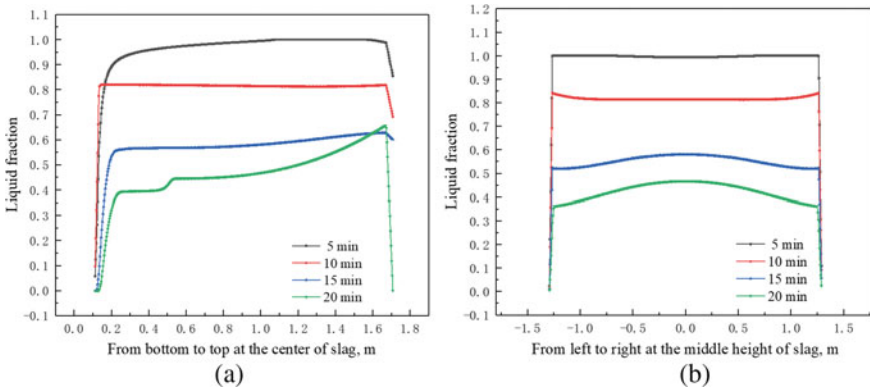


Fig. 7 Liquid fraction of different position of slag at different ... (Color figure online)

Heat Loss of Pot Outer Surface and Slag Upper Surface

Radiation and convection of pot outer surface and slag upper surface is the main mechanism of heat transfer to the environment. Figure 8 shows the heat flux from the outer surface of the pot and from the upper surface of the slag respectively. At the initial stage, the total heat flux from the slag is much bigger than that from the pot outer surface with the maximum of 3100 kW. The heat flux from the slag upper surface gradually decreases with time and the heat flux from the pot outer surface gradually increases, which is due to the conductive heat transfer from the molten slag

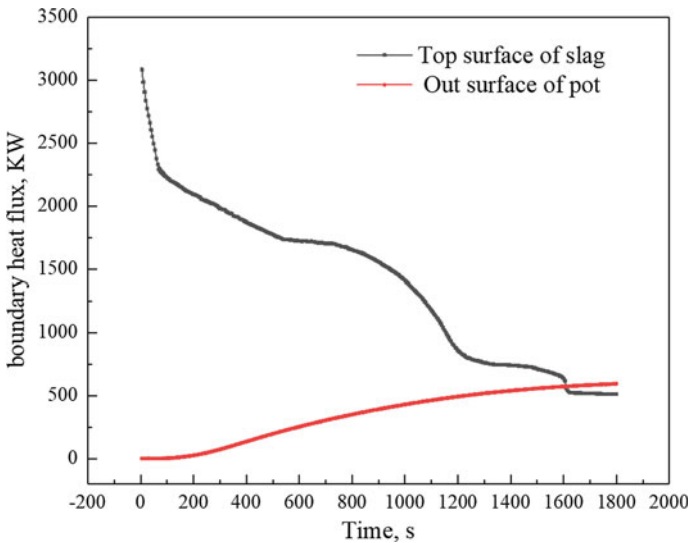


Fig. 8 The heat dissipation power on the different surfaces. (Color figure online)

to the pot. At 1600 s, the heat flux of the two surfaces are equal, at about 600KW. In the following stage (1600–1800s), the heat flux from the pot outer surface is higher than that from the slag upper surface. During the whole cooling stage, the total heat dissipation from the slag upper surface is more significant than that from the pot outer surface. Their total heat dissipating powers are 5.24×10^5 kW and 1.23×10^5 kW, which account for 81% and 19% respectively. We can find, the heat flux from the slag upper surface is higher than that from the pot outer wall. So the slag upper surface is the main path of the energy dissipation and has the greatest heat recovery potential.

Conclusions

This paper establishes a model that describes the inner transient flow and heat transfer of molten slag and the outer heat dissipation of pot wall and slag. The thermal behavior of molten slag and pot is evaluated for subsequent the waste heat recovery and resource utilization of molten slag. The major results are as follows:

- (1) At the initial stage, the natural convection of molten slag is fully developed. The slag temperature fell faster near the side wall and the edge corner of slag surface, and the pot temperature rises faster. After 30 min, the temperature of slag pot at bottom is 849 K, which is 169 K higher than that near the slag surface corner. The temperature at sidewall is higher than other parts, about 909 K.
- (2) After 30 min, the upper surface of slag has been completely solidified. The thickness of slag layer at bottom and top is 28.8 and 16 mm, respectively, and the thickness of slag layer at the sidewall is 16.6 mm.
- (3) The heat flux on slag upper surface gradually decreases with time, and the heat flux on pot outer surface gradually increases which is due to the heat transfer of the molten slag. The slag upper surface is the main path of the energy dissipation and accounts for 81% of the total, which has the greatest heat recovery potential.

Acknowledgements This work was supported by the National Key R&D Program of China [Grant numbers 2017YFB0304203 and 2017YFB0304201] and National Natural Science Foundation of China [Grant numbers 51774072, 51774073 and 52074077].

References

1. Lin GP (2007) Summary and prospects of sensible heat recovery technology of molten slag. *Iron Steel Scrap China* 4:30–36
2. Das B, Prakash S (2007) An overview of utilization of slag and sludge from steel industries. *Resour Conserv Recycl* 50(1):40–57
3. Koros J (2003) Dusts, scale, slags, sludges... Not wastes, but sources of profits. *Iron and Steel Society* 34B:769–778

4. Wang X (2006) Recovery and utilization of steel-making slag. *Wuhan Iron Steel Corporation Technol* 44(5):51–54
5. Li CW, Wang L, Sun BL et al The treatment and comprehensive utilization of steel slag. *Energy MetallInd* 26(4):54–57
6. Shu XW (2007) Steel slag characteristics and comprehensive utilization technology. *Nonferrous Metals Eng Res* 6:48–51
7. Wu QB, Yang JK (2001) A new technique for recycling molten steel slag. *Indu Saf Environ Prot* 27(9):11–13
8. Li H, Cang DQ, Bai H et al (2009) Research on dynamic cooling and temperature control of dual-use slag in insulation container. *Ind Heating* 38(6):6–10
9. Meng F, Chen L, Sun F et al (2014) Thermoelectric power generation driven by blast furnace slag flushing water. *Energy* 66:965–972
10. Sun K, Tseng CT, Wong DSH et al (2015) Model predictive control for improving waste heat recovery in coke dry quenching processes. *Energy* 80:275–283
11. Wu P, Yang CJ (2012) Identification and control of blast furnace gas top pressure recovery turbine unit. *ISIJ Int* 52(1):96–100
12. Liu X, Gao X (2016) A survey analysis of low carbon technology diffusion in China's iron and steel industry. *Cleaner Prod* 129:88–101
13. Guo J, Xu M, Cheng L (2010) Thermodynamic analysis of waste heat power generation system. *Energy* 35(7):2824–2835
14. Ammar Y, Joyce S, Norman R et al (2012) Low grade thermal energy sources and uses from the process industry in the UK. *Energy* 89(1):3–20
15. Zhan HR, Fan ZG, Zhou SJ et al (2008) Numerical simulation for the temperature field of boron-rich slag cooling process. *Min Metall* 17(2):34–38
16. Li C, Liu B, Zhu S (2012) Numerical simulation on the flow state of dross layer in the tundish. *Aasri Procedia* 3(4):313–318
17. Launder BE, Spalding DB (1974) The numerical computation of turbulent flows. *Comput Methods Appl Mech Eng* 3(2):269–289

Influence of Rotation Speed and Temperature on Dissolution Rate of Cr₂O₃ in Ti-Bearing Blast-Furnace Slag



Guibao Qiu, Ding Yang, Feng Zhang, and Jian Wang

Abstract The dissolution behavior of chromium ore has severe effects on reduction rate of blast-furnace slag. Therefore, the study of dissolution behavior of Cr₂O₃ in the slag has great significance for accelerating the melting reduction rate of chromium ore and optimizing the blast-furnace smelting process. The effects of different rotation speed and temperature on the dissolution rate of Cr₂O₃ were studied by using the rod sample rotation method in the temperature range from 1500 to 1540 °C. The results of the ICP analysis show that the dissolution rate of Cr₂O₃ in the slag increases with rotating speed and temperature.

Keywords Cr₂O₃ · Dissolution behavior · Ti-bearing slag

Introduction

Vanadium, widely used in various engineering fields, is a high-melting metal, such as machinery manufacturing, aerospace and railway [1]. Vanadium steel products in China used in the steel industry could account for 99% [2]. In recent years, with the improvement of Chinese comprehensive national strength, the amount of vanadium used in industry is also increasing. However, the application level of vanadium in domestic steel products is still on a low level. The vanadium consumption level in developed countries reaches 0.08 ~ 0.09 kg/t, while the vanadium consumption per ton of steel in China is only about 0.03 kg [3]. In the future, China's iron and steel production will still be at a high level, improving the application level of vanadium in iron and steel products and expanding the application of vanadium in other fields will become inevitable.

Titanium known as “space metal” [4] has excellent physical and chemical properties. Titanium and its alloys are widely used in various aspects, including aerospace, military, automobiles, agricultural food, medicine, etc. [5, 6].

G. Qiu (✉) · D. Yang · F. Zhang · J. Wang
College of Materials Science & Engineering, Chongqing University, Chongqing 400044, China
e-mail: qiuguibao@cqu.edu.cn

Chromium is a globally recognized strategic materials, including high hardness, corrosion resistance and high-temperature resistance [7]. Chromium is an important alloying element, formed by smelting with iron, nickel, tungsten and other elements, thus achieving the characteristics of corrosion resistance, wear resistance, easy welding and low price. Ferrochrome alloy has been widely used in coating materials due to its excellent corrosion resistance [8]. In addition, chromium compounds are also widely used. Chromium oxide can be used as a strong oxidant, mordant, catalyst, biological dye, ceramic glass, etc. [9]. Potassium dichromate can be used in electroplating, tanning, firewood, medicine and welding electrodes. By 2018, China's stainless steel production will reach about 25.728 million tons, about 29 times that of the early twenty-first century. Thus, the consumption of chromium resources increased rapidly [10]. However, due to the lack of chromium resources in China, the production of chromium products is highly dependent on imports, which will be more than 98% by 2020 [11].

The Cr_2O_3 content higher than 0.3% is called high-chromium vanadium-titanium magnetite. The Hongge mine in Panxi area is a typical high chromium vanadium titanium-magnetite with Cr_2O_3 content between 0.49 and 0.82% [11]. It has a potential mining capacity of 1.829 billion tons, Cr_2O_3 content in the ore is high, the valuable elements (such as Co, Cu and Ni) content is higher than other mining area, exploitation potential is great, but the mine's mineral composition is complicated, difficult to use, and the existence of Cr_2O_3 smelting reduction of blast furnace in iron ore, slag properties have a significant impact. Up to now, only preliminary exploration, ore phase composition characteristics and mineral processing and smelting analysis have been carried out on the red grid ore [12]. The development and utilization of the red grid ore have not been carried out, and the relevant basic research is also rare. Therefore, it is of great significance for the large-scale development of red lattice vanadium titanomagnetite ore to understand the smelting reduction process of ore and the viscous property of Cr-containing high titanium blast-furnace slag.

The melting reduction rate of chromium ore largely depends on the solubility, reduction rate and dissolution rate of MgCrAlO_4 in slag. So far, it has been found that the dissolution behavior of chromium ore seriously affects its reduction rate in slag. Therefore, it is important to study the dissolution behavior of chromium ore and Cr_2O_3 in slag for improving the melting reduction rate of chromium ore and improving the smelting process of blast furnace.

Experimental

Experimental Materials

The dissolution behavior of Cr_2O_3 in slag is studied by bar sample rotation method. The effect of Cr bar speed and temperature on the dissolution rate of Cr_2O_3 was studied in Table 1. Vacuum hot-pressing furnace was used for sintering of chromium

Table 1 Experimental factors and levels

Factors	Levels			
Dissolution time(min)	30	60	90	120
Rotation speed (r/min)	20	100	120	
Temperature (°C)	1500	1520	1540	

Table 2 Chemical composition of blast-furnace slag from Pan Steel

CaO	SiO ₂	MgO	Al ₂ O ₃	TiO ₂	Cr ₂ O ₃
25.88	24.91	9.25	14.69	21.58	*

Table 3 Chemical composition of experimental slag, wt%

No.	Composition					C/S	Melting temperature(°C)
	CaO	SiO ₂	MgO	Al ₂ O ₃	TiO ₂		
C1	28.29	25.71	9	15	22	1.1	1415

oxide bar samples at high temperature under isostatic pressure. According to the composition of on-site slag at Pangang, pure reagent is used to prepare the slag samples for the experiment. The composition of on-site slag and experimental slag samples at Pangang is shown in Tables 2 and 3. To ensure the accuracy of sample preparation, CaO was kept in muffle furnace at 1000 °C for 8 h to remove the water, and the other components were kept in an incubator at 120 °C for 2 h to remove the water.

Apparatus and Procedure

The rotating cylinder method was used in the present study. The experimental setup is schematically shown in Fig. 1. MoSi₂ was used as the heating element, and the tube in the furnace was made of alumina. The bottom of furnace was sealed, and the argon was blown into the furnace from the bottom to avoid the oxidation of the molybdenum crucible can be avoided oxidizing. It should be mentioned that the temperature was constant in the furnace.

The crucible used in the experimental was a molybdenum crucible. The corundum crucible with molybdenum crucible jacket was used to avoid the oxidation of molybdenum crucible. The graphite crucible with corundum crucible jacket can preserve the molybdenum crucible from oxidation. The size of rod used in the dissolution experiment was 50 mm long and 15 mm in diameter.

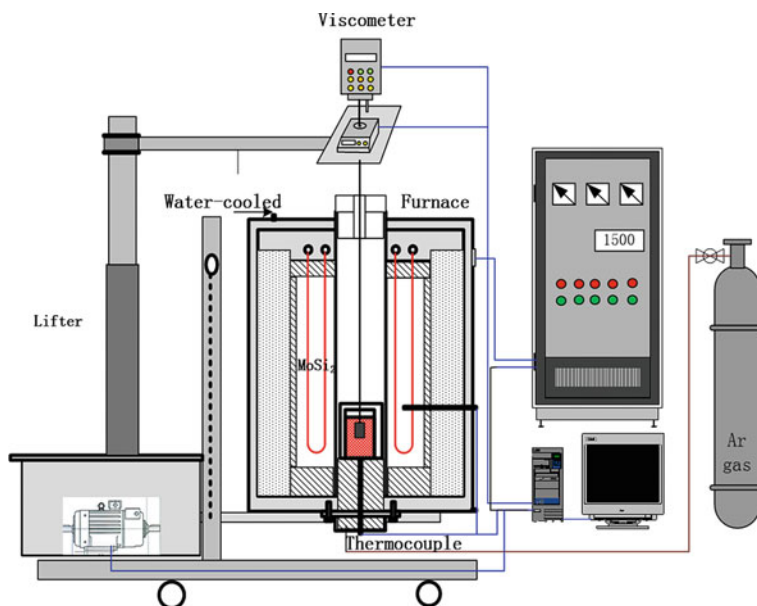


Fig. 1 Experimental setup. (Color figure online)

Results and Discussion

The water-cooled slag sample was ground to more than 200 mesh, and the ICP analysis was carried out after the sample was dissolved with the mixture of nitric acid, sulfuric acid and hydrochloric acid to obtain the mass fraction of Cr_2O_3 in the slag. The results of ICP analysis are shown in Table 4.

In this experiment, the rod-like rotation method is adopted to study the dissolution behavior of Cr_2O_3 in the slag and to explore the restrictive links affecting the

Table 4 Experimental results of dissolution

No.	Rotating speed(r/min)	Time(min)	Content of Cr_2O_3 (wt.%)	Loss of sample weight(g)	Temperature °C
1#	20	30	0.020	0.040	1500
2#	100	30	0.060	0.120	1500
3#	120	30	0.100	0.200	1500
4#	120	60	0.290	0.580	1500
5#	120	90	0.479	0.958	1500
6#	120	120	0.530	1.060	1500
7#	120	120	0.560	1.120	1520
8#	120	120	0.650	1.300	1540

dissolution of Cr_2O_3 in slag. The whole experimental reaction system is a steady state, and the mass of the sample loss is equal to the mass of Cr_2O_3 dissolved in the slag system. Therefore, a stable state can be established, and according to this system, the dissolution process of Cr_2O_3 can be divided into the dissolution reaction on the interface between the solid sample and the slag liquid and the diffusion of Cr_2O_3 in the dissolved liquid in the slag sample. Considering the rotation process of slag and rod sample, there is relative motion, so Cr^{3+} diffusion behavior in the slag can be viewed as a process of convection–diffusion. In the process of convective diffusion, the Cr_2O_3 dissolved in slag has not only the molecular diffusion caused by a concentration gradient, but also the migration of Cr_2O_3 molecules caused by the flow of molten slag stirred by the bar. Moreover, the diffusion coefficient caused by convection is usually far greater than the free diffusion coefficient. The convective diffusion coefficient of Cr_2O_3 in slag can be theoretically increased by increasing the rotation speed of Cr_2O_3 bar sample. If the dissolution amount of Cr_2O_3 rod in slag increases significantly after the increase of rotating speed, it can be considered that the diffusion process is a restrictive link in the dissolution process.

Effect of Rotation Speed on Dissolution Rate of Cr_2O_3 in Slag

The chrome rod rotation speed of 20 r/min, 100 r/min and 120 r/min was selected to dissolve the molten slag C1 sample at 1500 °C for 30 min. The interface of molten slag sample was found by using grating ruler and density sensor. The bar sample was immersed in a place 20 mm below the liquid level of the slag sample, and the rotation speed and rotation time were set by viscosity measuring instrument.

In order quantitatively to analyze the influence of rotating speed on the dissolution rate of Cr_2O_3 in slag, the percentage content of Cr element detected by ICP, and the dissolution mass, mass percentage and dissolution rate of Cr_2O_3 in slag are obtained by conversion. The results are illustrated in Fig. 2. As can be seen from the figure, the dissolution rate of Cr_2O_3 in the slag increases with the increase in rotation speed. When the rotation speed increases from 20r/min to 100r/min, the dissolution rate increases from 0.00133 g/min to 0.004 g/min, an increase of about three times. This is explained by the fact that the increase of rotation speed enhances the diffusion of solid–liquid interface, which significantly increases the dissolution rate.

Effect of Temperature on Dissolution Rate

Figure 3 shows the influence of temperature on the dissolution rate of Cr_2O_3 bar sample in slag at a rotating speed of 120 r/min and holding time of 120 min. As can be observed in the figure, the dissolution rate of Cr_2O_3 increases with the increase of temperature, which is because the diffusion is a restrictive link. The increase of temperature will accelerate the vibration of atoms which make atoms recover from

Fig. 2 Effect of different rotating speeds on dissolution rate. (Color figure online)

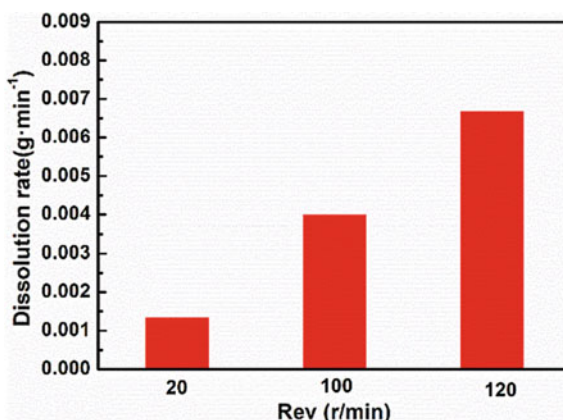
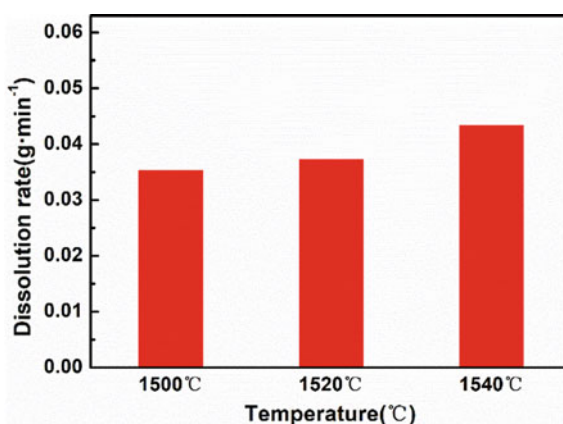


Fig. 3 Effect of temperature on dissolution rate. (Color figure online)



the energy barrier and become active particles, reducing the viscosity and making the diffusion of Cr_2O_3 in slag easier. Therefore, with the same other conditions, the dissolution rate of Cr_2O_3 in slag increases as the dissolution amount increases.

Influence of Cr_2O_3 on Slag Phase

After the dissolution experiment, the high-temperature slag was quenched in the water quickly. The components in the slag have no time to crystallize, so most of the slag is glass state, and its structure is very similar to that at high temperature. Therefore, XRD can use to detect the phase and represent the tissue composition of the whole liquid at high temperature. Figure 4 shows the XRD results of slag samples after the dissolution experiment.

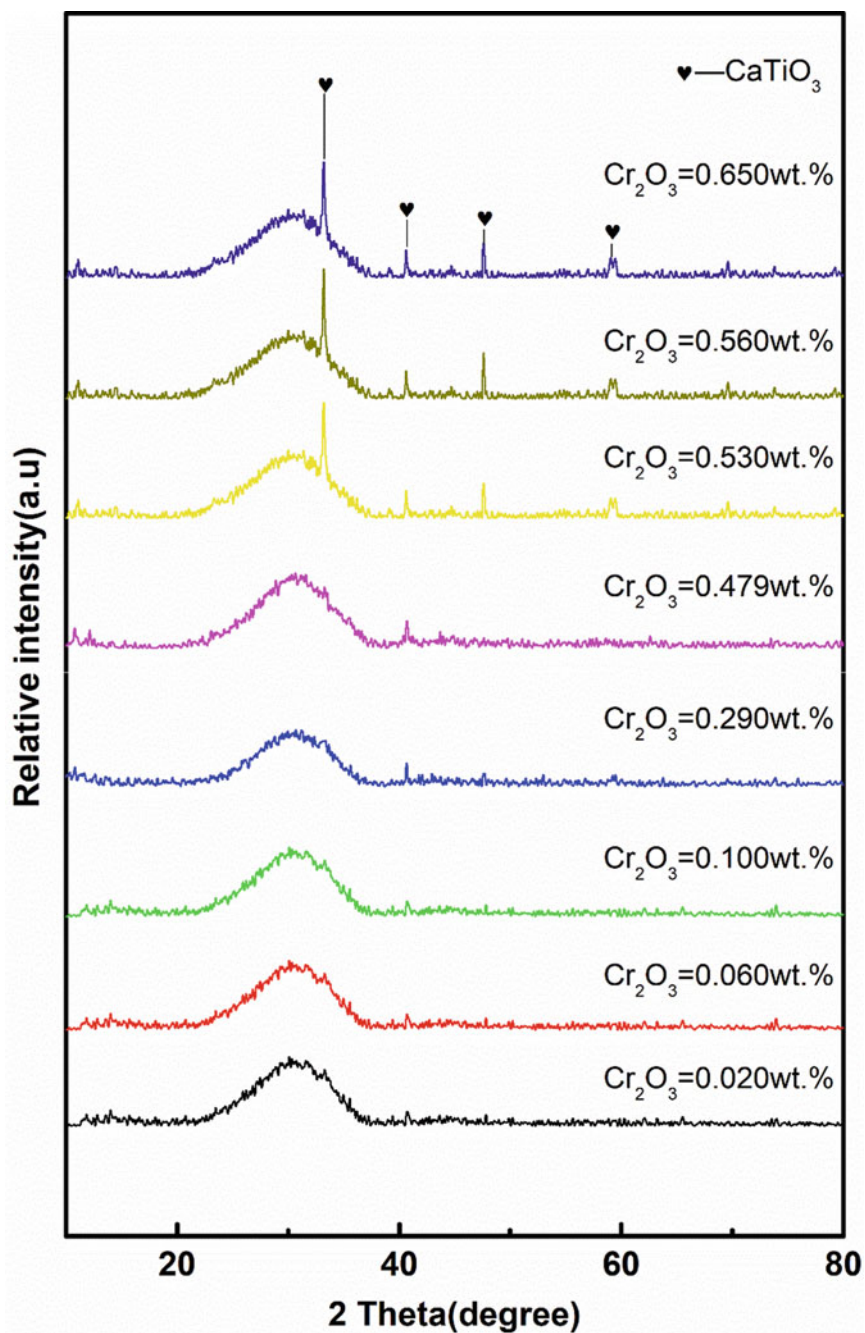


Fig. 4 XRD pattern of slags with different contents of Cr_2O_3 . (Color figure online)

According to the above XRD patterns, there is no observable diffraction intensity peak when the Cr_2O_3 content in the slag is lower than 0.530 wt%. At 1500 °C, the slag system has become homogeneous, and the influence factors of its viscosity are only related to the change of silicate structure caused by the composition of the slag. When the content of Cr_2O_3 in slag increased to 0.53 wt%, there was no significant change in the graph line. The characteristic diffraction peaks of perovskite phase also appeared, indicating that the perovskite phase was precipitated out of the slag. However, there is no characteristic line of spinel phase containing Cr element in the XRD diffraction pattern, so no chrome-magnesium or chrome-aluminum spinel phase was precipitated out of the slag at 1500 °C. On the one hand, the precipitation of perovskite phase is due to the high crystallization temperature and large amount of perovskite phase in the five-element slag system. On the other hand, Cr_2O_3 can significantly increase the crystallization temperature of perovskite phase in the six-element slag system and make the crystal become thick and appear as large equiaxial crystals in the process of perovskite phase precipitation. The reason why spinel phase is not precipitated is that the content of Cr_2O_3 is too thin and it is difficult to generate chrome-magnesium-spinel phase or chrome-magnesium-aluminum-spinel phase crystal nucleus.

The Solubility of Cr_2O_3 in Slag Based on FactSageTM Calculation

In order to continue to explore the influence of different components in slag on the solubility of Cr_2O_3 , the equilibrium module in the thermodynamic software FactSageTM was used to calculate the solubility of Cr_2O_3 in slag under different temperature, TiO_2 content and basicity conditions.

Table 5 shows the slag composition required for calculation. Fig. 5 shows the solubility of Cr_2O_3 in the slag of $\text{CaO-SiO}_2\text{-9MgO-15Al}_2\text{O}_3\text{-22TiO}_2$ at different temperatures. It can be observed that the solubility of Cr_2O_3 increases with the temperature in the slag. However, the increase was small, from 0.311wt% at 1500 °C to 0.384wt% at 1560 °C.

Table 5 Chemical composition of slag for thermodynamic calculation, wt%

No.	Temperature(°C)	Chemical composition of slag					CaO/SiO ₂
		CaO	SiO ₂	MgO	Al ₂ O ₃	TiO ₂	
1#	1500	28.29	25.72	9	15	22	1.10
2#	1520	28.29	25.72	9	15	22	1.10
3#	1540	28.29	25.72	9	15	22	1.10
4#	1560	28.29	25.72	9	15	22	1.10

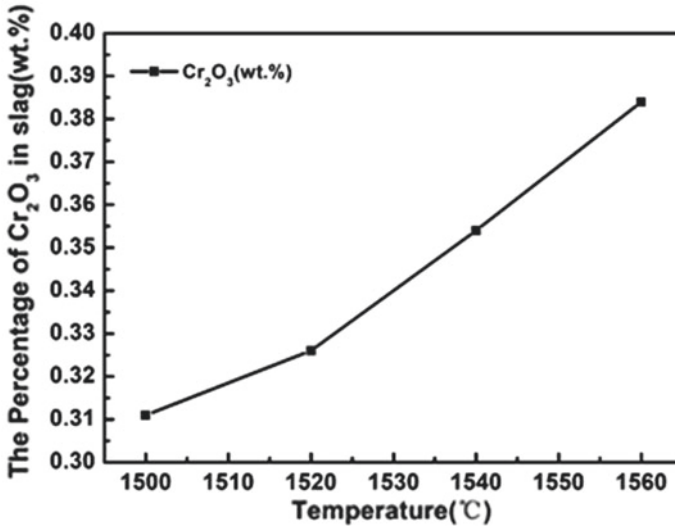


Fig. 5 Solubility of Cr₂O₃ in slag at different temperatures

Conclusion

In this paper, Cr₂O₃ bar samples prepared by hot-pressing sintering method were studied the influence of rotation speed, dissolution time and temperature on the dissolution behavior of Cr₂O₃ in the slag by using bar sample rotation method.

- (1) With the increase in rotation speed, the dissolution rate of Cr₂O₃ in five-element slag system increases. The higher the rotation speed, the higher the increase of dissolution rate. With the increase of holding time, the dissolution amount of Cr₂O₃ in five-element slag system increases, and the dissolution rate first increases and then decreases. With the increase of temperature, the dissolution rate of Cr₂O₃ in five-element slag system increases.
- (2) With the increase of temperature and TiO₂ content, the solubility of Cr₂O₃ in slag increases. With the increase of basicity, the solubility of Cr₂O₃ in the slag decreases first and then is usually stable. Under different TiO₂ content and basicity, the solubility of Cr₂O₃ in the slag is less than 1 wt%.

References

1. Wang BL (2017) Overview of titanium industry development, opportunities, challenges and countermeasures in China [J]. *New Mater Indus* (3). <https://doi.org/10.3969/j.issn.1008-892x.2017.03.002>
2. Liu XQ (1983) Application of vanadium in steel [J]. *Steel Vanadium and Titanium* 1983(04):52–59 CNKI:SUN:GTFT.0.1983-04-008

3. Mou WH, Chen DH (2010) Vanadium steel industry, technology development and market analysis in China [C]
4. Gu DY (2011). The preparation of rare metal vanadium and mechanism research. (Doctoral dissertation, Northeastern University). <https://doi.org/10.7666/d.j0119996>
5. Wu J (2016) Design and application of digital control titanium smelting power supply [D]. doi:CNKI:CDMD:2.1017.853829
6. Liao HW, Yz YU, Chen XJ (2011) Study and discussion on using waste chrome-cobalt catalyst as raw material to produce ceramic and glass coloration [J]. *Hunan Nonferrous Met* 27(4):60–63. <https://doi.org/10.3969/j.issn.1003-5540.2011.04.017>
7. Liu X, Chen QS, Zhang YF et al (2015) Prediction of chromium demand and security situation analysis of resource supply in China [J]. *Res Sci* 37(5):933–943 CNKI:SUN:ZRZY.0.2015-05-010
8. Liu J, Li L, Zheng S, Wang S, Du H, Xie H (2014) Extraction of vanadium from vanadium-containing slag by roasting-hydrothermal alkali leaching. *Chin J Process Eng*, pp 763–769
9. Ma GL, Cao QX, Qin G (2003) Effect of temperature on strengthening of ferrochrome alloy during plastic deformation. *Precis Form Eng* 21(6):101–102. <https://doi.org/10.3969/j.issn.1674-6457.2003.06.040>
10. Liao HW, Yu YZ, Chen XJ (2011) Study and discussion on using waste chrome-cobalt catalyst as raw material to produce ceramic and glass coloration. *Hunan Nonferrous Metals* 27(4):60–63. <https://doi.org/10.3969/j.issn.1003-5540.2011.04.017>
11. Liu SL (2010) Research on direct reduction of vanadium titanium iron concentrate to furnace melting process and theory. Chongqing university
12. Yang LZ (2011) Study on the preparation of high purity metal chromium by electrolysis [D]. Central South University. <https://doi.org/10.7666/d.y1914928>

Numerical Simulation of Microscale Metallic Particle Impact Using Eulerian Approach



Cal Vin Wong and Jonghyun Lee

Abstract A number of finite element (FE) models with Lagrangian formulation have been developed to simulate the high-speed particle impact. Although the Lagrangian formation-based FE models developed so far contributed significantly to unveiling the important questions on the mechanics of particle impact, they have a critical weakness. The Lagrangian models often diverge under large deformation due to mesh distortion. Recently, FE models based on Eulerian formation have been developed. This research describes a part of such efforts. A thin three-dimensional finite element model of high-speed impact of a micron-sized metallic particle was developed using Eulerian formulation. The meshes of a finite element model based on Eulerian formulation do not deform and therefore allow for dealing with a case with extreme plastic deformation. The two cases from the literature were reproduced to evaluate the validity of the developed model. After comparison, the model was used to simulate the impact of a stainless steel particle on a stainless steel substrate at an impact speed of 1000 m/s, which could not be readily simulated using the Lagrangian model.

Keywords Cold spraying · Lagrangian formulation · Eulerian formulation · Jetting

Introduction

Cold spraying (CS) is a high-speed material deposition process. It was first discovered at the Institute of Theoretical and Applied Mechanics of the Siberian Branch of the Russian Academy of Sciences [1]. Powder particles, typically 15–50 μm in diameter, are accelerated to a high velocity by a supersonic jet of nitrogen or helium generated through a converging–diverging de Laval nozzle. The particles with velocities ranging from 200 to 1200 m/s impact on a substrate at a temperature below the melting

C. V. Wong · J. Lee (✉)

Department of Mechanical Engineering, Iowa State University, Ames, IA 50011, USA

e-mail: jolee@iastate.edu

J. Lee

Division of Materials Science and Engineering, Ames Laboratory, Ames, IA 50011, USA

© The Minerals, Metals & Materials Society 2021

J. Lee et al. (eds.), *Materials Processing Fundamentals 2021*, The Minerals, Metals & Materials Series, https://doi.org/10.1007/978-3-030-65253-1_22

249

point of the particle materials undergo extensive plastic deformation and bond with the surface. Successive impacts form a dense and strain-hardened coating layer on the substrate surface with negligible adverse thermal effects and minimal oxidation. Therefore, cold spray possesses unique properties compared to conventional thermal spraying processes such as high-velocity oxy-fuel spray or plasma spray. The high deposition efficiency of cold spray attracted attention from industry and military. Applications of cold spray range from simple corrosion or wear resistance coatings to the repair of expensive metallic parts such as magnesium gear housing for military helicopters and skins of B-1 bomber [2]. The impact phenomenon of cold-sprayed particles has been studied extensively to understand the bonding mechanism during particle impact. However, the experiments provide limited description of the impact event due to the short impact duration. Therefore, a number of research groups developed numerical models to simulate the moment of particle impact. The Lagrangian model, where the mesh deforms along with the boundaries of materials, has been dominantly used in the field. The Lagrangian models have served well to help better understand the impact and bonding mechanism of cold spray. However, due to the nature of the mesh formulation, the Lagrangian models cannot deal with the case with high deformation. Recently, the Eulerian models were developed to address the issue of divergence of the model due to mesh distortion caused by high deformation. This paper describes our recent efforts on the development of a pseudo-three-dimensional model of high-speed particle impact using Eulerian mesh formulation on a commercial finite element analysis software, Abaqus. The developed model predicted the impact of a copper particle on a copper substrate, and the results were compared to those from the literature. The impact of a stainless steel particle at 1000 m/s was simulated using the developed model to show the capability of the model to deal with a case with large deformation of high-strength materials.

Lagrangian and Eulerian Formulations

For the last few decades, a number of finite element (FE) models based on Lagrangian formulation were developed to predict the high-speed impact behavior of metallic or polymeric particles [3–10]. For example, Li et al. have developed a three-dimensional Lagrangian model on Abaqus to simulate the impact of a cold-sprayed particle impact [8]. A copper particle of 20 μm in diameter impacted onto a copper substrate with a diameter and height of 80 μm and 30 μm , respectively, with an impact velocity of 500 m/s. An 8-node thermally coupled brick element with hourglass control capability (C3D8RT) was used for both particle and substrate. The mesh size used was 1 μm (1/20 of the particle diameter). Gravitational effects were neglected, and surface-to-surface contact algorithm was used with a friction coefficient of 0.2. The particle and substrate were assumed to be at room temperature (25 °C) before impact. Non-adiabatic conditions were assumed, meaning heat conduction between the particle and the substrate was considered while they were in contact. It was assumed that 90% of plastic work and 100% friction work were to be dissipated as

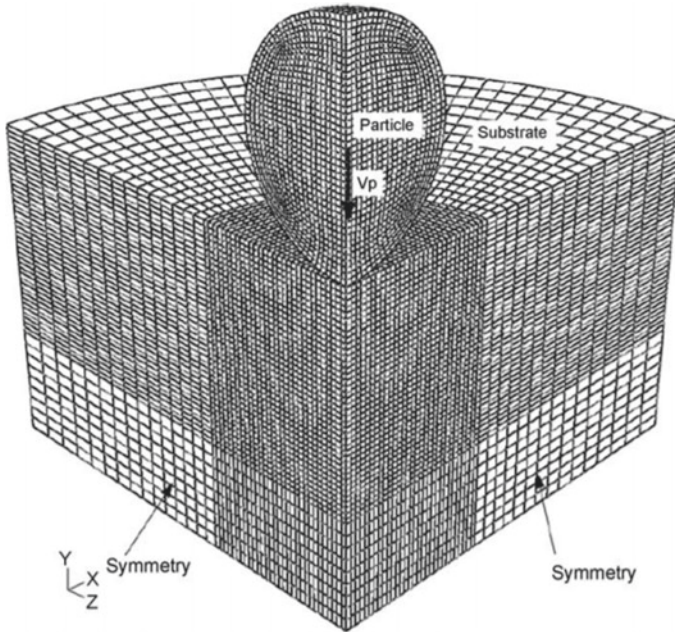


Fig. 1 Boundary conditions for Li’s model [8]

heat. The FE models based on Lagrangian formulation have a critical weakness—they cannot deal with large deformation effectively. This is because Lagrangian meshes deform as the particle and substrate deform. In the regions, especially along the particle–substrate interface where severe plastic deformation occurs, the meshes distort and the FE model diverges (Fig. 1).

Such weakness demanded the emergence of Eulerian model in which the meshes are fixed. Wang et al. developed an Eulerian FE model to simulate the high-speed impact of a single particle [7]. As a full 3D FE model with Eulerian formulation is computationally expensive, they used a thin 3D slice to simulate the axisymmetric surface (a half circle) of the particle and the substrate. The particle diameter was set as 20 μm . The substrate was modeled with a cylinder with a diameter of 160 μm . Particle velocities right before impact were between 350 and 1450 m/s. The ECRD8RT, 8-node thermally coupled linear brick element was used as it provided the capability of Eulerian formation, reduced integration, and hourglass control. Thermal coupling capability of the element is allowed for considering the heat generation due to severe plastic deformation, heat conduction between the particle and the substrate, and thermal softening of the material simultaneously during impact [11]. Wang’s model imposed boundary conditions on the bottom and lateral surface of the model. The particle and substrate were meshed with a mesh size of 0.2 μm for simulation stability. Gravitational and frictional effects were ignored. Eulerian-to-Eulerian contact was defined by default in the Eulerian analysis. The model had an initial temperature

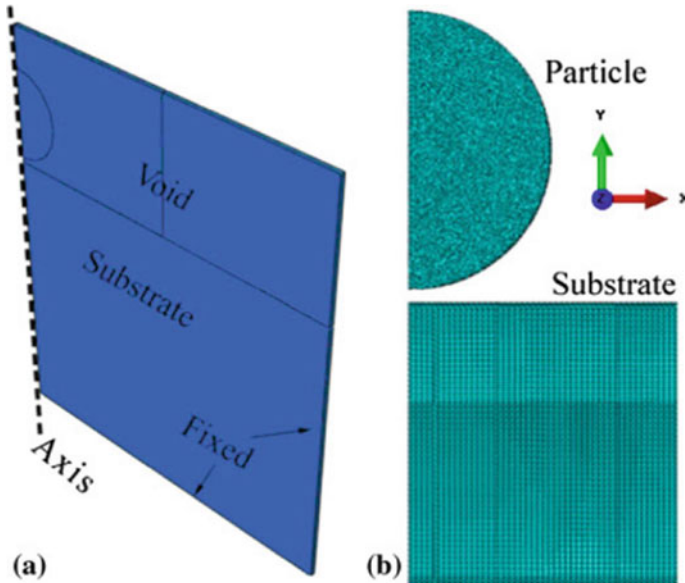


Fig. 2 Boundary conditions for Wang's model [7]. (Color figure online)

of 25 °C. Non-adiabatic conditions were assumed, and material damage option was not used in the simulation. Linear Mie–Grüneisen equation of state was used to describe the elastic behavior of the impact. The boundary conditions of the model are shown in Fig. 2. Wang's results showed a good correlation with the observation from the experiments reported by Schmidt et al. [6]. Yin et al. also mentioned that the Eulerian formulation described the particle and substrate deformation better than the Lagrangian formulation [12].

Development of an Eulerian FE Model

Recently, our group had a divergence issue which came from mesh distortion, when we attempted to simulate the impact of a stainless steel particle on a substrate of the same material at impact velocities higher than the critical impact velocities (>850 m/s) using our Lagrangian FE model. In order to circumvent the issue, we have developed an Eulerian FE model to predict the high-speed impact of a single particle on Abaqus. Inspired by Wang's model, an axisymmetric model with a thin slice ($1\ \mu\text{m}$) of the entity model is created. The two difference cases were reproduced to validate the developed model—one case with Eulerian formulation from Wang et al. [7] and the other with Lagrangian formulation from Li et al. [8].

First, copper was used for the particle and substrate with material data provided in Wang's paper [7]. The geometry of the particle and substrate was modeled

following Wang et al. as described above. The particle had a velocity of 400 m/s before impacting on the substrate. The ECRD8RT element was used for the model to obtain transient mechanical and thermal responses simultaneously. The particle and substrate were meshed with a mesh size of 0.2 μm for simulation stability. Gravitational and frictional effects were ignored. Eulerian analysis defined Eulerian-to-Eulerian contact by default. The initial temperature of the particle and substrate was set as 25 $^{\circ}\text{C}$, and non-adiabatic conditions were assumed. Heat conduction equation was used to consider thermal conduction between the particle and the substrate. Material damage was not used in the simulation. A linear Mie–Gruneisen equation of state was used to describe the elastic behavior during the impact. Boundary conditions are shown in Fig. 3. The bottom and lateral surfaces were applied with fixed boundary conditions, and extra boundary conditions were also introduced on all except the top surface of the model.

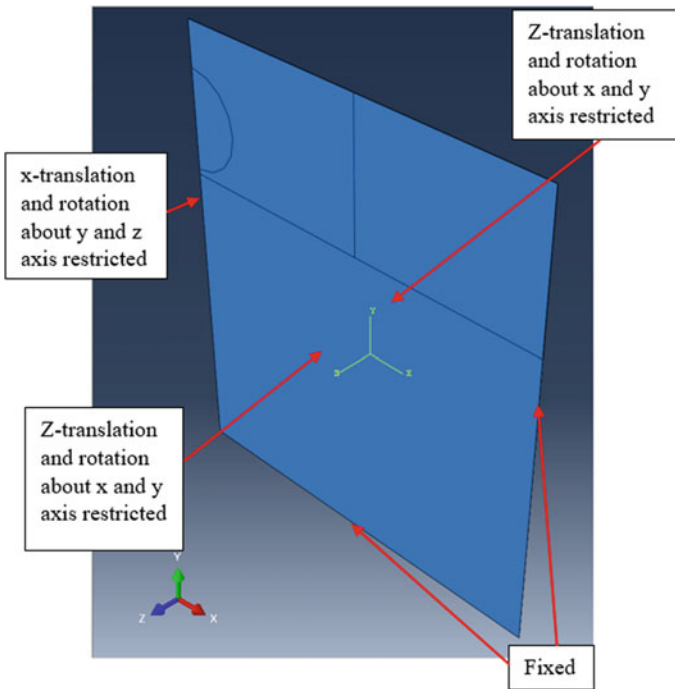


Fig. 3 Boundary conditions for our model. Lateral and bottom surfaces are fixed. (Color figure online)

Comparison Between the Developed Model and Other Eulerian Model

Figures 4 and 5 display the equivalent plastic strain (PEEQ) and temperature results from both models. Both models yield similar contour distribution. Particle flattening and jetting are observed after the impact. The models have approximately the same size for the area of strain and heat-affected zones. The maximum strain and temperature occurred at the particle–substrate interface and jetting region rather than at the bottom center of the particle where the particle–substrate interaction initiated. This observation indicates plastic deformation intensifies as the particle–substrate interface is closer to the jetting region due to the extreme plastic deformation caused by adiabatic shear instability. PEEQ is mainly contributed by shear strain. As the particle–substrate interface moves closer to the jetting region, more materials are squeezed outward to form the jetting, increasing the PEEQ at the interface region. Weaker jetting and the difference in the strain and temperature distribution are observed from our model. Our model has a slightly larger heat-affected zone and

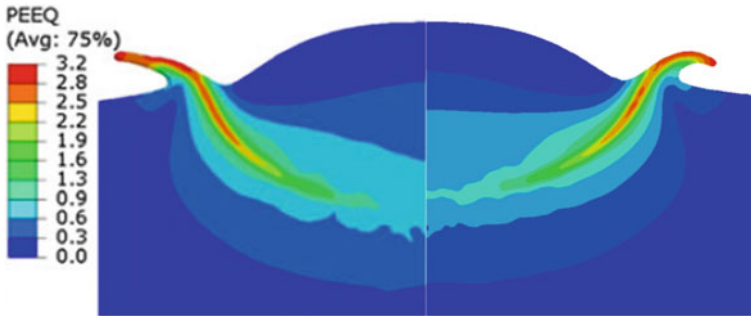


Fig. 4 Simulated results of equivalent plastic strain (PEEQ) from Wang (left) and our (right) model [7]. (Color figure online)

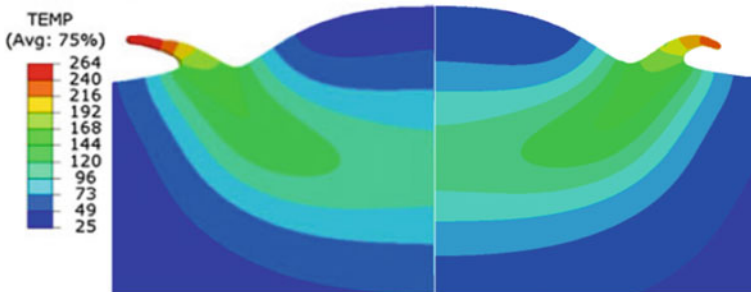


Fig. 5 Simulated results of temperature (°C) from Wang (left) and our (right) model [7]. (Color figure online)

higher temperature at the particle and the particle–substrate interface due to the boundary conditions at the model boundary restricting particle movement, reducing heat conduction at the boundary. Based on the observation above, our model agrees well with Wang et al.

Comparison Between the Developed Model and the Lagrangian Model

Ideally, there must be no or negligible difference in the simulation results between Eulerian and Lagrangian models if both models simulate the same physical phenomenon. However, the results could be different due to the difference in numerical treatment and solution processes. In order to check the difference between the developed model and a Lagrangian model, the PEEQ and temperature from the developed model are compared to those from the Lagrangian model from the literature [8]. Figures 6 and 7 show the PEEQ and temperature (°C) comparisons between Li’s and our model. Our model has a slightly larger but still comparable strain and heat-affected zone. The maximum strain is concentrated along the particle–substrate interface for both models. The maximum temperature is distributed at the edge of the particle with the substrate having a significantly lower temperature. It is different from our model in which the maximum temperature is distributed evenly at the particle–substrate interface. This phenomenon can be explained with the difference in formulation and surface interaction used for the simulation. Li’s model is a 3D Lagrangian model, and general surface-to-surface contact is used to define the interaction between particle and substrate. The presence of friction also contributes to

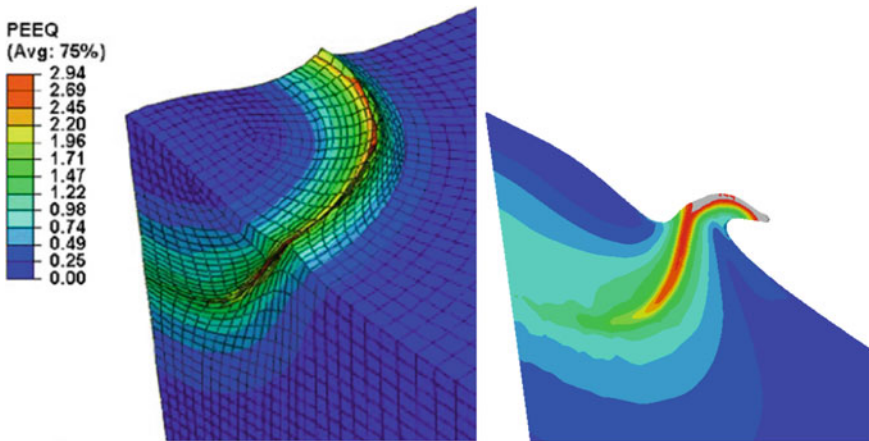


Fig. 6 Simulated results of equivalent plastic strain (PEEQ) from Li (left) and our (right) model. Grey contours are region with strains above 2.94 [8]. (Color figure online)

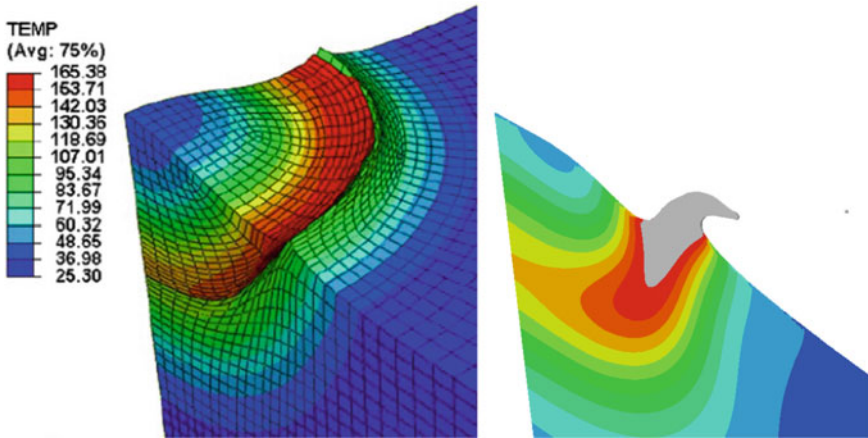


Fig. 7 Simulated results of temperature ($^{\circ}\text{C}$) from Li (left) and our (right) model. Grey contours are region with temperatures above 165.38°C [8]. (Color figure online)

this behavior. In contrast, materials behave in a sticky fluid-like behavior in Eulerian formulation [11]. Therefore, particle and substrate bonded at the moment of impact. Jetting is observed from both models with our model having a larger jetting. It is interesting to note that individual jetting from both the particle and the substrate is seen from Li's model. Li pointed out that the Lagrangian model experienced excessive mesh distortion during simulation. Large shear strain gradient associated with extensive plastic deformation present in the impact created the mesh distortion mentioned above, decreasing the accuracy of the model. The model failed prematurely for impact velocity above 500 m/s when Johnson–Cook material damage and adaptive Lagrangian–Eulerian meshing are not used in the simulation. Although Eulerian formulation greatly reduces the mesh distortion, some researchers prefer the Lagrangian formulation due to the highly visible boundary of particle, substrate, and their respective behaviors during the impact. Li mentioned severe mesh distortion present in the model decreasing the accuracy of the model, and more data is required for model verification [8]. Although there are some minor differences, it can be mentioned that the developed model showed a good agreement with the Lagrangian model from the literature.

Impact of AISI304 Steel Particle at 1000 M/S

In order to test the large deformation capability of the developed model, a simulation was run to predict the impact behavior of an AISI304 steel particle on a substrate made of the same material at 1000 m/s. This case was attempted using our Lagrangian model [10], but the simulation was ceased due to numerical instability. Material data was obtained from the literature [7, 13, 14]. Other parameters were kept the

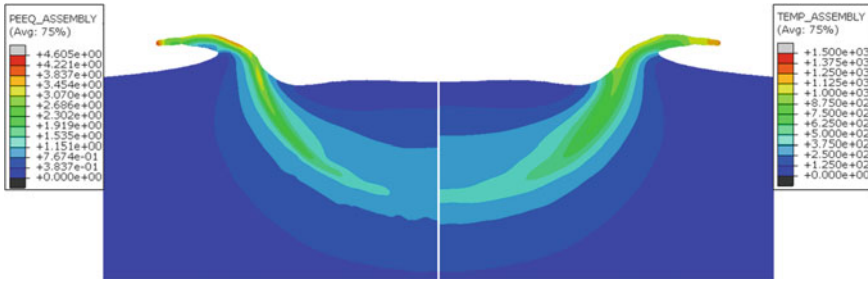


Fig. 8 Simulated results of equivalent plastic strain (PEEQ) and of temperature (°C) at $t = 60$ ns. (Color figure online)

same as in our previous simulations. Figure 8 displays the results of our model with AISI304 as the material for the particle and the substrate. The formation of strong jetting is observed starting at 2.8 ns. Jetting elongation is visible during the impact. At 5 ns, material loss by jetting was predicted at the front end of the jetting, breaking away from the jet, and jetting was no longer continuous. Deformation and reflection waves were observed on the entire substrate surface due to high-speed impact and high-strength material used. The particle has deformed and flattened more extensively compared to the lower velocity shown in Figs. 4 and 5. Figure 9 shows the impact evolution from 2.8 ns (where jetting begins) until 60 ns. The particle reached maximum displacement, and strain contour development slowed

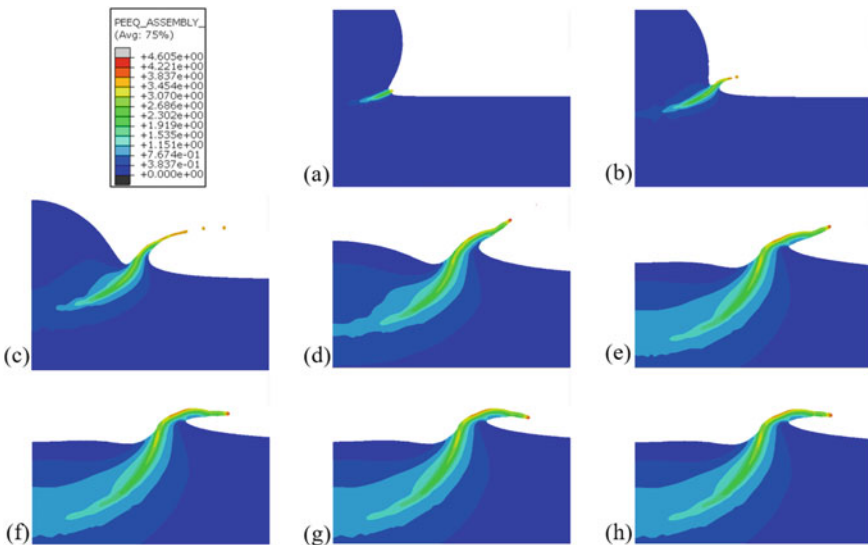


Fig. 9 Evolutions of equivalent plastic strain (PEEQ) at the impacting times: **a** 2.8 ns, **b** 5 ns, **c** 10 ns, **d** 20 ns, **e** 30 ns, **f** 40 ns, **g** 50 ns, and **h** 60 ns. (Color figure online)

Table 1 Parameters for simulations

	Wong	Wang et al. [7]	Li et al. [8]
Formulation	Eulerian	Eulerian	Lagrangian
Particle impact speed (m/s)	1000	400	500
Particle diameter (μm)	20	20	20
Substrate diameter (μm)	160	160	80
Substrate height (μm)	60	60	30
Mesh size (μm)	0.2	0.2	1
Coefficient of friction	0	0	0.2
Material	AISI304	Copper (Cu)	Copper (Cu)
Density (kg/m^3)	7800	8960	8960
Thermal conductivity, $\text{W}/(\text{m}^\circ\text{C})$	16.3	386	386
Specific heat, $\text{J}/(\text{kg }^\circ\text{C})$	450	383	383
Melting point ($^\circ\text{C}$)	1527	1083	1083
<i>Johnson–Cook parameters and equation of state</i>			
A (MPa)	310	0	90
B (MPa)	1000	292	292
n	0.65	0.31	0.31
C	0.034	0.025	0.025
m	1.05	1.09	1.09
Equation of state	Linear Mie–Gruneisen	Linear Mie–Gruneisen	–
C_0 (m/s)	4940	3940	–
S	1.49	1.49	–
γ_0	1.93	2.02	–

down at 30 ns. Impact behavior changed rapidly at the beginning of the impact and slowed down exponentially. Although the changes of strain contours and particle displacement are small after 40 ns, jetting was observed to fluctuate upwards and downwards, indicating thermal softening without reaching melting temperature. The parameters used for the Eulerian model developed in this research and the two results from the literature—Wang et al. [7] and Li et al. [8]—are listed in Table 1.

Summary

Through this research, an Eulerian FE model was developed to simulate the high-speed impact behavior of a micron-sized metallic particle. In order to circumvent the chronic divergence issues of the Lagrangian formulation, Eulerian approach

was employed. The two cases—one with Eulerian and the other with Lagrangian models—from the literature were reproduced using the developed Eulerian FE model. In both cases, the developed model showed a good agreement with the models from the literature. Using the validated model, the impact of an AISI particle on a substrate of the same material at 1000 m/s was simulated without divergence issues. The simulation predicted severe jetting even with material erosion due to high impact energy. The developed model is being extended to a full 3D Eulerian model.

References

1. Alkhimov AP, Papyrin AN, Kosarev VF, Nesterovich NI, Shuschpanov MM (1994) Gas dynamic spraying method for applying a coating, The United States
2. Champagne VK, Helfrich D (2014) Critical assessment 11: structural repairs by cold spray. *Mater Sci Technol* 31:627–634
3. Assadi H, Gaetner F, Stolenhoff T, Kreye H (2003) Bonding mechanism in cold gas spraying. *Acta Mater* 51:4379–4394
4. Wang X, Shi J (2013) Validation of Johnson-Cook plasticity and damage model using impact experiment. *Int J Impact Eng* 60:67–75
5. Yildirim B, Muftu S, Gouldstone A (2011) Modeling of high velocity impact of spherical particles. *Wear* 207:703–713
6. Schmidt T, Gartner H, Assadi H, Kreye H (2006) Development of a Generalized Parameter Window for Cold Spray Deposition. *Acta Mater* 54:729–742
7. Wang FF, Li W-Y, Yu M, Liao H (2014) Prediction of critical velocity during cold spraying based on a coupled thermomechanical Eulerian model. *J Therm Spray Technol* 23:60–67
8. Li W-Y, Gao W (2009) Some aspects on 3D numerical modeling of high velocity impact of particles in cold spraying by explicit finite element analysis. *Appl Surf Sci* 255:7878–7892
9. Li W-Y, Liao H, Li C-J, Bang HS, Coddet C (2007) Numerical simulation of deformation behavior of Al particles impacting on Al substrate and effect of surface oxide films on interfacial bonding in cold spraying. *Appl Surf Sci* 253:5084–5509
10. Shah S, Lee J, Rothstein JP (2017) Numerical Simulations of the High-Velocity Impact of a Single Polymer Particle During Cold-Spray Deposition. *J Therm Spray Technol* 26:970–984
11. Abaqus Analysis User's Manual. Dassault Systemes, 2007
12. Yin S, Wang XF, Xu BP, Li W-Y (2010) Examination on the Calculation Method for Modeling the Multi-Particle Impact Process in Cold Spraying. *J Therm Spray Technol* 19:1032–1041
13. Krasauskas P, Kilikevicius S, Cesnavicius R, Pacenga D (2014) Experimental analysis and numerical simulation of the stainless AISI 304 steel friction drilling process. *Mechanika* 20:590–595
14. Nahshon K, Pontin MG, Evans AG, Hutchinson JW, Zok FW (2007) Dynamic shear rupture of steel plates. *J Mech Mater Struct* 2:2049–2066

Optimal Design of the Submerged Entry Nozzle Structure and Modification of Technology for ASP Continuous Casting



Mingtao Xuan, Min Chen, Xiaojie Hua, and Kaizhu Zhang

Abstract To increase on both of the capacity and defectless thin slab production, the submerged entry nozzle (SEN) structure design and technology parameters of continuous casting were modified by studying the fluid flow and temperature distribution characteristics using physical and numerical simulation method. The results showed that the mold level fluctuation was strongly dependent to caster speed, and the average wave height exceeded 7 mm while the casting speed increased from 2.0 to 2.2 m/min for the section of 150 mm × 1540 mm. Compared to increase the angle of side-outlet or submerged depth of the SEN, the increase of the bottom port diameter of the three-port SEN was more effective on modification of level fluctuation although the maximal surface temperature was slightly decreased. Practical application also showed the effective performance of SEN design on improvement of the slab surface quality.

Keywords Thin slab · Fluid flow · Temperature distribution · Three-port SEN

Introduction

As well known, the flow pattern and temperature distribution in continuous casting molds plays a key role on the steel quality, the breakout and the productivity [1–3]. Therefore, many studies investigated the characteristics of the flow fluid and temperature distribution and operating parameters for the continuous casting of different types mold based on specific production conditions [4–7]. Specifically, SEN structures and the submergence depth play an important role in the continuous casting mold.

Compared to the thin slab continuous casting, the normal slab continuous casting cost more investment and space on the equipment, and the throughput is lower. However, the quality of normal slab continuous casting is usually higher than that of

M. Xuan · M. Chen (✉) · X. Hua · K. Zhang
School of Metallurgy, Northeastern University 313#, 3-11 Wen-Hua Road, Shenyang 110819,
China
e-mail: chenm@smm.neu.edu.cn

thin slab continuous casting. Combined with the advantages of normal slab continuous casting and thin slab continuous casting, the ASP continuous casting mold with the thickness of 150 mm has been used in China. For the purpose of low-cost manufacturing, the throughput was increased to 3.96 t/min by increasing casting speed. However, surface defects and breakout accidents often occurred in practical production, and it is considered that the flow field and temperature distribution has been worsened in the mold after increasing casting speed. Till now, little researchers [8, 9] focus on the flow field and temperature distribution in the medium-thin slab continuous casting mold, but they do not focus on such high throughput.

Based on the previous studies, physical and numerical simulations were established to study the flow field and temperature distribution in the medium-thin slab continuous casting mold. Especially, the effect of SEN structure and operating parameters was studied.

Water-Model Experiments

Based on the similarity principle, [5, 10] a 0.5: 1 scale water model was fabricated and visible tracer ink was used for investigating the flow field, as shown in Fig. 1. In addition, the mean wave height in the mold was measured by DJ800 multifunctional hydraulic monitoring system.

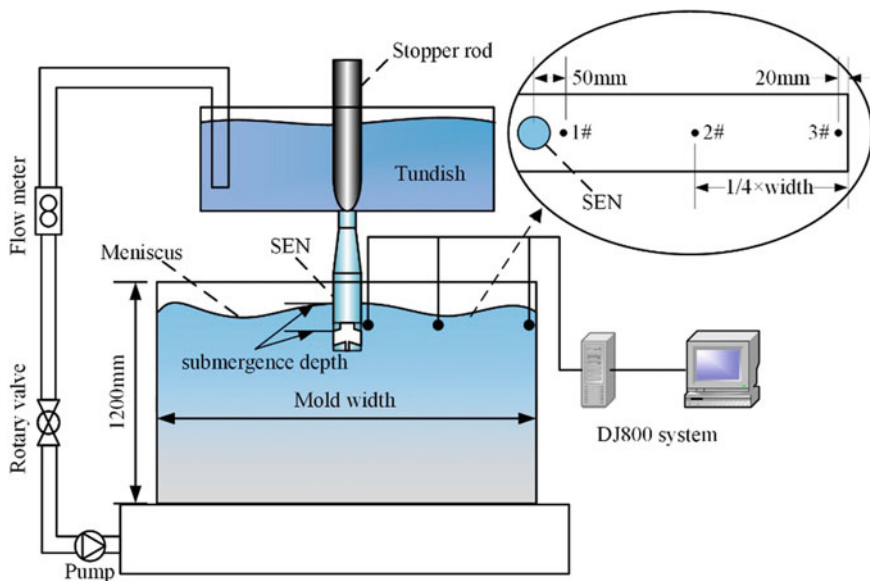


Fig. 1 Schematic of the water model. (Color figure online)

Figure 2 shows the schematic drawing of the 3P SEN. Table 1 lists structure parameters of SENs in this work, and the 3P-0 SEN is presently used ones. Table 2 shows operating parameters of prototype for simulation.

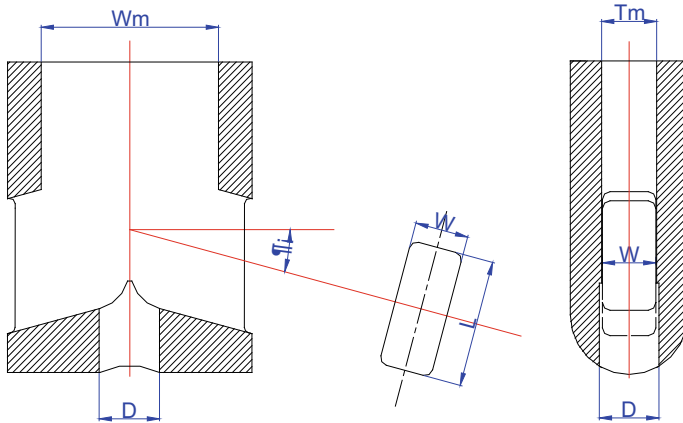


Fig. 2 Schematic of typical SENs investigated. (Color figure online)

Table 1 Parameters of SENs structure

SEN	Side port		Bottom port
	$L \times W(\text{mm} \times \text{mm})$	$\alpha(^{\circ})$	$D(\text{mm})$
3P-0	$L_0 \times W_0$	15	38
3P-1	$L_0 \times W_0$	18	38
3P-2	$L_0 \times W_0$	18	40

Table 2 Parameters of prototype for simulation

Parameter	Value
Mold width, mm	1540
Casting Speed, m/min	2.0 ~ 2.2
Mold thickness, mm	150
Effective length of mold, mm	1100
Throughput, t/min	3.60 ~ 3.96
SEN submergence depth, mm	80 ~ 140

Mathematical Model

Governing Equations

Conservation equations governing the mass and momentum are given as follows:

$$\frac{\partial(\rho u_i)}{\partial x_i} = 0 \quad (1)$$

$$\frac{\partial(\rho u_i u_j)}{\partial x_j} = -\frac{\partial P}{\partial x_i} + \frac{\partial}{\partial x_j} [\mu_{\text{eff}} (\frac{\partial u_i}{\partial x_j} + \frac{\partial u_j}{\partial x_i})] + \rho g + F \quad (2)$$

where the ρ is the density of molten steel, the u_i is the velocity, the x_i is the location of i direction, the μ_{eff} is the effective viscosity, and the F is the source term.

The standard k-epsilon equation, as shown in Eqs. (3) and (4), was used in simulated the turbulence phenomenon in the mold.

$$\frac{\partial(\rho u_i k)}{\partial x_i} = \frac{\partial}{\partial x_i} (\frac{\mu_{\text{eff}}}{\sigma_k} \frac{\partial k}{\partial x_i}) + G - \rho \varepsilon + S_k \quad (3)$$

$$\frac{\partial(\rho u_i \varepsilon)}{\partial x_i} = \frac{\partial}{\partial x_i} (\frac{\mu_{\text{eff}}}{\sigma_\varepsilon} \frac{\partial \varepsilon}{\partial x_i}) + C_1 \frac{\varepsilon}{k} G - C_2 \frac{\varepsilon^2}{k} + S_\varepsilon \quad (4)$$

To describe the flow and heat transfer phenomenon in the mushy zone, the enthalpy method was used as shown in Eq. (5).

$$\frac{\partial(\rho u_j H)}{\partial x_j} = \frac{\partial}{\partial x_j} \left(k_{\text{eff}} \frac{\partial T}{\partial x_j} \right) + S_H \quad (5)$$

Boundary Conditions and Numerical Details

Although the effective length of mold is 1100 mm, the computational domain is extended to 3000 mm to decrease the effect of circulation flow at the outlet of the mold. The specific boundary conditions are given as follows:

- (1) The inlet velocity is calculated by the inlet area and flow rate, the initial and inlet temperature are both assumed to the sum of the liquidus temperature and the superheat;
- (2) The free surface is defined as the adiabatic surface with zero-shear force;
- (3) The outlet velocity is casting speed;

- (4) The heat transfer boundary condition applied in mold is simplified as mean heat flux, and it is expressed as follows:

$$q = a - b\sqrt{t} \quad (5)$$

$$a = \bar{Q}_2 + \frac{\bar{Q}_1 - \bar{Q}_2}{\left(1 - \sqrt{\frac{V_2}{V_1}}\right)} \quad (6)$$

$$b = \frac{3(\bar{Q}_1 - \bar{Q}_2)}{2\left(\sqrt{\frac{h_m}{V_2}} - \sqrt{\frac{h_m}{V_1}}\right)} \quad (7)$$

where q is the local heat flux down the mold length, and t is the residence time (seconds) of the strand below the meniscus in the mold. \bar{Q}_1 and \bar{Q}_2 are the average heat flux from casting speed V_1 and V_2 , respectively. H_m is the effective mold length.

The heat transfer coefficients h_{spray} loaded into secondary cooling zone is constant [5].

Due to the complexity of the nozzle structure, tetrahedral meshes were used around the nozzle. To reduce the amount of calculations, other regions used hexahedral meshes. The SIMPLE algorithm was applied to discrete the governing equations. When the residual for energy equation was smaller than 10^{-6} and others were smaller than 10^{-4} , the converged solution was assumed to be achieved. The thermo-physical properties of steel used for simulation are listed in Table 3.

Table 3 Thermo-physical properties of steel used for numerical simulation

Parameter	Value
Density, kg m ⁻³	7000
Dynamic viscosity, kg m ⁻¹ s ⁻¹	0.0055
Specific heat, J kg ⁻¹ K ⁻¹	680
Thermal conductivity, W m ⁻¹ K ⁻¹	34
Liquidus temperature, K	1804
Solidus temperature, K	1769
Superheat, K	25
Latent heat, J kg ⁻¹	270000

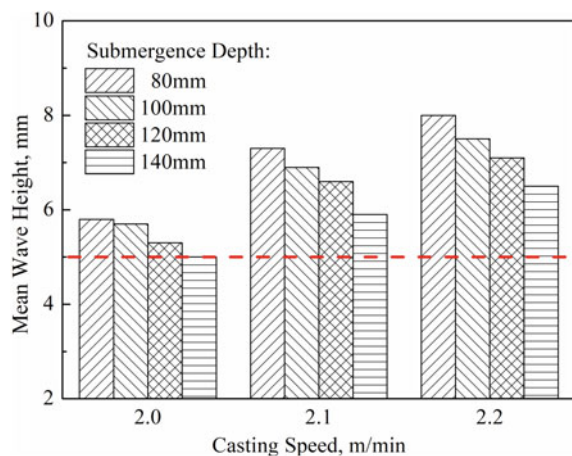
Results and Discussion

Free Surface Characteristics While 3P-0 SEN Used

The experimental results showed that the mean wave height in the ASP continuous casting mold was decreased from narrow face to the SEN, so the result of position 3# was used to evaluate the meniscus status. Figure 3 shows the mean wave height of different casting speed and submergence depths with the 3P-0 SEN. For the casting speed of 2.0 m/min, the mean wave height increased from 5.0 mm to 5.8 mm when the submergence depths decreased from 140 mm to 80 mm. For the casting speed of 2.2 m/min, the mean wave height increased from 6.5 mm to 8.0 mm when the submergence depths decreased from 140 mm to 80 mm. According to the practical experience, while the mean wave height was higher than the critical value of 5.0 mm, the meniscus status would be too active and oscillatory. Though the mean wave height decreased with the increasing of the submergence depth, but it could not reach a reasonable level. Thus, it is consider that the 3P-0 SEN is not suitable to the commercial operation even under the present casting speed.

Figure 4 shows the maximal surface velocity and temperature with the 3P-0 SEN using at the casting of 2.2 m/min. With the increase of the SEN submergence depth, the flow field and temperature distribution moved downward. So the velocity on the surface decreased from 0.49 m/s to 0.43 m/s, which indicated that the risk of slag entrapment was reduced. However, the surface temperature also decreased from 1805.3 K to 1804.3 K, which would affect the melting of mold powder. Thus, improve the meniscus by increasing the SEN submergence depth is not an ideal solution.

Fig. 3 Mean wave height of different casting speeds and submergence depths with the 3P-0 SEN. (Color figure online)



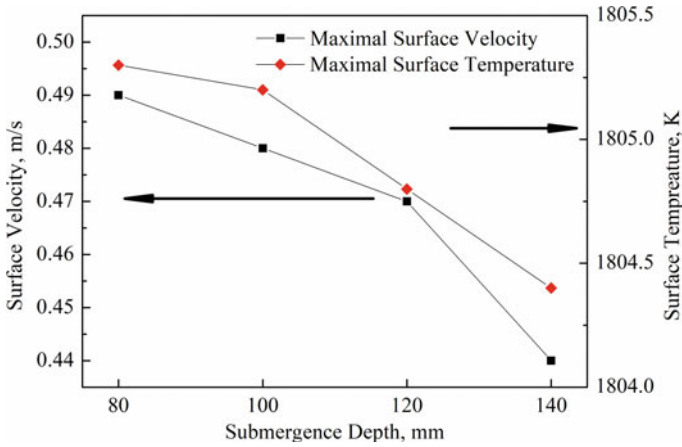
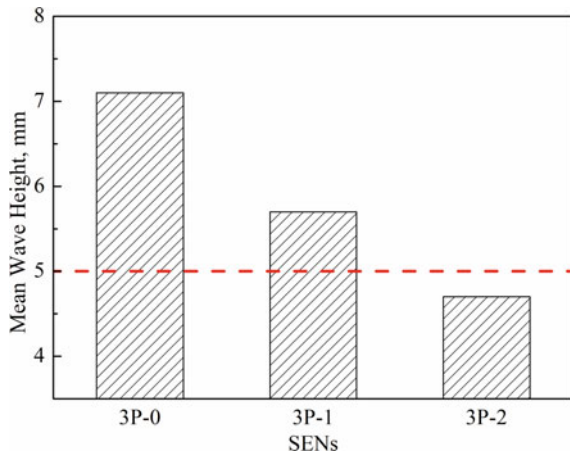


Fig. 4 Maximal surface velocity and temperature with the 3P-0 SEN using at the casting speed of 2.2 m/min. (Color figure online)

Effect SEN Structure Parameters on Free Surface Characteristics

Figure 5 shows the mean wave height while different SENs using at the casting speed of 2.2 m/min. It is indicated that the mean wave height could be effectively decreased from 7.1 mm to 5.7 mm by increasing the angle of side port from 15° to 18°, but it was still higher than empirical value. While increasing the diameter of bottom port based on the 3P-1 SEN, the mean wave height could be decreased to 4.7 mm, which was considered to be a reasonable level.

Fig. 5 Mean wave height while using different SENs. (Color figure online)



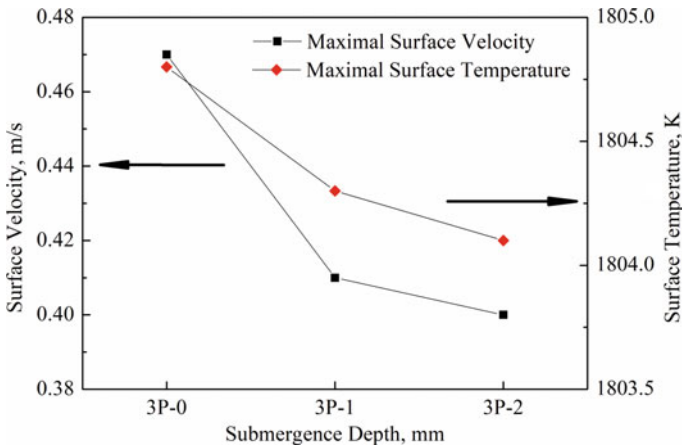


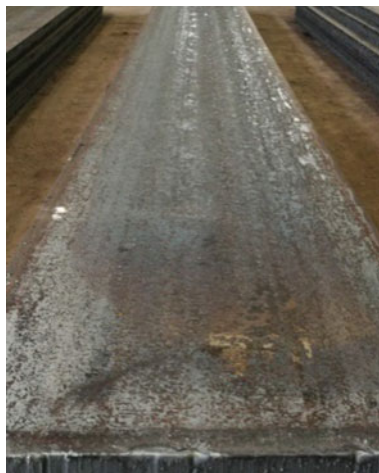
Fig. 6 Maximal surface velocity and temperature while using different SENs. (Color figure online)

Figure 6 shows the maximal surface velocity and temperature while using different SENs at the casting speed of 2.2 m/min. The surface velocity and temperature was decreased from 0.47 m/s and 1804.8 K to 0.41 m/s and 1804.3 K by increasing the angle of side port. The mechanism of decreasing mean wave height by increasing the angle of side port is the same as that by increasing the SEN submergence depth, which move the molten jet downward. But increasing the angle of side port is an effective way to solve it. Moreover, increasing the diameter of bottom port could decrease the surface velocity and temperature to 0.40 m/s and 1804.1 K. Thus, increasing the diameter of bottom port could effectively decrease surface velocity and have small effect on the temperature distribution, which means optimal structure is the most effective way to improve the meniscus status.

Practical Application Performance

The optimal SEN had been applied in practical production, with the throughput of 3.96t/min and the picture of the slab was shown in Fig. 7. The shape of the slab was regular, and there was no obviously defect on the slab. The statistics data of three months shows the surface quality defect decreased from 0.54% to 0.32%. In a word, the 3P-2 SEN could satisfy the steady production at high throughput of the ASP caster.

Fig. 7 Photos of slab.
(Color figure online)



Conclusion

1. The meniscus status in medium-thin slab mold was active and the mean wave height was 5.8 mm at the casting speed of 2.0 m/min. While the casting speed increased to 2.2 m/min, the mean wave height is up to 7.1 mm and it is not suitable to the commercial operation.
2. Compared to increasing the angle of side port and the SEN submergence depth, the increase of the bottom port diameter could decrease the mean wave height and the surface velocity to 4.7 mm and 0.4 m/s, and the surface temperature with smaller decrease.
3. Practical application showed that the shape of slab was regular and the surface quality defect decreased from 0.54% to 0.32% with the optimal SEN used at the casting speed of 2.2 m/min, and indicated that the 3P-2 SEN could satisfy the steady production at high throughput of the ASP caster.

Acknowledgements The authors gratefully acknowledge the National Key R&D Program of China (2017YFB0304203, 2017YFB0304201, 2016YFB0300602) and the National Natural Science Foundation of China (No. 51774072, 51774073, 51974080), which have made this research possible.

References

1. Liu Y, Wang XD, Sun Y, Yao M, Gao TL, Wang FW, Wang JY (2017) Research on a new detection method of slab surface crack in mould during continuous casting. *Res. Technol, Metall.* <https://doi.org/10.1051/metal/2017082>
2. Anjos TPDD, Pimenta PVDL, Marcondes F (2018) Analysis of the heat transfer coefficients of the whole process of continuous casting of carbon steel. *J Braz Soc Mech Sci Eng.* <https://doi.org/10.1007/s40430-018-1006-y>
3. Li YJ, Li L, Zhang JQ (2017) Study and application of a simplified soft reduction amount model for improved internal quality of continuous casting bloom. *Steel Res Int.* <https://doi.org/10.1002/srin.201700176>
4. Deng X, Ji C, Cui Y, Li L, Yin X, Yang Y, Mclean A (2017) Flow pattern control in continuous slab casting moulds: physical modelling and plant trials. *Ironmaking Steelmaking* 44(6):461–471
5. Shen JL, Chen DF, Xie X, Zhang LL, Dong ZH, Long MJ, Ruan XB (2013) Influences of SEN structures on flow characters, temperature field and shell distribution in 420 mm continuous casting mould. *Ironmaking Steelmaking* 40(4):263–275
6. Asad A, Kratzsch C, Schwarze R (2016) Numerical Investigation of the Free Surface in a Model Mold. *Steel Res Int* 87(2):181–190
7. Calderón-Ramos I, Morales RD (2015) The role of submerged entry nozzle port shape on fluid flow turbulence in a slab mold. *Metall Mater Trans B* 46(3):1314–1325
8. Zhao HM, Wang XH, Zhang JM, Wang WJ (2008) Effect of SEN structure on the mold level fluctuation and heat transfer for a medium thin slab caster. *J Univ Sci Technol B* 15(2):120–124
9. Thomas BG, O'Malley R, Shi T, Shi TB, Meng Y, Creech D, Stone D (2000) Validation of fluid flow and solidification simulation of a continuous thin-slab caster. Paper presented at the MCWASP IX. Aachen Germany, pp 769–776 August 2000
10. He ML, Wang N, Chen M, Xuan MT (2017) Physical and numerical simulation of the fluid flow and temperature distribution in bloom continuous casting mold. *Steel Res Int.* <https://doi.org/10.1002/srin.201600447>

Thermodynamic Examination of Quaternary Compounds in the Ag–Fe–(Ge, Sn)–Se Systems by the Solid-State EMF Method



Mykola Moroz, Fiseha Tesfaye, Pavlo Demchenko, Myroslava Prokhorenko, Bohdan Rudyk, Lyudmyla Soliak, Daniel Lindberg, Oleksandr Reshetnyak, and Leena Hupa

Abstract The equilibrium phase space of the Ag–Fe–X–Se (X: Ge, Sn) systems in the parts $\text{Ag}_8\text{XSe}_6\text{--XSe--FeSe}_2\text{--AgFeSe}_2\text{--Ag}_8\text{XSe}_6$ consists of four quaternary-phase regions formed with the participation of low-temperature modifications of the $\text{Ag}_2\text{FeGeSe}_4$ and $\text{Ag}_2\text{FeSnSe}_4$ compounds. The kinetic barriers of the formation of equilibrium four-phase regions that are observed under conditions of vacuum ampoule synthesis below 600 K were overcome by synthesis of phases at the positive electrodes of electrochemical cells (ECCs): $(-)\text{C}|\text{Ag}|\text{SE}|\text{R}(\text{Ag}^+)|\text{PE}|\text{C}(+)$, where C is graphite, Ag is left (negative) electrode, SE is the solid-state electrolyte, PE is the right (positive) electrode, and R (Ag^+) is the region of Ag^+ diffusion into PE. Silver cations Ag^+ that shifted from the left to the right electrode of ECCs acted as the seed centers of an equilibrium set of phases. Based on the temperature dependences of the EMF of the cells in the temperature range 430–485 K, the standard thermodynamic functions of the $\text{Ag}_2\text{FeGeSe}_4$ and $\text{Ag}_2\text{FeSnSe}_4$ compounds were calculated for the first time. The observed experimental results and thermodynamic calculations are in good agreement.

M. Moroz (✉) · B. Rudyk · L. Soliak
Department of Chemistry and Physics, National University of Water and Environmental
Engineering, Rivne 33028, Ukraine
e-mail: m.v.moroz@nuwm.edu.ua

M. Moroz · O. Reshetnyak
Department of Physical and Colloid Chemistry, Ivan Franko National University of Lviv, Lviv
79005, Ukraine

F. Tesfaye · L. Hupa
Johan Gadolin Process Chemistry Centre, Åbo Akademi University, 20500 Turku, Finland

P. Demchenko
Department of Inorganic Chemistry, Ivan Franko National University of Lviv, Lviv 79005, Ukraine

M. Prokhorenko
Department of Cartography and Geospatial Modeling, Lviv Polytechnic National University, Lviv
79013, Ukraine

D. Lindberg
Department of Chemical and Metallurgical Engineering, Aalto University, Kemistintie 1, 02150
Espoo, Finland

Keywords Silver-based phases · Magnetic semiconductors · Phase equilibria · Standard thermodynamic properties · EMF method · Gibbs energy

Introduction

Quaternary chalcogenides with a general formula is A_2BYZ_4 (A: Cu, Ag; B: Zn, Cd, Hg, Mn, Fe, Co, Ni; Y: Si, Ge, Sn, Pb; Z: S, Se, Te) are representative of a group of compounds, that mostly crystallize in the tetragonal stannite or in the orthorhombic wurtzite-stannite structures [1–9]. These compounds can be defined as tetrahedral chalcogenides, because all of the anions or cations are fourfold surrounded by their neighboring [10]. Many publications in recent decades are focused on study of these tetrahedral chalcogenides due to their potential application as economic functional materials in the solar cells, thermoelectric, photocatalytic, and photovoltaic devices [6, 10–12]. Moreover, tetrahedral chalcogenides with transition metal ions such as Ni^{2+} , Fe^{2+} , Co^{2+} , and Mn^{2+} exhibit large magneto-optical effects. According to some researchers [10, 13, 14], the $Cu_2FeGeSe_4$ and $Cu_2FeSnSe_4$ compounds are antiferromagnetic with a Neel temperature at $T_N = 20$ K and $T_N = 19$ K, respectively. The $Cu_2FeGeTe_4$ is ferromagnetic with $T_N \sim 160.1$ K [13]. The Ag-containing magnetic tetrahedral chalcogenides have been rarely discussed until now due to difficult condition of synthesis of a homogeneous material and narrow thermal stability range [2, 11, 15]. Nevertheless, physical properties of the $Ag_2FeGeSe_4$ compound have been investigated by several authors [3, 16, 17]. Wooley et al. [3] established the high field magnetic properties of the $Ag_2FeGeSe_4$ in the range of $T = (2–300)$ K. It was found that at $T_N = 240$ K quaternary compound shows mainly antiferromagnetic behavior, with a weak superimposed ferromagnetic component down to $T = 60$ K. Below $T = 60$ K, the ferromagnetic component becomes much bigger. The magnetic spin-flop, critical-fields, and magnetic saturation in the $Ag_2FeGeSe_4$ were reported in [16, 17]. Information on the $Ag_2FeSnSe_4$ compound is limited by data on the temperature of formation during cooling of the melt, the crystal structure of its high-temperature modification [2]. No information on the thermodynamic properties of quaternary compounds of the Ag–Fe–X–Se (X: Ge, Sn) system was found in the open literature.

The purpose of this work was to demonstrate the capabilities of solid-state synthesis from elements of equilibrium set of compounds in the Ag–Fe–X–Se systems in the range of $T = (400–500)$ K, where the energy of the thermal motion of atoms is insufficient for the formation of the nucleation centers of phases; and to determine thermodynamic properties of the quaternary compounds in the investigated systems by applying the electromotive force (EMF) method.

Experimental

Synthesis and Analysis

The starting materials for synthesis were high-purity elements (99.99 wt% Ag, 99.9 wt% Fe, 99.999 wt% Ge, 99.999 wt% Sn, 99.99 wt% S, and 99.99 wt% Se). The samples of the formula compositions 'Ag₂FeGeSe₄' and 'Ag₂FeSnSe₄' for X-ray diffraction (XRD) were synthesized by two methods:

1. Solid-state synthesis of the calculated mixture of elements in evacuated ($p \sim 10^{-2}$ Pa) quartz ampoules at $T = 630$ K during 5 days. The samples were cooled to room temperature at the rate of 2 K min^{-1} and ground to particle size of $\sim 5.0 \mu\text{m}$. Vacuum homogenization of the fine phase mixture was held at $T = 580$ K for 5 days.
2. Vacuum melting of the calculated mixture of elements at $T = 1100$ K followed by vacuum annealing of the finely disperse mixture at $T = 580$ K for 5 days.

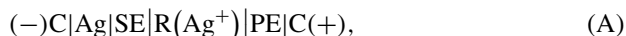
The synthesis of an equilibrium set of phases for the study of the thermodynamic properties of low-temperature modifications of the Ag₂FeGeSe₄ and Ag₂FeSnSe₄ compounds was performed in the positive electrodes (PE) of electrochemical cells (ECCs).

XRD patterns were collected on an STOE STADI P diffractometer equipped with a linear position-sensitive detector PSD, in a modified Guinier geometry (transmission mode, CuK α_1 radiation, a bent Ge (111) monochromator, $2\theta/\omega$ scan mode). Preliminary data processing and X-ray phase analyses were performed using STOE WinXPOW 3.03 [18] and Powder Cell 2.4 PC programs [19], using data on crystal structures for the phases taken from the database [20].

The Ag₂GeS₃ glass [21–23] was obtained by melt quenching of the corresponding elements from $T = 1200$ K in ice water.

Electromotive Force Measurements

For the EMF measurements, the following ECCs were assembled:



where C is graphite, Ag is left (negative) electrode, SE is the solid-state electrolyte, PE is the right (positive) electrode, R (Ag⁺) is the region of Ag⁺ penetration into PE. Pure silver powder was used as a left electrode. Ag₂GeS₃ glass was used as SE with purely Ag⁺ ionic conductivity [21, 24].

PE at the stage of the cell preparation is a well-mixed composition of finely ground mixtures of elements Ag, Fe, Ge (Sn), and Se, with particle size $\sim 5 \mu\text{m}$. The ratios of the elements were determined from the equations of the potential-forming reactions

in respective phase fields. ECC components in powder form were pressed at 10^8 Pa through a 2 mm diameter hole arranged in the fluoroplast matrix up to density $\rho = (0.93 \pm 0.02) \cdot \rho_0$, where ρ_0 is the experimentally determined density of cast samples [25].

EMF measurements were performed in a horizontal resistance furnace, similar to that described in [26]. As protective atmosphere, we used a continuously flowing highly purified (0.9999 volume fraction) Ar(g) at $P = 1.2 \times 10^5$ Pa, with a flow rate of $2 \times 10^{-3} \text{ m}^3 \text{ h}^{-1}$ from the left to right electrode of the ECCs. The temperature was maintained with an accuracy of ± 0.5 K. The EMF (E) of the cells were measured by high-resistance (input impedance of $>10^{12} \Omega$) universal U7-9 digital voltmeter and MTech PGP-550 M device. The heating and cooling rates were 2 K min^{-1} . The equilibrium in ECCs at each temperature was achieved within ≤ 1 h. The criterion of achieving the equilibrium state in the PE was the reproducibility of the E versus T dependences in the heating–cooling cycles. The scheme of ECCs and procedure of the EMF measurements have been described in our previous works [27–29].

Results and Discussion

The $\text{Ag}_2\text{FeGeSe}_4$ and $\text{Ag}_2\text{FeSnSe}_4$ compounds have not been obtained by vacuum ampoule melting and annealing of the components described in Sect. 2. The diffraction patterns of both samples are shown in Figs. 1 and 2. The presence of the phases (Ag_8GeSe_6 , Fe_2GeSe_4 , and GeSe_2) in the sample ‘ $\text{Ag}_2\text{FeGeSe}_4$ ’ and (Ag_8SnSe_6 , Ag_2Se , AgSnSe_2 , and Fe_3Se_4) in the sample ‘ $\text{Ag}_2\text{FeSnSe}_4$ ’ has been established by XRD method. Increasing the annealing time to 20 days in the range of $T = (450\text{--}600)$ K does not change the diffraction pattern of the samples. Thus, no signs of the

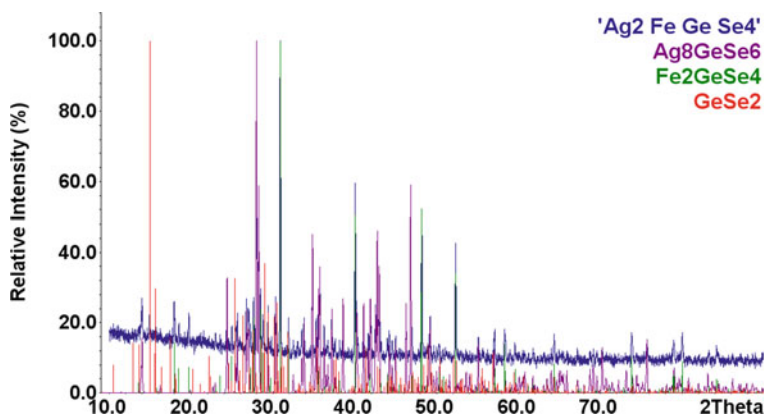


Fig. 1 Comparison of the experimental XRD pattern of the sample ‘ $\text{Ag}_2\text{FeGeSe}_4$ ’ with those theoretical patterns of the compounds. (Color figure online)

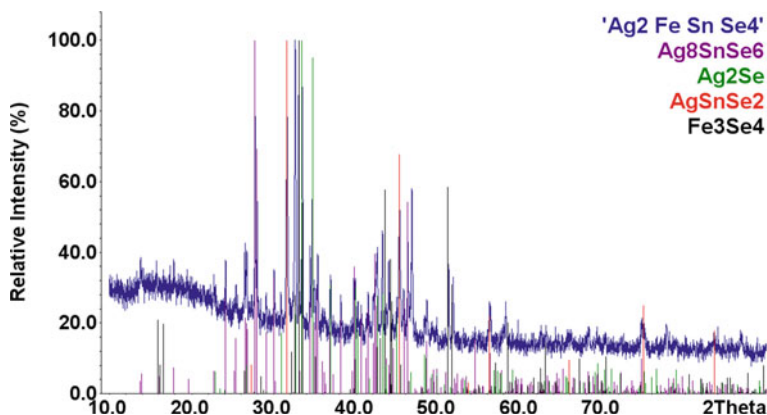


Fig. 2 Comparison of the experimental XRD pattern of the sample 'Ag₂FeSnSe₄' with those theoretical patterns of the compounds. (Color figure online)

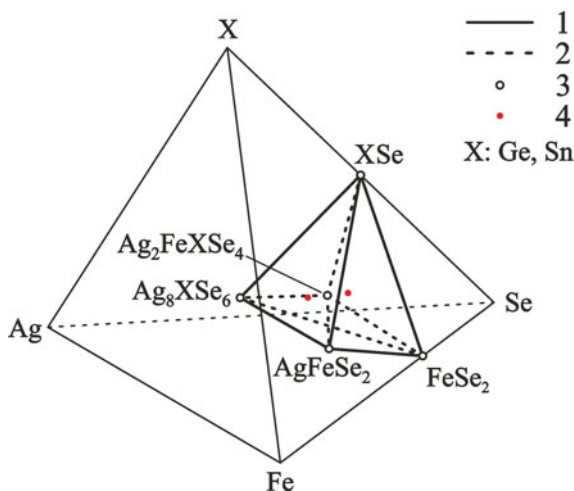
formation of the Ag₂FeGeSe₄ and Ag₂FeSnSe₄ compounds were detected under the described conditions of vacuum ampoule synthesis and annealing of the samples.

Our work on synthesis and study thermodynamic parameters of low-temperature modifications of the Ag₂FeGeSe₄ and Ag₂FeSnSe₄ compounds, as in case of Ag₂FePbSe₄ [15], are based on the following:

1. Identified by XRD method the phase compositions of the 'Ag₂FeGeSe₄' and 'Ag₂FeSnSe₄' samples is considered metastable for kinetic reasons at $T < 600$ K;
2. The validity of the proposed division of the equilibrium concentration space of the Ag–Fe–X–Se systems in the parts Ag₈XSe₆–XSe–FeSe₂–AgFeSe₂–Ag₈XSe₆ into separate four-phase regions;
3. Possibility of the solid-state synthesis of equilibrium set of phases in the PE of ECCs.

In type (A) ECC, self-motion of Ag⁺ cations from the left to the right electrode takes place due to differences in the chemical potentials of silver in these areas [30]. The consequence of such a movement is the appearance of a potential difference at the electrodes of the ECC. Solid-state synthesis of the equilibrium set of phases was performed in the PE of ECC at the penetration depth of Ag⁺ ions, i.e., the R (Ag⁺) region. It was found that EMF values in the newly assembled ECCs change over time at $T = \text{const}$. This is as a result of the diffusion processes and intermediate reactions in the metastable set of phases of the R(Ag⁺) region. The positive charge localized in the R(Ag⁺) region reduces the Coulomb repulsive forces between the components of the PE to the values of ≤ 0 . This is a condition for non-activation synthesis of the equilibrium set of phases. Ag⁺ cations are not a phase, do not chemically interact with a metastable set of elements, but act as a catalyst for non-activation synthesis. In the R(Ag⁺) region, the spatial grouping of individual phases of the equilibrium set is carried out by diffusion of atoms and is a function of temperature. The process of forming an equilibrium set of phases ends in ≤ 5 h for the particle size of the

Fig. 3 The phase equilibria of the Ag–Fe–X–Se (X: Ge, Sn) systems in the Ag_8XSe_6 – XSe – FeSe_2 – AgFeSe_2 – $\text{Ag}_2\text{FeXSe}_4$ parts, below 500 K. The solid and dashed tie lines (1 and 2) indicate two-phase equilibria, the open circle (3) indicates compounds, and the red closed circle (4) indicates compositions of positive electrodes of ECCs. (Color figure online)

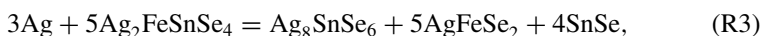
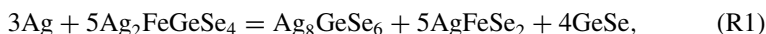


heterogeneous phase mixture $\sim 5 \mu\text{m}$ at $T = 500 \text{ K}$. It was not possible to isolate the equilibrium mixture of phases for XRD due to its negligible amount, similarly to the case in [31]. An example of solid-state synthesis of the rather simple phase AgTe in the ECC is presented in [32].

The phase equilibria of the Ag–Fe–X–Se systems in the parts Ag_8XSe_6 – XSe – FeSe_2 – AgFeSe_2 – $\text{Ag}_2\text{FeXSe}_4$ are shown in Fig. 3.

Division of the concentration space into separate regions was performed according to the results of Refs. [15, 33–37] and the present study by the EMF method. The presence of four four-phase regions has been established: Ag_8XSe_6 – $\text{Ag}_2\text{FeXSe}_4$ – XSe – AgFeSe_2 (I), Ag_8XSe_6 – $\text{Ag}_2\text{FeXSe}_4$ – XSe – FeSe_2 (II), Ag_8XSe_6 – $\text{Ag}_2\text{FeXSe}_4$ – AgFeSe_2 – FeSe_2 , and XSe – $\text{Ag}_2\text{FeXSe}_4$ – AgFeSe_2 – FeSe_2 . The correctness of the suggested limits of four-phase regions is confirmed by the following calculations of thermodynamic quantities for the $\text{Ag}_2\text{FeGeSe}_4$ and $\text{Ag}_2\text{FeSnSe}_4$ compounds.

The position of the phase regions (I) and (II) relative to Ag was used to write the equations of the overall potential-forming reactions of decomposition and synthesis of the quaternary compounds:



In accordance with reactions (R1)–(R4), the compositions of the positive electrodes in the phase regions (I) and (II) were determined by element ratios Ag: Fe: Ge: Se of 23:10:10:20 and 9:5:5:20 for the Ag–Fe–Ge–Se system, with the element ratios Ag: Fe: Sn: Se of 23:10:10:20 and 9:5:5:20, for the Ag–Fe–Sn–Se system, respectively.

The measured EMF values of the ECCs at various temperatures in the range of $T = (430\text{--}485)$ K are shown in Fig. 4 and can be expressed by Eqs. (1)–(4):

$$E_{(R1)}/\text{mV} = (110.15 \pm 0.87) + (380.26 \pm 1.90) \times 10^{-3}T/\text{K}, R^2 = 0.99973 \quad (1)$$

$$E_{(R2)}/\text{mV} = (160.58 \pm 0.79) + (350.15 \pm 1.72) \times 10^{-3}T/\text{K}, R^2 = 0.99973, \quad (2)$$

$$E_{(R3)}/\text{mV} = (207.50 \pm 1.22) + (225.17 \pm 2.67) \times 10^{-3}T/\text{K}, R^2 = 0.99846, \quad (3)$$

$$E_{(R4)}/\text{mV} = (225.07 \pm 0.60) + (262.78 \pm 1.32) \times 10^{-3}T/\text{K}, R^2 = 0.99972 \quad (4)$$

where R^2 is the coefficient of determination. The upper and lower limits of the temperature range of the measurements were determined by the linear part of the E versus T dependences that were reproducible in the heating-cooling cycles.

The Gibbs energies, entropies, and enthalpies of the reactions (R1)–(R4) can be calculated by combining the measured EMF values of each ECCs and the thermodynamic Eqs. (5)–(7):

Fig. 4 EMF values of the ECCs as a function of cell temperature. (Color figure online)

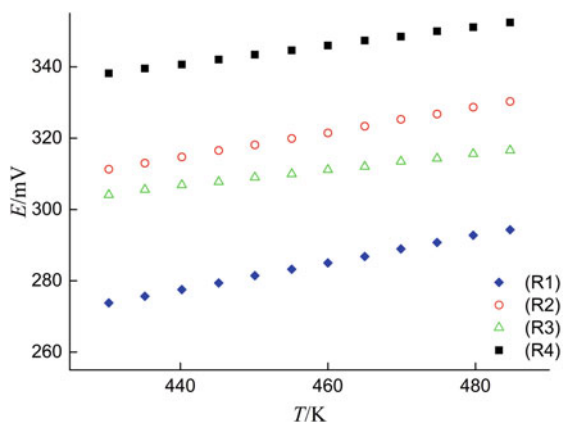


Table 1 Standard thermodynamic quantities of the reactions (R1)–(R4) in the ECCs

Reaction	$-\Delta_r G^\circ$	$-\Delta_r H^\circ$	$\Delta_r S^\circ$
	kJ mol ⁻¹		J (mol K) ⁻¹
(R1)	64.70 ± 0.86	31.88 ± 0.25	110.07 ± 0.55
(R2)	51.13 ± 0.52	30.99 ± 0.15	67.57 ± 0.33
(R3)	79.49 ± 1.44	60.06 ± 0.35	65.18 ± 0.77
(R4)	58.55 ± 0.47	43.43 ± 0.12	50.71 ± 0.25

$$\Delta_r G = -n \cdot F \cdot E, \quad (5)$$

$$\Delta_r H = -n \cdot F \cdot [E - (dE/dT) \cdot T], \quad (6)$$

$$\Delta_r S = n \cdot F \cdot (dE/dT), \quad (7)$$

where n is the number of electrons involved in the reactions (R1)–(R4), $F = 96485.33289 \text{ C mol}^{-1}$ is Faraday constant, and E in V is the EMF of the ECCs.

Standard thermodynamic quantities of the reactions (R1)–(R4) at $T = 298 \text{ K}$ were calculated using Eqs. (5)–(7) in the approximation $(\frac{\partial \Delta_r H}{\partial T})_p = 0$ and $(\frac{\partial \Delta_r S}{\partial T})_p = 0$ [32, 38]. The results of the calculations are presented in Table 1.

In the phase region (I), standard Gibbs energy and entropy of reaction (R1) are related to the Gibbs energy of formation and entropy of compounds and pure elements the following equations:

$$\Delta_{r(R1)} G^\circ = \Delta_f G_{\text{Ag}_8\text{GeSe}_6}^\circ + 5\Delta_f G_{\text{AgFeSe}_2}^\circ + 4\Delta_f G_{\text{GeSe}}^\circ - 5\Delta_f G_{\text{Ag}_2\text{FeGeSe}_4}^\circ, \quad (8)$$

$$\Delta_{r(R1)} S^\circ = S_{\text{Ag}_8\text{GeSe}_6}^\circ + 5S_{\text{AgFeSe}_2}^\circ + 4S_{\text{GeSe}}^\circ - 3S_{\text{Ag}}^\circ - 5\Delta_f G_{\text{Ag}_2\text{FeGeSe}_4}^\circ. \quad (9)$$

It follows from Eqs. (8) and (9) that:

$$\Delta_f G_{\text{Ag}_2\text{FeGeSe}_4}^\circ = 0.2 \left(\Delta_f G_{\text{Ag}_8\text{GeSe}_6}^\circ + 5\Delta_f G_{\text{AgFeSe}_2}^\circ + 4\Delta_f G_{\text{GeSe}}^\circ - \Delta_{r(R1)} G^\circ \right), \quad (10)$$

$$S_{\text{Ag}_2\text{FeGeSe}_4}^\circ = 0.2 \left(S_{\text{Ag}_8\text{GeSe}_6}^\circ + 5S_{\text{AgFeSe}_2}^\circ + 4S_{\text{GeSe}}^\circ - 3S_{\text{Ag}}^\circ - \Delta_{r(R1)} S^\circ \right). \quad (11)$$

The entropy of formations of the $\text{Ag}_2\text{FeGeSe}_4$ compound can be calculated as:

$$\Delta_f S_{\text{Ag}_2\text{FeGeSe}_4}^\circ = S_{\text{Ag}_2\text{FeGeSe}_4}^\circ - 2S_{\text{Ag}}^\circ - S_{\text{Fe}}^\circ - S_{\text{Ge}}^\circ - 4S_{\text{Se}}^\circ. \quad (12)$$

The corresponding reactions to determine $\Delta_f G^\circ$, S° , and $\Delta_f S^\circ$ for the $\text{Ag}_2\text{FeGeSe}_4$ in the phase region (II) and for the $\text{Ag}_2\text{FeSnSe}_4$ in the phase regions (I)

and (II) can be written similar to Eqs. (10)–(12) with their appropriate stoichiometric numbers.

Combining Eqs. (5)–(7) and (10)–(12), using thermodynamic data of the pure elements [39], and compounds GeSe [39], SnSe [39], FeSe₂ [40], AgFeSe₂ [15], Ag₈GeSe₆ [30], Ag₈SnSe₆ [30], the standard Gibbs energy of formations of quaternary compounds of the Ag–Fe–X–Se systems in the phase regions (I) and (II) were calculated. A comparative summary of the calculated values together with the available literature data is presented in Table 2.

The temperature dependences of the Gibbs energies of formation of the quaternary compounds in the phase regions (I) and (II) are described as:

$$\Delta_f G_{\text{Ag}_2\text{FeGeSe}_4, \text{(I)}} / (\text{kJ mol}^{-1}) = -(228.7 \pm 27.5) + (5.7 \pm 0.2) \cdot 10^{-3} T/\text{K}, \quad (13)$$

$$\Delta_f G_{\text{Ag}_2\text{FeGeSe}_4, \text{(II)}} / (\text{kJ mol}^{-1}) = -(221.1 \pm 31.2) - (14.6 \pm 0.3) \cdot 10^{-3} T/\text{K}, \quad (14)$$

$$\Delta_f G_{\text{Ag}_2\text{FeSnSe}_4, \text{(I)}} / (\text{kJ mol}^{-1}) = -(251.8 \pm 30.9) + (5.9 \pm 0.2) \cdot 10^{-3} T/\text{K}, \quad (15)$$

$$\Delta_f G_{\text{Ag}_2\text{FeSnSe}_4, \text{(II)}} / (\text{kJ mol}^{-1}) = -(252.4 \pm 36.3) - (2.1 \pm 0.1) \cdot 10^{-3} T/\text{K}. \quad (16)$$

Table 2 Standard thermodynamic quantities of selected phases in the Ag–Fe–X–Se systems

Phases	$-\Delta_f G^\circ$	$-\Delta_f H^\circ$	S°	[References]
	kJ mol ⁻¹		J (mol K) ⁻¹	
Ag	0	0	42.677	[39]
Fe	0	0	27.280	[39]
Ge	0	0	31.087	[39]
Sn	0	0	51.195	[39]
Se	0	0	42.258	[39]
GeSe	70.496	69.036	78.241	[39]
SnSe	87.533	88.701	89.538	[39]
FeSe ₂	101.3 ± 15.0	108.7 ± 15.0	86.8 ± 1.0	[40]
AgFeSe ₂	125.9 ± 15.0	128.8 ± 15.0	144.7 ± 3.3	[15]
Ag ₈ GeSe ₆	288.0 ± 2.3	255.0 ± 2.8	734.6 ± 30.4	[30]
Ag ₈ SnSe ₆	350.3 ± 1.8	320.4 ± 8.1	746.4 ± 23.8	[30]
Ag ₂ FeGeSe ₄ ^a	227.0 ± 34.6	228.7 ± 27.5	307.0 ± 9.9	This work
Ag ₂ FeGeSe ₄ ^b	225.5 ± 36.3	221.1 ± 31.2	327.3 ± 6.5	This work
Ag ₂ FeSnSe ₄ ^a	250.1 ± 38.6	251.8 ± 30.9	327.0 ± 10.4	This work
Ag ₂ FeSnSe ₄ ^b	253.0 ± 40.9	252.4 ± 36.3	334.9 ± 6.0	This work

^aphase region (I)

^bphase region (II)

It follows from Eqs. (13)–(16) that the enthalpy and entropy values of the Gibbs energy of formation of the quaternary compounds differ in phase regions (I) and (II), with entropy of the reaction differing not only in magnitude but also in sign. These differences are due to the different nature of the crystal lattice defects in the solid solutions of the compounds that is in equilibrium in these phase regions. At the same time, the convergence within the experiment error of the calculated $\Delta_f G^\circ$ values for the $\text{Ag}_2\text{FeGeSe}_2$ and $\text{Ag}_2\text{FeSnSe}_2$ compounds in the phase regions (I), (II) (the relative differences are $\sim 1\%$) serves as the validation to correctness:

1. Phase composition and division of the equilibrium concentration space of the Ag–Fe–X–Se systems in the parts Ag_8XSe_6 – XSe – FeSe_2 – AgFeSe_2 – Ag_8XSe_6 ;
2. Calculated values of the thermodynamic quantities of the quaternary compounds;
3. Reliability of the literature values of the thermodynamic properties of compounds GeSe, SnSe, FeSe₂, Ag₈GeSe₆, Ag₈SnSe₆, and AgFeSe₂; and
4. Negligible homogeneity region of the $\text{Ag}_2\text{FeGeSe}_4$ and $\text{Ag}_2\text{FeSnSe}_4$ compounds.

Conclusions

Division of the equilibrium concentration space of the Ag–Fe–X–Se (X: Ge, Sn) systems in the parts Ag_8XSe_6 – XSe – FeSe_2 – AgFeSe_2 – Ag_8XSe_6 into four quaternary-phase regions was established. The positions of the phase regions Ag_8XSe_6 – $\text{Ag}_2\text{FeXSe}_4$ – XSe – AgFeSe_2 and Ag_8XSe_6 – $\text{Ag}_2\text{FeXSe}_4$ – XSe – FeSe_2 versus the point of Ag were used to write the equations of overall potential-forming reactions. Solid-state synthesis of the equilibrium set of phases, including the quaternary compounds, was performed in the positive electrodes of electrochemical cells. Ag⁺ cations that shifted from the left electrode are catalysts for the formation of nucleation centers of individual phases.

Linear dependences of the EMF versus T of the ECCs were used for calculations of the standard Gibbs energies, enthalpies, and entropies of formations of the quaternary compounds. Calculations were performed in two fundamentally different potential-forming processes: the decomposition and synthesis of the quaternary compounds. The agreement of the determined $\Delta_f G^\circ$ values in the two potential-forming processes confirm that: the division of the concentration space of the Ag–Fe–X–Se systems and the phase composition of the positive electrodes in the ECCs used to calculate the thermodynamic properties of the $\text{Ag}_2\text{FeGeSe}_4$ and $\text{Ag}_2\text{FeSnSe}_4$. Furthermore, the reproducibility of the determined $\Delta_f G^\circ$ confirms the accuracy of the literature Gibbs energy data for GeSe, SnSe, FeSe₂, Ag₈GeSe₆, Ag₈SnSe₆, and AgFeSe₂.

Acknowledgements This work was partially supported by the Ministry of Education and Science of Ukraine (Grant No. 0119U002208). This work was also financially supported by the Academy of Finland project ‘Thermodynamic investigation of complex inorganic material systems for improved renewable energy and metals production processes’ (Decision number 311537), as part of the activities of the Johan Gadolin Process Chemistry Center at Åbo Akademi University.

Conflict of Interest The authors declare that they have no conflict of interest.

References

1. Fries T, Shapira Y, Palacio F, Morón MC, McIntyre GJ, Kershaw R, Wold A, McNiff EJ (1997) Magnetic ordering of the antiferromagnet $\text{Cu}_2\text{MnSnS}_4$ from magnetization and neutron-scattering measurements. *Phys Rev B* 56:5424–5431
2. Quintero M, Barreto A, Grima P, Tovar R, Quintero E, Porras GS, Ruiz J, Woolley JC, Lamarche G, Lamarche A-M (1999) Crystallographic properties of $\text{I}_2\text{-Fe-IV-VI}_4$ magnetic semiconductor compounds. *Mater Res Bull* 34:2263–2270
3. Woolley JC, Lamarche G, Lamarche A-M, Rakoto H, Broto JM, Quintero M, Morocoima M, Quintero E, Gonzalez J, Tovar R, Cadenas R, Bocoranda P, Ruiz J (2003) High field magnetic properties of $\text{Ag}_2\text{FeGeSe}_4$ in the temperature range 2–300 K. *J Magn Magn Mater* 257:87–94
4. Sachanyuk VP, Olekseyuk ID, Parasyuk OV (2006) X-ray powder diffraction study of the $\text{Cu}_2\text{Cd}_{1-x}\text{Mn}_x\text{SnSe}_4$ alloys. *Phys Status Solidi (a)* 203:459–465
5. Chen S, Walsh A, Luo Y, Yang J-H, Gong XG, Wei S-H (2010) Wurtzite-derived polytypes of kesterite and stannite quaternary chalcogenide semiconductors. *Phys Rev B* 82:195203(1–8)
6. Prabhakar RR, Zhenghua S, Xin Z, Baikie T, Woei LS, Shukla S, Batabyal SK, Gunawan O, Wong LH (2016) Photovoltaic effect in earth abundant solution processed $\text{Cu}_2\text{MnSnS}_4$ and $\text{Cu}_2\text{MnSn(S, Se)}_4$ thin films. *Sol Energy Mater Sol Cells* 157:867–873
7. Chen L, Deng H, Tao J, Cao H, Sun L, Yang P, Chu J (2016) Strategic improvement of $\text{Cu}_2\text{MnSnS}_4$ films by two distinct post-annealing processes for constructing thin film solar cells. *Acta Mater* 109:1–7
8. Rondiya S, Wadnerkar N, Jadhav Y, Jadkar S, Haram S, Kabir M (2017) Structural, electronic, and optical properties of $\text{Cu}_2\text{NiSnS}_4$: a combined experimental and theoretical study toward photovoltaic applications. *Chem Mater* 29:3133–3142
9. Heppke EM, Berendts S, Lerch M (2020) Crystal structure of mechanochemically synthesized $\text{Ag}_2\text{CdSnS}_4$. *Z Naturforsch B* 75:393–402
10. Chen M-M, Xue H-G, Guo S-P (2018) Multinary metal chalcogenides with tetrahedral structures for second-order nonlinear optical, photocatalytic, and photovoltaic applications. *Coord Chem Rev* 368:115–133
11. Heppke EM, Klenner S, Janka O, Pöttgen R, Lerch M (2020) Mechanochemical synthesis of $\text{Cu}_2\text{MgSn}_3\text{S}_8$ and $\text{Ag}_2\text{MgSn}_3\text{S}_8$. *Z Anorg Allg Chem* 646:5–9
12. Liu W, Hu J, Zhang S, Deng M, Han C-G, Liu Y (2017) New trends, strategies and opportunities in thermoelectric materials: a perspective. *Mater Today Phys* 1:50–60
13. Quintero E, Quintero M, Morocoima M, Bocaranda P (2007) Bound magnetic polarons in p-type $\text{Cu}_2\text{Cd}_{0.25}\text{Fe}_{0.75}\text{GeSe}_4$ and $\text{Cu}_2\text{FeGeTe}_4$. *J Appl Phys* 102:083905(1–5)
14. Quintero E, Quintero M, Moreno E, Lara L, Morocoima M, Pineda F, Grima P, Tovar R, Bocaranda P, Henao JA, Macías MA (2010) Magnetic properties for the $\text{Cu}_2\text{MnSnSe}_4$ and $\text{Cu}_2\text{FeSnSe}_4$ compounds. *J Phys Chem Solids* 71:993–998
15. Moroz M, Tesfaye F, Demchenko P, Prokhorenko M, Kogut Y, Pereviznyk O, Prokhorenko S, Reshetnyak O (2020) Solid-state electrochemical synthesis and thermodynamic properties of selected compounds in the Ag–Fe–Pb–Se system. *Solid State Sci* 107:106344(1–9)
16. Quintero M, Cadenas R, Tovar R, Quintero E, Gonzalez J, Ruiz J, Woolley JC, Lamarche G, Lamarche A-M, Broto JM, Rakoto H, Barbaste R (2001) Magnetic spin-flop and magnetic saturation in $\text{Ag}_2\text{FeGeSe}_4$, $\text{Ag}_2\text{FeSiSe}_4$ and $\text{Cu}_2\text{MnGeSe}_4$ semiconductor compounds. *Physica B* 294–295:471–474
17. Marquina J, Sierralta N, Quintero M, Rincon C, Morocoima M, Quintero E (2017) Study of the critical-fields and the thermal broadening in polycrystalline $\text{Ag}_2\text{FeGeSe}_4$ semiconducting compound. *Rev Mex Fis* 63:456–460
18. Diffractom. Stoe WinXPOW, Version 3.03 (2010) Stoe Cie GmbH Darmstadt
19. Kraus W, Nolze G (1996) Powder cell—a program for the representation and manipulation of crystal structures and calculation of the resulting X-ray powder patterns. *J Appl Crystallogr* 29:301–303

20. Villars P, Cenzual K (2014) Pearson's crystal data: crystal structure database for inorganic compounds. Release 2014/15. ASM International, Materials Park
21. Robinel E, Carette B, Ribes M (1983) Silver sulfide based glasses (I): glass forming regions, structure and ionic conduction of glasses in $\text{GeS}_2\text{-Ag}_2\text{S}$ and $\text{GeS}_2\text{-Ag}_2\text{S-AgI}$ systems. *J Non-Cryst Solids* 57:49–58
22. Moroz MV, Demchenko PYu, Mykolaychuk OG, Akselrud LG, Gladyshevskii RE (2013) Synthesis and electrical conductivity of crystalline and glassy alloys in the $\text{Ag}_3\text{GeS}_3\text{Br-GeS}_2$ system. *Inorg Mater* 49:867–871
23. Moroz M, Tesfaye F, Demchenko P, Prokhorenko M, Lindberg D, Reshetnyak O, Hupa L (2018) Determination of the thermodynamic properties of the $\text{Ag}_2\text{CdSn}_3\text{S}_8$ and $\text{Ag}_2\text{CdSnS}_4$ phases in the Ag-Cd-Sn-S system by the solid-state electrochemical cell method. *J Chem Thermodyn* 118:255–262
24. Moroz MV, Demchenko PYu, Prokhorenko SV, Moroz VM (2013) Physical properties of glasses in the $\text{Ag}_2\text{GeS}_3\text{-AgBr}$ system. *Phys Solid State* 55:1613–1618
25. Moroz MV, Prokhorenko MV, Prokhorenko SV (2015) Determination of thermodynamic properties of Ag_3SBr superionic phase using EMF technique. *Russ J Electrochem* 51:886–889
26. Tesfaye F, Taskinen P (2014) Electrochemical study of the thermodynamic properties of matildite ($\beta\text{-AgBiS}_2$) in different temperature and compositional ranges. *J Solid State Electrochem* 18:1683–1694
27. Moroz MV, Prokhorenko MV, Rudyk BP (2014) Thermodynamic properties of phases of the Ag-Ge-Te system. *Russ J Electrochem* 50:1177–1181
28. Moroz MV, Prokhorenko MV (2014) Thermodynamic properties of the intermediate phases of the Ag-Sb-Se system. *Russ J Phys Chem A* 88:742–746
29. Moroz MV, Prokhorenko MV, Reshetnyak OV, Demchenko PYu (2017) Electrochemical determination of thermodynamic properties of saturated solid solutions of Hg_2GeSe_3 , Hg_2GeSe_4 , $\text{Ag}_2\text{Hg}_3\text{GeSe}_6$, and $\text{Ag}_{1.4}\text{Hg}_{1.3}\text{GeSe}_6$ compounds in the Ag-Hg-Ge-Se system. *J Solid State Electrochem* 21:833–837
30. Babanly M, Yusibov Y, Babanly N (2011) The EMF method with solid-state electrolyte in the thermodynamic investigation of ternary copper and silver chalcogenides. In: S Kara (ed) *InTech*, pp 57–78
31. Moroz MV, Demchenko PYu, Prokhorenko MV, Reshetnyak OV (2017) Thermodynamic properties of saturated solid solutions of the phases $\text{Ag}_2\text{PbGeS}_4$, $\text{Ag}_{0.5}\text{Pb}_{1.75}\text{GeS}_4$ and $\text{Ag}_{6.72}\text{Pb}_{0.16}\text{Ge}_{0.84}\text{S}_{5.20}$ of the Ag-Pb-Ge-S system determined by EMF method. *J Phase Equilib Diffus* 38:426–433
32. Voronin MV, Osadchii EG, Brichkina EA (2017) Thermochemical properties of silver tellurides including empressite (AgTe) and phase diagrams for Ag-Te and Ag-Te-O . *Phys Chem Miner* 44:639–653
33. Moroz MV, Prokhorenko MV (2015) Measurement of the thermodynamic properties of saturated solid solutions of compounds in the Ag-Sn-Se system by the EMF method. *Russ J Phys Chem A* 89:1325–1329
34. Moroz MV, Prokhorenko MV (2015) Determination of thermodynamic properties of saturated solid solutions of the Ag-Ge-Se system using EMF technique. *Russ J Electrochem* 51:697–702
35. Alverdiev IDzh, Bagkheri SM, Imamalieva SZ, Yusibov YuA, Babanly MB (2017) Thermodynamic study of Ag_8GeSe_6 by EMF with an Ag_4RbI_5 solid electrolyte. *Russ J Electrochem* 53:551–554
36. Yusibov YuA, Alverdiev IDzh, Ibragimova FS, Mamedov AN, Tagiev DB, Babanly MB (2017) Study and 3D modeling of the phase diagram of the Ag-Ge-Se system. *Russ J Inorg Chem* 62:1223–1233
37. Yusibov YuA, Alverdiev IDzh, Mashadieva LF, Babanly DM, Mamedov AN, Babanly MB (2018) Experimental study and 3D modeling of the phase diagram of the Ag-Sn-Se system. *Russ J Inorg Chem* 63:1622–1635
38. Voronin MV, Osadchii EG (2013) Thermodynamic properties of silver and bismuth sulfosalts minerals, pavonite (AgBi_3S_5) and matildite (AgBiS_2) and implications for ore deposits. *Econ Geol* 108:1203–1210

39. Barin I (1995) Thermochemical data of pure substance. VCH, Weinheim
40. Olin Å, Nolang B, Ohman L-O, Osadchii EG, Rosen E (2005) Chemical thermodynamics of Selenium. Elsevier, Amsterdam

Author Index

A

Amatsu, Kenshiro, 201

C

Cárdenas-Falcón, Nilton, 93

Chen, Chao, 167

Chen, Min, 55, 167, 211, 227, 261

Cho, Yong Chan, 187

D

D´Abreu, José Carlos, 93

Demchenko, Pavlo, 271

Dionisio-Calderón, Enrique R., 93

E

Echeverry, Luver, 69

Eckert, Kerstin, 13

Eckert, Sven, 13

Estrada, Darwin, 69

G

Gómez-Marroquín, Mery C., 93

Gutierrez, Leopoldo, 69

H

Heitkam, Sascha, 13

Huamán-Pérez, Fernando, 93

Huarcaya-Nina, Jhony F., 93

Hua, Xiaojie, 261

Hupa, Leena, 271

I

Iloeje, Chukwunwike O., 107

J

Jiang, Silu, 177

K

Katamreddy, Sai, 187

L

Lappan, Tobias, 13

Lee, Geun Woo, 187

Lee, Jonghyun, 187, 249

Lee, Sooheyong, 187

Li, Ming, 155

Lindberg, Daniel, 271

Li, Xiaobao, 55

Luo, Jie, 3, 31

M

Mannes, David, 13

Miyasaka, Fumikazu, 201

Mori, Hiroaki, 201

Moroz, Mykola, 271

O

Olsen, Jan Erik, 83

P

Peng, Si-kun, 3

Peng, Yu, 177

Phatti-Satto, Kim J., 93
Prokhorenko, Myroslava, 271

Q

Qiu, Guibao, 221, 239
Quah, Titus, 107

R

Reddy, Ramana G., 141
Reshetnyak, Oleksandr, 271
Reynolds, Quinn Gareth, 83
Rudyk, Bohdan, 271

S

Sarma, Mārtiņš, 13
Shevchenko, Natalia, 13
Shinde, Pravin S., 141
Soliak, Lyudmyla, 271
Sun, Yanhui, 155

T

Tao, Biao, 155
Terrones-Ramirez, Abraham J., 93
Tsfaye, Fiseha, 271
Trtik, Pavel, 13

W

Wang, Hongpo, 177
Wang, Jian, 221, 239

Wang, Mingxing, 133
Wang, Nan, 55, 167, 227
Wang, Yijia, 133
Wang, Yu, 133
Wong, Cal Vin, 249
Wu, Huajie, 155

X

Xia, Yunxing, 201
Xuan, Mingtao, 261
Xu, Jiahao, 121

Y

Yang, Ding, 221, 239
Yue, Guikuan, 121

Z

Zhang, Ai-ping, 3, 31
Zhang, Chunming, 227
Zhang, Feng, 239
Zhang, Kaizhu, 261
Zhang, Lingxi, 211
Zhang, Tingan, 43
Zhang, Zimu, 43
Zhao, Li, 133
Zhao, Qiuyue, 43
Zheng, Mingzhao, 43
Zhong, Yong, 3
Zhou, Hanghang, 221
Zhou, Lei, 43
Zhu, Ming-mei, 31

Subject Index

A

Adsorption, [34](#), [69](#), [70](#), [72](#), [75](#), [76](#), [78](#), [183](#)
Adsorption test, [72](#)
Aeration leaching reaction, [44](#), [51](#)
A hybrid prediction model based on multiple BP neural network and decision tree model, [172](#)
A hybrid prediction model for end-point phosphorus content, [170](#)
Amount of escaped nitrogen and the solid solution limit of nitrogen, The, [207](#)
Analysis of aluminum and calcium mass fraction, [157](#)
Analysis of inclusions, [57](#)
Application of the optimized Iida model, [216](#)
Arsenic, [177–185](#)
Arsenic volatilization, [177](#), [182](#)
Attenuation characteristics, [15](#), [18](#), [19](#), [22](#), [23](#)

B

Base case results, [86](#)
Basic assumptions, [229](#)
Basic fit method, [109](#), [111](#), [112](#), [114](#), [115](#)
Basic fit method underpredicts cases with high feed concentrations, [114](#)
Blast furnace slag, [94](#), [221](#), [222](#), [225](#), [239–241](#)
BOF converter, [168](#)
Boundary conditions, [6](#), [10](#), [34](#), [46](#), [73](#), [229](#), [231](#), [251–253](#), [255](#), [264](#), [265](#)
Boundary conditions and CFD model validation, [46](#)
Boundary conditions and numerical details, [264](#)

Boundary conditions and numerical methods, [231](#)
BP neural network model, [168](#), [169](#), [171](#), [172](#)
Bubble column, [15](#), [16](#)
Bubble flotation, [13](#), [14](#)
Bubble flow in particle-laden liquid metal, [16](#), [20](#), [22](#), [23](#), [26](#)

C

Ca, [157](#), [159](#)
Calcium treatment, [155](#), [158](#), [161](#), [163](#), [164](#)
Calculated Species Distribution in Fe(II)-Fe(III)-Cu(II)-H₂SO₄-H₂O System from 25°C to 60°C, [125](#)
Calculated Species Distribution in Fe(II)-Fe(III)-H₂SO₄-H₂O System from 25°C to 60°C, [125](#)
Calculation method, [34](#)
CaO modification, [65](#), [67](#)
Carbon analysis, [96](#), [99](#)
Carbothermic reduction, [93–96](#), [99–104](#)
Carbothermic reduction tests, [96](#), [100](#)
Ceramic filter, [155–157](#), [160](#), [163](#)
Characterization and degradation, [70](#)
Characterization of LD steel sludges, [95](#)
Chemical compositions of steel and slag, [58](#)
Chronoamperometry (CA), [141](#), [143–152](#)
Cold spraying, [249](#)
Comparison between the developed model and other Eulerian model, [254](#)
Comparison between the developed model and the Lagrangian model, [255](#)
Comparison of flow fields, [8](#)
Comparison of inclusion removal effects, [10](#)
Comparison of redox potential between model result and experimental

- measurement from 25°C to 60°C, 128
 - Comparison of temperature fields, 9
 - Computational Fluid Dynamics (CFD), 43, 44, 46, 49, 51, 194, 196
 - Containerless processing, 188, 191, 198
 - Contrast-to-noise ratio, 17, 21, 25
 - Convection in melts, 188, 189, 228
 - Conversions (α) estimation, 97
 - Converter process, 94
 - Copper, 121–123, 129, 141, 143, 145, 151, 152, 188, 250, 252
 - C_p , 141, 143–146, 148, 149, 151, 152, 230
 - Cr_2O_3 , 211, 212, 216–218, 221, 222, 224, 225, 239–244, 246, 247
 - Crucible, 95, 96, 100, 134, 177–182, 184, 185, 213, 222, 223, 241
 - Crystallization of salt solutions, 193, 194
 - Cyclic Voltammetry (CV), 141, 143–149, 151
 - Cyclic voltammetry of Ti-free EMIC- $AlCl_3$ IL, 145
- D**
- Data collection and preprocess, 168
 - Data experiment with multiple BP neural network model, 171
 - Data overlapping, 167, 168, 170, 171, 175
 - Data pattern analysis by k -means method, 170
 - Decision tree algorithm, 167, 172, 173, 175
 - Deep layer neural network prediction model, 169
 - Design experiments and experimental planning, 99
 - Design of experiments and experimental planning, 96
 - Development of an Eulerian FE model, 252
 - Dissolution behavior, 239, 240, 242, 247
 - Duplex stainless steels, 201, 202, 204–206, 208
- E**
- Effectiveness of the hybrid prediction model, 174
 - Effect of operational parameters, 89
 - Effect of particle density changes on phase distribution, The, 50
 - Effect of rotation speed on dissolution rate of Cr_2O_3 in slag, 243
 - Effect of temperature on dissolution rate, 243, 244
 - Effect SEN structure parameters on free surface characteristics, 267
 - Effects of the magnetic field frequency, 138
 - Effects of the magnetic field intensity, 136, 137, 139
 - Electrochemical dissolution of Ti ions by CA-Electrolysis, 146
 - Electrochemical dissolution of Ti ions by CP-Electrolysis, 149
 - Electrochemical measurement, 124, 144, 145
 - Electrochemistry, 142, 152
 - Electrodeposition, 141–145, 148, 150, 152
 - Electrolyte preparation, 124
 - Electromagnetic and electrostatic levitators, 188
 - Electromagnetic field intensity, 133
 - Electromagnetic levitation, 187–189
 - Electromotive force measurements, 273
 - Electrophoretic mobility, 69, 72, 76–78
 - Electrophoretic mobility and aggregation measurements, 72
 - Electrostatic levitation, 187, 191
 - Electrowinning, 121, 122
 - EMF method, 276
 - EMIC- $AlCl_3$ ionic liquid, 141, 143, 144, 152
 - End-point phosphorus content, 167–170, 174
 - Eulerian formulation, 249–252, 256
 - Evolution of Inclusions during RH refining process, 58
 - Experimental measurements of viscosity of vanadium slag with different FeO, 214
- F**
- Ferromanganese, 83, 84, 88, 91
 - Filtered fit method, 112–115
 - Filtering improves prediction accuracy, 114
 - Flocculant characterization, 73
 - Flocculant preparation, 70
 - Flotation, 69–72, 75, 77, 78
 - Flow characteristics of molten slag, 231
 - Flow field, 3, 7, 17, 27, 31–33, 35, 37, 43, 44, 51, 231, 232, 262, 266
 - Flow field comparison, 37
 - Fluctuation of free surface, 31
 - Fluid flow, 6, 8, 31, 32, 35, 44, 83, 85, 229, 261
 - Fluid flow model, 229
 - Formation of CaO–MgO– Al_2O_3 ternary system inclusions, 62

Formation of MgO·Al₂O₃ spinel inclusions, 62
 Free surface characteristics while 3P-0 SEN used, 266
 Frequency, 16, 51, 94, 96, 98, 102, 133, 134, 136, 138, 139, 174, 175, 189, 191, 192, 196

G

GEM formulation, 108
 Geometrical description, 228
 Geometric model and mesh independence verification, 44
 Gibbs energy, 107–109, 277–280
 Gibbs minimization, 109
 Governing equations, 229, 264, 265

H

Heat loss, 6, 35, 227, 228, 231, 235
 Heat loss of pot outer surface and slag upper surface, 235
 Heat transfer and solidification equations, 230

I

Iida model, 211, 212, 214–218
 Impact of AISI304 steel particle at 1000 m/s, 256
 Impact of particle density changes on the flow field, The, 51
 Inclusion removal rate, 3, 10, 32, 39–41, 155
 Inclusions, 3–6, 8, 10, 11, 14, 31–35, 39, 55–67, 155–164, 178–180
 Inclusions evolution, 56, 58, 64
 Influence of Cr₂O₃ on slag phase, 244
 In-situ observation, 201, 202, 204
 Iron, 14, 26, 83, 94, 95, 97, 98, 101, 121–123, 141, 155, 190, 221, 224, 228, 239, 240
 Iterative fit increases prediction accuracy for multicomponent datasets, 116
 Iterative fit with mean squared error increases overall prediction accuracy, 117
 Iterative Pitzer fit method, 112–114, 116–118

J

Jetting, 254, 256–259

K

Kinetic parameters estimation, 98, 101
 K-means method, 167, 168, 170, 172, 175

L

Lagrangian and Eulerian formulations, 250
 Lagrangian formulation, 249–252, 256, 258
 Laser beam welding, 201–208
 Laser beam welding condition and shield gas, 203
 LD converter, 94
 LD steel sludges characterization, 98
 Linear parameter estimator, 109–111
 Linz Donawitz (LD), 93, 94
 Liquid level fluctuation, 32, 35, 40, 41
 Liquid metal, 13–20, 22–27
 Liquid metal loop, 16
 LLEPE implementation, 109
 Long shroud, 31, 32, 35, 37, 40, 41
 Low-temperature ESL, 188, 196–198

M

Magnetic semiconductors, 272
 Mass transport phenomena, 194, 198
 Materials and methods, 70, 178
 Materials of the mould flux, 134
 Mathematical model, 14, 31, 228, 229, 264
 Microflotation, 69, 72, 75, 77
 Microflotation test, 72
 Microstructural characteristics in the welds, 205
 Model description, 85
 Model development, 122, 123
 Model formulation, 4, 33
 Model hypothesis, 4, 32
 Modelling, 84, 85, 89
 Model particles, 13, 15, 17, 18, 20–27
 Modification of RH refining slag, 64
 Molecular dynamics simulation, 73, 76, 78
 Molten slag, 83, 133, 177, 191, 196, 227–229, 231–236, 243
 Molybdenite, 69–72, 75–78
 Morphology of typical Inclusions, 58
 Mould flux, 133–139
 Multi-pathway solidification, 193

N

Neural network model for end-point phosphorus content, 168
 Neutron radiography, 13, 15–18, 20–22, 26, 27

Nitrogen, 57, 58, 71, 72, 95, 161, 201–208, 213, 249
 Non-metallic inclusions, 3, 4, 13, 14, 27, 55, 56, 155, 161
 N slag and pot, 229, 231, 232, 236
 Numerical simulation, 3, 4, 6, 31, 32, 44, 48, 194, 231, 261, 262, 265
 Numerical simulation research method, 4

O

Optical microscope analysis, 158
 Optimization of Iida model, 215
 Optimize, 3, 65, 117

P

Parameter estimation, 107, 108, 118
 Particle-laden liquid metal flow around a cylindrical obstacle, 24
 Perovskite phase, 246
 Phase, 5, 15, 34, 35, 43–51, 56, 62–65, 83–86, 88, 91, 95, 97, 107–111, 119, 133, 139, 141, 142, 151, 152, 177, 188, 189, 193–197, 201, 202, 221–225, 234, 240, 244, 271–280
 Phase equilibria, 276
 Phase ratio, 202
 Physical parameters, 6, 35, 46
 Pitzer fit increases prediction accuracy for high feed concentrations, 115
 Pitzer fit method, 112–115, 117, 118
 Polyacrylamides, 69, 70, 73, 77, 78
 Practical application performance, 269
 Precipitation behavior, 202, 206
 Preheating of reactor and crucibles, 95
 Preparation and analysis of carbon, 96
 Preparation of EMIC-AICl₃ ionic liquid, 143
 Pyrometallurgy, 83, 122

R

Radiographic setup, 20
 Rare earth, 107, 111, 114, 115, 118, 119, 177, 183, 184
 Reaction between Rare Earth Element and slag, The, 183
 Reactions between REEs and Crucibles, 179, 182
 Redox potential, 122–124, 128, 129
 Reduction, 7, 27, 59, 93, 94, 96, 99–102, 115, 121, 122, 141–143, 145, 152, 190, 206, 211, 212, 215, 222, 239, 240
 Research method, 4, 228

Residence time distribution curve, 3, 31
 RH refining, 55–59, 64–67
 RTD curve, 11, 12, 37, 39
 RTD curve and flow pattern, 37

S

Samples and reagents, 71
 SEM-EDS analysis, 161
 Sensitivity to fluid properties, 88
 Shearing, 69–71, 74–78
 Silver-based phases, 272
 Simulation scheme, 6, 35
 Slag, 83–91
 Slag pot, 227–229, 231–233, 236
 Solidification, 15, 133, 187–189, 191, 193, 194, 196, 198, 202, 205, 206, 208, 230, 234
 Solidification characteristics of molten slag, 234
 Solubility of Cr₂O₃ in slag based on FactSage™ calculation, The, 246
 Solvent extraction, 107, 118
 Space experiments, 187, 189, 194, 196
 Speciation, 121, 122, 124–126, 129
 Spinel phase, 221, 225, 246
 Standard parameter estimator, 109–111
 Standard thermodynamic properties, 272
 Steel sludges, 93–95, 97–104
 Stirrer, 70, 144
 Structural analysis by XRD, 151
 Sulfuric acid, 121, 129, 242
 Synthesis and analysis, 273

T

Temperature, 3–7, 9–11, 13–15, 26, 31–35, 37, 39, 41, 59, 61, 72, 73, 83, 84, 88, 89, 93–96, 99–102, 108, 109, 121–123, 125–129, 133–139, 142–145, 148, 150, 156, 168, 178, 179, 188–194, 196–198, 213–217, 222, 227–234, 236, 239–244, 246, 247, 249–251, 253–258, 261, 262, 264–269, 271–275, 277, 279
 Temperature characteristics of molten, 232
 Temperature difference, 4, 9, 11, 37, 39, 190, 228, 233
 Temperature distribution, 9–11, 37, 232, 254, 261, 262, 266, 268
 Temperature field, 3, 5, 7, 9, 31–34, 133
 Test method, 135, 192
 Test system, 134, 135, 222

Thermodynamic calculation, [55](#), [61](#), [66](#), [246](#), [271](#)
Thermodynamic calculation for the formation of inclusions, [61](#)
Thermodynamic modeling, [121](#), [122](#), [128](#), [129](#)
Thermophysical and thermomechanical properties, [191](#)
Thermophysical properties, [187](#), [188](#), [190](#), [191](#), [194](#)
Thin slab, [261](#), [262](#)
Three-phase flow, [32](#)
Three-port SEN, [261](#)
Ti alloy, [142](#)
Ti-bearing slag, [222](#)
Tinplate steel, [55–57](#), [64–67](#)
Total oxygen mass fraction analysis, [157](#)
Tundish, [3–9](#), [11](#), [12](#), [31–38](#), [40](#), [41](#), [155–158](#), [161](#), [163](#), [196](#)
Turbulence suppressor, [9](#), [11](#), [32](#)

V

Vanadium slag, [211](#), [212](#), [218](#)
Vapor pressure, [180](#), [182](#), [190](#)
Viscosity, [4–6](#), [14](#), [16](#), [32–34](#), [65](#), [66](#), [71](#), [73](#), [74](#), [77](#), [87](#), [88](#), [91](#), [148](#), [189](#), [191](#), [192](#), [195](#), [211–218](#), [221–223](#), [225](#), [230](#), [243](#), [244](#), [246](#), [264](#)
Viscosity measurement, [69](#), [71](#), [212](#), [213](#), [223](#)

W

Water-model experiments, [262](#)

X

X-ray and neutron radiography, [13](#), [18](#), [26](#)
X-ray radiography, [15–18](#), [20–23](#), [26](#), [27](#)
X-ray transmission, [201–204](#)
X-ray transmission imaging system, [201](#), [203](#), [204](#)